

Electronic Theses and Dissertations, 2004-2019

2015

Nonlinear Optical Response of Simple Molecules and Two-Photon Semiconductor Lasers

Matthew Reichert
University of Central Florida

 Part of the [Electromagnetics and Photonics Commons](#), and the [Optics Commons](#)
Find similar works at: <https://stars.library.ucf.edu/etd>
University of Central Florida Libraries <http://library.ucf.edu>

This Doctoral Dissertation (Open Access) is brought to you for free and open access by STARS. It has been accepted for inclusion in Electronic Theses and Dissertations, 2004-2019 by an authorized administrator of STARS. For more information, please contact STARS@ucf.edu.

STARS Citation

Reichert, Matthew, "Nonlinear Optical Response of Simple Molecules and Two-Photon Semiconductor Lasers" (2015). *Electronic Theses and Dissertations, 2004-2019*. 717.
<https://stars.library.ucf.edu/etd/717>

NONLINEAR OPTICAL RESPONSE OF SIMPLE MOLECULES
AND
TWO-PHOTON SEMICONDUCTOR LASERS

by

MATTHEW REICHERT

B.S. Optical Engineering, Rose-Hulman Institute of Technology, 2010
M.S. Optics, University of Central Florida, 2012

A dissertation submitted in partial fulfillment of the requirements
for the degree of Doctor of Philosophy
in CREOL, the College of Optics and Photonics
at the University of Central Florida
Orlando, Florida

Summer Term
2015

Major Professors: Eric W. Van Stryland and David J. Hagan

© 2015 Matthew Reichert

ABSTRACT

This dissertation investigates two long standing issues in nonlinear optics: complete characterization of the ultrafast dynamics of simple molecules, and the potential of a two-photon laser using a bulk semiconductor gain medium.

Within the Born-Oppenheimer approximation, nonlinear refraction in molecular liquids and gases can arise from both bound-electronic and nuclear origins. Knowledge of the magnitudes, temporal dynamics, polarization and spectral dependences of each of these mechanisms is important for many applications including filamentation, white-light continuum generation, all-optical switching, and nonlinear spectroscopy. In this work the nonlinear dynamics of molecules are investigated in both liquid and gas phase with the recently developed beam deflection technique which measures nonlinear refraction directly in the time domain. Thanks to the utility of the beam deflection technique we are able to completely determine the third-order response function of one of the most important molecular liquids in nonlinear optics, carbon disulfide. This allows the prediction of essentially any nonlinear refraction or two-photon absorption experiment on CS₂. Measurements conducted on air (N₂ and O₂) and gaseous CS₂ reveal coherent rotational revivals in the degree of alignment of the ensemble at a period that depends on its moment of inertia. This allows measurement of the rotational and centrifugal distortion constants of the isolated molecules. Additionally, the rotational contribution to the beam deflection measurement can be eliminated thanks to the particular polarization dependence of the mechanism. At a specific polarization, the dominant remaining contribution is due to the bound-electrons. Thus both the bound-electronic nonlinear refractive index of air, and second hyperpolarizability of isolated CS₂ molecules, are measured directly. The later agrees well with liquid CS₂ measurements, where local field effects are significant.

The second major portion of this dissertation addresses the possibility of using bulk semiconductors as a two-photon gain medium. A two-photon laser has been a goal of nonlinear optics since shortly after the original laser's development. In this case, two-photons are emitted from a single electronic transition rather than only one. This process is known as two-photon gain (2PG). Semiconductors have large two-photon absorption coefficients, which are enhanced by ~ 2 orders of magnitude when using photons of very different energies, e.g., $\hbar\omega_a \approx 10\hbar\omega_b$. This enhancement should translate into large 2PG coefficients as well, given the inverse relationship between absorption and gain. Here, we experimentally demonstrate both degenerate and nondegenerate 2PG in optically excited bulk GaAs via pump-probe experiments. This constitutes, to my knowledge, the first report of nondegenerate two-photon gain. Competition between 2PG and competing processes, namely intervalence band and nondegenerate three-photon absorption (ND-3PA), in both cases are theoretically analyzed. Experimental measurements of ND-3PA agree with this analysis and show that it is enhanced much more than ND-2PG. It is found for both degenerate and nondegenerate photon pairs that the losses dominate the two-photon gain, preventing the possibility of a two-photon semiconductor laser.

To my wife.

ACKNOWLEDGMENTS

I gratefully acknowledge my advisors Eric W. Van Stryland and David J. Hagan for the opportunity to work in their research group. I also would like to acknowledge the other members of my dissertation committee, Patrick L. LiKamWa and Robert E. Peale for their time and effort in helping with my thesis. I must extend great appreciation and thanks to Arthur L. Smirl for his helpful discussions and great interest in our two-photon gain problem. I'd like to thank Greg Salamo for providing the thin GaAs samples on which the experimental work was conducted. I particularly thank Scott Webster for introducing me to the group and showing me the ropes.

I would also like to thank all of the member of the NLO group, especially those individuals who helped contribute directly to this dissertation. Manuel R. Ferdinandus for development of Dual-Arm Z-scan and Beam Deflection techniques, as well as beam deflection measurements of CS₂. Honghua Hu and Marcus Seidel for pulse width dependent Z-scan measurements of CS₂. Dmitri Fishman for help with degenerate four-wave mixing measurements and his amazing experimental skills and teaching ability in the laboratory. Jennifer M. Reed and Peng Zhao for theoretical and experimental work on coherent rotational revivals in air and gaseous CS₂. Davorin Peceli for picosecond Z-scan measurements of CS₂ and D-3PA measurements of GaAs. Claudiu M. Cirloganu and Peter D. Olszak for D-3PA measurements on GaAs, ZnSe, and ZnS, and theoretical work on Kane's 4-band model. Himansu S. Pattanaik for discussions of theoretical solid-state physics, particularly with regard to multi-photon absorption spectra. An especially great thanks to Brendan Turnbull for his great assistance on the 2PG problem. Finally, a special thanks Trenton R. Ensley, and to all of the other NLO group members, for the great discussions and though provoking contributions over the last five years.

TABLE OF CONTENTS

LIST OF FIGURES	xi
LIST OF TABLES	xx
LIST OF ACRONYMS AND ABBREVIATIONS	xxi
CHAPTER 1: INTRODUCTION	1
1.1. Ultrafast Nonlinear Dynamics of Molecules	1
1.2. Two-Photon Emission.....	4
1.3. Dissertation Outline	6
CHAPTER 2: NONLINEAR OPTICAL INTERACTIONS	8
2.1. Power Series Expansion of Polarization	8
2.2. Bound-electronic Third-Order Nonlinearities.....	13
2.2.1. Origins of bond-electronic third-order response.....	15
2.3. Noninstantaneous Third-order Nonlinearities.....	20
CHAPTER 3: EXPERIMENTAL METHODS	24
3.1. Linear Characterization.....	24
3.2. Nonlinear Characterization	24
3.2.1. Light Sources	25
3.2.1.1. Laser Sources	25
3.2.1.2. Optical Parametric Generators/Amplifiers	28

3.2.1.3. White-Light Continuum.....	30
3.2.2. Dual-arm Z-scan	30
3.2.3. Pump-probe.....	37
3.2.4. Degenerate Four-Wave Mixing	43
3.2.5. Beam Deflection	49
3.2.6. Two-photon Stimulated Emission Depletion.....	56
CHAPTER 4: ULTRAFAST NONLINEAR DYNAMICS OF MOLECULES	59
4.1. Origin of noninstantaneous third-order response of molecular liquids	60
4.1.1. Diffusive Reorientation.....	62
4.1.2. Libration.....	65
4.1.3. Vibration	66
4.1.4. Collision.....	67
4.2. Noninstantaneous response in Beam Deflection measurements.....	68
4.3. Response Function of Carbon Disulfide	73
4.3.1. Beam Deflection Measurements	73
4.3.2. Degenerate Four-Wave Mixing Measurements	83
4.3.3. Z-scan Measurements	85
4.4. Nonlinear Response of Molecular Gases	92
4.4.1. Theory of Rotational Revivals	92

4.4.2. Beam Deflection Measurement of Coherent Rotational Revivals	99
CHAPTER 5: TWO-PHOTON GAIN IN SEMICONDUCTORS.....	111
5.1. Two-Photon Emission.....	111
5.2. Experimental Observation of Two-Photon Gain	120
5.2.1. Degenerate Two-Photon Gain.....	121
5.2.2. Extremely Nondegenerate Two-Photon Gain.....	134
5.3. Competing Processes	138
5.3.1. Kane's Band Structure	139
5.3.2. Three-Photon Absorption.....	145
5.3.3. Intervalence Band Absorption	157
5.3.4. Free-carrier Absorption.....	162
5.4. Prospect of a Semiconductor Two-Photon Laser.....	164
5.4.1. Degenerate Two-Photon Laser	164
5.4.2. Nondegenerate Two-Photon Laser	168
5.4.3. Other Semiconductors.....	173
CHAPTER 6: CONCLUSIONS AND FUTURE WORK.....	179
6.1. Ultrafast Nonlinear Response of Simply Molecules.....	179
6.2. Two-Photon Gain in Semiconductors	181
APPENDIX A: NOTATION AND SYMBOLS	184

APPENDIX B: PAULI EXCLUSION PRINCIPLE IN 2PA	193
APPENDIX C: NUCLEAR SPIN STATISTICS	197
APPENDIX D: CONSISTENCY BETWEEN ONE AND TWO BEAM EXPERIMENTS	202
D.1. One Versus Two Beam Experiments	203
D.2 Relation between $\alpha^2(\omega a; \omega b)$ and $\alpha^2(\omega b; \omega a)$	207
APPENDIX E: SCALED MOMENTUM MATRIX ELEMENTS	210
APPENDIX F: COPYRIGHT PERMISSION	213
LIST OF REFERENCES	216

LIST OF FIGURES

Figure 1.1 Ellipsoidal model polarizability of molecule with three independent axes.....	2
Figure 1.2 Energy level transitions for a) 2PA, b) spontaneous 2PE, c) singly-stimulated 2PE, and d) doubly-stimulated 2PE	5
Figure 2.1 Energy diagram for perturbation approach to two-photon transitions	18
Figure 3.1. Schematic diagram of Clark-MXR CPA-2010 laser system.....	25
Figure 3.2 Schematic diagram of Coherent Legend Elite Duo HE+ laser system.....	26
Figure 3.3 Principle of operation of Light Conversion TOPAS.	28
Figure 3.4 Z-scan schematic showing a sample with positive n_2 showing (top) an increased beam size at the aperture when the sample is before focus, and (bottom) a reduced beam size when the sample is after focus.....	31
Figure 3.5 Examples of Z-scan signals (left) CA for positive NLR and zero NLA, (middle) OA signal for 2PA, and (right) open, closed, and divided signals with both positive NLR and 2PA. 32	32
Figure 3.6 Example of problems with measuring NLR of a thin film on a thick substrate. (left) Sequential Z-scan measurements of (red) a 3 μm film of ZnO on a 1 mm fused silica substrate, and (blue) bare fused silica substrate. (right) Difference between the two measurements.	34
Figure 3.7. Schematic diagram of Dual-arm Z-scan setup (reproduced with permission from Ref. [49]).....	35
Figure 3.8 Procedure of processing dual-arm Z-scan. (a) low energy scan of the (red) solution and (lack) solvent and (b) their difference which is the LEB, (c) high energy (11 nJ, $I_0 = 18 \text{ GW/cm}^2$) and (d) their difference, (e) direct comparison of (b) and (d), and (f) corrected solute signal and fit with $n_2 = -0.4 \times 10^{-19} \text{ m}^2/\text{W}$, and $\alpha_2 = 0.02 \text{ cm/GW}$ [49].	37
Figure 3.9 Diagram of Pump-probe experiment	38

Figure 3.10 Pump-probe measurement example showing normalized probe transmission versus delay where the signal originates from (black) 2PA with the pump, (red) 2PA induced FCA/ESA, and (blue) total.	39
Figure 3.11 Example of Pump-probe measurement of 2PA with varying GVM for (black) $\rho = 0$, (red) $\rho = \pm 5$, and (blue) $\rho = \pm 10$, where solid curves are positive ρ and dashed curves are negative ρ	42
Figure 3.12 Boxcar phase matching geometry	45
Figure 3.13 Illustration of beam deflected due to a thin prism.	49
Figure 3.14 (a) Diagram of Beam Deflection experimental setup. (b) Irradiance profile at sample plane showing position relative positioning and size of (red) excitation and (green) probe beams. (c) Zoom in of the beam overlapping within the sample from (a) showing irradiance dependent refractive index change and probe deflection. (d) Probe beam location on segmented quad-cell detector without and with deflection. (Reproduced with permission from Ref. [62]).....	50
Figure 3.15 Beam deflection measurements of a 1 mm sample of fused silica. (left) Measurement (circles) and fit (curves) for parallel (black) and perpendicular (red) polarizations. (right) Reduced pump irradiance to observe noise floor. (Modified with permission from Ref. [61])	55
Figure 3.16 Illustration of 2P-STED experimental setup.	57
Figure 4.1 Ellipsoidal molecule showing (left) polarizability and (right) local field induced dipole moment	63
Figure 4.2 (a) Calculated BD signal with only instantaneous material response with varying GVM for (black) $\rho = 0$, (red) $\rho = \pm 5$, and (blue) $\rho = \pm 10$, where solid curves are positive ρ and dashed curves are negative ρ . (b) Calculated (black circles) normalized temporal resolution T_{res} as a function of ρ and approximated by Equation (4.28) (red curve).	71

Figure 4.3 Calculated BD signal including both instantaneous and noninstantaneous response of the form of Equation with varying GVM for (black) $\rho = 0$, (red) $\rho = -5$, and (blue) $\rho = -10$ 72

Figure 4.4 Three CS₂ molecules of (top row) different initial orientations. When a field polarized in the y axis is applied, (bottom row) all of three align towards the y axis. 76

Figure 4.5 Measure (circles) beam deflection signal from a 1 mm cell of CS₂ for (black) parallel, (red) perpendicular, and (blue) magic angle polarizations. Solid curves are fits for the response function. (Reproduced with permission from Ref. [62].) 79

Figure 4.6 Noninstantaneous response function Rt of CS₂ (see Table 4.1) decomposed into (blue) collision, (green) libration, (red) diffusive reorientation, as well as the (black) total. (Reproduced with permission from Ref. [62]) 82

Figure 4.7 Fourier transform of Response function of CS₂, including (blue) collision, (green) libration, (red) diffusive reorientation, and (black) total. 83

Figure 4.8 (circles) Measured normalized DFWM signal, and (red) prediction from the response function, using Equation (3.22), on both (left) linear and (right) logarithmic scale. (Modified with permission from Ref. [62].) 84

Figure 4.9 Example (open points) measurements and (curves) fits of (left) OA Z-scans of ZnSe, and (right) CS Z-cans of CS₂ where that energies of (black squares) 3.5 nJ, (blue circles) 7.4 nJ, and (red triangles) 11 nJ. (Reproduced with permission from [62].) 86

Figure 4.10 n_2, eff of CS₂ for linear polarization from both (points) Z-scan measurements at (black) 700 nm and (green) 1064 nm, using both (closed) Clark-MXR and (open) EKSPLA laser systems, and (red curve) prediction from response function using Equation (4.42). The pink shaded

region corresponds to errors in the response function (see Table 4.1). (Reproduced with permission from [62].).....	87
Figure 4.11 Ratio of n_2 , eff of CS ₂ for circular and linear polarizations from both (black circles) Z-scan measurements at 700 nm and (red curve) prediction from response function. (Reproduced with permission from [62].)	89
Figure 4.12 (left) Z-scan measurements (points) of (black) NLR of CS ₂ with the noninstantaneous contribution subtracted, and (blue) 2PA. Curves are fit with sum-over-states model, where the prediction of n_2 , el has been multiplied by 2. (right) Measurements of n_2 , eff]long for (open) 13-20 ps pulses (closed) 2.5-17 ns pulses, and (blue) prediction from BD measurements of response function [62]......	90
Figure 4.13 Calculated normalized refractive index change from coherent rotational revivals from O ₂ for (dashed) only rotational ground state, and (solid) thermal distribution at 300 K. Insets illustrate probability distribution of molecular ensemble for positive (top) and negative (bottom) Δnt	96
Figure 4.14 (top) Relative occupation probability and (bottom) TJ versus J of (red) ¹⁴ N ₂ and (blue) ¹⁶ O ₂ at 300 K via Equations (4.55) and (4.59), respectively.....	99
Figure 4.15 Illustration of BD geometry where the (red) pump and (blue) probe cross in the vertical (yz) plane (top left) but the deflection is in the horizontal (xz) plane (bottom left). (Left) Beam profiles at overlap [120]......	100
Figure 4.16 (top) Measured (black) BD signal from air and fit (violet), which is a sum of both the individual contributions of (bottom left, red) N ₂ and (bottom right, blue) O ₂ [120].	101
Figure 4.17 Measured (black) and fit (violet) BD signal of air out to 300 ps of delay. Inset shows revival signal and fit about 197 ps. (Reproduced with permission from Ref. [120]).	103

Figure 4.18 (top) Fourier transform of the BD signal for air (black) with the fitting for N₂ (red) and O₂ (blue). Zoomed in plots for (lower left) low and (lower right) high rotational states along with fits both neglecting (dashed) and including (solid) centrifugal distortion. (Reproduced with permission from Ref. [120].) 104

Figure 4.19 (circles) Measurements of linewidth $\Gamma_J, J - 2$ versus J for (red) N₂ and (blue) O₂, with (curves) exponential fits. (Reproduced with permission from [120].)..... 106

Figure 4.20 Polarization dependence of BD signal from air for (black) parallel, (red) perpendicular, and (blue) magic angle polarizations. Inset shows signal about a delay of 6 ps. (Reproduced with permission from [120].) 107

Figure 4.21 Measured (black) BD signal from gaseous CS₂ and fit (red), including (top) full delay range, as well as zoom ins at the (bottom left) 1/4, (bottom center) 1/2, and (bottom right) 1/2 revival of ¹²C³²S³⁴S. (Modified with permission from [120].) 108

Figure 4.22 (circles) Measured and (curves) fit BD measurements of CS₂ gas. (left) Polarization dependence for (black) parallel, (red) perpendicular, and (blue) magic angle with (right) zoomed in plot at the magic angle [120]. 109

Figure 5.1 (left) Possible paths for 2PA in semiconductors interband (line) followed by intraband (circle), or *vice versa*. (right) Spectral dependence of 2PA in direct gap semiconductors for (black) degenerate, Equation (5.6), and nondegenerate, Equation (5.5), for (red) $\hbar\omega b = 0.2Eg$, and (blue) $\hbar\omega b = 0.1Eg$ 118

Figure 5.2 (left) Energy-momentum diagram illustrating doubly-stimulated ND-2PE (ND-2PG) in semiconductors [152]. (right) Two-photon gain spectrum for GaAs at $T = 20$ K, $N = 2 \times 10^{18}$ cm⁻³ for (black) degenerate, for (red) $\hbar\omega b = 0.2Eg$, and (blue) $\hbar\omega b = 0.1Eg$ 119

Figure 5.3 (a) Example structure of unprocessed GaAs samples. Here, $x = 0.47$ for the Al concentration of the AlGaAs buffer layers. The 4 μm thick GaAs was very similar. (b) Transmission spectrum of 1 μm thick GaAs sample glued to sapphire after processing	121
Figure 5.4 Plot of the transmission of the 1.59 eV (780 nm) excitation pulse versus input fluence.	122
Figure 5.5 Illustration of setup for one-photon gain excite-probe experiments	123
Figure 5.6 Results of excite-probe experiment showing change in transmission (color axis) of probe versus delay (horizontal axis) for several photon energies (vertical axis). The Black line indicates the photon energy (wavelength) of maximum transmission change.	124
Figure 5.7 Results of excite-probe experiment to observe net one-photon gain, where (a) is the directly measured total transmission, and (b) is the absorption coefficient calculated from (a) using Equation (5.7). The straight line with error indicates gain threshold where stimulated emission dominates absorption.	126
Figure 5.8 (a) Illustration of experimental setup for fluorescence experiments, and (b) measured fluorescence spectrum of 4 μm thick GaAs sample with only 0.73 eV (1700 nm) pump beam.	128
Figure 5.9 Measured (symbols) change in fluorescence due to the 0.73 eV ($\lambda = 1700$ nm) pump beam versus irradiance for several 1.59 eV (780 nm) excitation fluences. Curves are third order polynomial fits.	129
Figure 5.10 Illustration of setup for degenerate excite-pump-probe experiments.....	130
Figure 5.11 Measured transient normalized transmission from a degenerate pump-probe. Curves represent fits from Equations (5.8) - (5.10).	131
Figure 5.12 Results of excite-pump-probe experiment showing change in normalized transmission ΔT demonstrating (black) 2PA and (blue) 2PG.....	132

Figure 5.13 (left) Normalized probe transmission with an excitation fluence of 1.3 mJ/cm^2 for pump irradiances (black) 7 GW/cm^2 , (red) 10 GW/cm^2 , (red) 22 GW/cm^2 , and (blue) change in normalized transmission at zero delay versus pump irradiance where circles are data, and solid line is a linear fit. 134

Figure 5.14 Measured spectrum of DFG output using Orielt Monochromator (Cornerstone 130 1/8m) and HgCdTe detector for a nominal wavelength of (left) $3.7 \text{ }\mu\text{m}$ and (right) $8 \text{ }\mu\text{m}$. Black curves are measured data, and red curves are smoothed. 135

Figure 5.15 (left) Normalized probe transmission versus pump-probe delay for parallel (solid) and perpendicular (dashed) polarizations both with excitation fluence F_0 of zero (black) and 2.8 mJ/cm^2 (red). (right) Difference in normalized probe transmission ΔT for parallel and perpendicular polarizations versus pump-probe delay with (red) and without (black) excitation. 137

Figure 5.16 (left) Difference in normalized probe transmission ΔT for parallel and perpendicular polarizations versus excitation fluence at zero pump-probe delay. (right) Ratio of ΔT at $F_0 = 2.8 \text{ mJ/cm}^2$ to $F_0 = 0$ versus photon energy sum..... 138

Figure 5.17 Energy band diagram including heavy-hole, light-hole, and split-off valence bands showing phonon assisted FCA, intervalence band absorption, and 3PA..... 139

Figure 5.18 Kane's band structure of GaAs including (black) condition, (red) heavy-hole, (blue) light-hole, and (magenta) split-off bands..... 144

Figure 5.19 Possible pathways for 3PA..... 146

Figure 5.20 Calculated D-3PA spectrum of GaAs including individual contributions from each initial band (red) heavy-hole, (blue) light-hole, (magenta) split-off, and (black) total. 152

Figure 5.21 (circles) Z-scan measurements, (black curves) theory, as well as (red curve) scaled theory of D-3PA spectrum of (left) GaAs, (middle) ZnSe, and (right) ZnS, with scaling factors 4.5, 2, and 2.5, respectively. 153

Figure 5.22 (left) 3D plot and (right) 2D projection of the ND-3PA spectrum of GaAs plotted versus three-photon energy sum and nondegeneracy factor. The white-shaded region in the left plot is where 2PA is possible. 154

Figure 5.23 Enhancement of (black) 2PA (at $\hbar\omega a + \hbar\omega b = 1.44$ eV) and (red) 3PA (at $\hbar\omega a + 2\hbar\omega b = 1.6$ eV) versus photon energy ratio. 155

Figure 5.24 (top) Pump-probe measurements of $\alpha 3\omega a; \omega b, \omega b$ in GaAs. (black) D- and (red) END-3PA coefficient where $\lambda b = 7.75$ μm (circles) measured in GaAs and both (solid curves) theory and (dashed curves) theory $\times 2.5$ 156

Figure 5.25 Energy difference for (black) heavy-hole to light-hole, (red) heavy-hole to split-off, and (blue) light-hole to split-off intervalence band absorption. 158

Figure 5.26 Intervalence band absorption coefficients (neglecting carrier distributions) on (left) linear and (right) logarithmic scales, for (red) heavy-hole to split-off, (blue) light-hole to split-off, and (black) heavy-hole to light-hole transitions. Vertical dashed lines indicate cut off wavelengths. 159

Figure 5.27 Calculated intervalence band (left) absorption coefficient and (right) coefficient divided by hole number density for (solid) $2 \times 10^{18} \text{ cm}^{-3}$ and (dotted) 10^{15} cm^{-3} at 300 K for (red) heavy-hole to split-off, (blue) light-hole to split-off, and (black) heavy-hole to light-hole transitions. 160

Figure 5.28 Temperature dependence of intervalence band absorption on (left) linear and (right) logarithmic scales. Carrier temperatures of (solid) 300 K, (dash-dot) 500 K, (dash) 700 K, and

(dot) 900 K are shown for (red) heavy-hole to split-off, (blue) light-hole to split-off, and (black) heavy-hole to light-hole transitions.	162
Figure 5.29 Plot of the right hand side of Equation (5.68) divided by I (i.e., the total gain) versus irradiance. The shaded region represents the error based on literature values quoted in the text.	167
Figure 5.30 Plot of the (red) ND-2PG and (blue) D-2PA terms in the coefficient of Ia^2 of Equation (5.75) versus the nondegeneracy factor $\hbar\omega a/\hbar\omega b$	171
Figure 5.31 Net gain for a END-2PSL ($\hbar\omega a/\hbar\omega b = 10$) in GaAs via Equation (5.76) versus irradiance. The shaded region represents the error based on values quoted in the text.	172
Figure 5.32 Kane's band structure of zinc blende GaN, including (black) conduction (red) heavy-hole, (blue) light-hole, and (magenta) split-off bands.	173
Figure 5.33 Calculated (left) D-2PA and (right) D-3PA coefficients in GaN including contributions from the (red) heavy-hole, (blue) light-hole, and (magenta) split-off bands, as well as (black) total.	174
Figure 5.34 (left) Intervalence band absorption coefficient and (right) its division by the number density for (solid) $Nh = 8 \times 10^{18} \text{ cm}^{-3}$ and (dotted) 10^{15} cm^{-3} , showing both (red) heavy-hole to split-off and (blue) light-hole to split-off transitions, as well as (black) their total.	175
Figure 5.35 Net gain in GaN for both (left) degenerate and (nondegenerate) cases.	177

LIST OF TABLES

Table 4.1. Fit Parameters of Third-Order Response of CS ₂ . n_2, m are given in units of $10^{-19} \text{ m}^2/\text{W}$	80
Table 4.2 Bound-electronic third-order susceptibility and second hyperpolarizability of CS ₂	81
Table 4.3 CS ₂ sum-over-states model fit Parameters.....	91
Table 4.4 Weighting factor gJ based on nuclear spin statistics.....	98
Table 4.5 Molecular parameters for Coherent Rotational Revivals	103
Table 5.1 Parameters for zinc blende semiconductors.....	151
Table 5.2 Parameters for GaN 2PSL analysis.....	176

LIST OF ACRONYMS AND ABBREVIATIONS

2PA	Two-photon absorption
2PG	Two-photon gain
2PE	Two-photon emission
2PF	Two-photon induced fluorescence
2PL	Two-photon laser
2PSL	Two-photon semiconductor laser
AlGaAs	Aluminum gallium arsenide
AlGaInP	Aluminum gallium indium phosphide
BBO	Beta barium borate
CA	Closed aperture (Z-scan)
cm	centimeter (10^{-2} m)
CW	Continuous-wave
D-	Degenerate (equal energy)
DWFM	Degenerate four-wave mixing
eV	Electronvolt ($\sim 1.602 \times 10^{-19}$ J)
FCA	Free-carrier absorption
fs	femtosecond (10^{-15} s)
FWHM	Full width at half maximum
GaAs	Gallium arsenide
GaN	Gallium nitride
GW	gigawatt (10^9 W)
GVM	Group velocity mismatch

HW $1/e$ M	Half with at $1/e$ of maximum
HW $1/e^2$ M	Half with at $1/e^2$ of maximum
ISRE	Intermediate state resonance enhancement
K-shell	Lowest energy electric orbital
LBO	Lithium triborate
LEB	Low energy background
LHS	Left-hand side
meV	millielectronvolt (10^{-3} eV)
mW	milliwatt (10^{-3} W)
ND	Nondegenerate (unequal energy), Neutral density
Nd:YAG	neodymium-doped yttrium aluminum garnet
Nd:YLF	neodymium-doped yttrium lithium fluoride
nm	nanometer (10^{-9} m)
OA	Open aperture (Z-scan)
OPA/G	Optical parametric generator/amplifier
OPL	Optical path length
PPLN	Periodically polled lithium niobate
PBS	Polarizing beam splitter
<i>p-i-n</i>	p-type, intrinsic, n-type
Q	Quality factor
QD	Quantum dot
QW	Quantum well

RHS	Right-hand side
SPA	Single-pass amplifier
SPDC	Spontaneous parametric down-conversion
STED	Stimulated emission depletion
SVEA	Slowly-varying-envelope-approximation
TDSE	Time-dependent Schrödinger equation
TEM	Transverse Electromagnetic
THz	Terahertz ($= 10^{12} \text{ s}^{-1}$)
TISE	Time-independent Schrödinger equation
ZnO	Zinc oxide
μm	micrometer, micron ($= 10^{-6} \text{ m}$)

CHAPTER 1: INTRODUCTION

Typically, the optical properties (e.g., refractive index and absorption coefficient) of materials are independent of the irradiance (optical power per unit area). In nonlinear optics, however, these properties are altered by the presence light itself, which can give rise to a wide range of novel phenomena. Two principle nonlinear interactions are nonlinear refraction and nonlinear absorption, which are the changes in refractive index and absorption coefficient due to high irradiance. This thesis covers two main bodies of work within the realm of nonlinear optical spectroscopy. The first is on the development of a novel nonlinear optical spectroscopic technique, beam deflection, and its application to study the ultrafast nonlinear dynamics of molecules. This work includes a complete characterization the nonlinear refractive dynamics of liquid carbon disulfide as well as molecular gases such as air. The second is an experimental investigation of two-photon gain in bulk semiconductors, specifically GaAs, for the purpose of determining the possibility of a two-photon semiconductor laser.

1.1. Ultrafast Nonlinear Dynamics of Molecules

The dynamics of molecules can give rise to large nonlinear refraction. Simple linear molecules that have a larger polarizability α along their axis than in the perpendicular directions, as shown in Figure 1.1. An incident electric field, which in general is at some angle θ with respect to the molecular axis, loosely speaking, displaces the electrons along this axis thereby inducing a dipole. The electric field then applies a torque to this dipole, causing the molecules to rotate towards the field direction. With the molecules aligned with it, the field now experiences an increased polarizability and therefore an increased refractive index. This can be the dominant mechanism of nonlinear refraction in simple molecular gases and liquids.

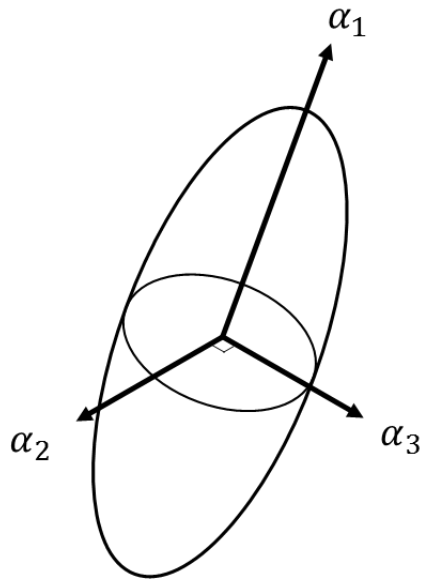


Figure 1.1 Ellipsoidal model polarizability of molecule with three independent axes.

There is, however, a time delay between the arrival of the electric field to the sample and the resulting change in refractive index due to inertia. It takes some time for the molecules to align towards the incident field direction. In liquids, where the density is high, the molecules collide with one another causing decay of the alignment back to a random thermal distribution that occurs on a picosecond timescale. In dilute gases the collision rate is orders of magnitude lower, and so the molecules continue to rotate, giving rise to periodic oscillations, or “revivals”, in the refractive index change. For the molecules studied here, the revival period is on the order of 10 to 100 ps, depending on the moment of inertia.

This dynamical nature of nonlinear refraction makes measurements difficult to analyze. Practically, the high irradiances necessary to induce significant changes in refractive index requires the use of ultrashort optical pulses. Measurements of the refractive index change are generally indirect in the sense that the induced phase change itself is not directly measurable. Its impact on

measurable quantities, such as the irradiance distribution upon propagation or on the spectrum of the pulse, allows the phase change to be inferred. However, measurement of material properties depends on the assumed formulation of the induced refractive index change. Neglect of the temporal dynamics exhibited by molecular systems can lead to perceived material properties that depend on the experimental parameters, specifically, pulse width dependent nonlinear refractive indices. This is, of course, not an accurate description of the actual underlying physical processes.

To correctly determine the dynamics of these molecular systems, we developed a pump-probe measurement technique capable of measuring nonlinear refraction in the time-domain, beam deflection. The technique consists of an ultrashort pump pulse that induces a temporally varying refractive index change in the material, which is measured by a probe pulse that is displaced to the wings of the pump beam in the sample. The probe experiences a spatial gradient in the refractive index, much like a thin prism, and is deflected by a small angle. Upon propagation, the deflection angle causes a shift in the far-field, which is measured with a position sensitive detector. The technique is very robust, capable of measuring polarization dependences, nondegenerate nonlinearities, and temporal dynamics. This allows the complete determination of the time dependent nonlinear response function, including sign and absolute magnitudes of each mechanism, their rise and fall time constants, and polarization dependencies. Knowledge of the response function allows prediction of any nonlinear refraction measurement on the material, truly establishing it as a proper reference material.

1.2. Two-Photon Emission

Multi-photon processes, predicted by Dirac [1], have been understood theoretically since the foundational work of Göppert-Mayer [2], in which the both the simultaneous emission or absorption of two quanta by a single electronic transition was described by second-order perturbation theory. The latter has become known as two-photon absorption (2PA) (see Figure 1.2 (a)). The opposite process, where an excited electron decays with the simultaneous emission of two-photons, is also possible as illustrated in Figure 1.2 (b). Breit and Teller [3] first showed that the lifetime of the metastable $2s$ level of hydrogen is dominated by spontaneous two-photon emission (2PE). A major difference from one-photon decay is that the individual photons may take on any energy value so long as the sum matches the transition energy, i.e., $\hbar\omega_a + \hbar\omega_b = E_{fi}$. Thus, spontaneous 2PE produces a continuous spectrum of photon energies less than E_{fi} . It was found that this form of emission could explain a portion of the continuum from planetary nebulae and other celestial bodies composed predominantly of atomic hydrogen.

The relation between the absorption and stimulated emission of a single photon also exists in the two-photon case. When two photons interact with an electron in an excited state, there is a probability that they will stimulate a transition to the ground state producing two additional photons. These stimulated photons have all the same properties as one-photon stimulated emission, i.e. equal energy, polarization, phase, direction, etc. as the stimulating photons. Again, the individual photon energies are not determined, so long as their sum matches the transition energy. Thus, stimulated 2PE may not only be observed for equal, or degenerate (D-2PE), photon energies, but also for unequal, or nondegenerate (ND-2PE), photon energies as well. Therefore, an amplifier based on this process may be continuously tunable for photon energies less than E_{fi} . In addition, if a single photon with energy $\hbar\omega_a < E_{fi}$ interacts with an excited electron there is a probability

that a stimulated photon at $\hbar\omega_a$ and a *spontaneous* photon at the complementary energy $\hbar\omega_b$ will be emitted (see Figure 1.2 (c)). While the stimulated photon at $\hbar\omega_a$ has the same stimulated emission properties listed above, the complementary photon does not, but rather has characteristics just as one-photon spontaneous emission. This is referred to as singly-stimulated 2PE, in contrast to doubly-stimulated 2PE, or two-photon gain (2PG), shown in Figure 1.2 (d), involving two input photons.

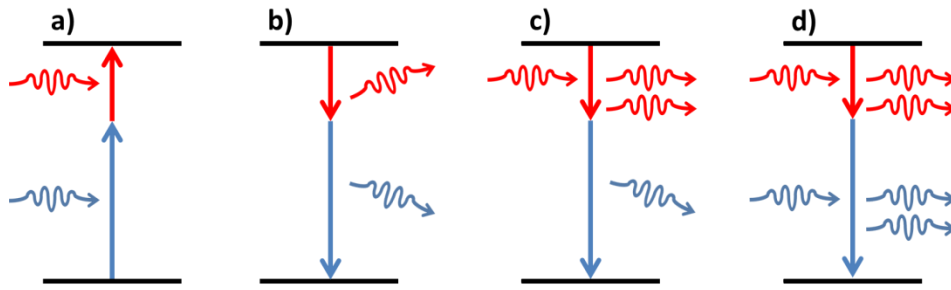


Figure 1.2 Energy level transitions for a) 2PA, b) spontaneous 2PE, c) singly-stimulated 2PE, and d) doubly-stimulated 2PE

There has been theoretical interest [4, 5] in making use of stimulated 2PE to create an amplifier and ultimately a two-photon laser (2PL). Numerous studies have suggested that a two-photon gain (2PG) medium will exhibit many interesting traits, owing to the intrinsic nonlinearity of the process, including pulse compression [6], self-mode-locking [7], and the requirement of an injection signal to initiate lasing [5]. In addition, several quantum properties of 2PL's have also been explored, including unique photon statistics [8], the production of squeezed states [9], and entanglement [10]. The majority of work has been done with discrete atomic systems in mind, due to the initial observations of spontaneous 2PE in atomic hydrogen, and two-photon amplifiers and lasers have been demonstrated in atomic systems [11, 12].

Most experimental work on 2PE has been done in dilute atomic beams, which suffer from the problem of low densities which limit the potential gain. Semiconductors, on the other hand, are advantageous in this regard benefiting from large carrier concentrations, meaning they have great potential for large power output. Moreover, they lack electronic states within the band gap that would allow cascaded one-photon emission to compete with 2PE. Recently, semiconductors have become of interest for use as 2PG media, and spontaneous as well as both singly- and doubly-stimulated 2PE have been reported [13]. Direct-gap semiconductors also have a large and well characterized 2PA coefficient which is greatly enhanced for nondegenerate photon pairs. Thus a 2PL with a bulk, direct gap, semiconductor gain medium may be continuously tunable from the band gap energy far out into the infrared. We are particularly motivated by the predicted [14] and recently observed [15] enhancement of the two-photon absorption coefficient when using extremely nondegenerate (END) photon pairs. This enhancement of the 2PA should also translate into enhancement of the 2PG. There are, of course, a multitude of competing processes that will limit the applicability of such a device, including free-carrier absorption (FCA) and higher order absorption such as three-photon absorption (3PA). The goal of this work is to observe 2PG in bulk GaAs, both in the degenerate and nondegenerate cases, to determine whether net gain $>$ losses is possible, and thus determine the viability of a semiconductors 2PL.

1.3. Dissertation Outline

This dissertation, the nonlinear response of materials, including nearly instantaneous bound-electronic nonlinear refraction and two-photon absorption as well as and noninstantaneous nuclear nonlinear refraction, is discussed in CHAPTER 2: CHAPTER 3: discusses the laser sources and the experimental methods used in this work, including Z-scan, pump-probe, and beam deflection

techniques. The origin of the ultrafast nonlinear response of simple molecules is discussed in CHAPTER 4: in liquid CS₂ and gaseous media. Discussion of 2PG in CHAPTER 5: includes an overview on the work done on two-photon emission, including spontaneous, singly-, and doubly-stimulated, followed by experimental observations of D- and ND-2PG follow in bulk GaAs in § 5.2. The dominant competing processes, specifically free-carrier, intervalence band, and three-photon absorption, are also discussed in § 5.3. , and the latter two are theoretically analyzed based on Kane's band structure. § 5.4. contains analysis of the viability of a GaAs 2PL in light of these results, as well as other potential materials. CHAPTER 6: provides conclusions and summary of the report, and discusses future possible directions to continue perusing.

CHAPTER 2: NONLINEAR OPTICAL INTERACTIONS

The group of phenomena involving the manipulation of light with light through some intermediary material is known as nonlinear optics. It can usually be thought of in the sense that a light beam interacts with a material and changes its properties that another light beam observes. This group of phenomena covers a large span of time domains, from relatively slow effects such as thermal (\sim ms), or electrostriction (\sim ns), to nearly instantaneous bound-electronic nonlinearities (limited by uncertainty relations, $<$ fs). In addition, an entire regime known as nonlocal nonlinearities, where a light beam in one location influences the properties of the material that another beam observes elsewhere, usually via some diffusion mechanism, is not addressed here.

2.1. Power Series Expansion of Polarization

In a source free, nonmagnetic material, from Maxwell's equations we can arrive at [16-18]

$$\nabla \times \nabla \times \tilde{\mathbf{E}}(t) = -\mu_0 \epsilon_0 \frac{\partial^2 \tilde{\mathbf{E}}(t)}{\partial t^2} - \mu_0 \frac{\partial^2 \tilde{\mathbf{P}}(t)}{\partial t^2} \quad (2.1)$$

where $\tilde{\mathbf{E}}(t)$ and $\tilde{\mathbf{P}}(t)$ are the real, time varying electric field and polarization vectors, respectively, t is time, and μ_0 and ϵ_0 are the permeability and permittivity of free space, respectively.

We may use the vector identity $\nabla \times \nabla \times \mathbf{A} = \nabla(\nabla \cdot \mathbf{A}) - \nabla^2 \mathbf{A}$, along with the Gauss's law $\nabla \cdot \tilde{\mathbf{D}}(t) = \rho_f = 0$, and the definition $\tilde{\mathbf{D}}(t) = \epsilon_0 \tilde{\mathbf{E}}(t) + \tilde{\mathbf{P}}(t)$ to write the left hand side (LHS) of Equation (2.1) as

$$\nabla \times \nabla \times \tilde{\mathbf{E}}(t) = -\frac{1}{\epsilon_0} \nabla (\nabla \cdot \tilde{\mathbf{P}}(t)) - \nabla^2 \tilde{\mathbf{E}}(t). \quad (2.2)$$

Typically one assumes $\left| \frac{1}{\varepsilon_0} \nabla \left(\nabla \cdot \tilde{\mathbf{P}}(t) \right) \right| \ll |\nabla^2 \tilde{\mathbf{E}}(t)|$, meaning that the material polarization (both linear and nonlinear) changes more slowly in space than the electric field oscillates. Neglecting this first term, we then arrive at the wave equation

$$\nabla^2 \tilde{\mathbf{E}}(t) - \frac{1}{c^2} \frac{\partial^2 \tilde{\mathbf{E}}(t)}{\partial t^2} = \mu_0 \frac{\partial^2 \tilde{\mathbf{P}}(t)}{\partial t^2}, \quad (2.3)$$

where $c = 1/\sqrt{\mu_0 \varepsilon_0}$ is the speed of light. The polarization of the material may be expressed as a sum of convolutions of the material susceptibility tensor functions $\boldsymbol{\chi}^{(i)}(t)$ with the electric field

$$\begin{aligned} \tilde{\mathbf{P}}(t) = & \varepsilon_0 \int_{-\infty}^{\infty} \boldsymbol{\chi}^{(1)}(t - t_1) \cdot \tilde{\mathbf{E}}(t_1) dt_1 \\ & + \varepsilon_0 \iint_{-\infty}^{\infty} \boldsymbol{\chi}^{(2)}(t - t_1, t - t_2) : \tilde{\mathbf{E}}(t_1) \tilde{\mathbf{E}}(t_2) dt_1 dt_2 \\ & + \varepsilon_0 \iiint_{-\infty}^{\infty} \boldsymbol{\chi}^{(3)}(t - t_1, t - t_2, t - t_3) : \tilde{\mathbf{E}}(t_1) \tilde{\mathbf{E}}(t_2) \tilde{\mathbf{E}}(t_3) dt_1 dt_2 dt_3 \\ & + \dots \end{aligned} \quad (2.4)$$

where $\boldsymbol{\chi}^{(1)}$, $\boldsymbol{\chi}^{(2)}$, and $\boldsymbol{\chi}^{(3)}$ are the first, second, and third order susceptibility tensors, and $:$ denotes the tensor product. Each term represents the response of the material to the incident electric field to successively higher order; the first term is linearly dependent on the electric field, the second term depends on the square of the electric field, and so on. The polarization then acts a source, or driving term, which via Equation (2.3) impacts the electric field itself. In this way both the linear and nonlinear interaction of light with a material can be described. The first term in Equation (2.4) gives rise to linear refraction and one-photon absorption, while the second is responsible for parametric processes such as second harmonic generation. The third term can be used to describe a number of processes, including third harmonic generation, four-wave mixing, Raman scattering,

as well as both nonlinear refraction and two-photon absorption. Higher order terms are of decreasing interest, but may still result in observable phenomenon. For example the fifth term which contains $\chi^{(5)}$, describes (among other things) three-photon absorption.

For bound-electronic nonlinearities, it is often convenient to work in the frequency domain, rather than in the time domain since the convolutions appearing in Equation (2.4) simply become products. The Fourier transform of Equation (2.4) yields

$$\begin{aligned}
\mathbf{P}(\omega) = & \varepsilon_0 \chi^{(1)}(\omega) \cdot \mathbf{E}(\omega) \\
& + \varepsilon_0 \iint_{-\infty}^{\infty} \chi^{(2)}(\omega; \omega_n, \omega_m) : \mathbf{E}(\omega_n) \mathbf{E}(\omega_m) \delta(\omega - \omega_n - \omega_m) d\omega_n d\omega_m \\
& + \varepsilon_0 \iiint_{-\infty}^{\infty} \chi^{(3)}(\omega; \omega_n, \omega_m, \omega_o) : \mathbf{E}(\omega_n) \mathbf{E}(\omega_m) \mathbf{E}(\omega_o) \delta(\omega - \omega_n - \omega_m \\
& \quad - \omega_o) d\omega_n d\omega_m d\omega_o \\
& + \dots
\end{aligned} \tag{2.5}$$

where $\mathbf{E}(\omega)$ and $\mathbf{P}(\omega)$ are Fourier transforms of the real, time varying electric field and polarization, respectively, and ω is the optical frequency (typically of the order 10^{15} rad/s). The notation used here for the arguments of $\chi^{(i)}$ indicates that the frequency argument appearing before the semicolon is given by the sum of those appearing after, e.g., for the second term $\omega = \omega_n + \omega_m$, as indicated by the Dirac delta function.

If we assume the linear term dominates the response of the material, as is usually the case, we may approximate the solutions to Equation (2.3) as plane waves oscillating at a particular frequency. We may then write the total field as a sum of these plane waves

$$\tilde{\mathbf{E}}(t) = \sum_n \tilde{\mathbf{E}}_n(t) = \sum_n \frac{1}{2} \mathcal{E}_i(\omega_n) e^{i(\mathbf{k}_n \cdot \mathbf{r} - \omega_n t)} + c. c. \quad (2.6)$$

where \mathcal{E}_i is the complex electric field amplitude, \mathbf{k}_n is the real wavevector of magnitude $|\mathbf{k}_n| = k_n = \text{Re} \left\{ \sqrt{1 + \chi_{ii}^{(1)}(\omega_n)} \right\} \omega_n / c = n_i(\omega_n) \omega_n / c$, where $n_i(\omega_n)$ is the refractive index, \mathbf{r} is the unit direction vector, the subscript i indicates the field direction (x , y , or z directions), and $c. c.$ indicates the complex conjugate of the preceding term. We also assume the polarization to consist of plane waves

$$\tilde{\mathbf{P}}(t) = \sum_n \tilde{\mathbf{P}}_n(t) = \sum_n \frac{1}{2} \mathcal{P}_i(\omega_n) e^{i(\mathbf{k}_n \cdot \mathbf{r} - \omega_n t)} + c. c. \quad (2.7)$$

where $\mathcal{P}_i(\omega_n)$ is the complex polarization amplitude. We assume that both $\mathcal{E}_i(\omega_n)$ and $\mathcal{P}_i(\omega_n)$ vary slowly in space with respect to the wavelength λ_n , and in time with respect to the optical period $2\pi/\omega_n$. This allows us to neglect their second derivatives in both time and space. The complex polarization amplitude can be expanded in terms of orders of the field, $\mathcal{P}_i(\omega_n) = \mathcal{P}_i^{(1)}(\omega_n) + \mathcal{P}_i^{(NL)}(\omega_n)$, where linear term is

$$\mathcal{P}_i^{(1)}(\omega_n) = \varepsilon_0 \chi_{ij}^{(1)}(\omega_n; \omega_n) \mathcal{E}_j(\omega_n), \quad (2.8)$$

where a summation over the subscript j is implied (so called Einstein notation). Furthermore, we

use $\sqrt{1 + \chi_{ii}^{(1)}(\omega_n; \omega_n)} = n_i(\omega_n) + i\kappa_i(\omega_n)$, where $\kappa_i(\omega_n)$ is the imaginary portion of the complex refractive index, and is related to the one-photon absorption coefficient $\alpha_1(\omega_n) = 2\kappa(\omega_n)\omega_n/c$. If we assume the plane waves to be propagating in the z direction, Equation (2.3) then becomes (suppressing frequency arguments and subscripts)

$$i2k \left\{ \frac{\partial \mathcal{E}}{\partial z} + \frac{n}{c} \frac{\partial \mathcal{E}}{\partial t} + \frac{\alpha_1}{2} \mathcal{E} \right\} e^{ikz} = -\mu_0 \omega \left\{ i2 \frac{\partial \mathcal{P}}{\partial t} + \omega \mathcal{P} \right\} e^{ik_{NL}z} \quad (2.9)$$

where $\mathcal{P} = \mathcal{P}^{(NL)}(\omega_n)$, and we have assumed $\kappa^2 \ll n^2, 2n\kappa$, and thus neglected these terms. Since \mathcal{P} is assumed to be slowly varying in time, and ω is very large ($\sim 10^{15}$ rad/s), $2|\partial \mathcal{P}/\partial t| \ll \omega|\mathcal{P}|$, we neglect the first term on the right hand side (RHS). Furthermore, the second term on the LHS may be neglected for continuous waves (CW) or long pulses. For short pulses, however, we may always transform into the reference frame of the moving pulse, which causes the second term to cancel. Finally, we neglect one-photon absorption, which is typically the case in practice since it would necessarily reduce the nonlinear interaction by depleting the electric field. In either case, the result is the slowly varying envelope approximation (SVEA) nonlinear wave equation

$$\frac{\partial \mathcal{E}}{\partial z} = i \frac{\omega}{2nc\epsilon_0} \mathcal{P} e^{i(k_{NL}-k)z}. \quad (2.10)$$

The evolution of \mathcal{E} is then found by substituting the expression for \mathcal{P} given by Equation (2.5) that corresponds to the frequency ω , and solving. For example, for second harmonic generation of a particular input frequency $\omega_b = 2\omega_a$, $\mathcal{P} = \mathcal{P}_b^{(2)} = \frac{\epsilon_0}{2} \chi_{xyy}^{(2)}(\omega_b; \omega_a, \omega_a) \mathcal{E}_b^2$, where the subscript on $\chi_{xyy}^{(2)}$ indicates that the electric field at ω_a is polarized along the y direction, and the second harmonic polarization is along the x direction, and the SVEA equation becomes

$$\frac{\partial \mathcal{E}_b}{\partial z} = i \frac{\omega_b}{2n_b c} \chi_{xyy}^{(2)}(\omega_b; \omega_a, \omega_a) \mathcal{E}_a^2 e^{i(2k_a - k_b)z}. \quad (2.11)$$

Likewise, the SVEA equation governing the evolution of the electric field at ω_a is

$$\frac{\partial \mathcal{E}_a}{\partial z} = i \frac{\omega_a}{2n_a c} \left\{ \chi_{yxy}^{(2)}(\omega_a; \omega_b, -\omega_a) + \chi_{yyx}^{(2)}(\omega_a; -\omega_a, \omega_b) \right\} \mathcal{E}_b \mathcal{E}_a^* e^{-i(2k_a - k_b)z}. \quad (2.12)$$

Thus the two field amplitudes are coupled through a set of equations. It is important to notice that this coupling depends strongly on the wavevectors of the two fields appearing in the exponential

phase term. If this phase mismatch, here $2k_a - k_b$, is large, meaning that the two waves propagate with different phase velocities, the coupling will be weak. This occurs because the field \mathcal{E}_b generated at a particular location, say $z = 0$, will, upon propagation, have a different phase than the field generated at a further distance, and thus does not add constructively. The optimum condition for the greatest interaction, known as the phase matching condition, occurs here when $2k_a - k_b = 0$, and thus the waves add constructively throughout the material.

In general Equation (2.10) may also be used to describe higher order processes, such as third-order nonlinearities, which will be discussed in the following section.

2.2. Bound-electronic Third-Order Nonlinearities

We now look specifically at the material response that depends on the field amplitude to third order. As mentioned above, third-order processes include third harmonic generation, four-wave mixing, and Raman scattering. However, we are particularly interested in the material response which directly influences the incident field itself, meaning we look at terms in the third-order polarization which oscillate at the same frequency as the incident electric field. One special feature of this type of third-order nonlinearity is that it is automatically phase matched, since the generated field is at the same frequency of the incident field, and thus has the same wavevector.

For two input fields, at ω_a and ω_b , and an instantaneous material response, the third-order polarization amplitude at frequency ω_a is given by

$$\begin{aligned} \mathcal{P}_a^{(3)} = \frac{\epsilon_0}{4} \{ & 3\chi_{yyyy}^{(3)}(\omega_a; \omega_a, -\omega_a, \omega_a) |\mathcal{E}_a|^2 \mathcal{E}_a \\ & + 6\chi_{yyyy}^{(3)}(\omega_a; \omega_a, -\omega_b, \omega_b) |\mathcal{E}_b|^2 \mathcal{E}_a \}, \end{aligned} \quad (2.13)$$

It has been assumed that the polarization is oriented along the same direction as the applied electric field, and propagates in the same direction. Intrinsic permutation symmetry, i.e. the fact that the order in which the fields are multiplied makes no physical difference (they commute), has been utilized. The first term in brackets of Equation (2.13) corresponds to self-nonlinearity where the single wave at frequency ω_a acts upon itself, while the second term corresponds to cross-nonlinearity where a second wave acts upon the first. Note that the cross term is twice that of the self term. This arises from the fact that there are more permutations of the third-order susceptibility, 6 versus 3, which need to be added.

It is often very useful to separate the field into amplitude and phase $\mathcal{E}_a(z) = \sqrt{\frac{2}{\varepsilon_0 n_a c}} I_a(z) e^{i\Delta\phi_a(z)}$, where $I_a(z)$ is the irradiance, and $\Delta\phi_a(z)$ is the induced nonlinear phase change. Using this, and substituting Equation (2.13) into (2.10), we can arrive at

$$\frac{\partial \Delta\phi_a(z)}{\partial z} = k_{0,a} n_2(\omega_a; \omega_a) I_a(z) + 2k_{0,a} n_2(\omega_a; \omega_b) I_b(z), \quad (2.14)$$

$$\frac{\partial I_a(z)}{\partial z} = -\alpha_2(\omega_a; \omega_a) I_a^2(z) - 2\alpha_2(\omega_a; \omega_b) I_b(z) I_a(z), \quad (2.15)$$

and likewise for wave b . In Equations (2.14) and (2.15) k_0 is the free space wavenumber, n_2 is the nonlinear refractive index, and α_2 is the two-photon absorption (2PA) coefficient, and the frequency argument $(\omega_a; \omega_b)$ specifies the nonlinearity observed by the wave at ω_a due to the wave at ω_b . In the absence of linear absorption [19, 20], these parameters are related to $\chi^{(3)}$ by

$$n_{2,el}(\omega_a; \omega_b) = \frac{3}{4\varepsilon_0 n_a n_b c} \text{Re}\{\chi_{el}^{(3)}(\omega_a; \omega_a, -\omega_b, \omega_b)\}, \quad (2.16)$$

$$\alpha_2(\omega_a; \omega_b) = \frac{3\omega_a}{2\varepsilon_0 n_a n_b c^2} \text{Im}\{\chi_{el}^{(3)}(\omega_a; \omega_a, -\omega_b, \omega_b)\}. \quad (2.17)$$

We can think of Equations (2.14) and (2.15) in terms of the change in refractive index and absorption coefficient, respectively,

$$\frac{\partial \Delta \phi_a(z)}{\partial z} = k_{0,a} \Delta n, \quad (2.18)$$

$$\frac{\partial I_a(z)}{\partial z} = -\Delta \alpha I_a(z), \quad (2.19)$$

where, in for the bound-electronic nonlinear treated here

$$\Delta n_{el} = n_{2,el}(\omega_a; \omega_a) I_a(z) + 2n_{2,el}(\omega_a; \omega_b) I_b(z), \quad (2.20)$$

$$\Delta \alpha_{el} = \alpha_2(\omega_a; \omega_a) I_a(z) + 2\alpha_2(\omega_a; \omega_b) I_b(z). \quad (2.21)$$

This formulation, can be useful to generalize to other effects that change the refractive index or absorption coefficient directly. Terms of higher even orders give rise to similar type nonlinearities. For example $\chi^{(5)}$ gives rise to higher order nonlinear refraction, n_4 , and three-photon absorption α_3 ¹.

2.2.1. Origins of bond-electronic third-order response

The material response depends on the electronic energy levels, as well as the transition dipole moments between them. Therefore, with knowledge of the energy levels and wave functions, predictions of the dispersion of n_2 and spectrum of α_2 can be made. Alternatively, measurements of n_2 and α_2 can provide information about the energy levels and wave functions. In this

¹ It is unfortunate that the subscript notation for 5th order (in the field) NLR and 3PA is different, n_4 versus α_3 , but this is the common notation in the literature.

section, we briefly describe the relationship between the bound-electronic NLR and 2PA and the quantum mechanical wave functions of the material system.

For an unperturbed time-independent Hamiltonian \hat{H}_0 , a system satisfies the time-independent Schrödinger equation (TISE) $\hat{H}_0|\psi_n\rangle = E_n|\psi_n\rangle$, where $|\psi_n\rangle$ and E_n are the eigenstates and eigenvalues, respectively, of \hat{H}_0 . In general, an arbitrary time-dependent state $|\Psi(t)\rangle$, which satisfies the time-dependent Schrödinger equation (TDSE)

$$i\hbar \frac{\partial}{\partial t} |\Psi(t)\rangle = \hat{H} |\Psi(t)\rangle \quad (2.22)$$

can be written in the form of a linear superposition of the eigenstates

$$|\Psi(t)\rangle = \sum_n c_n |\psi_n\rangle e^{-iE_n t/\hbar} \quad (2.23)$$

where c_n are the complex probability amplitudes, and $|c_n|^2$ gives the probability of finding the system in the n^{th} state. If a small time-dependent perturbation $\hat{H}_{int}(t)$ is then applied to the system the resulting state can be expressed in the same manner, but with the normalized expansion coefficients taking on time dependence, $c_n \rightarrow c_n(t)$. The TDSE, Equation (2.22), then becomes

$$i\hbar \frac{\partial}{\partial t} \sum_n c_n(t) |\psi_n\rangle e^{-iE_n t/\hbar} = \left(\hat{H}_0 + \hat{H}_{int}(t) \right) \sum_n c_n(t) |\psi_n\rangle e^{-iE_n t/\hbar} \quad (2.24)$$

Since $|\psi_n\rangle$ are the eigenstates of \hat{H}_0 , the second term in the chain rule expansion of the LHS can be cancelled with the term on the RHS proportional to \hat{H}_0 . Taking the inner product with $e^{-iE_m t/\hbar} |\psi_m\rangle$ on both sides yields

$$i\hbar \frac{\partial c_m(t)}{\partial t} = \sum_n c_n(t) \langle \psi_m | \hat{H}_{int}(t) | \psi_n \rangle e^{iE_{mn} t/\hbar} \quad (2.25)$$

where $E_{mn} = E_m - E_n$ is the energy difference between the two states $|\psi_m\rangle$ and $|\psi_n\rangle$. The term $\langle \psi_m | \hat{H}_{int}(t) | \psi_n \rangle \equiv M_{mn}$, and is referred to as the matrix elements of the interaction. Thus we now

have the ability to determine the evolution of the system when a perturbation is applied. However, for a complicated system with many states, and for an arbitrary $\hat{H}_{int}(t)$, Equation (2.25) may become very difficult to solve. To simplify the problem, we expand $c_m(t)$ in a series $c_m(t) = c_m^{(0)} + c_m^{(1)}(t) + c_m^{(2)}(t) + \dots$, where the zeroth order term corresponds to the unperturbed solution to Equation (2.22), and higher order terms calculated iteratively give corrections.

The above approach is true in general for any sort of perturbation. Of interest to us is the perturbation due to a light wave, in which case the first order term $c_m^{(1)}(t)$ corresponds to an electronic transition involving a single photon, the second order term $c_m^{(2)}(t)$ corresponds to two-photon transitions, and so on. Fermi's Golden Rule, which expresses the transition rate W from an initial state $|\psi_i\rangle$ to a final state $|\psi_f\rangle$, for a two-photon process can be found [2] from the time derivative of $|c_f^{(2)}(t)|^2$, and is given by

$$W_{fi}^{(2)} = \frac{2\pi}{\hbar} \left| \sum_j \frac{M_{fj}^b M_{ji}^a}{E_{ji} - \hbar\omega_a} + \frac{M_{fj}^a M_{ji}^b}{E_{ji} - \hbar\omega_b} \right|^2 \delta(E_{fi} - \hbar\omega_a - \hbar\omega_b) \quad (2.26)$$

where the indices a and b indicate the two photons involved, which in general may be of different frequency, and the summation is over all intermediate states $|\psi_j\rangle$. The 2PA coefficient is related to the transition rate by

$$\alpha_2(\omega_a; \omega_b) = \frac{N\hbar\omega_a W_{fi}^{(2)}}{2I_a I_b} \quad (2.27)$$

where N is the number density of absorbers. While only terms related to the energy difference between initial and intermediate states E_{ji} are shown explicitly, the sum does include terms related to the energy difference between the intermediate and final states E_{fj} owing to the fact that, on

resonance, $E_{fj} - \hbar\omega_a = E_{ji} - \hbar\omega_b$, and likewise if the photon energies are reversed. These intermediate states can greatly affect the transition rate, given the resonance terms in the denominators of Equation (2.26), as one of the photon energies approaches either energy difference E_{ji} or E_{fj} (see Figure 2.1).

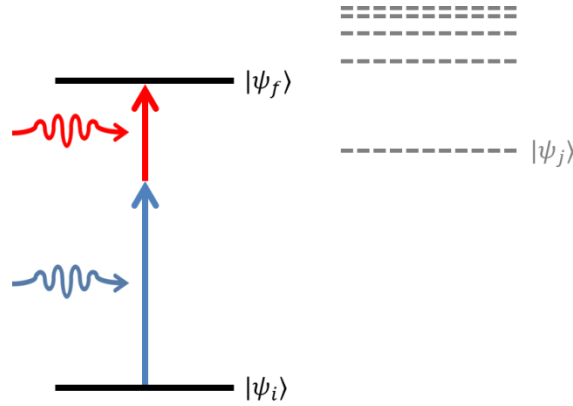


Figure 2.1 Energy diagram for perturbation approach to two-photon transitions

For states with definite parity, i.e., $|\psi_n(\mathbf{r})\rangle$ are strictly either even or odd functions of \mathbf{r} , within the dipole approximation one-photon transitions may only occur between states of opposite parity. Such transitions are called *one-photon allowed* transitions, while transitions between equal parity states are *one-photon forbidden*. This can easily be seen in the one dimensional case by analyzing the electric dipole operator $\hat{\mathbf{u}} = -e\hat{\mathbf{r}}$, which in one dimension means the matrix elements $M_{mn} \propto \langle \psi_m(x) | \hat{x} | \psi_n(x) \rangle$. If $|\psi_n(x)\rangle$ and $|\psi_m(x)\rangle$ are even and odd functions of x , respectively, $M_{mn} \neq 0$. This is because the product of an even function ($|\psi_n(x)\rangle$), an odd function (x), and a second odd function ($|\psi_m(x)\rangle$), yields an even function, which when integrated over $x = \pm\infty$ is non-zero. However, if $|\psi_m(x)\rangle$ is an even function of x , the product is now odd, giving zero upon integration.

This concept also impacts the two-photon transition rate since the matrix elements M_{ji} in Equation (2.26) correspond to *virtual* one-photon transitions between initial (or final) and intermediate states. Thus only intermediate states possessing opposite parity from both the initial and final states will contribute to the two-photon transition rate. These contributions are said to be from *virtual* transitions because one way to interpret the process is that the electron in the initial state $|\psi_i\rangle$ is excited by one photon to the intermediate state $|\psi_j\rangle$. However, because the photon energy is not equal to the transition energy E_{ji} , it may only remain in $|\psi_j\rangle$ for a time Δt given by the uncertainty relation $\Delta E \Delta t \geq \hbar/2$ [21], where in this case $\Delta E = E_{ji} - \hbar\omega_a$. The quantity Δt is typically less than one femtosecond and much shorter than the shortest laser pulses used; thus the process is considered nearly *instantaneous*. The second photon must come along within this time to cause a second transition from $|\psi_j\rangle$ to the final state $|\psi_f\rangle$. This uncertainty relation is reflected in the resonance energy denominators of Equation (2.26). As the photon energy comes close to the intermediate state transition energy, i.e. as $\Delta E \rightarrow 0$, the time window for the second photon to arrive is greatly increased, resulting in an enhanced two-photon transition rate. This is known as intermediate state resonance enhancement (ISRE) [22]. Virtual transitions stand in contrast to *real* transitions in which, for $\Delta E \approx 0$ (or at least less than the linewidth), the electron goes directly into $|\psi_j\rangle$ via a one-photon transition where it may stay for roughly its lifetime, and from which the second photon may cause another transition to $|\psi_f\rangle$. This is typically referred to as a *cascaded* process, and is distinct from the instantaneous two-photon transition. Equation (2.26) may describe any two-photon transition between two states. If the initial state is of lower energy than the final state, this corresponds to 2PA. However, if the initial state is of higher energy than the final, it describes doubly-stimulated 2PE.

This analysis can also give insight into the dispersion of n_2 . If the two-photon energy sum is not resonant, $E_{fi} \neq \hbar\omega_a + \hbar\omega_b$, (or rather detuned many linewidths) there will be no two-photon absorption. However, the lifetime of the virtual state does still have a real impact on the material response. Loosely speaking, the electron in the virtual state takes a longer time to transition back down to the ground state and reradiate the incident fields. The longer the virtual state lifetime, the greater the phase shift between the reradiated field and the incident one, and the larger the nonlinear refractive index. Therefore, large magnitudes of n_2 (typically negative in sign) are found near linear absorption resonances [20].

2.3. Noninstantaneous Third-order Nonlinearities

In the Born-Oppenheimer approximation, the nonlinear optical response of the bound-electron and nuclei of the material may be separated. This allows us to write the [23]

$$\chi^{(3)} = \chi_{el}^{(3)} + \chi_{nu}^{(3)}, \quad (2.28)$$

where the subscripts *el* and *nu* indicate the bound-electronic and nuclear origins, respectively. Nonresonant Raman type nonlinearities give rise to a noninstantaneous third-order susceptibility of the form [18, 23]

$$\chi_{nu}^{(3)}(t - t_1, t - t_2, t - t_3) = \chi_{nu}^{(3)}(t - t_1)\delta(t - t_2)\delta(t_1 - t_3). \quad (2.29)$$

Substituting this expression into Equation (2.4) yields

$$\tilde{\mathbf{P}}_{nu}^{(3)}(t) = \varepsilon_0 \tilde{\mathbf{E}}(t) \int_{-\infty}^{\infty} \chi_{nu}^{(3)}(t - t_1) \tilde{\mathbf{E}}(t_1) \tilde{\mathbf{E}}(t_1) dt_1. \quad (2.30)$$

We refer to this as a Raman type nonlinearities since it is related to the Raman spectrum by Fourier transform $\mathcal{F}\{\chi_{nu}^{(3)}(t)\} \propto \chi_{nu}^{(3)}(\Delta\omega)$ [24]. We assume the optical frequencies are far from nuclear

resonances, so the only terms of the product of the two fields within the integrand that survive integration are those that are complex conjugates of one another, e.g., $e^{\pm i\omega t} e^{\mp i\omega t} = 1$. This essentially says that the material response is too slow to respond to the rapid variations of the field, and terms of the integrand containing the second harmonic, i.e., $e^{\pm i\omega t} e^{\pm i\omega t} = e^{\pm i2\omega t}$, integrate to zero. For the case of a single beam input, the third-order polarization amplitude is

$$\mathcal{P}_{nu}^{(3)}(t) = \frac{\epsilon_0}{2} \mathcal{E}(t) \int_{-\infty}^{\infty} \chi_{nu}^{(3)}(t - t_1) |\mathcal{E}(t_1)|^2 dt_1. \quad (2.31)$$

In the two beam case, things become a bit more complicated. The electric fields of the two beams interfere where they are overlapped in the medium. In the degenerate case this interference pattern is stationary, while in the nondegenerate case, the pattern moves at the frequency difference between the two input beams. The interference pattern results in a sinusoidal grating (e.g., refractive index grating) created in the material. We can see this if we imagine two beams at frequency inputs, ω_a and ω_b , propagating at a slight angle with respect to one another ($\hat{\mathbf{k}}_a \neq \hat{\mathbf{k}}_b$). The product of the fields appearing in the integrand of Equation (2.30) (keeping only slowly varying terms) is

$$\begin{aligned} \frac{1}{2} (& |\mathcal{E}_a|^2 + |\mathcal{E}_b|^2 + \mathcal{E}_a \mathcal{E}_b^* e^{i((\mathbf{k}_a - \mathbf{k}_b) \cdot \mathbf{r} - (\omega_a - \omega_b)t)} \\ & + \mathcal{E}_a^* \mathcal{E}_b e^{-i((\mathbf{k}_a - \mathbf{k}_b) \cdot \mathbf{r} - (\omega_a - \omega_b)t)}). \end{aligned} \quad (2.32)$$

Here we can see that there are both “smooth” terms given by only the square moduli of the field amplitudes, as well as “grating” terms due to the interference of the two fields that oscillate at the frequency difference $\omega_a - \omega_b$. When this difference is close to nuclear resonances in the material there can be energy transfer from the high frequency beam to the low frequency beam [16]. This is stimulated Raman scattering. In the degenerate case the “grating” terms result in an additional

phase shift at zero delay when the two pulses are overlapped [25]. In addition, if the pulses are chirped, there is a small difference between the frequencies on either side of zero delay. This will give energy transfer from one beam to the other at positive delay, and the other way around at negative delay, depending on the sign of the chirp [26]. This effect is often called two-beam coupling [16].

To avoid these issues, and only retain the “smooth” terms in Equation (2.32) we must operate in the nondegenerate case far from nuclear resonances. So long as the frequency difference $\omega_a - \omega_b$ is sufficiently large, the “grating” terms will integrate to zero, leaving only the “smooth” terms. In this case, the polarization amplitude, oscillating at ω_a and propagating in the \mathbf{k}_a direction is

$$\mathcal{P}_{nu}^{(3)}(t) = \frac{\epsilon_0}{2} \mathcal{E}_a(t) \int_{-\infty}^{\infty} \chi_{nu}^{(3)}(t - t_1) |\mathcal{E}_b(t_1)|^2 dt_1. \quad (2.33)$$

Note that that for the noninstantaneous nuclear nonlinearity, the two beam case is the same as for the single beam case, Equation (2.31). This stands in contrast to the bound-electronic third-order response where there is a factor of two difference between the one- and two-beam cases, Equation (2.13). This is because instantaneous bound-electronic response is able to follow the rapidly moving interference pattern. The noninstantaneous nuclear component, however, is too slow to follow the interference pattern, and does not add to the nonlinear polarization [62].

Substituting Equation (2.33) into (2.10), we have

$$\frac{\partial \mathcal{E}_a}{\partial z} = i \frac{\omega_a}{4n_a c} \mathcal{E}_a \int_{-\infty}^{\infty} \chi_{nu}^{(3)}(t - t_1) |\mathcal{E}_b(t_1)|^2 dt_1. \quad (2.34)$$

Converting the complex field amplitude to irradiance and phase

$$\frac{\partial \Delta \phi_a}{\partial z} = \frac{\omega_a}{c} \int_{-\infty}^{\infty} \frac{2\chi_{nu}^{(3)}(t-t_1)}{4n_a n_b \epsilon_0 c} I_b(t_1) dt_1, \quad (2.35)$$

$$\frac{\partial I_a}{\partial z} = 0. \quad (2.36)$$

We can thus see that we only have a change in the phase of the beam, and no change in the irradiance. We can therefore define a response function for the noninstantaneous nonlinear refraction in terms of the nuclear component of the third-order susceptibility,

$$R(t) = \frac{2\chi_{nu}^{(3)}(t)}{4n_a n_b \epsilon_0 c}. \quad (2.37)$$

Equation (2.35) then becomes

$$\frac{\partial \Delta \phi_a}{\partial z} = k_{0,a} \int_{-\infty}^{\infty} R(t-t_1) I_b(t_1) dt_1. \quad (2.38)$$

Comparing this to Equation (2.18) reveals that the integral is simply the refractive index change

$$\Delta n_a(t) = \int_{-\infty}^{\infty} R(t-t_1) I_b(t_1) dt_1. \quad (2.39)$$

CHAPTER 3: EXPERIMENTAL METHODS

The purpose of this chapter is to describe the experimental approaches used to measure the nonlinear optical properties of various media within this work.

3.1. Linear Characterization

The first, and perhaps most important, part of characterizing the nonlinear optical properties of a material is to first determine its linear optical properties.² Here, the main characteristics of interest are the dispersion of the linear refractive index $n_0(\omega)$, and the spectrum of the linear (one-photon) absorption coefficient $\alpha_1(\omega)$. The materials concentrated on in this work, liquid CS₂, air, and GaAs, are generally well characterized, and references for their linear optical properties can be found in the literature. Sources used for the linear optical properties of CS₂ are [27, 28], for air [29], and for GaAs [30-36]. In addition, the spectrum of the absorption coefficient of both CS₂ and GaAs samples used were measured using a Cary 500 spectrophotometer.

3.2. Nonlinear Characterization

Measurement of the nonlinear optical characteristics of materials differs significantly from the procedures used to characterize the linear optical properties. This is principally due to the requirement of high irradiances in order to induced changes in the materials. For this purpose high peak power pulsed laser sources are used throughout this work. The following discusses the laser

² The website <http://refractiveindex.info/> is an excellent resource for linear optical properties of a wide range of materials. Also, <http://www.ioffe.ru/SVA/NSM/> has a wealth of information about semiconductor materials.

systems used as well as several measurement techniques including Z-scan, pump-probe, and two-photon stimulated emission depletion. Novel techniques that were developed over the course of this work, namely the Dual-arm Z-scan and Beam Deflection techniques, are described in detail.

3.2.1. Light Sources

Two laser systems were used for the majority of this work. Both were Ti:sapphire [37] based regenerative amplifier systems operating at 1 kHz repetition rate that were used to pump optical parametric generator/amplifiers capable of tuning the output wavelength from 300 nm to 10 μm .

3.2.1.1. Laser Sources

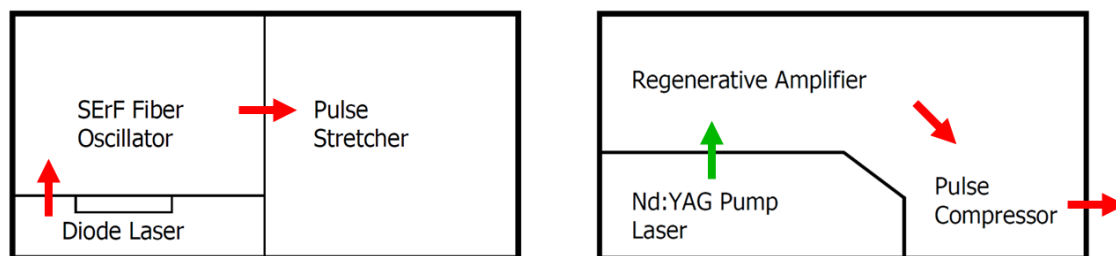


Figure 3.1. Schematic diagram of Clark-MXR CPA-2010 laser system.

The first laser system was a Clark-MXR model CPA 2010 with 1 mJ output energy, a central wavelength of 776 nm, with a bandwidth of 7 nm (FWHM), which produced 150 fs pulses. The laser system consists of a dual level design, consisting of six sections; a diode laser, Er fiber oscillator, pulse stretcher, Nd:YAG pump laser, regenerative amplifier, and pulse compressor (see Figure 3.1). The systems starts with a diode laser at 980 nm, which pumps an erbium doped uni-directional, polarization rotation additively pulsed mode-locked fiber ring laser at a wavelength of

1550 nm and a repetition rate of 27 MHz. A periodically poled lithium niobate (PPLN) crystal generates the second harmonic at 775 nm, which is sent to a diffraction grating pulse stretcher to temporally extend the pulse before amplification. This is done to minimize the peak irradiance within the optical components to prevent damage. A single pulse is switched into the amplifier cavity through the use of a Pockels cell, which is then amplified by the Ti:sapphire gain medium. The gain medium is pumped by a Q-switched Nd:YAG laser, which itself is pumped by a flash-lamp, that has been doubled by a lithium triborate (LBO) crystal from 1064 nm to 532 nm to coincide with the absorption band of the Ti ions, and synchronized to the system at 1 kHz repetition rate. After several amplification passes, a second Pockels cell is used to switch the amplified pulse, out of the cavity. The pulse is then sent to a diffraction grating compressor to yield 150 fs pulses (FWHM) at the output.

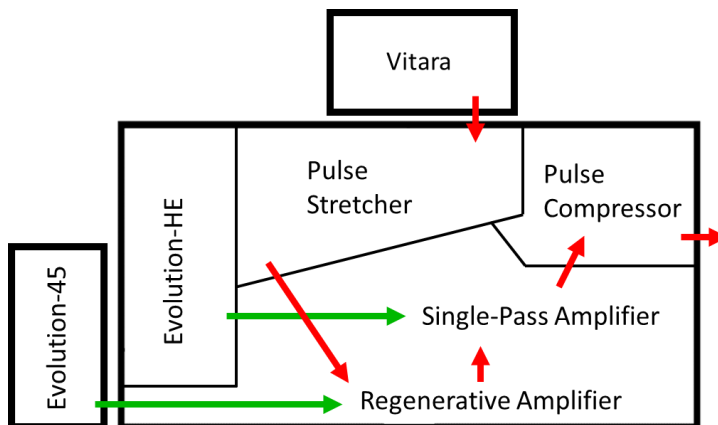


Figure 3.2 Schematic diagram of Coherent Legend Elite Duo HE+ laser system.

The second laser system was a Coherent model Legend Elite Duo HE+ chirped pulse amplifier system with 12 mJ output energy at 800 nm, with a bandwidth of 28 nm (FWHM), and a repetition rate of 1 kHz, and capable of producing pulses as short as 35 fs (FWHM) (see Figure 3.2). The system is seeded with a Coherent Vitara mode-locked Ti:sapphire laser. This consists of

a Coherent Verdi G-Series laser head, which has a CW diode laser at 808 nm that optically pumps a semiconductor quantum well chip that acts as the gain medium for a vertical-external-cavity surface-emitting-laser (VECSEL) operating at 1064 nm. The output coupler is highly reflective at 1064 nm, so the beam is doubled within the cavity by a LBO crystal to 532 nm, where the output coupler is transmissive. This beam is then used to pump the Ti:sapphire gain medium in the Vitara. The Vitara laser itself is a passively Kerr lens mode-locked laser that operates at 800 nm with a tunable bandwidth and a repetition rate of 80 MHz. A Pockels cell picks off one pulse and sends it to the Legend Elite Duo HE+ amplifier. The pulse is first sent into a diffraction grating stretcher to reduce the peak irradiance and minimize damage to the gain medium and optical components. The pulse is then sent through a Ti:sapphire crystal within the regenerative amplification cavity. The Ti:sapphire gain medium is optically pumped by a Coherent Evolution-45 laser system. This system is similar to the Verdi G-series pump laser within the Vitara. It is semiconductor diode pumped, acousto-optic Q-switched Nd:YLF laser that is intra-cavity frequency doubled (with a temperature tuned LBO crystal). The output at a wavelength of 527 nm, an energy of 28 mJ, and pulse width of less than 250 ns is synchronized to the 1 kHz repetition rate of the pulse selector from the Vitara. The seed pulse is amplified through several passes of the regenerative amplifier up to an energy of 7 mJ. It is then switched to a second Ti:sapphire crystal constituting the single pass amplifier (SPA), which is pumped by a second Coherent Evolution (model HE) with 45 mJ of energy. The pulse is then sent to a grating compressor which compresses the pulse down to 35 fs.

3.2.1.2. Optical Parametric Generators/Amplifiers

Nonlinear spectroscopy requires a broadly tunable source of high peak power radiation. Currently, the best way to do this is by use of optical parametric generators/amplifiers OPG/A, which, through $\chi^{(2)}$ nonlinearities, alter the frequency of an input to generate potentially any wavelength from 300 nm to 10 μm . Three OPG/A's were used in this work, each Light Conversion's Traveling wave Optical Parametric Amplifier of Superfluorescence (TOPAS), models -800, -C, and -HE.

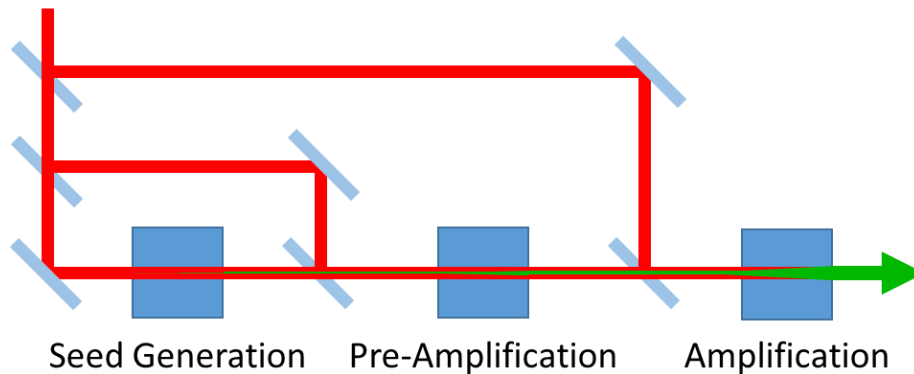


Figure 3.3 Principle of operation of Light Conversion TOPAS.

The TOPAS-800 is really the only one of the three that is true to its name. Approximately 1.3 mJ of the Coherent laser output pumps the system. A small portion (~2%) is transmitted through the first two beam splitters and focused into a barium borate (BBO) crystal where photons at 800 nm are split into a signal photon and an idler photon via spontaneous parametric down conversion, which are then amplified as they co-propagate within the crystal (see Figure 3.3). This process is sometimes referred to as superfluorescence [38] (not to be confused with cooperative radiation emitted from an excited atomic system, which is also called superfluorescence [39]). Determination of the wavelengths is selected by angle tuning the BBO crystal to phase match the

desired wavelength. The generated superfluorescence signal (and idler) reflected off mirrors and sent back through the same crystal another two times. Approximately ~2 % of the input energy is reflected from the second beam splitter and is used as a pre-amplifier, which is temporally and spatially overlapped in the same BBO crystal with the fourth pass of the initial seed. The remaining pump energy was split off from the first beam splitter to act as a main amplifier, which is then overlapped in a second BBO crystal within the same mount housing. The system is tunable with computer controlled delay stages for timing the arrival of the pre- and main-amplifier pulses, as well as the orientation angle of the BBO crystal. There are also several attachments to the output that produce the second and fourth harmonics of both signal and idler, the sum frequency between signal (or idler) and the remaining 800 nm pump beam, and the difference frequency between signal and idler. All but the DFG crystal, which is AgGaSe, are BBO. The TOPAS-800 is difficult to align, since the generation and both amplification passes happen through the same crystal and troubleshooting can be problematic. In addition, due to the inherently noisy nature of the spontaneous parametric down conversion process, the TOPAS-800 suffers from large energy instability.

Both the TOPAS-C and the TOPAS-HE have white-light continuum (see section 3.2.1.3.) seed generation stages, each using ~2 μJ of pump energy in a 5 mm sapphire plate. This seed generation process is inherently more stable than spontaneous parametric down conversion. The wavelength selection is done by chirping the generated white light by passing it through a ZnSe plate and pre-amplifying only the desired spectral range. Additionally, the pre-amplification and main-amplification stages are done in different BBO crystals, making alignment troubleshooting much simpler. The TOPAS-HE (high energy) accepts 10 mJ input from the Coherent laser system, and has an additional amplification stage to boost the total output energy of the signal plus idler pulses up to 4 mJ.

3.2.1.3. White-Light Continuum

When an ultrashort pulse propagates through a medium, it experiences a temporal gradient in the refractive index due to nonlinear refraction (optical Kerr effect) at its leading and trailing edges. This induces a temporally varying phase change on the pulse. Since the instantaneous frequency is defined as the temporal derivative of the phase, this results in phase shifts at the edges of the pulse. This effect, known as self-phase modulation, leads to a broadening of the frequency content of the pulse. In addition, self-focusing can overcome diffraction and cause the beam to collapse, increasing the irradiance, and further enhancing the nonlinear interaction. This effect is arrested by multiphoton absorption generating a plasma (or excited states in solid-state media) causing a reduction in the refractive index [40]. The interplay between diffraction, Kerr-lens self-focusing, and multiphoton ionization induced defocusing yielding a narrow beam of high irradiance over a long distance, known as filamentation [41-44]. The output of such a filament is an ultra-broadband white-light continuum that may span several octaves [44, 45].

3.2.2. Dual-arm Z-scan

Since its invention in 1989 [46] and expansion in 1990 [47], Z-scan has been a staple of nonlinear optical materials characterization and spectroscopy, owing to its simplicity and ease of implementation. It is a single beam technique capable of measuring both the nonlinear refraction and absorption of a wide variety of materials. The technique relies on focusing a single beam into a nonlinear sample, and measuring its transmission through both a partially closed and fully open aperture in the far-field (see Figure 3.4) as the sample is scanned through the focus of the beam.

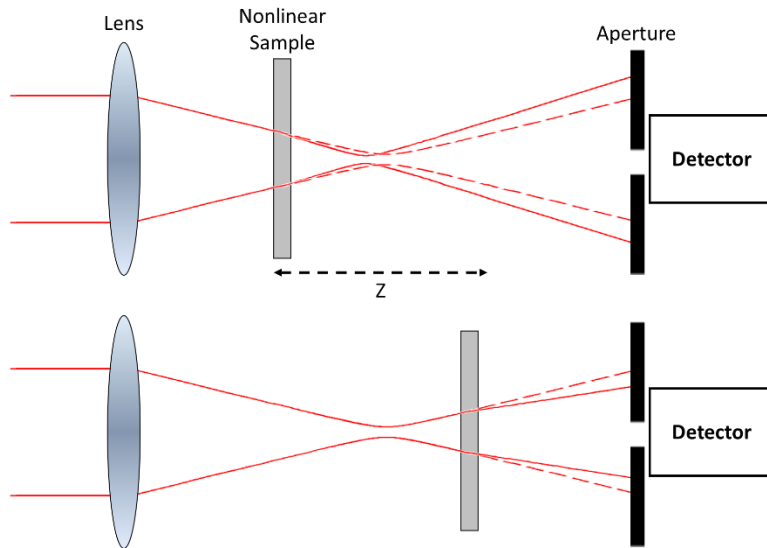


Figure 3.4 Z-scan schematic showing a sample with positive n_2 showing (top) an increased beam size at the aperture when the sample is before focus, and (bottom) a reduced beam size when the sample is after focus.

To measure nonlinear absorption, e.g., 2PA, the entire beam is measured, which is known as the Open-Aperture (OA) Z-scan, which shows the largest reduction in transmission at focus, where the irradiance is maximum (see left plot in Figure 3.5). Nonlinear refraction can be measured by closing the aperture partially (this research group typically reduces the transmission to $\sim 33\%$), so that the measurement is now sensitive to changes in the beam size on the aperture. For a TEM₀₀ Gaussian beam, a sample with positive n_2 will have an increased refractive index in the center of the beam, where the irradiance is greatest, more than in the wings. The sample now looks like a positive lens, in the sense that the optical path length (OPL) is greatest in the center and smaller towards the edge. Therefore, the beam experiences self-focusing, since it “wrote” a positive lens into the material, and caused itself to focus. When the sample is placed before focus, this causes the beam to focus sooner than it would normally, and diverge more on the other side of focus, causing the spot size on the aperture to be larger, so less energy is transmitted. When the sample

is on the other side of focus, self-focusing tends to collimate the beam, reducing the spot size on the aperture, and increasing the transmission. The result is a characteristic antisymmetric Closed-Aperture (CA) Z-scan curve demonstrated in the middle plot of Figure 3.5. For a negative n_2 , or self-defocusing nonlinearity, this signal is flipped in sign. The difference between the normalized transmissions at the peak and valley $\Delta T_{p-v} \propto \Delta n$ is a characteristic feature.

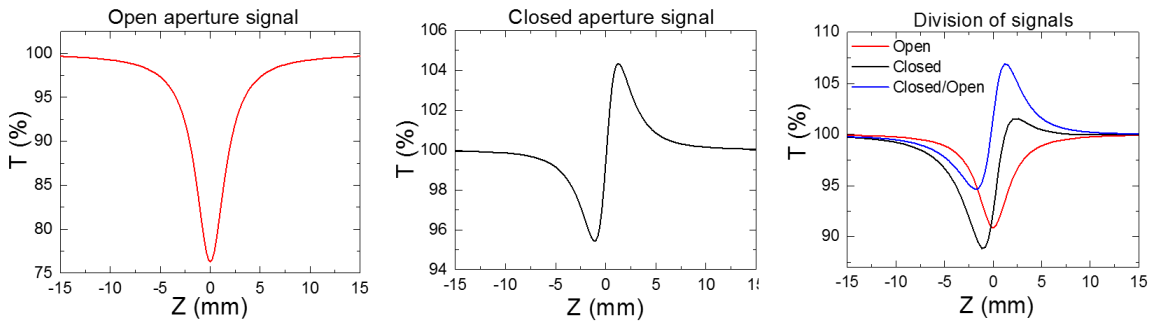


Figure 3.5 Examples of Z-scan signals (left) CA for positive NLR and zero NLA, (middle) OA signal for 2PA, and (right) open, closed, and divided signals with both positive NLR and 2PA.

If there is significant NLA, it will contaminate the CA Z-scan signal, and yield a distorted curve, such as the black curve on the right plot of Figure 3.5. However, if we divide the CA scan by the OA scan (red), which we have also measured, we find that the division (blue) is very similar to what would have been measured if the sample had no NLA. This of course fails if the NLA completely dwarfs the NLR signal, and can make determination of n_2 in the presence of large NLA very difficult.

In general the analysis of a Z-scan experiment requires numerical propagation of the electric field of the beam through the sample, followed by Fresnel propagation to the aperture plane [48]. However, approximations can simplify the analysis if the sample is sufficiently thin, meaning less than the Rayleigh range, $L \ll z_0$, such that the beam size doesn't change within the sample. Additionally, the nonlinear refraction must also be sufficiently small, $L \ll z_0/\Delta\phi_0$, meaning self-

focusing does not cause the beam size to change within the sample itself. This is the thin sample approximation, and allows the separation of the electric field into irradiance and phase, as in Equations (2.14) and (2.15). In this case, the effect of the sample on the beam is the same as if it were simply a thin phase (and/or amplitude) mask, which is sometimes referred to as “external self-action”. In this case, standard Z-scan analysis based on analytical and/or numerical solutions to Equations (2.14) and (2.15) may be applied to extract the material properties from the measurements [47].

Z-scan only measures the total NLA and NLR; it does not give information about the underlying physical mechanism. This can be particularly problematic during analysis, since there are many different means to alter the absorption coefficient or refractive index. Care must be taken when analyzing data, and several scans at multiple energies should be performed to ensure the correct energy dependence the applied model. For example, the Z-scan signals from bound-electronic third-order nonlinear refraction and 2PA scale linearly with input energy. Noninstantaneous nonlinearities, including excitation effects such as saturable and excited state absorption, thermal effects, and molecular dynamics must be analyzed with care, and typically other time domain experiments are required.

Another issue arises when trying to measure the nonlinearities of solutes dissolved in solution or thin films on thick substrates. Typically solvents and substrates may be selected which have negligible NLA in the spectral range of interest. However, NLR is always present, and the resulting CA Z-scan signal from the solvent/substrate can completely mask that from the material being studied. This can become particularly problematic when limited to low solute concentrations, thin film thickness, or when the nonlinearity is very small. Figure 3.6 shows an example of a sequential Z-scan measurements of a thin film of ZnO deposited on a fused silica substrate (left

figure, red curve) and a bare substrate (left figure, blue curve). The differences between these two scans is very small, such that when taking the difference (right figure), the signal due to only this thin film is buried within the noise. To overcome this problem, we developed the Dual-arm Z-scan, which is differential method that measures both the solution (thin film on substrate) and solvent (bare substrate) simultaneously to determine only the nonlinearity of the solute (thin film) itself [49-51].

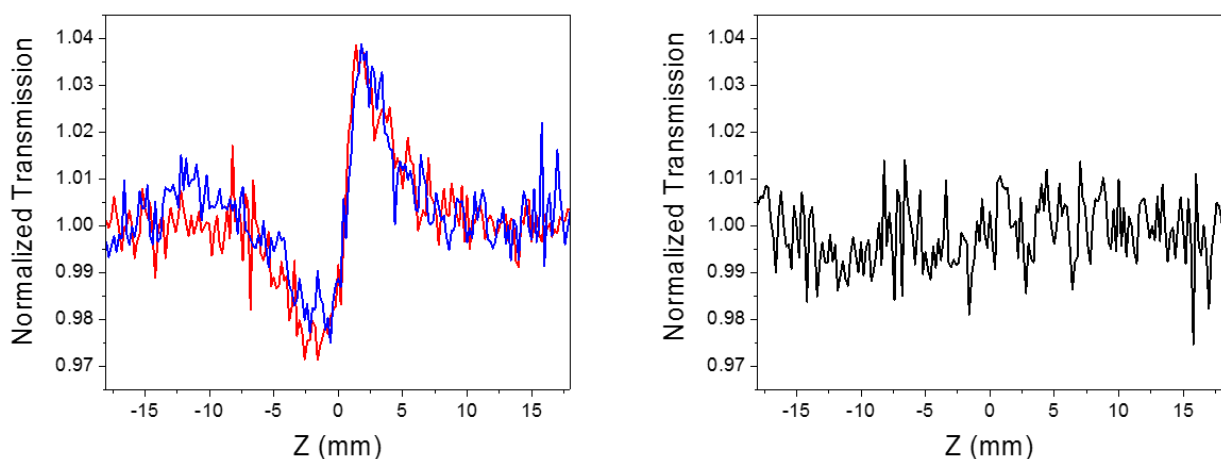


Figure 3.6 Example of problems with measuring NLR of a thin film on a thick substrate. (left) Sequential Z-scan measurements of (red) a 3 μm film of ZnO on a 1 mm fused silica substrate, and (blue) bare fused silica substrate. (right) Difference between the two measurements.

A schematic of the experimental setup is shown in Figure 3.7. A small portion of the laser pulse energy is split off and sent to a reference detector which is used to window pulses of a desired energy range. The remainder of the pulse is split into two arms, one with a cuvette containing the solution, and the other with a cuvette containing only the solvent. Both CA and OA Z-scans are measured simultaneously. To ensure that the resulting difference between the two signals originates only from the nonlinearity of the solute itself much care needs to be taken. The irradiance

distribution in each beam needs to be identical. The OPLs between the beam splitter and the focusing lenses in each arm are matched to account for any slight vergence of the beam that would otherwise result in different beam waist locations and radii. A continuously variable neutral density (ND) filter is placed in one arm to make sure the energies are equal. A compensation plate may also be used to compensate the dispersion in the ND filter and beam splitter which could alter the pulse width in one arm. Furthermore, matched best form lenses and cuvettes are used. Much overhead is required to guarantee that the two arms are balanced. This is done by scanning identical samples (usually cuvettes filled with CS_2 due to its large nonlinearity) in each arm, and balancing the sample z-position and pulse energy iteratively until the subtraction of the CA Z-scan signals yields a uniform trace.

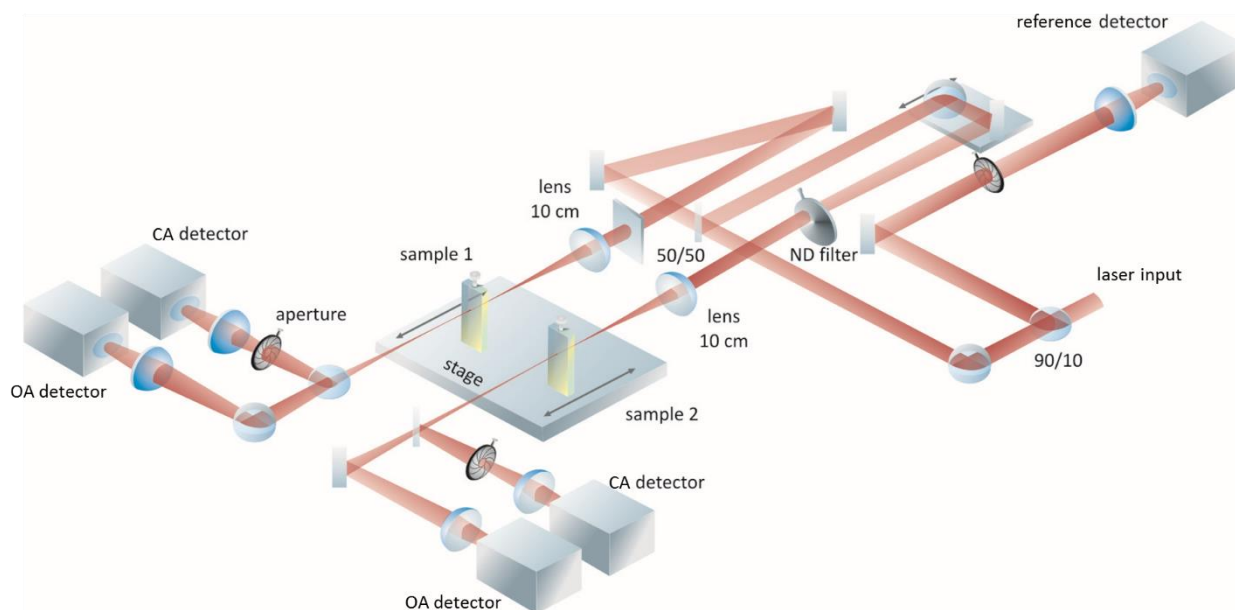


Figure 3.7. Schematic diagram of Dual-arm Z-scan setup (reproduced with permission from Ref. [49]).

Once the system is properly balanced cuvettes filled with solution and solvent are placed in each arm. Figure 3.8 shows an example of the procedure for measurement. The first step in the

procedure is to first perform a scan at low energy such that no nonlinearity is observed (see Figure 3.8 (a)). The resulting difference between the two arms yields the Low Energy Background (LEB), which is due to linear differences between the two arms, such as cell mismatch (see Figure 3.8 (b)). The LEB is minimized by using matched optics and cuvettes, and then translating the sample positions until a sufficiently small LEB signal is found (typically $< 3\%$ is acceptable, but as below the noise floor is desirable). Next, the energy is increase such that the nonlinearity of both the solvent and solution can be seen (see Figure 3.8 (c)), and the difference between the two arms is taken (see Figure 3.8 (d)). This difference contains both the nonlinear signal from only the solute, as well as the LEB, as can be seen in Figure 3.8 (e) where the two are overlaid. Subtracting the LEB from the uncorrected scan yields the Dual-arm Z-scan trace with only the nonlinearity of the solute, Figure 3.8 (f), which has been corrected for by residual linear differences in the two arms. This curves may then be fit, along with the OA Z-scans, to obtain α_2 and n_2 due to the solute. This procedure clearly reduces the noise floor of the measurement of the nonlinear refraction due to the solute itself, and greatly improves our ability to distinguish small solute nonlinearities in the presence of large backgrounds. For example, at a signal-to-noise ratio of unity, with a noise floor of standard deviation 0.1% (which are typical best results) the peak on axis phase change $\Delta\phi_0 = 4$ mrad (OPL change of $\lambda/1600$). Additionally, this technique has been expanded to measuring NLR of thin films on thick substrates [51, 52].

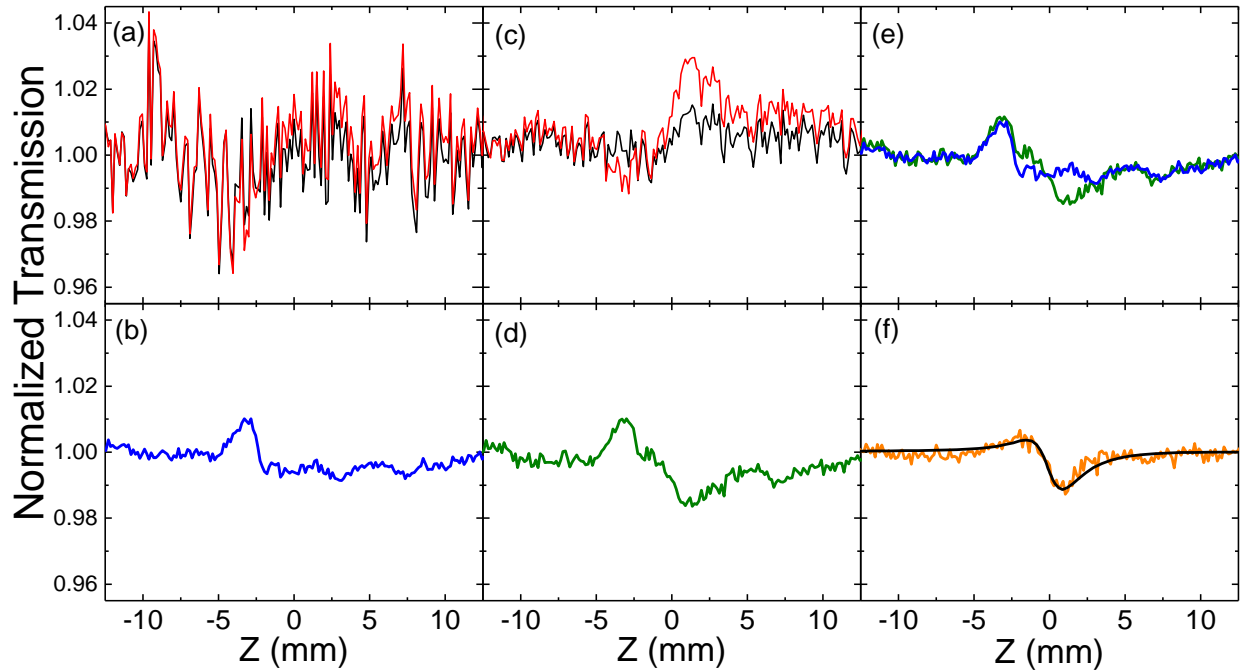


Figure 3.8 Procedure of processing dual-arm Z-scan. (a) low energy scan of the (red) solution and (black) solvent and (b) their difference which is the LEB, (c) high energy (11 nJ , $I_0 = 18 \text{ GW/cm}^2$) and (d) their difference, (e) direct comparison of (b) and (d), and (f) corrected solute signal and fit with $n_2 = -0.4 \times 10^{-19} \text{ m}^2/\text{W}$, and $a_2 = 0.02 \text{ cm/GW}$ [49].

3.2.3. Pump-probe

A complementary technique to Z-scan for measuring NLA is known as the pump-probe technique. It involves two individual beams, a strong pump, which induces a change in the absorption in a sample, and weak probe, whose transmission is then measured (see Figure 3.9). With femtosecond pulses, a temporal delay between the two beams is added by means of a delay stage to allow temporally resolved NLA measurements. This allows isolation of various NLA mechanisms that may be difficult to distinguish in Z-scan experiments. For example, 2PA will yield a reduction in the probe transmission only when the two pulses are temporally overlapped within the sample, while when the probe arrives after the pump (positive delay) FCA/ESA will reduce the probe's transmission.

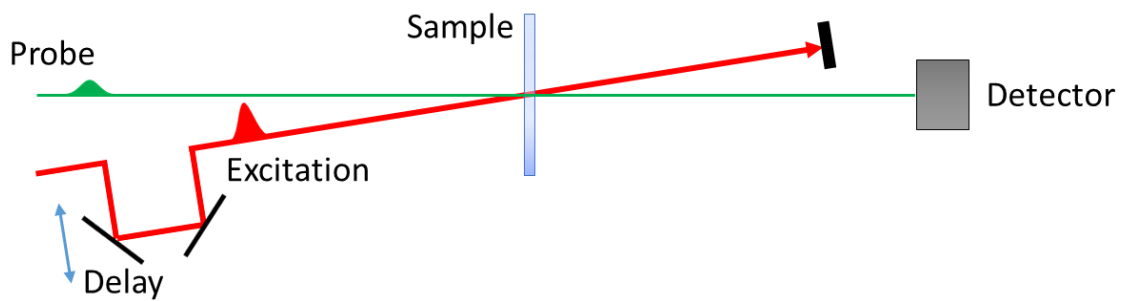


Figure 3.9 Diagram of Pump-probe experiment

Figure 3.10 shows an example of a pump-probe measurement on a sample that exhibits both 2PA and FCA/ESA. The black curve shows the signal due to 2PA of the probe with the pump (one photon from each pulse). The red curve shows the signal due to 2PA of the pump itself populating excited states within the material, which then increases the absorption coefficient of the sample, reducing the probe transmission at positive delays. The blue curve shows the sum of the two contributions, which is what is actually measured. While the 2PA signal is only about zero delay, due to its nearly instantaneous nature, the ESA signal will remain for the lifetime of the excited state.

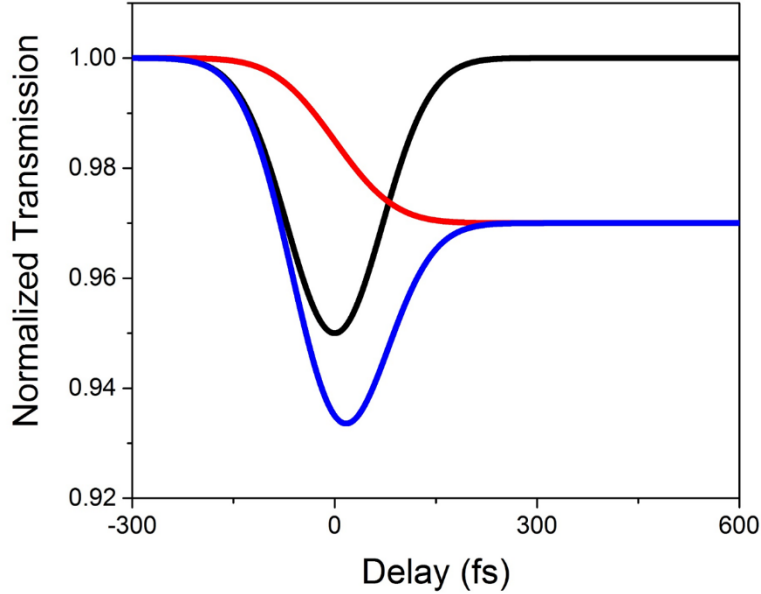


Figure 3.10 Pump-probe measurement example showing normalized probe transmission versus delay where the signal originates from (black) 2PA with the pump, (red) 2PA induced FCA/ESA, and (blue) total.

This experiment can be expressed in terms of the equations

$$\frac{\partial I_a}{\partial z} = -\alpha_2(\omega_a; \omega_a)I_a^2 - 2\alpha_2(\omega_a; \omega_b)I_aI_b - \sigma_{FCA}(\omega_a)NI_a, \quad (3.1)$$

$$\frac{\partial I_b}{\partial z} = -\alpha_2(\omega_b; \omega_b)I_b^2 - 2\alpha_2(\omega_b; \omega_a)I_bI_a - \sigma_{FCA}(\omega_b)NI_b, \quad (3.2)$$

$$\frac{\partial N}{\partial t} = \frac{\alpha_2(\omega_a; \omega_a)}{2\hbar\omega_a}I_a^2 + \frac{\alpha_2(\omega_b; \omega_b)}{2\hbar\omega_b}I_b^2 + 2\frac{\alpha_2(\omega_a; \omega_b)}{\hbar\omega_a}I_aI_b - \frac{N}{\tau}. \quad (3.3)$$

Here I_a and I_b are the probe and pump irradiances, respectively, and N is the number density of excited electrons. In general, the probe irradiance is kept small, allowing us to neglect the first term in both Equations (3.1) and (3.3), as well as the second term in Equation (3.2). The third term in Equation (3.3) is only nonzero about zero delay, and generally much smaller than the second term, and may also be neglected. Also, for ultrashort pulses, the 2PA of the strong pump is much greater than FCA/ESA, so the third term in (3.2) is typically dropped. We can see in Equation (3.1)

the 2PA (second term) contains the product of the pump and probe irradiances, thus only influencing the probe when it is temporally overlapped with the pump. Additionally FCA/ESA (third term) depends on N which is generated by 2PA of the pump itself, represented by the first term in Equation (3.2). The measurement should be performed at several pump irradiances to ensure the correct dependence of each mechanism. For 2PA, the signal will be linear in the pump irradiance, while for FCA/ESA it will be quadratic. Fitting all measurements allows the determination the material properties $\alpha_2(\omega_a; \omega_b)$, $\alpha_2(\omega_b; \omega_b)$, and $\sigma_{FCA}(\omega_a)$. Measuring the signal out to longer delays also allows the determination of the excited state lifetime τ .

Thus far, the analysis assumes several things about the sample being measured. One assumption is that the group velocities v_g of the two pulses are identical such that they remain overlapped throughout the entire sample thickness. When different frequencies are used, the material dispersion may cause the group velocities to differ significantly from one another. This is characterized by the group index $n_g = c/v_g$ given by

$$n_g = n + \omega \frac{\partial n}{\partial \omega}. \quad (3.4)$$

To account for this group velocity mismatch (GVM) we follow Negres et al. [53] and go back to Equation (2.9). This wave equation governing the weak probe field in the case of only (nearly) instantaneous bound-electronic third-order nonlinearities, Equation (2.13), due to the strong pump (which is assumed to be undepleted)

$$i \left\{ \frac{\partial \mathcal{E}_a}{\partial z} + \frac{n_{g,a}}{c} \frac{\partial \mathcal{E}_a}{\partial t} \right\} = -3 \frac{\omega_a}{4n_a c} \chi_{aabb}^{(3)}(\omega_a; \omega_a, -\omega_b, \omega_b) |\mathcal{E}_b|^2 \mathcal{E}_a, \quad (3.5)$$

where we have neglected the $\partial \mathcal{P} / \partial t$ term. We now transform in to a dimensionless coordinate system that travels with the group velocity of the pump pulse, $T = (t - z/v_{g,b})/\tau_b$, where τ_b is

the pulse width (HW1/eM) of the pump, and $Z = z/L$, where L is the sample thickness. The spatial derivative becomes $\frac{\partial}{\partial z} = \frac{1}{L} \frac{\partial}{\partial Z} - \frac{1}{v_{g,b}\tau_b} \frac{\partial}{\partial T}$, and the temporal derivative becomes $\frac{\partial}{\partial t} = \frac{1}{\tau_b} \frac{\partial}{\partial T}$, and

Equation (3.5) becomes

$$i \left\{ \frac{\partial \mathcal{E}_a}{\partial Z} + \rho \frac{\partial \mathcal{E}_a}{\partial T} \right\} = -3 \frac{\omega_a L}{4n_a c} \chi_{aabb}^{(3)}(\omega_a; \omega_a, -\omega_b, \omega_b) |\mathcal{E}_b|^2 \mathcal{E}_a, \quad (3.6)$$

where

$$\rho = \frac{L}{\tau_b c} \Delta n_g = \frac{L}{\tau_b c} (n_{g,a} - n_{g,b}), \quad (3.7)$$

is the GVM parameter. Converting the pump field to irradiance, and $\chi^{(3)}$ to n_2 and α_2 via Equations (2.16) and (2.17), respectively, yields

$$i \left\{ \frac{\partial \mathcal{E}_a}{\partial Z} + \rho \frac{\partial \mathcal{E}_a}{\partial T} \right\} = - \left(2k_{0,a} n_2(\omega_a; \omega_b) + i\alpha_2(\omega_a; \omega_b) \right) I_b L \mathcal{E}_a. \quad (3.8)$$

The first term on the RHS of Equation (3.8) is NLR that causes phase change in the probe, and the second term is 2PA which reduced the its transmission. Since in a pump-probe experiment measures only the probe's transmission, we neglect the phase change terms, yielding

$$\left\{ \frac{\partial \mathcal{E}_a}{\partial Z} + \rho \frac{\partial \mathcal{E}_a}{\partial T} \right\} = -\alpha_2(\omega_a; \omega_b) I_b L \mathcal{E}_a. \quad (3.9)$$

For Gaussian shaped pulses, Equation (3.9) may be solved analytically to yield [53] (suppressing the frequency argument of the 2PA coefficient)

$$\mathcal{E}_a(\mathbf{r}, T) = \mathcal{E}_{0,a}(\mathbf{r}) \exp \left(-\frac{(T + T_d - \rho)^2}{2\mathcal{T}^2} - \frac{\alpha_2 L}{\rho} I_{0,b}(\mathbf{r}) [\text{erf} T - \text{erf}(T - \rho)] \right), \quad (3.10)$$

where \mathbf{r} is the radial coordinate, $\mathcal{E}_{0,a}(\mathbf{r})$ is the spatial distribution of the probe field, and $I_{0,b}(\mathbf{r})$ is the spatial distribution of the pump irradiance. Equation (3.10) may then be integrated over time and space to find the total energy of the probe transmitted.

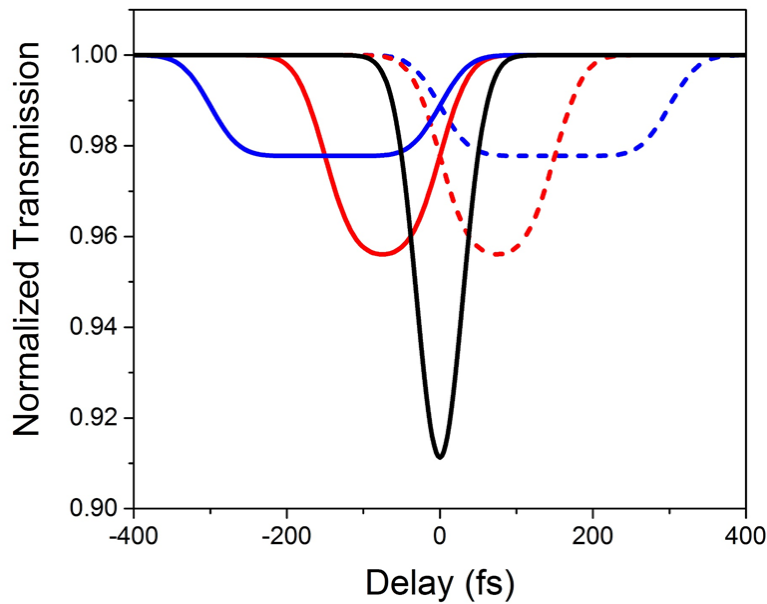


Figure 3.11 Example of Pump-probe measurement of 2PA with varying GVM for (black) $\rho = 0$, (red) $\rho = \pm 5$, and (blue) $\rho = \pm 10$, where solid curves are positive ρ and dashed curves are negative ρ .

Examples of the probe transmission for various values of ρ are shown in Figure 3.11. Compared to the case of zero GVM ($\rho = 0$), shown in black, increasing GVM results in a reduced signal magnitude. This is because the pulses only interact in a smaller region of the sample, rather than throughout its entire thickness. Additionally, the signal broadens in delay with increasing $|\rho|$. At zero delay, when both pulses arrive at the front of the sample simultaneously, the pulse with the higher group velocity (lower n_g) propagates faster through the sample, causing the pulses to walk off of one another. For a positive ρ the pump travels faster than the probe. At negative delay, where the probe arrives at the front of the sample first, the pump is able to catch up with it within the sample. This causes a the signal to broaden towards negative delay for positive ρ and towards positive delay for negative ρ .

The pump-probe technique has distinct advantages over the Z-scan technique. The use to two beams allows it to measure the spectrum of nondegenerate NLA (where there may be significant GVM) [15, 53]. Additionally it is also able to more directly measure noninstantaneous NLA (e.g. FCA) due to the ability to temporally delay the pump and probe. Additionally, pump-probe benefits greatly from the use of a lock-in amplifier, where the pump beam is externally modulated, and the signal at the modulation frequency is detected [54-56]. This eliminates extraneous signals, reduces the noise level, and only shows changes in the probe transmission due to the modulated pump beam. The technique is readily generalizable to measure different processes with the addition of more beams, such as in the Double Pump-Probe technique [57]. In § 5.2. a generalization of the pump-probe technique used to measure two-photon gain, with the addition of a third pulse to provide population inversion, is described. There are, however, disadvantages as well, for pump-probe only measures NLA, and is incapable of measuring NLR.

3.2.4. Degenerate Four-Wave Mixing

Degenerate Four-Wave Mixing is a similar pump-probe type technique, where two pump beams are overlapped in a sample at a small angle, such that they interfere and generate an irradiance grating within the sample. The material response then causes a refractive index grating in the material. A third beam, the probe, is diffracted off of the refractive index grating, and the diffracted energy is measured [16, 17, 58, 59]. In this sense, it is capable of measuring not only NLA, but NLR as well. Here we derive the signal measured in a DWFDM measurement on a sample that includes both nearly instantaneous bound-electronic and noninstantaneous nuclear responses.

When three beams overlap in a sample, the resulting third-order nonlinear interaction depends on $\tilde{\mathbf{E}}^3(t)$, and results in a whole host of nonlinear effects, including self- and cross-phase modulation (and/or NLA), third-harmonic generation, as well as the generation of new beams. The incident electric field may be written as

$$\tilde{\mathbf{E}}(t) = \sum_{n=1}^3 \tilde{\mathbf{E}}_n(t) = \sum_{n=1}^3 \frac{1}{2} \mathcal{E}_n(t) e^{i(\mathbf{k}_n \cdot \mathbf{r} - \omega_n t)} \hat{\mathbf{x}} + c. c., \quad (3.11)$$

where we have assumed that all three beams are linearly polarized in the x-direction. Here, beams 1 and 2 are considered the pumps, and 3 is the probe. When the field is cubed we get a total of $6^3 = 216$ terms. Given the complexity of the problem, we shall try to simplify it by only dealing with those that end up yielding new beams. We assume that the three beams are all at the same frequency (thus the “degenerate” in degenerate four-wave mixing). The field cubed is then

$$\begin{aligned} \tilde{\mathbf{E}}^3(t) = & \frac{1}{8} \{ (e^{-i3\omega t} [\text{THG}] + c. c.) \\ & + (e^{-i\omega t} [\text{Self- and Cross- Nonlinearities}] + c. c.) \\ & + (e^{-i\omega t} [\text{New Beams}] + c. c.) \}. \end{aligned} \quad (3.12)$$

The first term, [THG], includes $2 \times 3^3 = 54$ products (when you include the *c. c.*) that result in frequencies at 3ω , including those that do not propagate in the same direction as the initial beams, for example $\mathcal{E}_1 \mathcal{E}_2 \mathcal{E}_3 e^{i(\mathbf{k}_1 + \mathbf{k}_2 + \mathbf{k}_3) \cdot \mathbf{r}}$. The second term, [Self- and Cross- Nonlinearities], includes 90 terms (when you include the *c. c.* that propagate in the same direction as the initial beams, for example $|\mathcal{E}_1|^2 \mathcal{E}_1 e^{i\mathbf{k}_1 \cdot \mathbf{r}}$ and $|\mathcal{E}_1|^2 \mathcal{E}_2 e^{i\mathbf{k}_2 \cdot \mathbf{r}}$. The third term, [New Beams], contains $216 - 54 - 90 = 72$ terms that propagate in new directions (i.e., not along \mathbf{k}_1 , \mathbf{k}_2 , or \mathbf{k}_3) at frequency ω . We are particularly interested in those new beams that are due to an interaction of all incident three beams, which not all 72 terms are, for example, terms such as $\mathcal{E}_1^2 \mathcal{E}_2^* e^{i(2\mathbf{k}_1 - \mathbf{k}_2) \cdot \mathbf{r}}$. Only half of the

terms in [New Beams] originate from products of all three incident beams, leaving a total of 36 (when you include the *c. c.*). Since many of these terms are equal, they can be written simply as

$$\begin{aligned} & \frac{3}{4} [\mathcal{E}_1 \mathcal{E}_2 \mathcal{E}_3^* e^{i(\mathbf{k}_1 + \mathbf{k}_2 - \mathbf{k}_3) \cdot \mathbf{r}} + \mathcal{E}_1 \mathcal{E}_2^* \mathcal{E}_3 e^{i(\mathbf{k}_1 - \mathbf{k}_2 + \mathbf{k}_3) \cdot \mathbf{r}} \\ & + \mathcal{E}_1^* \mathcal{E}_2 \mathcal{E}_3 e^{i(-\mathbf{k}_1 + \mathbf{k}_2 + \mathbf{k}_3) \cdot \mathbf{r}}] e^{-i\omega t} + c. c. \end{aligned} \quad (3.13)$$

We now introduce a particular experimental geometry, known as the “boxcar” geometry, as illustrated in Figure 3.12. Only the last term explicitly shown in Equation (3.13) results in a beam that propagates in the \mathbf{k}_4 direction.

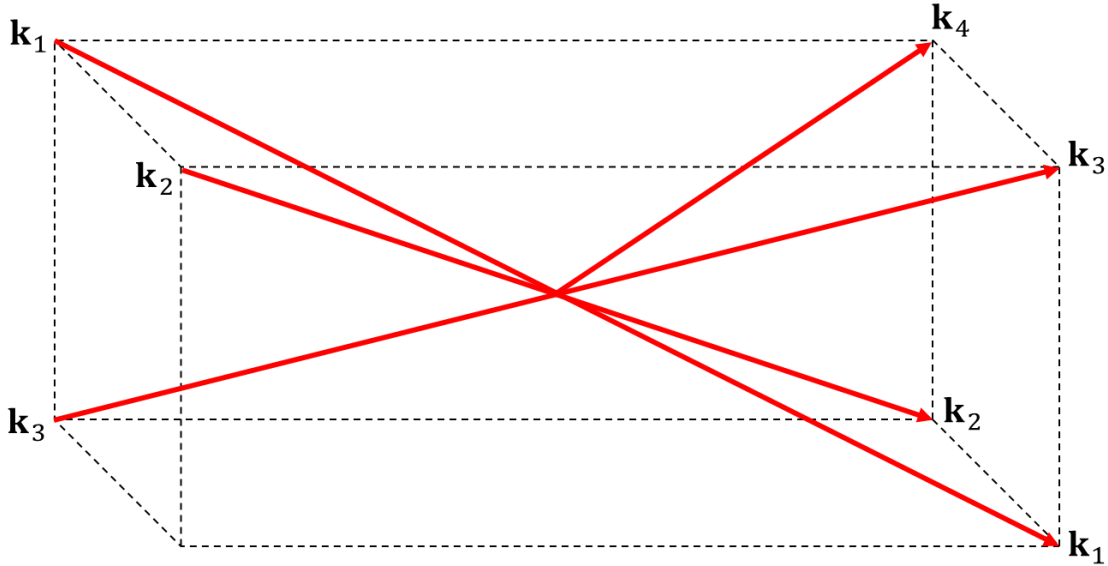


Figure 3.12 Boxcar phase matching geometry

The bound-electronic contribution to the third-order polarization in the $\mathbf{k}_4 = -\mathbf{k}_1 + \mathbf{k}_2 + \mathbf{k}_3$ direction is then given by

$$\mathbf{P}_{el,x}^{(3)}(\omega) = \frac{3}{4} \epsilon_0 \chi_{el}^{(3)} \mathcal{E}_1^*(t) \mathcal{E}_2(t) \mathcal{E}_3(t) e^{i(\mathbf{k}_4 \cdot \mathbf{r} - \omega t)} + c. c.. \quad (3.14)$$

The nuclear contribution is

$$\tilde{\mathbf{P}}_{nu}^{(3)}(t) = \varepsilon_0 \tilde{\mathbf{E}}(t) \int_{-\infty}^{\infty} \boldsymbol{\chi}_{nu}^{(3)}(t - t_2) : \tilde{\mathbf{E}}^2(t_2) dt_2 \quad (3.15)$$

When the field is squared in the integrand we get a total of $6^2 = 64$ terms, which have frequencies that are either at 0 or 2ω .

$$\tilde{\mathbf{E}}^2(t) = \frac{1}{4} \{ (e^{-i2\omega t} [\text{SH}] + c. c.) + ([\text{DC}] + c. c.) \} \quad (3.16)$$

The first term, [SH], includes 36 terms (when you include the *c. c.*) that result in frequencies at $\pm 2\omega$, and the second term, [DC] contains the remaining 36 terms (again when including the *c. c.*). Terms within the integrand with at frequency $\omega \neq 0$ integrate to zero assuming we are far from any resonances with $\boldsymbol{\chi}_{nu}^{(3)}(t)$. This is equivalent to assuming that the frequency range where $\mathcal{F}\{\boldsymbol{\chi}_{nu}^{(3)}(t)\} = \boldsymbol{\chi}_{nu}^{(3)}(\omega)$ is appreciable is much less than the optical frequency. These terms can be written as (where we temporarily drop the time argument)

$$\frac{1}{2} [\varepsilon_1 \varepsilon_2^* e^{i(\mathbf{k}_1 - \mathbf{k}_2) \cdot \mathbf{r}} + \varepsilon_1 \varepsilon_3^* e^{i(\mathbf{k}_1 - \mathbf{k}_3) \cdot \mathbf{r}} + \varepsilon_2 \varepsilon_3^* e^{i(\mathbf{k}_2 - \mathbf{k}_3) \cdot \mathbf{r}} + c. c.] \quad (3.17)$$

Substituting Equations (3.17) into the integrand of Equation (3.15)

$$\begin{aligned} \tilde{\mathbf{P}}_{nu,x}^{(3)}(t) = & \frac{\varepsilon_0}{4} \left(\sum_{n=1}^3 \varepsilon_n(t) e^{i(\mathbf{k}_n \cdot \mathbf{r} - \omega t)} \hat{\mathbf{x}} + c. c. \right) \int_{-\infty}^{\infty} \boldsymbol{\chi}_{nu}^{(3)}(t - t_2) \\ & \cdot (\varepsilon(t_2) \varepsilon_2^*(t_2) e^{i(\mathbf{k}_1 - \mathbf{k}_2) \cdot \mathbf{r}} + \varepsilon_1(t_2) \varepsilon_3^*(t_2) e^{i(\mathbf{k}_1 - \mathbf{k}_3) \cdot \mathbf{r}} \\ & + \varepsilon_2(t_2) \varepsilon_3^*(t_2) e^{i(\mathbf{k}_2 - \mathbf{k}_3) \cdot \mathbf{r}} + c. c.) dt_2. \end{aligned} \quad (3.18)$$

Keeping only terms that end up propagating in the $\mathbf{k}_4 = -\mathbf{k}_1 + \mathbf{k}_2 + \mathbf{k}_3$ direction

$$\begin{aligned} \tilde{\mathbf{P}}_{nu}^{(3)}(t) = & \frac{\varepsilon_0}{4} e^{i(\mathbf{k}_4 \cdot \mathbf{r} - \omega t)} \left(\varepsilon_3(t) \int_{-\infty}^{\infty} \chi_{nu}^{(3)}(t - t_2) \varepsilon_1^*(t_2) \varepsilon_2(t_2) dt_2 \right. \\ & \left. + \varepsilon_2(t) \int_{-\infty}^{\infty} \chi_{nu}^{(3)}(t - t_2) \varepsilon_1^*(t_2) \varepsilon_3(t_2) dt_2 \right) + c. c. \end{aligned} \quad (3.19)$$

It is interesting here to note that there are only two terms (plus the *c. c.*) in Equation (3.19), as compared to Equation (3.14) which has three (plus the *c. c.*). This is because even though the equivalent “missing” term

$$\frac{\varepsilon_0}{4} e^{i\mathbf{k}_4 \cdot \mathbf{r}} \left(\varepsilon_1^*(t) e^{i\omega t} \int_{-\infty}^{\infty} \chi_{nu}^{(3)}(t - t_2) \varepsilon_2(t_2) \varepsilon_3(t_2) e^{-i2\omega t_2} dt_2 \right) + c. c., \quad (3.20)$$

does propagate in the $\mathbf{k}_4 = -\mathbf{k}_1 + \mathbf{k}_2 + \mathbf{k}_3$ direction, the integrand contains $e^{-i2\omega t}$, and therefore integrates to zero.

The two terms in Equation (3.19) may be thought of as coming from two distinct origins. In the first term, pump fields ε_1^* and ε_2 interfere and generate a refractive index (assuming $\chi^{(3)}$ is real) grating, of which the probe field ε_3 diffracts. The delay between the two pump pulses is always kept fixed, so this term contributes to the measured signal for all probe delays. However, the second term results from the interference of the first pump field ε_1^* with the probe field ε_3 , and the second pump field ε_2 diffracts off of the resulting grating. This term will only contribute to the signal when the probe and pump fields are temporally overlapped within the sample, i.e., at zero delay.

The total third-order polarization amplitude, using Equation (2.7) is then given by

$$\begin{aligned}
\mathcal{P}^{(3)}(t) = & \frac{\varepsilon_0}{4} \left\{ 3\chi_{el}^{(3)} \mathcal{E}_1^*(t) \mathcal{E}_2(t) \mathcal{E}_3(t) \right. \\
& + \mathcal{E}_3(t) \int_{-\infty}^{\infty} \chi_{nu}^{(3)}(t-t_2) \mathcal{E}_1^*(t_2) \mathcal{E}_2(t_2) dt_2 \\
& \left. + \mathcal{E}_2(t) \int_{-\infty}^{\infty} \chi_{nu}^{(3)}(t-t_2) \mathcal{E}_1^*(t_2) \mathcal{E}_3(t_2) dt_2 \right\}.
\end{aligned} \tag{3.21}$$

The SVEA equation governing the evolution of the diffracted field \mathcal{E}_4 (the fourth wave in DWF), Equation (2.10), may then be integrated for low efficiency (assuming none of the initial three beams are depleted, or change irradiance distributions), we may simply approximate \mathcal{E}_4 at the output the (thin) sample as

$$\begin{aligned}
\mathcal{E}_4(L, t) \approx & i \frac{\omega L}{8n_0 c} \left\{ 3\chi_{el}^{(3)} \mathcal{E}_1^*(t) \mathcal{E}_2(t) \mathcal{E}_3(t) \right. \\
& + \mathcal{E}_3(t) \int_{-\infty}^{\infty} \chi_n^{(3)}(t-t_2) \mathcal{E}_1^*(t_2) \mathcal{E}_2(t_2) dt_2 \\
& \left. + \mathcal{E}_2(t) \int_{-\infty}^{\infty} \chi_n^{(3)}(t-t_2) \mathcal{E}_1^*(t_2) \mathcal{E}_3(t_2) dt_2 \right\}.
\end{aligned} \tag{3.22}$$

The signal is then given by the diffracted energy

$$E_4 = \frac{2}{\varepsilon_0 n_0 c} \iiint_{-\infty}^{\infty} |\mathcal{E}_4(\mathbf{r}, L, t)|^2 d^2 \mathbf{r} dt. \tag{3.23}$$

By measuring only the diffracted energy, only information about the square magnitude of the nonlinearity is gained, meaning the sign and phase (real vs. imaginary) information is lost. The phase of the diffracted field does depend on these parameters, but their measurement requires interferometric techniques [60].

3.2.5. Beam Deflection

To measure NLR we have developed the Beam Deflection (BD) technique [50, 61, 62]. It was originally motivated by the photothermal beam deflection technique, where a strong pump source would undergo weak absorption in a sample, and a probe beam would be deflected by the resulting thermal refractive index change. The concept was based on a thin prism, which causes a beam to be deflected by an angle $\theta \approx (n - 1)\alpha$, which depends on the difference in refractive index n of the glass of the prism and the surrounding air, and the angle of the prism α (see Figure 3.13). This can easily be seen from a geometrical optics point of view, but may also be thought of as a linear phase gradient applied to the beam causing deflection.

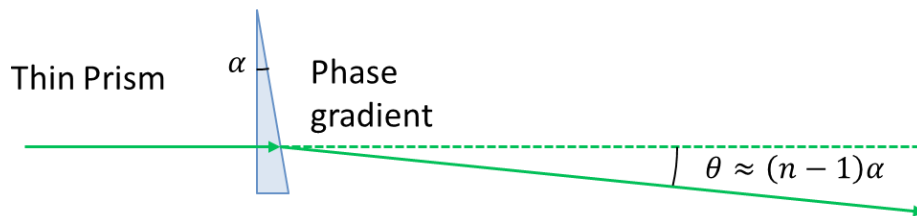


Figure 3.13 Illustration of beam deflected due to a thin prism.

In the case of photo thermal beam deflection, a CW Gaussian beam is incident on a weakly absorbing sample, and induce a refractive index change that followed the irradiance distribution via thermal nonlinearity [63, 64]. The angle of deflection is then measured by a position sensitive detector (e.g. segmented photodiode, or camera) placed in the far-field. The extension we have made is to use femtosecond pulsed lasers, rather than CW, to look at ultrafast NLR, rather than photothermal. Figure 3.14 shows a diagram of the BD experimental setup. It is very similar to that of pump-probe, with two significant differences. A spatially Gaussian pump beam will induce a

refractive index change that follows its irradiance distribution (see Figure 3.14 (c)). There is a region towards the wings of this index change where the refractive index gradient is linear and appears very similar to the spatially linear phase gradient of a thin prism. A probe beam is then focused to this location to a much smaller spot size than the pump ($\sim 4\text{-}10\times$), and essentially experiences a thin prism and is deflected by a small angle. This deflection causes the beam to shift on a segmented quad-cell detector placed in the far-field, such that there is now a difference between the energy falling on the two sides. The quad-cell detectors used are the same as those in atomic force microscopes, which have been well refined for high performance and low noise [65].

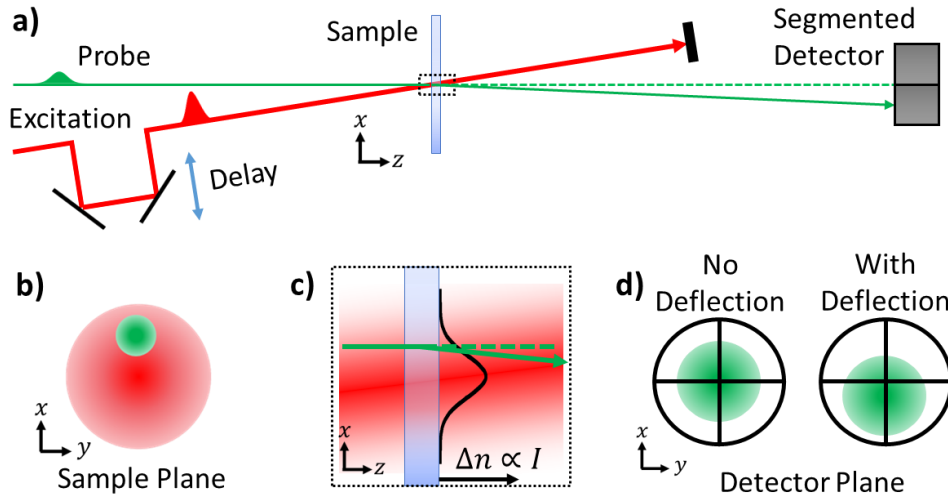


Figure 3.14 (a) Diagram of Beam Deflection experimental setup. (b) Irradiance profile at sample plane showing position relative positioning and size of (red) excitation and (green) probe beams. (c) Zoom in of the beam overlapping within the sample from (a) showing irradiance dependent refractive index change and probe deflection. (d) Probe beam location on segmented quad-cell detector without and with deflection. (Reproduced with permission from Ref. [62]).

The phase change accumulated by the weak probe beam due to the strong pump is (within the thin-sample approximation)

$$\Delta\phi_a(\mathbf{r}, t) = k_{0,a}\Delta n(\mathbf{r}, t)L. \quad (3.24)$$

If the probe spot size is much smaller than the pump's, the spatially Gaussian refractive index change may be expanded about the location of the probe,

$$\Delta n(\mathbf{r}, t) = \Delta n(t) \exp\left(-2 \frac{(x + x_0)^2 + y_0^2}{w_b^2}\right), \quad (3.25)$$

$$\Delta n(\mathbf{r}, t) \approx \Delta n(t) \left(1 - \frac{4x_0}{w_b^2} x\right) \exp\left(-2 \frac{x_0^2}{w_b^2}\right). \quad (3.26)$$

Here $x_0 = w_b/2$ is the displacement of the probe from the pump's center, which is selected where the spatial gradient of I_b (and thus Δn) is maximized, and w_b is the pump spot size (HW1/e²M).

The phase change is then given by

$$\Delta\phi_a(\mathbf{r}, L, t) = k_{0,a} \Delta n(t) L \left(1 - \frac{2}{w_b} x\right) e^{-1/2}, \quad (3.27)$$

and the probe field distribution given by

$$\mathcal{E}_a(\mathbf{r}, L, t) = \mathcal{E}_a(\mathbf{r}, 0, t) \exp\left(ik_{0,a} \Delta n(t) L \left(1 - \frac{2}{w_b} x\right) e^{-1/2}\right). \quad (3.28)$$

Equation (3.28) shows the field has a phase shift imposed on it by the pump. Fourier transforming the field distribution to the detector plane in the far-field alters the phase shift into a displacement [66]

$$\mathcal{E}_a(\mathbf{r}, d, t) = \mathcal{E}_a(x + \Delta x, y, d, t), \quad (3.29)$$

where d is the distance from the sample plane to the detector plane, and the displacement Δx is given by

$$\Delta x = \frac{2L}{w_b \sqrt{e}} \Delta n(t) d. \quad (3.30)$$

Thus we see that the gradient in the induced refractive index change leads to a displacement of the probe beam on the detector.

A quad-segmented detector is unable to measure this displacement directly, but rather measures the amount of energy falling on each segment. For a TEM₀₀ Gaussian probe beam with the beam waist located at the sample, the irradiance at the detector in the absence of the deflection is given by

$$I_a(x, y, d, t - \tau_d) = I_{0,a} \left(\frac{w_{0,a}}{w_a(d)} \right)^2 \exp \left(-2 \frac{x^2 + y^2}{w_a^2(d)} - \frac{(t - \tau_d)^2}{\tau_a^2} \right) \quad (3.31)$$

where w_a and τ_a are the spot size and pulse width of the probe, respectively, τ_d is the temporal delay of the probe with respect to the pump, and

$$w_a(d) = w_{0,a} \sqrt{1 + \left(\frac{d}{z_{0,a}} \right)^2} \approx w_{0,a} \frac{d}{z_{0,a}}, \quad (3.32)$$

where $z_{0,a} = k_{0,a} w_{0,a}^2 / 2$ is the Rayleigh range of the probe beam. In the far-field $d \gg z_{0,a}$, and the probe spot size may be approximated by

$$w_a(d) \approx \frac{2d}{k_{0,a} w_{0,a}}. \quad (3.33)$$

The BD signal is taken to be the energy falling on the left half of the detector minus that on the right half, $\Delta E = E_{left} - E_{right}$. We first calculate the difference in power falling on each side of the detector by integrating over the xy-plane

$$\Delta P_a(t - \tau_d) = \int_{-\infty}^{\infty} \left(\int_{-\infty}^0 I_a(x + \Delta x, y, d, t) dx - \int_0^{\infty} I_a(x + \Delta x, y, d, t) dx \right) dy, \quad (3.34)$$

which simplifies to

$$\Delta P_a(t - \tau_d) = \operatorname{erf} \left(\sqrt{\frac{2}{e}} \frac{w_{0,a}}{w_b} k_{0,a} \Delta n(t) L \right) P_a(t - \tau_d), \quad (3.35)$$

where $P_a(t - \tau_d) = \frac{\pi w_{0,a}^2}{2} I_{0,a} e^{-\frac{(t-\tau_d)^2}{\tau_a^2}}$. We now assume the refractive index change is sufficiently small that we may approximate $\text{erf}(x) \approx 2x/\sqrt{\pi}$. Applying this small signal approximation yields

$$\Delta P_a(t - \tau_d) = \frac{2\sqrt{2} w_{0,a}}{\sqrt{e\pi} w_b} \cdot k_{0,a} \Delta n(t) L \cdot P_a(t - \tau_d) \quad (3.36)$$

The BD signal is then found by integrating Equation (3.36) and dividing by the total energy

$$\frac{\Delta E_a(\tau_d)}{E_a} = \frac{2\sqrt{2} w_{0,a}}{\sqrt{e\pi} w_b} \cdot k_{0,a} L \langle \Delta n(\tau_d) \rangle, \quad (3.37)$$

where

$$\langle \Delta n(\tau_d) \rangle \equiv \int_{-\infty}^{\infty} \Delta n(t) I_a(t - \tau_d) dt / \int_{-\infty}^{\infty} I_a(t - \tau_d) dt \quad (3.38)$$

is the change in refractive index averaged over the probe pulse duration. Thus far we have not assumed a functional form of the refractive index change, only that it is third-order in the field. This allows us to treat noninstantaneous NLR, as we will in CHAPTER 4: . Here, we assume bound-electronic NLR, where $\Delta n(t) = 2n_2(\omega_a; \omega_b) I_b(t)$. Substituting this into Equation (3.38) gives

$$\langle \Delta n(\tau_d) \rangle = \frac{2n_2(\omega_a; \omega_b) I_{0,b}}{\sqrt{1 + \tau_b^2/\tau_a^2}} \exp\left(-\frac{\tau_d^2}{\tau_a^2 + \tau_b^2}\right), \quad (3.39)$$

and Equation (3.37) becomes

$$\frac{\Delta E_a(\tau_d)}{E_a} = \frac{\sqrt{2} w_{0,a}}{\sqrt{e\pi} w_b} k_{0,a} L \frac{4n_2(\omega_a; \omega_b) I_{0,b}}{\sqrt{1 + \tau_b^2/\tau_a^2}} \exp\left(-\frac{\tau_d^2}{\tau_a^2 + \tau_b^2}\right). \quad (3.40)$$

This signal is proportional to the n_2 , and thus both the sign and amplitude of the NLR can be measured directly. This has distinct advantages over other multi-beam techniques, such as OKE and DFWM, which require heterodyne (interferometric) detection to get the sign of the nonlinearity [67, 68].

This analysis may be generalized to the case where many of the approximations made here are not valid, including when $w_{0,a}$ approaches w_b , the signal is not small, and in the presence of 2PA. A numerical analysis program has been written to take into account the actual irradiance distributions of both beams within the sample, which calculates induced changes in both the phase and amplitude of the probe field at the back of the sample. It then performs a Fresnel propagation [66] to the detector plane where it then integrates the irradiance distribution on the each detector segment to calculate $\Delta E(\tau_d)/E(\tau_d)$.

Figure 3.15 shows an example of BD measurements on a 1 mm sample of fused silica where the NLR is predominantly bound-electronic in origin [69]. These measurements were made using the fundamental output from the Clark-MXR laser as the pump (with parameters $\lambda_b = 780$ nm, $w_b = 170$ μm , $\tau_b = 241$ fs) and probe generated from the TOPAS-C (with parameters $\lambda_a = 650$ nm, $w_b = 35$ μm , $\tau_b = 170$ fs). The signal from the quad-cell was sent through a lock-in amplifier (SR830) that detected at the 286 Hz modulation frequency of an optical chopper in the pump beam. The polarization of the pump and the probe were both linear, but the angle between the two was changed from parallel to perpendicular. In Figure 3.15 (a) $I_{0,b} = 51$ GW/cm² ($E_b = 9.9$ μJ), and the fitting shown in corresponds to $n_{2,\parallel} = (0.24 \pm 0.05) \times 10^{-19}$ m²/W and $n_{2,\perp} = (0.08 \pm 0.02) \times 10^{-19}$ m²/W, which agrees both with literature values [69], and the theoretical ratio for isotropic medium $n_{2,\parallel}/n_{2,\perp} = 3$ [16, 17].

Figure 3.15 (b) shows the measurement (with parallel polarizations) where the pump irradiance has been reduced to $I_{0,b} = 0.35 \text{ GW/cm}^2$ ($E_b = 68 \text{ nJ}$) such that the noise floor can be observed. The standard deviation of the noise is $\sigma(\Delta E/E) = 5 \times 10^{-5}$ (0.005 %), which corresponds to a peak on axis (center of pump beam) phase change $\Delta\phi_{0,a} = 0.3 \text{ mrad}$, or an OPL change of $\lambda_a/20,000 = 32.5 \text{ pm}$. This high sensitivity is largely due to the advances in the electronics used in quad-segmented detectors that have been developed primarily for atomic-force microscopy applications [65], which do an excellent job of subtracting out probe energy fluctuations.

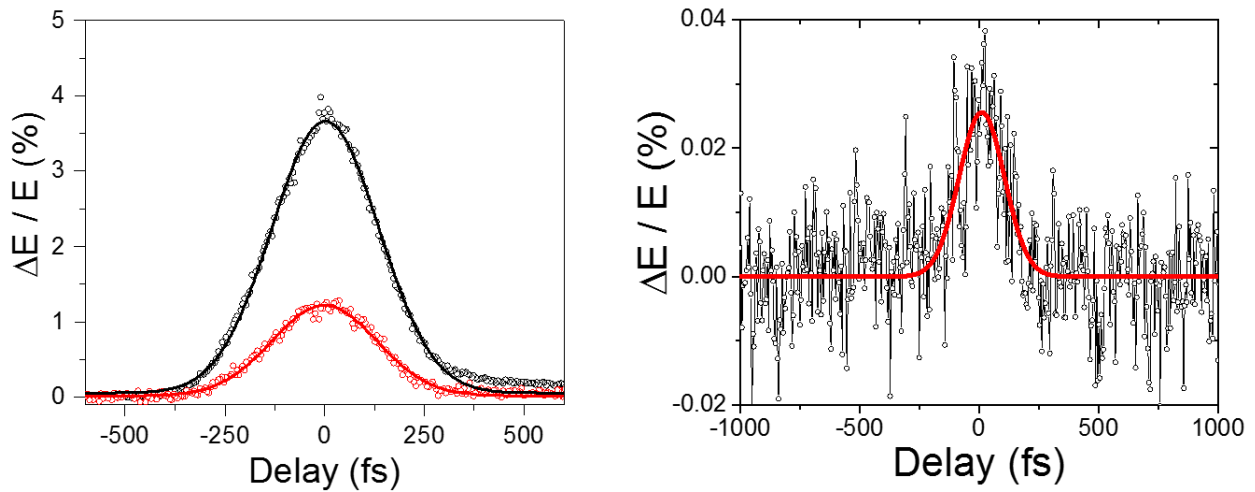


Figure 3.15 Beam deflection measurements of a 1 mm sample of fused silica. (left) Measurement (circles) and fit (curves) for parallel (black) and perpendicular (red) polarizations. (right) Reduced pump irradiance to observe noise floor. (Modified with permission from Ref. [61])

Furthermore, BD can measure the total probe transmission, from which NLA may be determined. It can be shown that the BD signal is very well adapt at measuring NLR and NLA simultaneously [50, 70]. BD is able to measure small NLR even in the presence of large 2PA without contamination of the NLR signal, as with Z-scan. The inclusion of GVM is also possible, and is a

straightforward application of the analysis in § 3.2.3. This analysis has assumed only nearly instantaneous bound-electronic NLR. The true strength of this technique is its capability to measure temporally varying NLR, as will be discussed in CHAPTER 4: .

3.2.6. Two-photon Stimulated Emission Depletion

Observing the fluorescence from a material can provide information on the way the electrons were excited. Specifically, by measuring the dependence of the fluorescence on the irradiance of the excitation can distinguish 2PA, which will present a quadratic dependence, from one-photon, which has a linear dependence.

Two-photon induced fluorescence (2PF) utilizes a pump beam that experiences significant 2PA to generate an excited state population. To verify that the carrier generation is indeed due to 2PA, the fluoresced energy is observed as a function of the pump irradiance and the dependence is checked to be quadratic, that is

$$E_{2PF} \propto \int I^2 dt. \quad (3.41)$$

This allows much more rapid characterization of the 2PA spectrum of materials (compared to Z-scan), so long as they are sufficiently fluorescent [71, 72]. This method has been used to measure the 2PA coefficients of various materials [71], and has been applied to observe two-photon gain as well [73, 74].

Stimulated emission depletion (STED) experiments rely on observing the reduction in fluorescence due to one-photon stimulated emission removing electrons from the excited state so that there are fewer remaining to fluoresce. This first requires a population inversion, typically generated optically by a laser beam of higher photon energy than the stimulating beam, which then

stimulates emission and depletes the excited state. The technique has been applied to microscopy to beat the classical diffraction resolution limit [75].

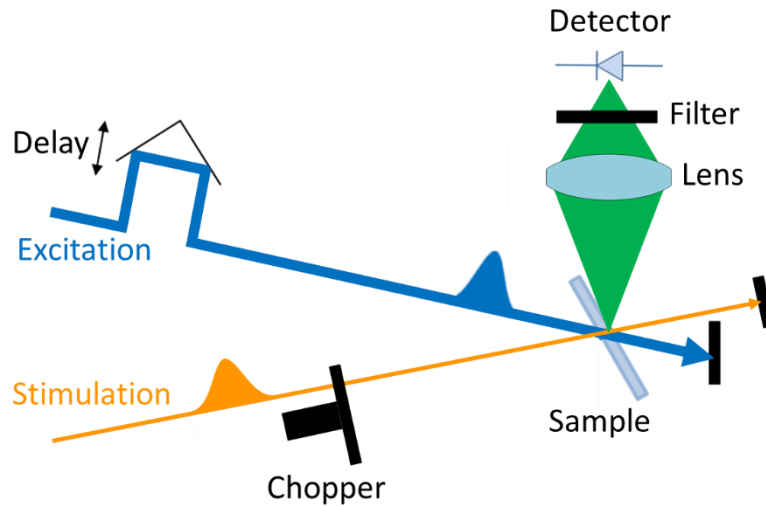


Figure 3.16 Illustration of 2P-STED experimental setup.

The same approach may be applied to the two-photon case. Doubly-stimulated two-photon emission may be induced in a material with an inverted population between excited and ground states. This stimulated 2PE removes the population from the excited states, so that there are fewer electrons remaining to fluoresce. By measuring the irradiance dependence of the reduction in fluorescence the nature of the stimulated emission, one-photon (linear) or two-photon (quadratic), can be determined.

Experimentally, this involves exciting a large population to the excited state via one-photon absorption, and then stimulating emission via two-photon gain with a femtosecond pulse with photon energy that is half of the transition energy, $2\hbar\omega = E_{eg}$. The temporal delay may be adjusted between the excitation and stimulation pulses to maximize the change in fluorescence, or observe

the decay rate of the excited state. The emitted fluorescence at the transition energy is then collected, typically at a 90° angle with respect to the excitation and stimulating laser beams to reduce the detection of scattered light (see Figure 3.16). A spectral filter is used to collect only the wavelengths of fluorescence, and block those of the excitation and stimulation beams. Furthermore, lock-in detection may be utilized, where the detection is synchronized to the modulation frequency of the optical chopper in the stimulating beam. This is done to directly measure the change induced by the 2P-STED, and help eliminate the large fluorescence signal from the excitation beam itself. This technique is complementary to the pump-probe measurements of doubly-stimulated two-photon emission, which will be discussed in § 5.2.

CHAPTER 4: ULTRAFAST NONLINEAR DYNAMICS OF MOLECULES

Understanding of the temporal dynamics of the nonlinear refraction is important for nonlinear photonics applications, such as ultrafast time-resolved imaging [76], soliton propagation [77, 78], filamentation and supercontinuum generation [79], slow light [80], and all-optical switching [81]. The nonlinear optical properties of simple molecules may be drastically different than those of atomic systems. This is because the dynamics of the molecules themselves may play a large role in the material's response to an applied electric field. This can lead to large non-instantaneous nonlinear refractive responses, as discussed in § 2.3.

Here we present a thorough experimental study of the ultrafast nonlinear refractive dynamics of molecular systems, focusing primarily on liquid carbon disulfide. Carbon disulfide is the most popular material for applications of nonlinear optical liquids, and is frequently used as a reference standard for NLO measurements. However, its nonlinearity varies by over an order of magnitude depending on pulse duration [82]. The application of our recently developed beam deflection technique [61] provides complete determination of the ultrafast response function, including absolute magnitudes, temporal dynamics, and symmetry properties of each mechanisms' contribution [62]. The response function allows prediction of any nonlinear refractive measurement on CS₂, and establishes it as a proper reference material. This experimental approach may also be applied to a wide variety of other materials, including molecular gases such as air.

4.1. Origin of noninstantaneous third-order response of molecular liquids

The optical properties of individual molecules depend primarily on both permanent dipoles and those induced by the applied electric field [16, 17]. This may be expanded as a power series of the local field, much like the macroscopic polarization³ [83]

$$\boldsymbol{\mu} = \boldsymbol{\mu}^{(0)} + \boldsymbol{\alpha} \cdot \mathbf{E}_{loc} + \boldsymbol{\beta} : \mathbf{E}_{loc}^2 + \boldsymbol{\gamma} : \mathbf{E}_{loc}^3 + \dots, \quad (4.1)$$

where $\boldsymbol{\mu}^{(0)}$ is the permanent dipole moment, $\boldsymbol{\alpha}$ is the (linear) polarizability, $\boldsymbol{\beta}$ is the (first) hyperpolarizability, $\boldsymbol{\gamma}$ is the second hyperpolarizability, and $\mathbf{E}_{loc} = f^{(1)}\mathbf{E}$, where $f^{(1)}$ is the local field correction factor [16, 17], which is the local electric field experienced by the molecule. In general these molecular response depends on the orientation of the field with respect to the molecular axis. For example, molecules that do not possess spherical symmetry have a polarizability $\boldsymbol{\alpha}$ that depends on the molecular axis. The dipole moment is related to the macroscopic polarization by $\mathbf{P} = \langle \boldsymbol{\mu} \rangle N$, where the angular brackets indicates ensemble averaging [16, 17]. From this, and Equations (2.5) and (4.1), the linear susceptibility is given by

$$\boldsymbol{\chi}^{(1)} = \frac{N}{\epsilon_0} f^{(1)} \langle \boldsymbol{\alpha} \rangle, \quad (4.2)$$

and, using $\mathbf{n}^2 = 1 + \boldsymbol{\chi}^{(1)}$,

$$\mathbf{n}^2 = 1 + \frac{N}{\epsilon_0} f^{(1)} \langle \boldsymbol{\alpha} \rangle. \quad (4.3)$$

Similarly the third-order susceptibility is related to the second hyperpolarizability by

³ Equation (4.1) as written assume that the induced dipole is always exactly in phase with the applied local field, i.e., there is no dispersion or absorption. A more general treatment would appear similar to the treatment of the macroscopic polarization in Equation (2.4). Additionally, it is common to use a Taylor series expansion, rather than a power series expansion, in which case there is a factor of 1/2 on the \mathbf{E}^2 term, and 1/6 on the \mathbf{E}^3 term

$$\chi^{(3)} = \frac{N}{\epsilon_0} f^{(3)} \langle \gamma \rangle, \quad (4.4)$$

where $f^{(3)}$ is the Lorentz-Lorenz local field correction factor for third-order nonlinearities, which for the degenerate case is simply $(f^{(1)})^4$ [16, 17, 20]. The first hyperpolarizability leads to $\chi^{(2)}$ in a similar fashion.

Changes in the refractive index of a molecular ensemble may arise from not only the bound-electronic response, via γ , but also through changes in $\langle \alpha \rangle$ by either changes in the amplitude of individual tensor elements or orientational effects. There are several mechanisms by which an incident optical field can alter the refractive index of an ensemble of molecules in liquid or gas phase. Here we give a detailed description of the dominant processes observed in this work. The noninstantaneous third order response of the form in Equation (2.29) may be further decomposed into the various mechanisms, each corresponding to a particular type of molecular motion. Strictly speaking, these motions are not linearly independent, and there have been many theoretical studies of their correlation [84, 85]. However, many experiments have been successfully analyzed by treating them as linearly independent [67, 86, 87], and we take the same approach here. In this case, the nonlinear response function may be written [62]

$$R(t) = \sum_m n_{2,m} r_m(t), \quad (4.5)$$

where $n_{2,m}$ is the magnitude of the m th mechanism, and $r_m(t)$ is the temporal response function, which is normalized by

$$\int_{-\infty}^{\infty} r_m(t) dt = 1. \quad (4.6)$$

In the following we describe a total of four nuclear mechanisms that contribute to the non-instantaneous nonlinear optical response of molecular liquids; diffusive reorientation, libration, vibration, and collision. For each mechanism, the underlying physical origin that gives rise to the response, and the temporal response functions that may be used to model them are discussed.

4.1.1. Diffusive Reorientation

For linear molecules, e.g. CS₂, O₂, N₂, etc., the polarizability along the molecular axis α_{\parallel} is greater than that along the perpendicular directions α_{\perp} . At thermal equilibrium, the ensemble has a random (isotropic) distribution of orientations, and the orientational averaging of the polarizability is

$$\langle \alpha \rangle = \langle \cos^2 \theta \rangle \Delta \alpha + \alpha_{\perp}, \quad (4.7)$$

where $\Delta \alpha = \alpha_{\parallel} - \alpha_{\perp}$, and θ is the angle between the molecular axis and the incident field. $\langle \cos^2 \theta \rangle$ is a measure of the degree of alignment of the molecules, and reduces to 1/3 for an isotropic, randomly distributed, system. From Equations (4.3) and (4.7) we see that changes in the degree of alignment of a system of linear molecules can induced large changes in the refractive index.

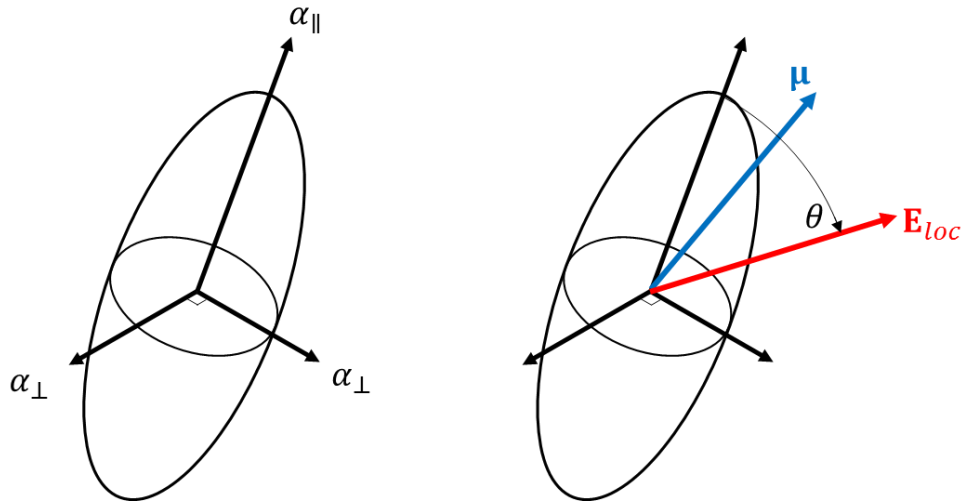


Figure 4.1 Ellipsoidal molecule showing (left) polarizability and (right) local field induced dipole moment

These changes can be brought about by an applied electric field. Given the anisotropic polarizability, an applied field at angle θ with respect to the molecular axis will displace the electron distribution more so along the molecular axis than perpendicular to it (see Figure 4.1). Therefore the induced dipole is not parallel to the applied field and a torque

$$\boldsymbol{\tau} = \boldsymbol{\mu} \times \mathbf{E}_{loc} \quad (4.8)$$

is applied to the molecule. In the case of a permanent dipole, the time variation of the field would cause the torque to be in one direction for half a period, and then the opposite for the next half period, such that over many optical cycles the torque would cancel out. However, for an induced dipole of the form $\boldsymbol{\mu} = \boldsymbol{\alpha} \cdot \mathbf{E}_{loc}$, the dipole oscillates in phase with the applied field, and thus the torque over an optical cycle is all of the same sign. The dipole induced dipole on an individual molecule by an applied field is

$$\boldsymbol{\mu} = \boldsymbol{\alpha} \cdot \mathbf{E}_{loc} = \alpha_{\parallel} \mathbf{E}_{loc} \cos(\theta) \hat{\parallel} + \alpha_{\perp} \mathbf{E}_{loc} \sin(\theta) \hat{\perp}_1, \quad (4.9)$$

where $\hat{\parallel}$ is the unit vector in the direction parallel to the molecular axis, and $\hat{\perp}_1$ is the unit vector perpendicular to the molecular axis in the plane of $\hat{\parallel}$ and \mathbf{E}_{loc} . This results in a torque

$$\boldsymbol{\tau} = \boldsymbol{\mu} \times \mathbf{E}_{loc} = \Delta\alpha \mathbf{E}_{loc}^2 \cos(\theta) \sin(\theta) \hat{\mathbf{I}}_2, \quad (4.10)$$

where $\hat{\mathbf{I}}_2$ is the unit vector perpendicular to both $\hat{\mathbf{I}}$ and $\hat{\mathbf{I}}_1$. Because $\boldsymbol{\tau}$ depends on \mathbf{E}_{loc}^2 , it is always positive over an optical cycle.

This torque causes the molecules to rotate towards the field direction. With the orientation of the molecules now different from their initially isotropic distribution, the degree of alignment $\langle \cos^2 \theta \rangle$ now deviates from 1/3, and the refractive index changes. For an ultrashort pulse, the molecules will continue to rotate even after the field has passed simply due to inertia. In liquids, where the number density of molecules is high, this rotation will cease once they begin colliding with one another, and the orientation will return to its initial isotropic distribution. The rate of thermal randomization depends on the viscosity of the liquid, and follows a diffusive relaxation according to the Debye-Stoke-Einstein relation [88]. For this reason this mechanism is often referred to as diffusive reorientation.

The applied field induces a change in the angle of orientation of the molecule by $\delta\theta$. The evolution of the orientation angle of an individual molecule may be modelled as a classical driven damped harmonic oscillator [67, 89]. In the liquid, averaging over the isotropic distribution of molecular orientations in the ensemble allows a description of the refractive index change due to this reorientation [67]. The overdamped solution may be written in the form of Equation (2.39) where the normalized response function is

$$r_d(t) = C_d \left(1 - e^{-\frac{t}{\tau_{r,d}}} \right) e^{-\frac{t}{\tau_{f,d}}} \Theta(t). \quad (4.11)$$

where $C_d = (\tau_{r,d} + \tau_{f,d})/\tau_{f,d}^2$ is a normalization constant, $\tau_{r,d}$ and $\tau_{f,d}$ are the rise and fall times, respectively, and $\Theta(t)$ is the Heaviside (step) function, which ensures causality, and the subscript

d indicates the diffusive reorientation mechanism. The time constants and magnitude, $n_{2,d}$, are then fit parameters based on experimental measurements.

4.1.2. Libration

The diffusive reorientation dominates on long time scales, but during the first few 100 fs, the molecules may oscillate in their local potential as they collide and rebound off neighboring molecules. This results in an oscillatory rocking motion causing a change in the refractive index due to the coherent oscillation of many molecules in the ensemble. This mechanism may be modeled by an underdamped oscillator, which retains oscillatory character. However, loss of coherence among the many oscillating molecules in the ensemble, rather than damping of the oscillation of individual molecules, is the dominant decay mechanism of the induced refractive index change [24, 67]. Thus the distribution of libration frequencies must be included. The librational response function may be more accurately modeled by a quantum harmonic oscillator, and is given by [24]

$$r_l(t) = C_l e^{-\frac{t}{\tau_{f,l}}} \Theta(t) \int_0^{\infty} \frac{\sin(\omega t)}{\omega} g(\omega) d\omega, \quad (4.12)$$

where the subscript l refers to the librational response, and $g(\omega)$ is the distribution function of librational frequencies. Each molecule experiences its own local environment based on its relative orientation and separation from neighboring molecules. Since the oscillatory librational response depends heavily on the interaction of molecules with their local environment, the total response is inhomogeneously broadened. Following McMorro et al. [24], we model this distribution with an “antisymmeterized” Gaussian distribution function

$$g(\omega) = \exp\left(-\frac{(\omega - \omega_0)^2}{2\sigma^2}\right) - \exp\left(-\frac{(\omega + \omega_0)^2}{2\sigma^2}\right), \quad (4.13)$$

where ω_0 is the central oscillation frequency, and σ is the standard deviation.

4.1.3. Vibration

On top of motions of the molecule as a whole, the nuclei within a molecule may move with respect to one another. This causes a vibrational motion of the molecule that alters the components of the polarizability tensor α , and therefore changes the refractive index via Equation (4.3). The vibrational modes of molecules are quantized, where each mode oscillates at a specific frequency. For example, in CS₂, the possible vibrational modes include symmetric stretch modes, where both S nuclei move away from and then back towards the central C nucleus.

Not all vibrational modes may be excited by a femtosecond pulse; the mode must be Raman active [17]. Additionally, these modes will not contribute significantly to the refractive index change [25, 90], and the pulse width of the pump pulse is less than half the vibration period. This may be thought of in the time domain by the first portion of the pulse exciting a vibration, and then the second portion of a pulse exciting another vibration, but which now has the opposite phase as the initial one. Thus over the duration of a long pulse, the vibrations cancel one another.

When the pulse is shorter than the vibrational period of a Raman active mode, it results in a coherent (impulsive) excitation. This may alternatively be thought of in the frequency domain as stimulated Raman scattering. Since the pulse width is shorter than the vibrational period it has a bandwidth that is greater than the vibrational frequency. Different frequency components within the pulse may excite and stimulate Raman transitions from the vibrational ground state to the excited modes.

Since the vibration of the molecules alters the polarizability tensor, the corresponding refractive index change oscillates at the same frequency. The response function may be modeled as

$$r_v(t) = C_v \sin(\omega_v t) e^{-\frac{t}{\tau_{f,v}}} \Theta(t), \quad (4.14)$$

where the subscript v refers to the vibrational mechanism, and ω_v is the frequency of the vibrational mode.

4.1.4. Collision

In addition to libration, another bulk liquid phenomena having to do with the interaction of neighboring molecules are collisions. As molecules collide with one another within the dense liquid, they alter their distributions via dipole-induced dipole and electron overlap effects [67, 87, 91]. These effects change the refractive index, since a strong incident electric field induces a large dipole in a molecule, which is then experienced by the neighboring molecules in its vicinity. This results in a distortion of the electron distribution in the surrounding molecules and therefore changes the polarizability [92]. This causes variations in the average equilibrium molecular separation (and thus density), and is thus described by a local translational anisotropy that decays away on the timescale of the density fluctuations [67]. The corresponding response function may be modelled by a simple exponential rise and decay in the same form of Equation (4.11)

$$r_c(t) = C_c \left(1 - e^{-\frac{t}{\tau_{r,c}}} \right) e^{-\frac{t}{\tau_{f,c}}} \Theta(t), \quad (4.15)$$

where the subscript c refers to the collision induced mechanism. This effect has been observed in a number of liquid systems, including atomic liquids of Ar and Xe, which possess isotropic polarizabilities [91].

4.2. Noninstantaneous response in Beam Deflection measurements

The analysis presented in § 3.2.5. assumed the material response was instantaneous. Here we expand this analysis to include the noninstantaneous third-order response of the form presented in § 2.3. In addition, since the molecular liquid studied experimentally, CS₂, is highly dispersive [27, 28], GVM is included. Similar to the derivation presented in § 3.2.3. we begin with the wave equation governing the weak probe field due to the strong pump (which is assumed to be undepleted) Equation (2.9)(2.13). The nonlinear polarization originates from both nearly instantaneous bound-electronic response, Equation (2.13), as well as noninstantaneous nuclear contributions, Equation (2.33). We assume negligible linear absorption ($\alpha_1(\omega_a) \approx 0$, although including it is straightforward [53]), and $|\partial\mathcal{P}_a/\partial t| \ll \omega_a\mathcal{P}_a$. Based on these assumptions, Equation (2.9) becomes

$$i\left(\frac{\partial\mathcal{E}_a}{\partial z} + \frac{1}{v_{g,a}}\frac{\partial\mathcal{E}_a}{\partial t}\right) = -\frac{\mu_0\omega_a^2}{2}\left(\mathcal{P}_{el,a}^{(3)} + \mathcal{P}_{nu,a}^{(3)}\right), \quad (4.16)$$

where

$$\mathcal{P}_{el,a}^{(3)} = 3\frac{\epsilon_0}{2}\chi_{el}^{(3)}(\omega_a; \omega_a, \omega_b, -\omega_b)\mathcal{E}_a|\mathcal{E}_b|^2, \quad (4.17)$$

and

$$\mathcal{P}_{nu,a}^{(3)}(t) = \frac{\epsilon_0}{2}\mathcal{E}_a(t) \int_{-\infty}^{\infty} \chi_{nu}^{(3)}(t-t_1)|\mathcal{E}_b(t_1)|^2 dt_1. \quad (4.18)$$

Equation (4.16) may be simplified using the definitions in Equations (2.16) and (2.37) (assuming no NLA),

$$\frac{\partial \mathcal{E}_a}{\partial z} + \frac{1}{v_{g,a}} \frac{\partial \mathcal{E}_a}{\partial t} = ik_{0,a} \left(2n_{2,el} I_b(t) + \int_{-\infty}^{\infty} R(t-t') I_b(t') dt' \right) \mathcal{E}_a, \quad (4.19)$$

where the frequency arguments of $n_{2,el}$ has been suppressed. The factor within the parenthesis on the RHS of Equation (4.19) is the time dependent refractive index change experienced by the probe, $\Delta n_a(t)$. Note that, as discussed in § 2.2. and 2.3. in this two-beam experiment the bound-electronic contribution yields twice the index change as a single beam, while the noninstantaneous nuclear contribution is the same.

We now follow Negres et al. [53], and transform into a dimensionless coordinate system that travels with the group velocity of the pump pulse (see § 3.2.3.

$$\frac{\partial \mathcal{E}_a}{\partial Z} + \rho \frac{\partial \mathcal{E}_a}{\partial T} = f(T) \mathcal{E}_a, \quad (4.20)$$

where

$$f(T) = ik_{0,a} L \left(2n_{2,el} I_b(T) + \int_{-\infty}^{\infty} R(T-T') I_b(T') dT' \right). \quad (4.21)$$

With a change of variables $\xi = Z - T/\rho$, and $\zeta = T$, Equation (4.20) becomes

$$\rho \frac{\partial \mathcal{E}_a}{\partial \zeta} = f(\zeta) \mathcal{E}_a(\xi, \zeta). \quad (4.22)$$

Substituting $\mathcal{E}_a(\xi, \zeta) = \exp(u(\xi, \zeta))$, the solution to Equation (4.22) is

$$u(\xi, \zeta) = u_0(\xi) + \frac{1}{\rho} \int_{-\infty}^{\zeta} f(\zeta') d\zeta', \quad (4.23)$$

where $u_0(\zeta)$ depends on the initial incident probe field. Transforming back to the variables T and Z ,

$$\begin{aligned} \mathcal{E}_a(\mathbf{r}, Z, T) = \mathcal{E}_a(\mathbf{r}, 0, T) \exp \left(i \frac{k_0 L}{\rho} \int_{T-\rho Z}^T \left\{ 2n_{2,el} I_b(T_2) \right. \right. \\ \left. \left. + \int_{-\infty}^{\infty} R(T_2 - T_1) I_b(T_1) dT_1 \right\} dT_2 \right). \end{aligned} \quad (4.24)$$

For Gaussian temporal profiles

$$\mathcal{E}_a(\mathbf{r}, 0, T) = \mathcal{E}_a(\mathbf{r}, 0) \exp \left(-\frac{(T + T_d - \rho)^2}{2\mathcal{J}^2} \right), \quad (4.25)$$

$$I_b(\mathbf{r}, T) = I_{0,b}(\mathbf{r}) \exp(-T^2), \quad (4.26)$$

and evaluating the solution at the back of the sample, $Z = 1$ ($z = L$), Equation (4.24) becomes

$$\begin{aligned} \mathcal{E}_a(\mathbf{r}, 1, T) = \mathcal{E}_a(\mathbf{r}, 0) \exp \left(-\frac{(T + T_d - \rho)^2}{2\mathcal{J}^2} + i \frac{k_0 L}{\rho} I_{0,b}(\mathbf{r}) \right. \\ \left. \cdot \left\{ 2n_{2,el} [\operatorname{erf}(T) - \operatorname{erf}(T - \rho)] \right. \right. \\ \left. \left. + \int_{T-\rho Z}^T \int_{-\infty}^{\infty} R(T_2 - T_1) e^{-T_1^2} dT_1 dT_2 \right\} \right). \end{aligned} \quad (4.27)$$

This is similar to the solution for a pump-probe measurement in the presence of GVM, see Equation (3.10), but accounts for phase changes in the probe field due to both instantaneous and non-instantaneous NLR. The effect of 2PA of the probe due to the pump is straightforward to include, and gives an additional term within the exponential that is the same as in Equation (3.10). The field distribution at the end of the sample may then be Fresnel propagated to the detector plane and analyzed the same way as previous BD measurements.

With the inclusion of time dynamics, evaluating the temporal resolution of a given beam deflection experiment becomes of interest. In typical pump-probe experiments where GVM is neglected, the temporal resolution is simply the width of the cross-correlation of the pump and probe pulses. The effect of GVM is to cause the two pulses to overlap at different positions within the sample at different time delays, which results in a broadening and smoothing of the measured signal in delay [93]. Thus the temporal resolution of a given experiment depends not only on the pulse widths, but also on the GVM parameter ρ , and is no longer simply a specification of the experimental apparatus, but now depends on dispersion of the material under investigation.

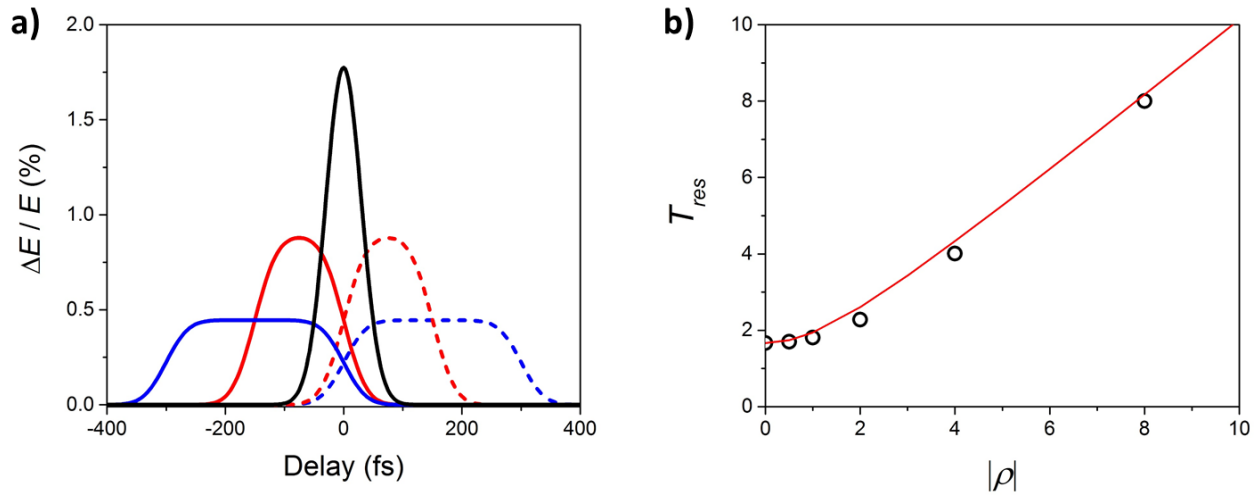


Figure 4.2 (a) Calculated BD signal with only instantaneous material response with varying GVM for (black) $\rho = 0$, (red) $\rho = \pm 5$, and (blue) $\rho = \pm 10$, where solid curves are positive ρ and dashed curves are negative ρ . (b) Calculated (black circles) normalized temporal resolution T_{res} as a function of $|\rho|$ and approximated by Equation (4.28) (red curve).

Figure 4.2 (a) shows the response of a BD experiment with only an instantaneous nonlinearity for various values of ρ . The magnitude of the BD signal is reduced for nonzero ρ due to the reduced extent of pulse overlap over the thickness of the sample. In addition, the peak of the signal is also shifted with respect to zero delay, where the pulses are overlapped in time at the entrance

surface. For positive ρ ($v_{g,a} < v_{g,b}$), when the probe arrives at the front surface of the sample first (negative delay, $T_d < 0$), the pump pulse travels faster and is able to catch up to the excitation at the back of the sample, giving a signal at negative delays. For negative ρ ($v_{g,a} > v_{g,b}$) the opposite occurs; when the pump pulse arrives at the front surface of the sample first (positive delay, $T_d < 0$), the probe pulse travels faster and catches up to the pump. For equal probe and pump pulse widths, the normalized temporal resolution $T_{res} = t_{res}/\tau_b$ resulting from GVM may be approximated by the full width at half maximum (FWHM) of the signal by

$$T_{res} = \sqrt{4 \ln 2 (1 + \mathcal{J}^2) + \rho^2}. \quad (4.28)$$

Figure 4.2 (b) shows the calculated FWHM as a function of $|\rho|$ in black circles, and Equation (4.28) as a red curve.

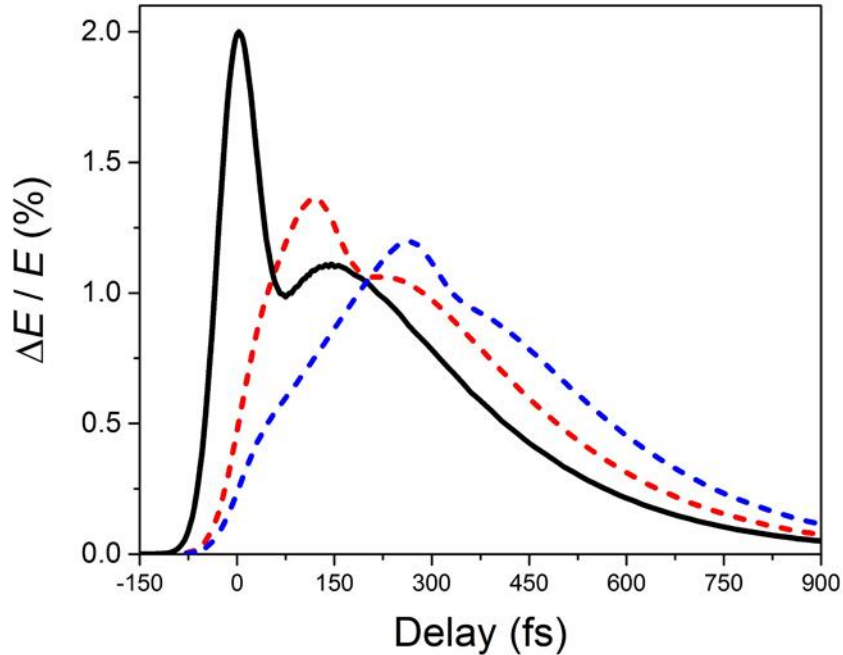


Figure 4.3 Calculated BD signal including both instantaneous and noninstantaneous response with varying GVM; (black) $\rho = 0$, (red) $\rho = -5$, and (blue) $\rho = -10$.

One consequence of this broadening is to reduce the ability for measuring time constants of the noninstantaneous response of materials. Figure 4.3 shows example calculations that include a noninstantaneous material response of the form

$$R(t) \propto \left(1 - \exp\left(-\frac{t}{\tau_r}\right)\right) \exp\left(-\frac{t}{\tau_f}\right) \Theta(t), \quad (4.29)$$

Here with $\tau_a = \tau_b = 30$ fs, $\tau_r = \tau_f = 200$ fs. In the $\rho = 0$ case (black curve), the rise time of the non-instantaneous component can be just resolved, giving the dip in $\Delta E/E$ at about $\tau_d = 75$ fs. However, for $\rho = -5$ (red curve) the dip is no longer resolved, and for $\rho = -10$ (blue curve) the rise time of the noninstantaneous component is washed out. It is very important, therefore, to consider GVM in the preparation of a BD experiment intent on measuring rise times, for the improper choice of wavelengths and sample thickness may cause a loss of temporal resolution.

4.3. Response Function of Carbon Disulfide

In this section we present a complete characterization of the nonlinear response function of liquid carbon disulfide (CS₂), done by application of the BD technique. Additionally, the resulting response function was verified by predicting the results of two independent NLR measurements: degenerate four-wave mixing (DWM), and Z-scans at many pulse widths. Confirmation of the response function confirms that we are able to predict the outcome of essentially any nonlinear refraction measurement of liquid CS₂.

4.3.1. Beam Deflection Measurements

Here we apply the BD technique to measure the response function of liquid carbon disulfide. The experimental setup utilized the Coherent laser system (see § 3.2.1.1.) where the 800 nm

fundamental from the laser was used as a pump. A white-light continuum was generated by splitting off a portion of the fundamental energy and focusing into a 1 cm cuvette filled with water. A narrow bandpass filter was then used to select a probe wavelength of 650 nm. The pulse energy of each beam was controlled by a half-wave plate and polarizer pair, and the polarization angle of the probe was controlled by a second half-wave plate. The pump pulse width was determined to be 50 fs (FWHM) by autocorrelation measurements [94]. The spot sizes at the location of the probe beam waist were measured via knife-edge scan [95] to be $w_{0,a} = 38 \mu\text{m}$ and $w_b = 170 \mu\text{m}$ (each $\text{HW}1/e^2\text{M}$) for the probe and pump, respectively. The probe beam was aligned to be centered on the quad-cell, which was placed ~ 17 cm past the sample plane. The crossing angle between the pump and probe was kept small, $< 2^\circ$, to prevent walk-off of the beams throughout the thickness of the sample. The pump beam was shifted with respect to the probe by $w_b/2$ to maximize the deflection of the probe.

Measurements were first performed on a 1 mm sample of fused silica, which serves a dual purpose. In the absence of GVM, the BD signal is proportional to the cross-correlation of the pulses, and since the pump pulse width is known, provides an *in situ* measure of the probe pulse width. In this case, $\rho = 1.35$ for fused silica [96], which requires GVM to be included in the analysis. The pulse width of the probe was determined to be 158 fs (FWHM). Additionally, the nonlinear refractive index may be determined and compared to literature, finding good agreement, which ensures that the system is properly aligned and calibrated.

Beam deflection measurements of CS_2 (Sigma-Aldrich, 270660, $\geq 99.9\%$) were conducted at three different polarizations of the probe with respect to that of the pump. The symmetry properties of each mechanism giving rise to a refractive index change causes an interesting polarization

dependence of the BD signal. The refractive index of a (uniaxial) birefringent material may be described by an index ellipsoid [16, 97]

$$\frac{1}{n^2(\varphi)} = \frac{\cos^2(\varphi)}{n_{\parallel}^2} + \frac{\sin^2(\varphi)}{n_{\perp}^2}. \quad (4.30)$$

where n_{\parallel} and n_{\perp} are the refractive indices experienced by a field polarized parallel and perpendicular to the optic axis, and φ is the angle between the field and the optic axis. Since the birefringence here is induced in an otherwise isotropic media, $n(\varphi) = n_0 + \Delta n(\varphi)$, $n_{\parallel} = n_0 + \Delta n_{\parallel}$, and $n_{\perp} = n_0 + \Delta n_{\perp}$. For small refractive index changes, $\Delta n(\varphi)$ may be approximated by

$$\Delta n(\varphi) = \Delta n_{\parallel} \cos^2(\varphi) + \Delta n_{\perp} \sin^2(\varphi). \quad (4.31)$$

The relationship between Δn_{\parallel} and Δn_{\perp} depends on the symmetry properties of the response mechanism. We can decompose the refractive index change into its symmetry components by

$$\Delta n(\varphi) = \Delta n^{iso}(\varphi) + \Delta n^{re}(\varphi), \quad (4.32)$$

where the superscripts *iso* and *re* refer to isotropic and reorientational symmetries, respectively. Both the bound-electronic and collision induced mechanisms do not arise from changes in the molecular orientation, and therefore follow the isotropic symmetry of the bulk liquid. Third-order nonlinear refraction in isotropic media (in the nonresonant Kleinman limit) follows $\Delta n_{\perp}^{iso} = \Delta n_{\parallel}^{iso} / 3$ [16, 17].

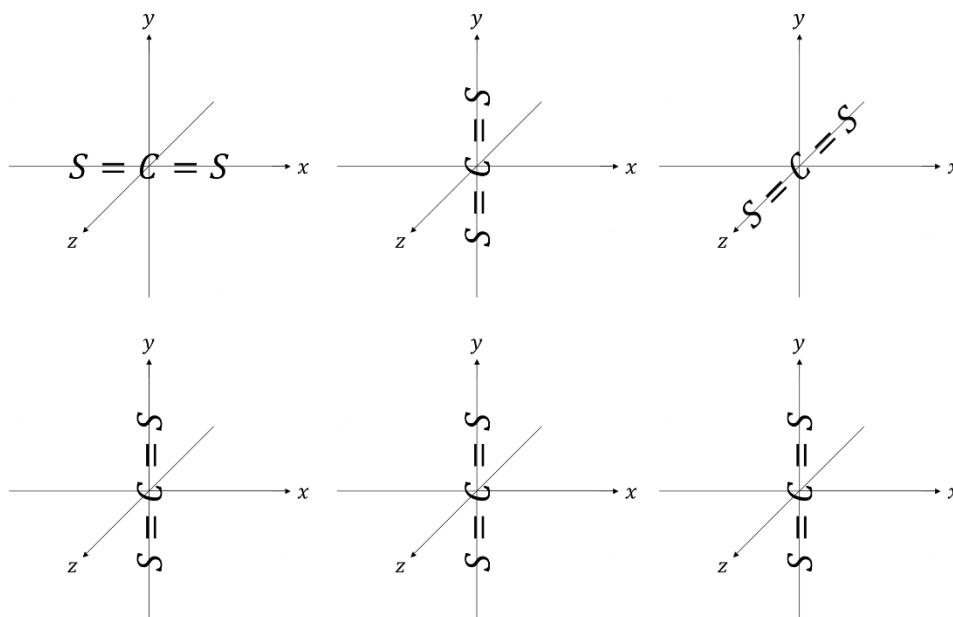


Figure 4.4 Three CS_2 molecules of (top row) different initial orientations. When a field polarized in the y axis is applied, (bottom row) all of three align towards the y axis.

Both diffusive orientation and libration have reorientational symmetry, since they originate from reorientation of the molecules themselves, for which $\Delta n_{\perp}^{re} = -\Delta n_{\parallel}^{re}/2$. The factor of negative two difference in the reorientational nonlinearities may be understood by examining three sample molecules. Take each molecule to be oriented mostly along the three principle axis x , y , and z , as shown in the top row of Figure 4.4. For a pump field polarized in the y -direction, the molecules oriented in the x and z directions will rotated towards the y -axis and change the refractive index. However, the molecule that is already oriented along the y -axis doesn't experience any torque and doesn't rotate. This means that only two of the three molecules, those initially not along the pump field polarization contribute to the refractive index change. For a probe field polarized along the y -axis (parallel to the pump), the rotation of these molecules increases the refractive index. For a probe field polarized perpendicular to the pump, say along the x -axis, the molecule initially oriented along the x -axis rotates away from the probe polarization direction. This reduces

the polarizability along the x -direction, and decreases the refractive index. However, the molecule initially oriented along the z -axis, is rotated towards the y -axis, but it is still orthogonal to the x -axis, and has the same polarizability in the x -direction. This means only the single molecule (the one initially oriented in the x -axis) contributes to the refractive index change for perpendicular polarization. Since there are half as many molecules that contribute, and the polarizability is reduced rather than increased, the refractive index change for perpendicular polarizations is $-1/2 \times$ that of the parallel case.

We can now apply the symmetry properties to write the angular dependent refractive index change by combining Equations (4.31) and (4.32) as

$$\Delta n(\varphi) = \Delta n_{\parallel}^{iso} \left(\cos^2(\varphi) + \frac{1}{3} \sin^2(\varphi) \right) + \Delta n_{\parallel}^{re} \left(\cos^2(\varphi) - \frac{1}{2} \sin^2(\varphi) \right). \quad (4.33)$$

Because the reorientational nonlinearity has the opposite sign for parallel and perpendicular polarizations, there is some angle where the two contributions cancel, and it does not contribute to the refractive index change experienced by the probe. This angle can be found by setting $\cos^2(\varphi) - \frac{1}{2} \sin^2(\varphi) = 0$ and solving for the angle, which yields $\varphi = \arctan(\sqrt{2}) \approx 54.7^\circ$. This angle is known as the “magic angle” [98]. At this angle, only the isotropic components contribute. Measurements were performed on CS_2 for parallel ($\varphi = 0^\circ$), magic angle ($\varphi = 54.7^\circ$), and perpendicular ($\varphi = 90^\circ$) polarizations. For these angles

$$\Delta n(0^\circ) = \Delta n_{\parallel}^{iso} + \Delta n_{\parallel}^{re}, \quad (4.34)$$

$$\Delta n(54.7^\circ) = \frac{5}{9} \Delta n_{\parallel}^{iso}, \quad (4.35)$$

$$\Delta n(90^\circ) = \frac{1}{3} \Delta n_{\parallel}^{iso} - \frac{1}{2} \Delta n_{\parallel}^{re}. \quad (4.36)$$

Figure 4.5 shows the (circles) measured BD signal for a 1 mm cuvette filled with CS₂ that includes (black) parallel, (red) perpendicular, and (blue) magic angle polarizations. Here $\rho = 4.7$ [27, 28]. For these data the peak pump irradiance was $I_{b,0} = 28.5 \text{ GW/cm}^2$ ($E_b = 730 \text{ nJ}$). The large positive signal in the parallel case is dominated by the libration and diffusive reorientation responses, especially at long delays. For perpendicular polarizations (red) the signal initially is positive, where the (nearly) instantaneous bound-electronic response dominates, but quickly turns negative as the reorientational nonlinearities turn on. These mechanisms even dominate the signal at zero delay, where for perpendicular polarizations the BD signal is negative. The polarization dependence for the reorientational symmetry components can readily be observed out at large delay, where the parallel polarization measurement is twice the amplitude and opposite sign of the perpendicular polarization measurement. At the magic angle the mechanisms with reorientational symmetries are completely eliminated, leaving only those with isotropic symmetry. Clearly the bound-electronic response dominates the magic angle measurement. However, there is a small noninstantaneous response, which we attribute to the collision induced mechanism, and is consistent with other previous observations [98-100].

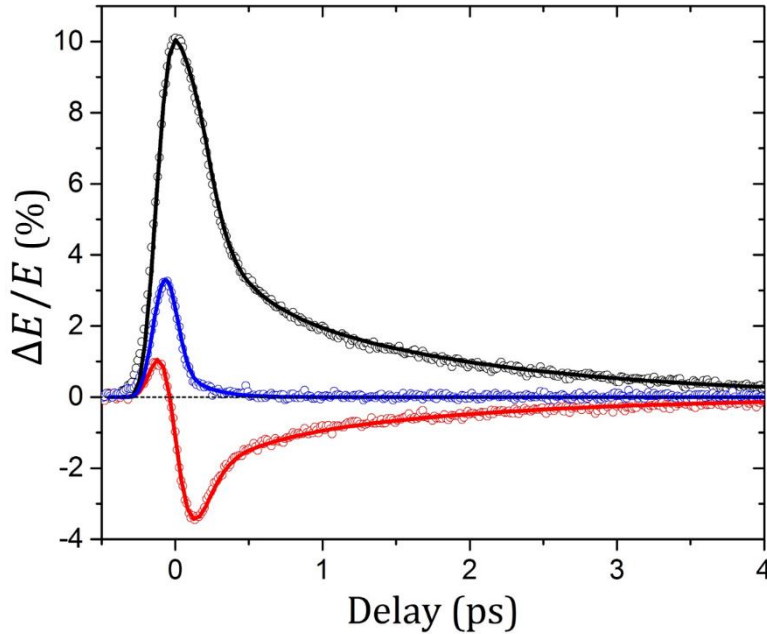


Figure 4.5 Measure (circles) beam deflection signal of CS₂ for (black) parallel, (red) perpendicular, and (blue) magic angle polarizations. Solid curves are fits for the response function. (Reproduced with permission from Ref. [62].)

The solid curves in Figure 4.5 represent fits that include four responses: bound-electronic, collision, libration, and diffusive reorientation. A vibrational component was not included because there was no oscillatory behavior observed for any of the measurements. This is due to the fact that the lowest Raman active vibrational mode of CS₂ has a frequency of 19.7 THz (658 cm⁻¹) [101], and a period of 51 fs, which is less than the cross-correlation width of the pump and probe (see § 4.1.3.). In this case it effectively acts as an instantaneous response, but is expected to be small [25, 90]. The BD measurements were fit using Equation (4.27) by the following procedure. The magic angle data was fit first since it only has contributions from the bound-electronic, $n_{2,el}$ and collisional response, Equation (4.15) first, since both the libration and diffusive reorientation responses do not contribute to the measurement. The magnitudes were scaled by 9/5 to find $\Delta n_{\parallel}^{iso}$ in accordance with Equation (4.35). This was then applied to the parallel and perpendicular measurements with the addition of the librational and diffusive reorientational responses (Equations

(4.11) and (4.12), respectively), which have reorientational symmetry. The best fit of both the parallel and perpendicular data were used to determine the final response function.

Table 4.1. Fit Parameters of Third-Order Response of CS₂. $n_{2,m}$ are given in units of 10^{-19} m²/W

Mechanism	$n_{2,m}$	$\tau_{r,m}$ (fs)	$\tau_{f,m}$ (fs)	Symmetry
Electronic	2.0 ± 0.4	Instantaneous		<i>iso</i>
Collision	1.0 ± 0.2	150 ± 50	140 ± 50	<i>iso</i>
Libration	7.6 ± 1.5	*	450 ± 100	<i>re</i>
Diffusive	18 ± 3	150 ± 50	1610 ± 50	<i>re</i>

$$* \omega_0 = 8.5 \pm 1.0 \text{ ps}^{-1}, \sigma = 5 \pm 1 \text{ ps}^{-1}$$

We do not resolve the rise times for either the collision or diffusive reorientation mechanisms since the cross-correlation is relatively long. We therefore follow McMorro et al. [67] and assume them both to be equal since the inertial delay effects should effect both equally, and chose 150 fs in accordance with [67]. Table 4.1 shows the results of the fitting procedure of the BD data, including the magnitude, response times, and symmetries of each mechanism. The error quoted in Table 4.1 for $n_{2,m}$ are estimated from the uncertainty in the irradiance (~20%) as well as the noise level of the BD measurements. Error bars on the remaining parameters were determined by allowing a single variable to change, while keeping the others constant, until the calculated cures no longer agreed with experimental measurements. The results agree well with previous relative measurements that have applied similar models, but we include absolute measurements of the magnitudes of each individual mechanism in addition to the response times [24, 67, 86, 102, 103]. The bound-electronic third-order susceptibility may be calculated from $n_{2,el}$ in Table 4.1 using

Equation (2.16). Furthermore, the values of the orientationally averaged second hyperpolarizability $\langle \gamma \rangle$ may be calculated using Equation (4.4). These results are given in Table 4.2.

Table 4.2 Bound-electronic third-order susceptibility and second hyperpolarizability of liquid CS₂

Element	$\chi^{(3)}$ (10^{-21} m ² /V ²)	$\chi^{(3)}$ (10^{-13} esu)	$\langle \gamma \rangle$ (10^{-61} C ⁴ m ⁴ /J ³) ⁴ [90]	$\langle \gamma \rangle$ (10^{-36} esu)
<i>xxxx</i>	1.8 ± 0.4	1.3 ± 0.3	2.9 ± 0.6	2.3 ± 0.5
<i>xyyy</i> ⁵ [16]	0.6 ± 0.1	0.4 ± 0.1	1.0 ± 0.2	0.8 ± 0.2

A plot of the noninstantaneous response function is shown in Figure 4.6. The libration mechanism dominates the noninstantaneous response at short times, but it dampens quickly due to dephasing of the broad distribution of oscillator frequencies. The diffusive reorientation mechanism has the slowest decay time due to its Debye-Stoke-Einstein diffusive decay nature. Because of this, it has the greatest impact on the nonlinear refraction of long pulses, i.e., it has the greatest $n_{2,m}$ (see Equation (4.5) and Table 4.1). The collisional response is relatively small, and quickly damped. It is only measurable thanks to the measurements at the magic angle, since it has isotropic symmetry.

⁴ $\gamma_{MKS} = \frac{e^4 a_0^4}{E_h^3} \gamma_{au} = 6.23538063 \times 10^{-65} \gamma_{au} = \frac{400\pi\epsilon_0}{c^2} \gamma_{esu} = 1.23799015 \times 10^{-25} \gamma_{esu}$

⁵ In isotropic media in the nonresonant (Kleinman) limit, $\chi_{xyyy}^{(3)} = \chi_{xyyx}^{(3)} = \chi_{xyyx}^{(3)}$

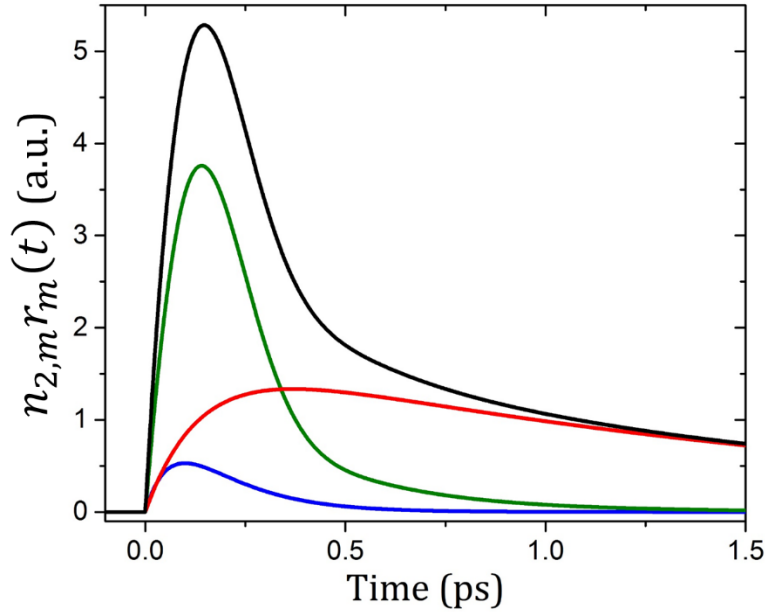


Figure 4.6 Noninstantaneous response function $R(t)$ of CS_2 (see Table 4.1) decomposed into (blue) collision, (green) libration, (red) diffusive reorientation, as well as the (black) total. (Reproduced with permission from Ref. [62])

The Raman spectrum of a material is related to the noninstantaneous third-order response function via [24]

$$R(\Delta\omega) \propto \mathcal{F}\{R(t)\}, \quad (4.37)$$

where $\Delta\omega$ is the frequency shift, and \mathcal{F} indicates the Fourier transform. In a Raman scattering measurement, the spectral power density measured depends only on $\text{Im}\{R(\Delta\omega)\}$ [23, 24]. Figure 4.7 shows the $\text{Im}\{R(\Delta\omega)\}$ for each mechanism of the response of CS_2 as well as the total. This spectrum agrees well with measurements from [104] and [105].

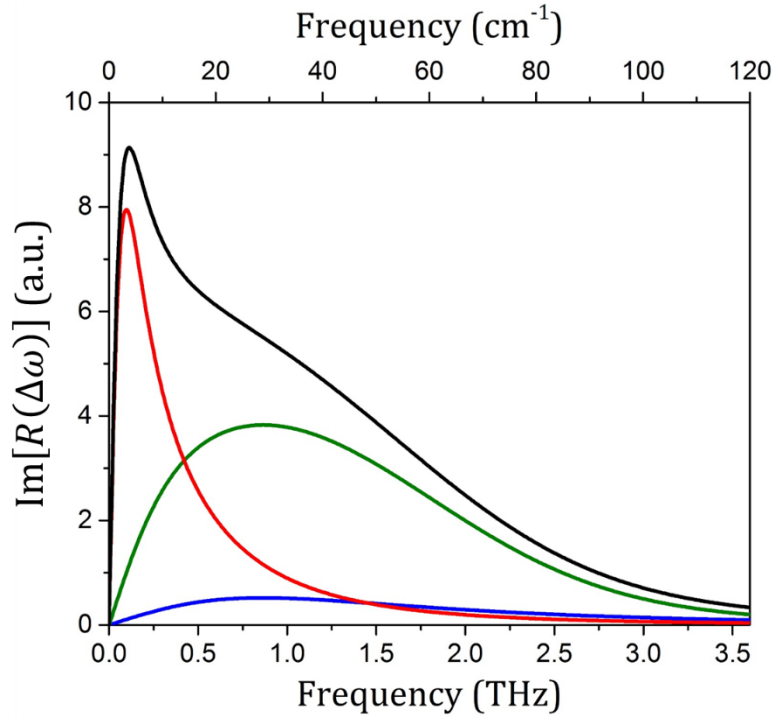


Figure 4.7 Fourier transform of response function of CS₂, including (blue) collision, (green) libration, (red) diffusive reorientation, and (black) total.

4.3.2. Degenerate Four-Wave Mixing Measurements

To verify the response function measured by the BD technique, degenerate four-wave mixing (DFWM) measurements were also performed (see § 3.2.4.). This experiment was conducted using the Clark-MXR laser system (see § 3.2.1.1.) with the TOPAS-C (see § 3.2.1.2.) tuned to 700 nm, which was sent to a prism compressor (SF10) to compress the pulse [106]. A 50/50 beam splitter was used to split the single beam into pump and probe, and the probe beam was sent to a delay line. The beams were then aligned parallel to one another, but displaced vertically by ~ 1 cm. A 15 cm focal length mirror was then used to focus both beams through a transmissive diffraction grating, and diffracted orders ± 1 of the top beam were used as the pump (\mathcal{E}_1 and \mathcal{E}_2 in § 3.2.4.), and the diffracted order +1 in the lower beam was used as the probe. A second 15 cm focal length mirror was used to collect and collimate the three beams, and a third focused them into the

sample in the so called “boxcars” geometry [59, 107]. The energy of the diffracted beam, \mathcal{E}_4 , was measured as a function of delay between the pumps and probe. The prism compressor was iteratively optimized to yield the narrowest signal about zero delay (see Figure 4.8).

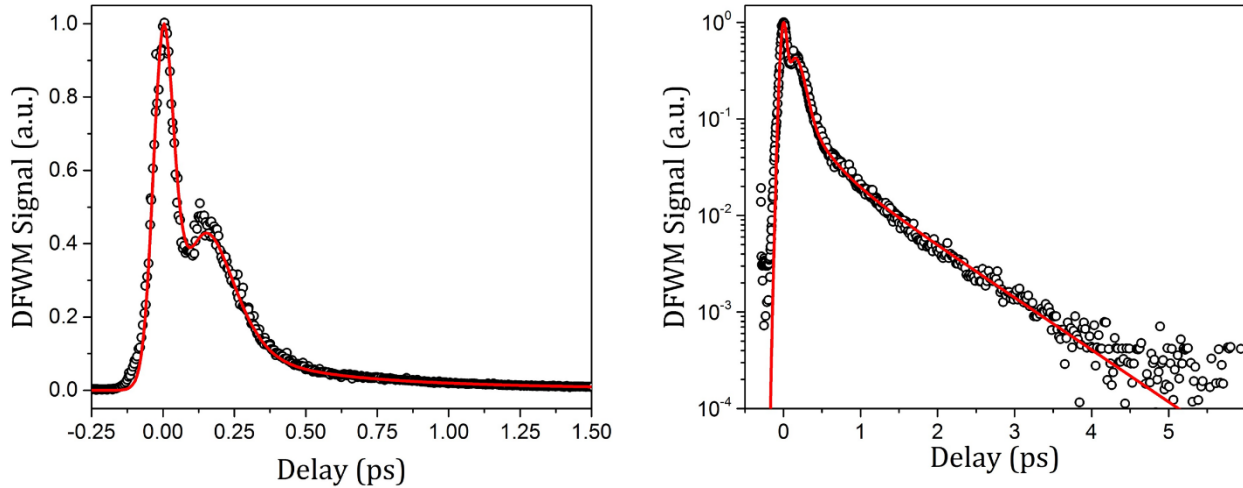


Figure 4.8 (circles) Measured normalized DFWM signal, and (red) prediction from the response function, using Equation (3.22), on both (left) linear and (right) logarithmic scale. (Modified with permission from Ref. [62].)

Figure 4.8 shows the normalized signal from the DFWM measurement of CS_2 in black circles, on both a linear and logarithmic scale. The red curve shows the prediction based on the response function measured by beam deflection as calculated via Equations (2.16), (2.37), (3.22), and (3.23). The pulse widths used in the prediction were 88 fs and 42 fs (both FWHM) for the pump and probe pulses, respectively. This is consistent with the minimization of the DFWM signal procedure when the dispersion through the ~ 11 mm of glass (8 mm thick beam splitter at 45°) is included in the probe path (ThorLabs BSW16) [96]. The excellent agreement between the measurement and prediction validates the response function determined from the BD technique

4.3.3. Z-scan Measurements

CS₂ is a standard reference material for Z-scan measurements, even though its large non-instantaneous NLR makes its effective nonlinearity pulse width dependent. Typically, an effective nonlinear refractive index, defined by

$$\Delta n(t) = n_{2,\text{eff}} I(t), \quad (4.38)$$

is used to fit the Z-scan measurements. This completely neglects the temporal dynamics of the underlying mechanisms that cause NLR, and the resulting $n_{2,\text{eff}}$ is therefore pulse width dependent. Using the response function, however, we may predict $n_{2,\text{eff}}$ for any pulse width.

The Z-scan technique measures the changes in phase that a single pulse induces on itself. Thus the CA Z-scan signal depends on the refractive index change weighted over the temporal profile of the irradiance [47],

$$\langle \Delta n(t) \rangle \equiv \frac{\int \Delta n(t') I(t') dt'}{\int I(t') dt'}. \quad (4.39)$$

Treating the response as if it were instantaneous, i.e., Equation (4.38), yields

$$\langle \Delta n(t) \rangle \equiv n_{2,\text{eff}} \frac{\int I^2(t') dt'}{\int I(t') dt'}. \quad (4.40)$$

Using Equations (2.20) and (2.39), the actual refractive index change for a single-beam experiment, such as Z-scan, is

$$\Delta n(t) \equiv n_{2,el} I(t) + \int_{-\infty}^{\infty} R(t - t_1) I(t_1) dt_1. \quad (4.41)$$

Combining Equations (4.39), (4.40), and (4.41) and solving for $n_{2,\text{eff}}$ gives

$$n_{2,\text{eff}} \equiv n_{2,el} + \frac{\int_{-\infty}^{\infty} I(t) \int_{-\infty}^{\infty} R(t - t_1) I(t_1) dt_1 dt}{\int_{-\infty}^{\infty} I^2(t) dt}. \quad (4.42)$$

To verify this prediction, we perform Z-scan measurements on a 1 mm cuvette filled with CS₂ using the same laser, TOPAS, and prism compressor as the DFWM experiments, at wavelengths of both 700 nm and 1064 nm. The prism was adjusted to give pulse widths ranging from bandwidth limited at 32 fs, up to 2.3 ps (both FWHM), which was limited by the available table space for the setup and pulse energy. The beam was then spatially filtered to produce a TEM₀₀ Gaussian beam [108]. Approximately 10 % of the pulse energy was split off and sent to a reference detector used to window the pulse energy. A half-wave plate and polarizer was used to adjust the energy, and a quarter-wave plate was used to select either linear or circular polarization. A beam splitter located after the sample allowed for the simultaneous measurement of the OA and CA Z-scans. Additionally, a Q-switched mode-locked Nd:YAG laser system (ESKPLA PL2143), at 1064 nm, with a repetition rate of 10 Hz, was also used to measure out to a pulse width of 25 ps. An OPA/G (EKSPLA, PG401) pumped by the third harmonic was tuned to 700 nm to give measurements at 8 ps. For all measurements, the CA linear transmission $S = 0.33 \pm 0.01$.

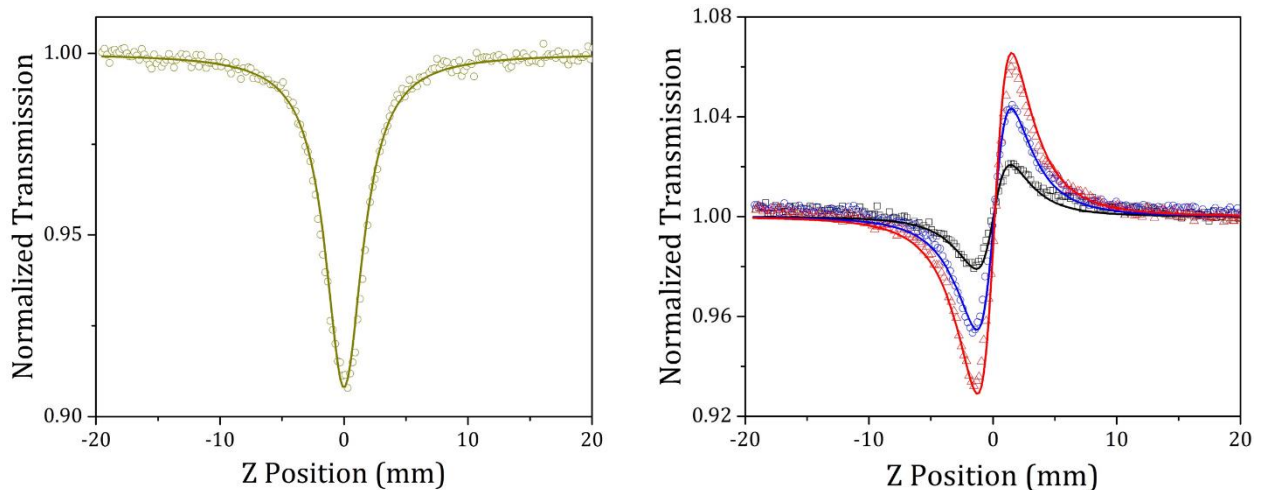


Figure 4.9 Example (open shapes) measurements and (curves) fits of (left) OA Z-scan of ZnSe, and (right) CA Z-scan of CS₂ where the energies are (black squares) 3.5 nJ, (blue circles) 7.4 nJ, and (red triangles) 11 nJ. (Reproduced with permission from [62].)

Determination of the pulse width and spot sizes for each wavelength was done by performing OA Z-scans on samples of known 2PA coefficient. For 700 nm, a 511 μm thick sample of ZnSe was used, where $\alpha_2 = 5.6 \times 10^{-11}$ m/W, and for 1064 nm CdSe was used with $\alpha_2 = 23 \times 10^{-11}$ m/W [14]. Additionally CA Z-scans measurements of fused silica were also performed as a verification, with $n_2 = 0.25 \times 10^{-19}$ m²/W [69]. An example of the OA Z-scan of ZnSe is shown in Figure 4.9, where $\lambda = 700$ nm, the energy was 1.5 nJ, $I_0 = 1.3$ GW/cm², from which the spot size and pulse width were determined to be 19.5 μm (HW1/e²M) and 180 fs (FWHM), respectively. This method of determining the spot sizes and pulse widths minimizes the relative error between successive measurements in the same Z-scan setup.

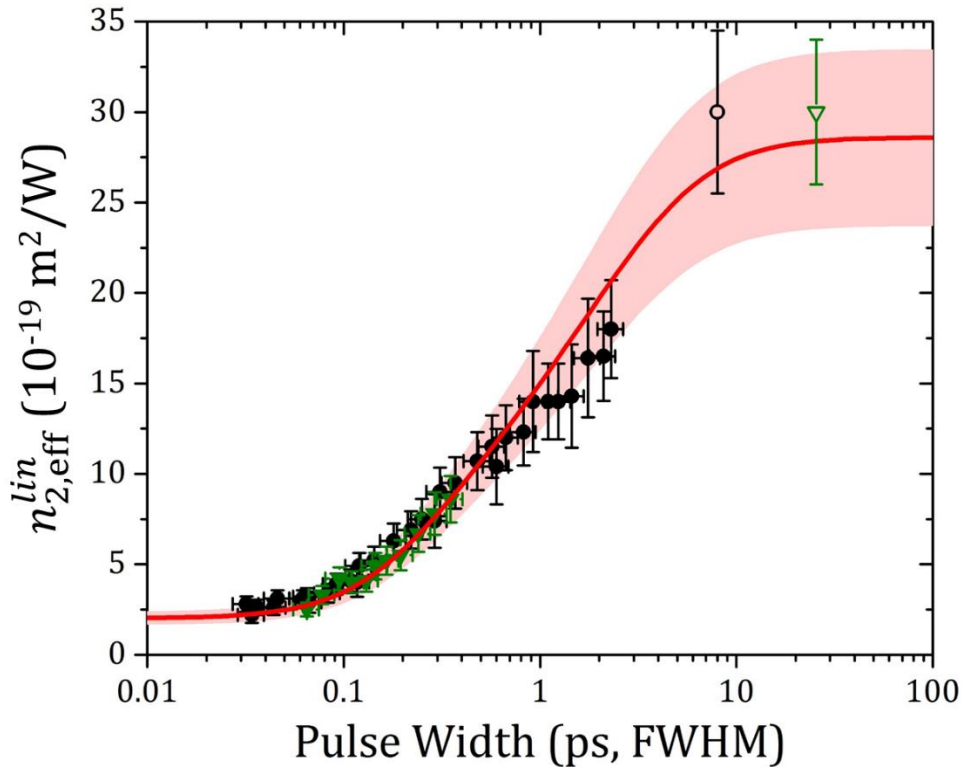


Figure 4.10 $n_{2,\text{eff}}$ of liquid CS_2 for linear polarization from both (points) Z-scan measurements at (black) 700 nm and (green) 1064 nm, using both (closed) Clark-MXR and (open) EKSPLA laser systems, and (red curve) prediction from response function using Equation (4.42). The pink shaded region corresponds to errors in the response function (see Table 4.1). (Reproduced with permission from [62].)

CA Z-scan measurements of CS₂ were performed at multiple energies to ensure the linearity of ΔT_{p-v} with irradiance, all of which were used to determine the best fit value of $n_{2,\text{eff}}$ at each pulse width. Figure 4.9 shows an example measurement, with the same wavelength, spot size, and pulse width as above. The fit of these data corresponds to $n_{2,\text{eff}} = 6.9 \times 10^{-19} \text{ m}^2/\text{W}$. Figure 4.10 shows the Z-scan measurements of $n_{2,\text{eff}}$ versus pulse width for linear polarizations as well as the prediction from the response function using Equation (4.42). We observe excellent agreement between the measurements and the prediction, further validating the response function measured by beam deflection. For short pulses, less than ~ 50 fs, $n_{2,\text{eff}} = n_{2,\text{el}}$, since only the bound electronic response is fast enough to significantly contribute. For increasing pulse width, the noninstantaneous contributions adds more and more to $n_{2,\text{eff}}$ and quickly dominate. For long pulses, greater than ~ 10 ps, $n_{2,\text{eff}}$ plateaus to a value given simply by the sum of each component's magnitude

$$n_{2,\text{eff}}|_{\text{long}} = \sum_m n_{2,m} = (28.6 \pm 3.4) \times 10^{-19} \text{ m}^2/\text{W}. \quad (4.43)$$

Circular polarization measurements were also performed. The ratio of $n_{2,\text{eff}}$ for linear and circular polarizations depends on the symmetry of the underlying mechanism. For isotropic symmetry this ratio is 1.5, while for reorientational it is 4 [16]. Thus, we can predict result of a Z-scan measurement with circular polarization from the response function using $\Delta n_{\text{circ}} = \Delta n_{\parallel}^{\text{iso}}/1.5 + \Delta n_{\parallel}^{\text{re}}/4$. Figure 4.11 shows the ratio of $n_{2,\text{eff}}^{\text{lin}}/n_{2,\text{eff}}^{\text{circ}}$ versus pulse width for both the Z-scan measurements and the prediction from the response function. At short pulse widths the ratio becomes 1.5 since the bound-electronic response follows isotropic symmetry in the liquid. As the pulse width increases, the ratio increases as the libration and diffusive reorientation mechanism, which follow reorientational symmetry, contribute more. This ratio eventually plateaus at

$$\frac{n_{2,\text{eff}}^{\text{lin}}}{n_{2,\text{eff}}^{\text{circ}}} = \frac{n_{2,\text{eff}}^{\text{long}}}{\frac{(n_{2,\text{el}} + n_{2,\text{c}})}{1.5} + \frac{(n_{2,\text{l}} + n_{2,\text{d}})}{4}} = 3.40 \pm 0.06, \quad (4.44)$$

where the numerator is given by Equation (4.43). The weighting factors in the denominator correspond to the polarization dependence of each mechanism. The agreement between measurement and prediction validates not only the magnitudes and time constants, but also the symmetries of the response function measured by beam deflection.

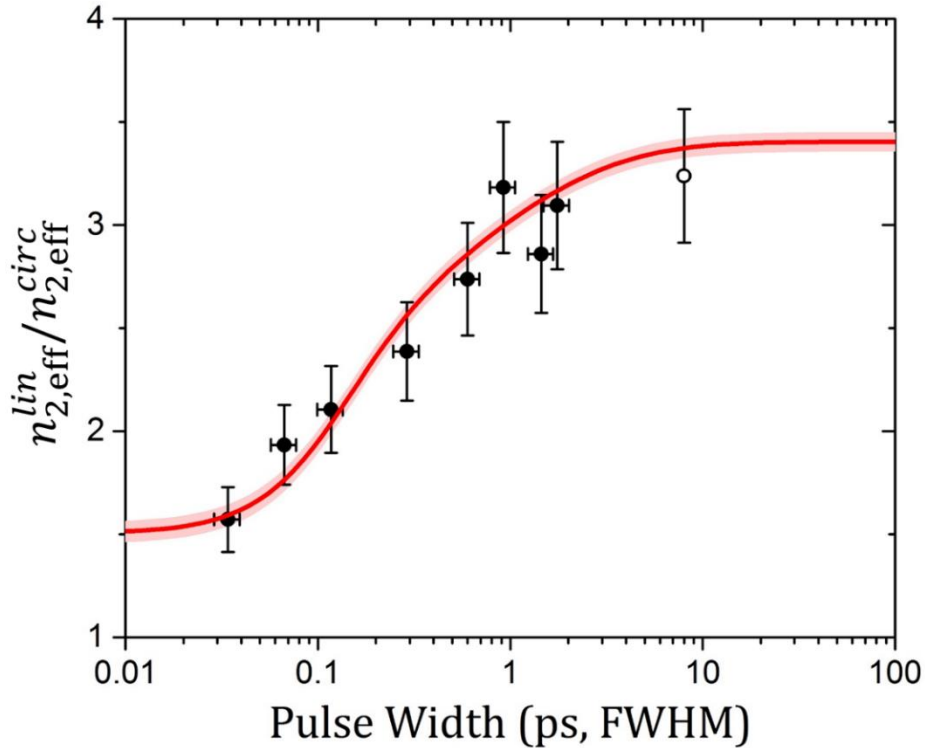


Figure 4.11 Ratio of $n_{2,\text{eff}}$ of CS_2 for circular and linear polarizations from both (black circles) Z-scan measurements at 700 nm and (red curve) prediction from response function. (Reproduced with permission from [62].)

Additionally, Z-scan measurements were performed over a broad spectral range from 390 nm to 1550 nm. The shortest pulse width achieved by the prism compressor depended on the wavelength, which varied from 32 fs to 165 fs. For these pulse widths the bound-electronic response dominates, but for the longer pulse widths the noninstantaneous mechanisms can contribute

up to a factor of 2 increase in $n_{2,\text{eff}}$. The bound-electronic nonlinear response can still be isolated for relatively long pulses if we assume the noninstantaneous response is independent of wavelength. We can then simply subtract off the noninstantaneous contribution to $n_{2,\text{eff}}$, and thus obtain the dispersion of $n_{2,\text{el}}$. To validate this assumption, Z-scan measurements were made using long pulses where the noninstantaneous mechanisms dominate. Both ps (EKSPLA) and ns (Continuum PL9010) Nd:YAG laser systems, which pumped optical parametric devices were used, where effects of electrostriction were extracted in the ns measurements [109]. The right plot in Figure 4.12 shows $n_{2,\text{eff}}$ for both ns (open) and ps (closed) pulses is independent of wavelength to within the measurement error. The prediction from the response function measured by BD, shown in the blue diamond, also agrees with these measurements. Therefore, subtracting out the noninstantaneous response from the short fs pulse measurements is a valid method of extracting $n_{2,\text{el}}$.

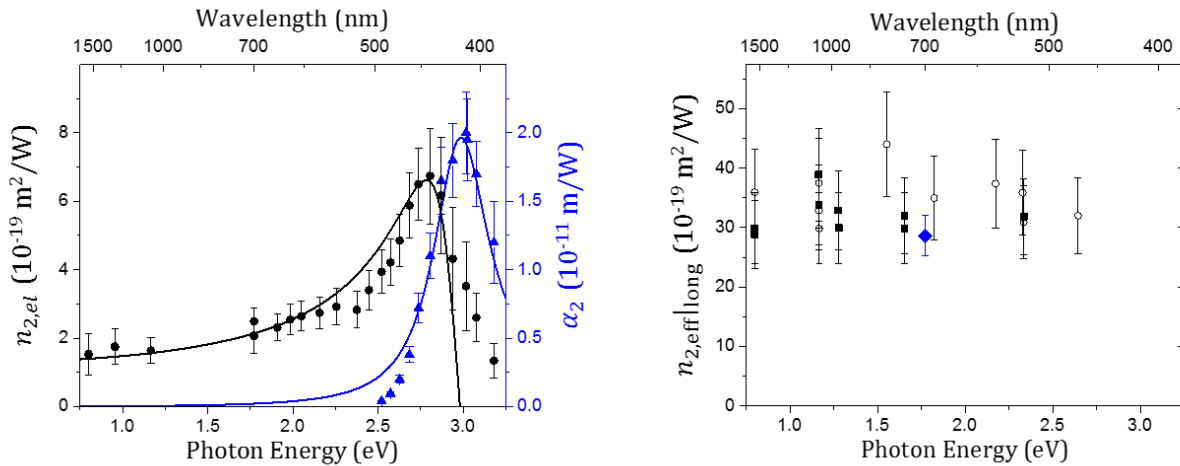


Figure 4.12 (left) Z-scan measurements (points) of (black) NLR of CS_2 with the noninstantaneous contribution subtracted, and (blue) 2PA. Curves are fit with sum-over-states model, where the prediction of $n_{2,\text{el}}$ has been multiplied by 2. (right) Measurements of $n_{2,\text{eff|long}}$ for (open) 13-20 ps pulses (closed) 2.5-17 ns pulses, and (blue) prediction from BD measurements of response function [62].

The plot in Figure 4.12 shows the measured values of (black) $n_{2,el}$ and (blue) α_2 over the spectral range measured. For photon energies above 2.5 eV (wavelengths below 500 nm) 2PA is possible, since linear absorption occurs for photon energies >5 eV (wavelengths <250 nm) [110]. The curves represent fits based a simplified quantum mechanical sum-over-states model relating the third-order nonlinearity to the energy levels and transition dipole moments between electronic states of the molecule [20, 110-112]. Only three state are included in the fit, the ground state g , one-photon allowed excited state e , and two-photon allowed excited state e' . Given the symmetry of the molecule, definite parity is assumed, where wave functions of the states g and e' have the same symmetry (either even or odd) and e has the opposite. This means the only nonzero transition dipole moments are those between the ground and one-photon allowed state, μ_{ge} , and between the two excited states, $\mu_{ee'}$. Both the linear and 2PA spectrum were used to determine the energy levels and values of the transition dipole moments, the results of which are shown in Table 4.3. The corresponding prediction of the dispersion of $n_{2,el}$ agrees with the measured trend, but it is smaller by a factor of two, which may be due to the over simplicity of the model. Based on this fit, the parameters may be used to calculate predictions of $\chi^{(3)}$ for other frequencies, including third-harmonic generation [113].

Table 4.3 CS₂ sum-over-states model fit Parameters

State	Energy (eV)	HWHM (eV)	μ (D)
e	6.00 ± 0.01	0.17 ± 0.01	$\mu_{ge} = 3.6 \pm 0.2$
e'	5.95 ± 0.05	0.40 ± 0.05	$\mu_{ge'} = 8.7 \pm 0.9$

4.4. Nonlinear Response of Molecular Gases

Similar third-order nonlinear effects to those observed in liquid CS₂ occur in gases made up of simple linear molecules. Due to the low density, the many-body effects, including libration and collision mechanisms, do not contribute to the nonlinear response. However, thanks to the low collision rate in dilute gases, the induced rotation is not damped nearly as much as it is in liquids, and the molecules may continue to rotate for over 100 ps. Because the rotational energy levels are quantized, and separated in energy appropriately, this results in periodic revivals of the degree of alignment, and therefore refractive index.

4.4.1. Theory of Rotational Revivals

One must treat the rotation quantum mechanically. The rotational eigenstates are $|J, M\rangle$, where J is the total angular momentum (rotational) quantum number, and M is the second total angular momentum quantum number, which is the projection of J along the axis of the pump polarization. The energy of each rotational state is given by [114]

$$E_J = hcBJ(J + 1) - hcDJ^2(J + 1)^2, \quad (4.45)$$

where h is Planck's constant, B is the rotational constant related to the average moment of inertia J

$$B = \frac{h}{8\pi^2 c} \left\langle \frac{1}{J} \right\rangle_{av}, \quad (4.46)$$

and D is the centrifugal distortion constant [114]. In general, these constants depend on the vibrational state of the molecule. Here we are interested in O₂, N₂, and CS₂, which predominantly populate the lowest vibrational level [115]. The classical explanation for the rotational nonlinearity given in § 4.1.1. now must be quantized, where the induced rotation can be thought of as rotational

Raman scattering from one rotational state to another. Due to the definite parity of the rotational wave functions, which are spherical harmonics, the selection rules for such a two-photon Raman process are $\Delta J = \pm 2$, and $\Delta M = 0$ due to the symmetry about the molecular axis. If the pump field is sufficiently short, less than half the rotational period (of bandwidth greater than the transition frequency), it will excite a coherent superposition between states $|J, M\rangle$ and $|J \pm 2, M\rangle$.

The density matrix approach is now applied to find the coherence between the two states. The density matrix associated with a combination of eigenstates states a and b (which depend on J and M) is

$$\rho = \begin{pmatrix} \rho_{aa} & \rho_{ab} \\ \rho_{ba} & \rho_{bb} \end{pmatrix}, \quad (4.47)$$

which evolves according to

$$\dot{\rho} = \frac{i}{\hbar} [\hat{H}, \rho]. \quad (4.48)$$

where $[,]$ denotes the commutator. Here the Hamiltonian \hat{H} is given by

$$\hat{H} = \begin{pmatrix} E_a & -\boldsymbol{\mu} \cdot \mathbf{E}(t) \\ -\boldsymbol{\mu} \cdot \mathbf{E}(t) & E_b \end{pmatrix}. \quad (4.49)$$

Equation (4.48) then becomes

$$\dot{\rho} = \frac{i}{\hbar} \begin{pmatrix} \boldsymbol{\mu} \cdot \mathbf{E}(\rho_{ba} - \rho_{ab}) & \boldsymbol{\mu} \cdot \mathbf{E}(\rho_{bb} - \rho_{aa}) - (E_a - E_b)\rho_{ab} \\ \boldsymbol{\mu} \cdot \mathbf{E}(\rho_{aa} - \rho_{bb}) - (E_b - E_a)\rho_{ba} & \boldsymbol{\mu} \cdot \mathbf{E}(\rho_{ab} - \rho_{ba}) \end{pmatrix}. \quad (4.50)$$

Since we are interested in the evolution of the coherence, we look specifically at the off diagonal elements

$$\dot{\rho}_{ab} = \frac{i}{\hbar} (\boldsymbol{\mu} \cdot \mathbf{E}(\rho_{bb} - \rho_{aa}) - (E_a - E_b)\rho_{ab}). \quad (4.51)$$

We now define $\omega_{ab} = (E_a - E_b)/\hbar$, and phenomenologically add damping, of rate Γ_{ab} . The off-diagonal elements of the Hamiltonian are

$$\hat{H}_{ab} = -\Delta\alpha|\mathbf{E}(t)|^2\langle a|\cos^2(\theta)|b\rangle, \quad (4.52)$$

where θ is the angle between the pump polarization and the molecular axis (see Equation (4.7) and Figure 4.1). With this, Equation (4.51) becomes

$$\dot{\rho}_{ab} = \frac{i}{\hbar}\Delta\alpha|\mathbf{E}(t)|^2\langle a|\cos^2(\theta)|b\rangle(\rho_{bb} - \rho_{aa}) - (i\omega_{ab} + \Gamma_{ab})\rho_{ab}. \quad (4.53)$$

We now solve Equation (4.53) using first order perturbation theory where [116]

$$\begin{aligned} \rho_{ab}^{(1)}(t) = & \frac{i}{\hbar}\Delta\alpha\langle a|\cos^2(\theta)|b\rangle\left(\rho_{bb}^{(0)} - \rho_{aa}^{(0)}\right) \\ & \cdot \int_{-\infty}^t |\mathbf{E}(t')|^2 e^{-(i\omega_{ab} + \Gamma_{ab})(t-t')} dt'. \end{aligned} \quad (4.54)$$

where the $\rho_{JJ}^{(0)}$ are the initial populations of the rotational states. At thermal equilibrium the populations are described by a Boltzmann distribution [117]

$$\rho_{JJ}^{(0)} = \frac{g_J e^{-\frac{E_J}{k_B T}}}{\sum_K g_K (2K + 1) e^{-\frac{E_K}{k_B T}}}, \quad (4.55)$$

where g_J is a statistical weighting factor based on the nuclear spin statistics, which will be elaborated on below. The electric field is given by $\mathbf{E}(t) = \mathcal{E}\hat{\mathbf{e}}\cos(\omega t)$, and the square will result in a component at zero frequency, and one at 2ω . Since $2\omega \gg \omega_{ab}$, this term integrates to zero, and does not significantly contribute to the result [117]. We therefore approximate $|\mathbf{E}(t')|^2 \approx |\mathcal{E}(t)|^2/2$.

We are interested in changes in the degree of alignment of the molecular ensemble, which is given by [116]

$$\langle \cos^2(\theta) \rangle = \text{tr}[\rho(t) \cos^2(\theta)], \quad (4.56)$$

where $\text{tr}[\]$ indicates the trace operation. Before the interaction, $\langle \cos^2(\theta) \rangle = \text{tr}[\rho^{(0)} \cos^2(\theta)] = 1/3$, while after the interaction

$$\rho^{(1)} \cos^2(\theta) = \begin{pmatrix} \rho_{ab}^{(1)} \langle b | \cos^2(\theta) | a \rangle & \rho_{ab}^{(1)} \langle b | \cos^2(\theta) | b \rangle \\ \rho_{ba}^{(1)} \langle a | \cos^2(\theta) | a \rangle & \rho_{ba}^{(1)} \langle a | \cos^2(\theta) | b \rangle \end{pmatrix}, \quad (4.57)$$

and therefore Equation (4.56) becomes

$$\langle \cos^2(\theta) \rangle = \frac{1}{3} + \rho_{ab}^{(1)} \langle b | \cos^2(\theta) | a \rangle + \rho_{ba}^{(1)} \langle a | \cos^2(\theta) | b \rangle. \quad (4.58)$$

The second and third terms are simply complex conjugates of one another, and the sum of something plus its conjugate is simply twice its real part. Substituting Equation (4.54) into Equation (4.58), the deviation of the degree of alignment from thermal equilibrium becomes

$$\begin{aligned} \langle \cos^2(\theta) \rangle - \frac{1}{3} = & -\frac{1}{\hbar} \Delta\alpha |\langle a | \cos^2(\theta) | b \rangle|^2 (\rho_{aa}^{(0)} - \rho_{bb}^{(0)}) \\ & \cdot \text{Im} \left\{ \int_{-\infty}^t |\mathcal{E}(t')|^2 e^{-i(\omega_{ab} + \Gamma_{ab})(t-t')} dt' \right\}. \end{aligned} \quad (4.59)$$

Since the only coupling is between states of J and $J \pm 2$ of the same M , we let $|a\rangle = |J, M\rangle$ and $|b\rangle = |J - 2, M\rangle$, for which the matrix element summed over M is [117, 118]

$$\sum_M \langle J, M | \cos^2(\theta) | J - 2, M \rangle = \frac{2}{15} \frac{J(J-1)}{2J-1}. \quad (4.60)$$

Equation (4.59) then becomes

$$\left(\langle \cos^2(\theta) \rangle - \frac{1}{3} \right) = -\Delta\alpha \sum_J T_J \text{Im} \left\{ \int_{-\infty}^t |\mathcal{E}(t')|^2 e^{-i(\omega_{J,J-2} + \Gamma_{J,J-2})(t-t')} dt' \right\}, \quad (4.61)$$

where

$$T_J = \frac{2}{15\hbar} \frac{J(J-1)}{2J-1} (\rho_{JJ}^{(0)} - \rho_{J-2,J-2}^{(0)}). \quad (4.62)$$

The resulting degree of alignment modulation causes a refractive index change via Equations (4.3) and (4.7), which for small refractive index changes is given by

$$\Delta n(t) = \frac{N\Delta\alpha}{2\varepsilon_0 n_0} \left(\langle \cos^2(\theta) \rangle - \frac{1}{3} \right). \quad (4.63)$$

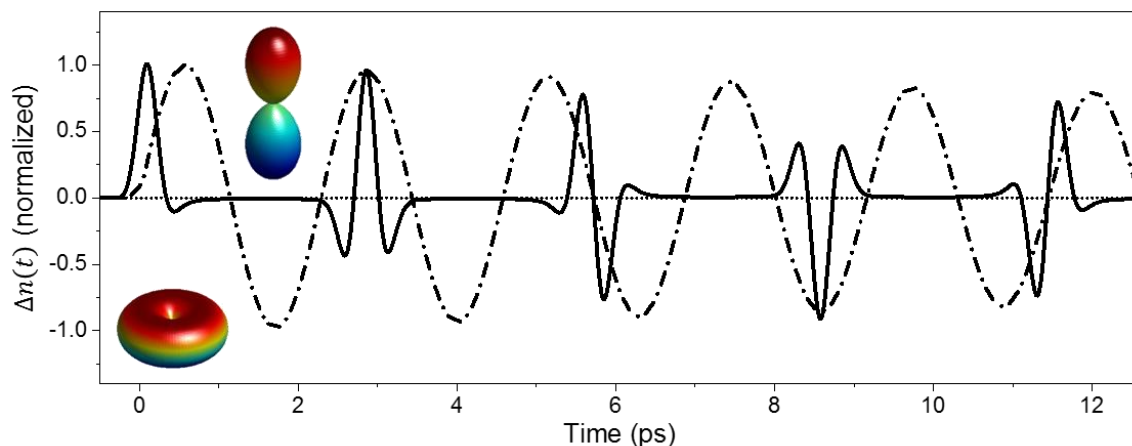


Figure 4.13 Calculated normalized refractive index change from coherent rotational revivals from O₂ for (dashed) only the rotational ground state, and (solid) a thermal distribution at 300 K. Insets illustrate probability distribution of molecular ensemble for positive (top) and negative (bottom) $\Delta n(t)$.

For a delta function pulse the refractive index change becomes a sum of damped sinusoids, each equally spaced in frequency since (neglecting centrifugal distortion)

$$\omega_{J,J-2} = 2hcB(2J - 1). \quad (4.64)$$

For an initial distribution entirely in the ground rotational state, the degree of alignment, and thus refractive index change, oscillates sinusoidally as in Figure 4.13. As the number of initially occupied states increases, more sinusoids are added together and interfere, resulting in periodic beats or “revivals” in the degree of alignment. The full revival period is given by $T = (2cB)^{-1}$ which in O₂ is 11.59 ps, and revival features can also occur at half and quarter multiples of T . Figure 4.13 shows a comparison of the refractive index change for O₂ of only the ground state occupied (dashed) with a distribution at room temperature with over 14 states initially occupied (solid). The

rotational states are coherent with an ensemble average degree of alignment that arises from quantum interference of the many contributing rotational eigenstates. Due to their equally spaced rotational frequencies, the components share a constant phase such that the molecules periodically realign along the polarization vector of the excitation pulse. As a result of the periodic dephasing and rephasing of the rotational eigenstates, a modulation of the refractive index occurs with a change in alignment distribution between aligned and anti-aligned events. This is the result of the spectral lines for rotational transitions being evenly spaced, much like frequency comb. The short excitation pulse then imposes a fixed phase relationship between them the modes, resulting in periodic revivals. This is analogous to a mode-locked laser, where the longitudinal modes of a cavity are evenly spaced, and the mode-locking imposes a fixed spectral phase between them, resulting in a pulse laser output [119].

When the excitation and probe beams are co-polarized (parallel), an increase in the refractive index occurs when the net alignment of the molecular ensemble is parallel to the probe polarization axis. The angular distribution of rotational states forms a dumbbell-like shape, as shown in the inset in Figure 4.13 in the positive $\Delta n(t)$ region. A decrease in the refractive index occurs when the molecules are anti-aligned, or perpendicular, to the probe polarization axis, forming a disc-like distribution, as shown in the inset in Figure 4.13 in the negative $\Delta n(t)$ region. In between events, the rotational states walk out of phase resulting in an isotropic ensemble similar to that before the pump pulse.

Table 4.4 Weighting factor g_J based on nuclear spin statistics

Molecule	Even J	Odd J
$^{14}\text{N}_2$	2/3	1/3
$^{16}\text{O}_2$	0	1
$^{12}\text{C}^{32}\text{S}_2$	1	0
$^{12}\text{C}^{32}\text{S}_2(v_2)$	1/2	1/2
$^{12}\text{C}^{32}\text{S}^{34}\text{S}$	1/2	1/2

The spin statistics of the nuclei affect the coherent rotational revivals through the occupation probability characterized by g_J . The population distribution between odd and even rotational levels is determined by the symmetry of the total molecular wave function, which may be written as a product of the electronic, vibrational, rotational, and nuclear spin wave functions [114]

$$\psi_{total} = \psi_{el}\psi_{vib}\psi_{rot}\psi_{ns}. \quad (4.65)$$

Bosons have an integer nuclear spin, S_n , where ψ_{total} must be symmetric upon nuclear interchange. The number of nuclear states which can populate a given even or odd rotational level can be determined by evaluating the symmetry of each constituent wave function with respect to nuclear interchange. The wave function symmetry for the ground electronic and vibrational states of the most abundant isotopologues of N_2 , O_2 , and CS_2 is shown in Table 1 [114]. Figure 4.14 illustrates the impact of nuclear spin statistics on $\rho_J^{(0)}$ and T_J for both $^{14}\text{N}_2$ (red) and $^{16}\text{O}_2$ (blue) calculated at 300 K using Equations (4.55) and (4.62), respectively. For $^{16}\text{O}_2$ only even J states are occupied, while for $^{14}\text{N}_2$ odd states are occupied twice as much as even. See APPENDIX C: more information.

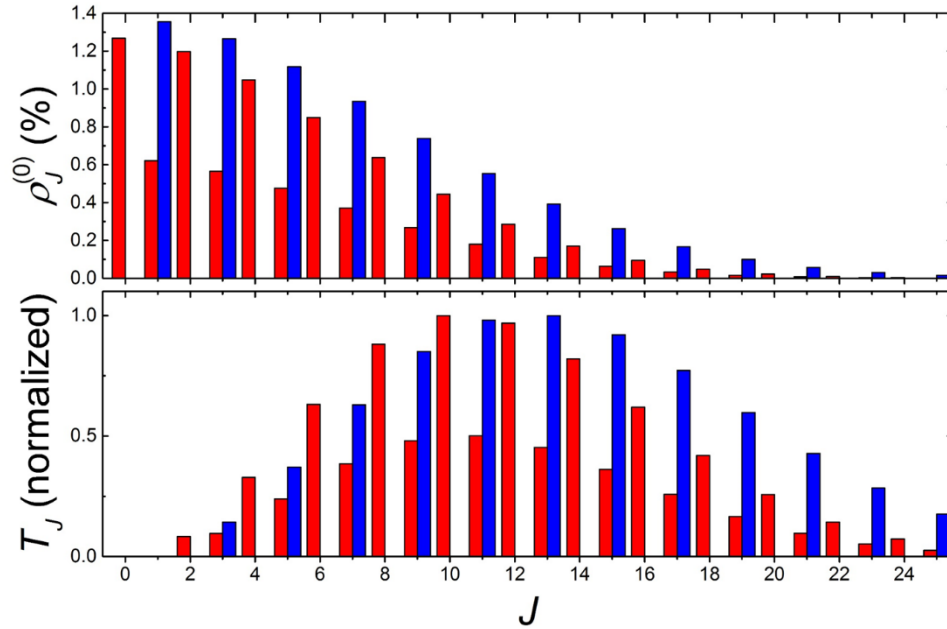


Figure 4.14 (top) Occupation probability and (bottom) T_J versus J of (red) $^{14}\text{N}_2$ and (blue) $^{16}\text{O}_2$ at 300 K via Equations (4.55) and (4.62), respectively.

4.4.2. Beam Deflection Measurement of Coherent Rotational Revivals

To demonstrate the applicability of the BD technique for measuring the optical nonlinearity of gases, including both the instantaneous bound-electronic and rotational responses, we first perform experiments on ambient air (predominantly N_2 and O_2) [118]. The BD experimental setup to measure coherent rotational revivals in air was very similar to that used for the measurements of liquid CS_2 . A 30 cm motorized translation stage, providing up to 2 ns of delay, was used to delay the pump pulse with respect to the probe pulse. The pump and probe beams were focused to spot sizes $w_b = 160 \mu\text{m}$ and $w_{0,a} = 60 \mu\text{m}$ (both $\text{HW}1/e^2\text{M}$), respectively. The crossing angle of the pump and the probe was kept small ($< 1^\circ$) to maximize the interaction length ($\sim 2 \text{ cm}$) while still being able to spatially separate the excitation from the probe at the detector. As illustrated in Figure 4.15, the excitation beam crossed the probe beam in the vertical (yz -) plane, but was displaced in

the horizontal (xz -) plane, causing deflection in the x -direction. This was done to maximize the probe deflection and prevent the cancellation of the deflection by different regions along the length of overlap.

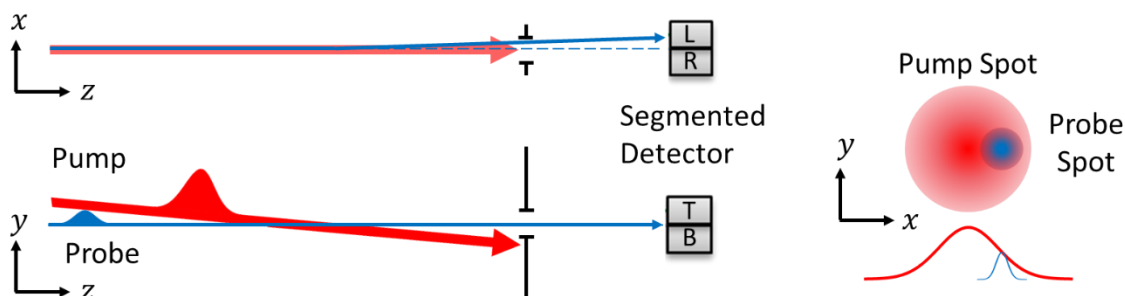


Figure 4.15 Illustration of BD geometry where the (red) pump and (blue) probe cross in the vertical (yz) plane (top left) but the deflection is in the horizontal (xz) plane (bottom left). (Left) Beam profiles at overlap [120].

In gaseous samples, the resulting total NLR transients occur at zero delay as well as at quarter multiples of the revival period (see Figure 4.13). Fitting was conducted by numerically evaluating the degree of alignment via Equation (4.61), where $\mathcal{E}(t)$ is taken to be the pump field, and then calculating the refractive index change via Equations (2.20) and (4.63) considering both bound-electronic and nuclear rotational contributions. The BD signal was then calculated as a function of delay by Equations (3.37) and (3.38). This assumes small interaction lengths such that the probe and pump do not spatially walk off one another and the phase change induced in the probe is uniform across the sample thickness. For our gaseous samples that assumption is no longer valid given the large thickness. To quantitatively measure the bound-electronic NLR of gases, we therefore perform relative measurements using the well-known values of $\Delta\alpha$ measured from gas phase Raman spectroscopy. The relative contribution between the second hyperpolarizability γ and $\Delta\alpha$ can be obtained by evaluating the ratio of the magnitudes of the bound-electronic and

rotational contributions to the BD signal. It can be shown from Equations (2.16), (2.20), and (4.4), as well as Equations, (4.61) and (4.63) that

$$\frac{\Delta n_{el}}{\Delta n_{rot}} \propto \frac{\langle \gamma \rangle}{(\Delta \alpha)^2}. \quad (4.66)$$

Within one self-consistent BD measurement, where Δn_{el} and Δn_{rot} are intrinsically separated, γ can be more precisely determined by using $\Delta \alpha$ as a reference, such that the errors from a determination of the interaction length, number density and focusing conditions, that exist in absolute measurements, will not affect the result. With a known number density N , $n_{2,el}$ can be calculated from Equations (2.16) and (4.4).

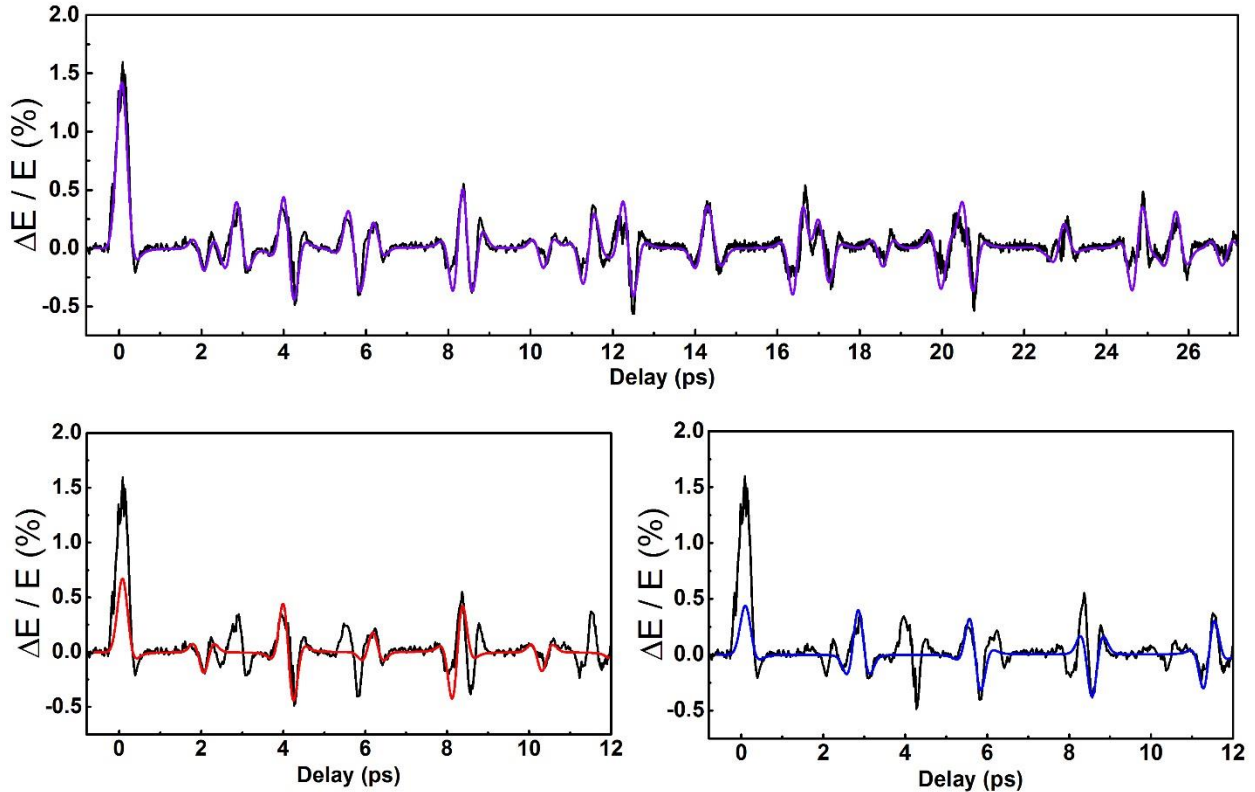


Figure 4.16 (top) Measured (black) BD signal from air and fit (violet), which is a sum of both the individual contributions of (bottom left, red) N_2 and (bottom right, blue) O_2 [120].

Figure 4.16 (a) shows the measured BD signal (black) of the ambient lab air for co-polarized excitation and probe over a 28 ps delay range, along with a numerical fit (violet) which includes contributions of both N₂ and O₂ weighted by their relative atmospheric concentrations at 1 atm. The total BD signal for the gas phase mixture can be decomposed into a sum of the individual contributions from the individual molecular species. We therefore obtain a good measure of $\Delta\alpha(\text{O}_2)/\Delta\alpha(\text{N}_2)$ since we measure both at the same time, which agrees well with the values in Table 4.5. The first 12 ps of delay of the measured air signal contains the first revival periods of both molecules, where the fits of the individual contributions from O₂ (blue) and N₂ (red) are shown in the lower plots of Figure 4.16. The rotational constants were found to be $B(\text{O}_2) = 1.4381(2)^6 \text{ cm}^{-1}$, and $B(\text{N}_2) = 1.9901(2) \text{ cm}^{-1}$, respectively, corresponding to full revival periods $T(\text{O}_2) = 11.597(2) \text{ ps}$ and $T(\text{N}_2) = 8.3806(9) \text{ ps}$, which agree well with literature values [114, 121]. From these measurements we can determine the bond length via Equation (4.46) and $J = ml^2/2$, where m is the mass of the atoms, and l is their separation. This results in $l(^{16}\text{O}_2) = 121.048(8) \text{ pm}$, and $l(^{14}\text{N}_2) = 110.005(5) \text{ pm}$, which agrees well with [122, 123] (see Table 4.5). Due to the contributions of both molecules to the total measured signal, certain revivals display features from the sum of each constituent. At a delay of 6.2 ps, the feature in the signal arises from the $\frac{1}{2}$ revival of O₂ and the $\frac{3}{4}$ revival of N₂. The positive signal, due to the aligned distribution of the N₂ ensemble increasing the refractive index, is enhanced by the aligned O₂ ensemble increasing the refractive index. At other delays, for example about 4 ps, only one species contributes to the BD signal, in this case N₂.

⁶ The number in parenthesis indicates the error (one standard deviation) in the last reported digit.

Table 4.5 Molecular parameters for Coherent Rotational Revivals

Molecule	$\Delta\alpha$ (10^{-40} Fm ²)	B (cm ⁻¹)	l (pm)	D (10^{-4} cm ⁻¹)	Δl (fm)
¹⁴ N ₂	0.77 [124]	1.9901(2)	110.005(5)	5.1(4)	29(2) ($J=14$)
¹⁶ O ₂	1.21 [124]	1.4381(2)	121.048(8)	5.6(6)	90(10) ($J=19$)
¹² C ³² S ₂	10.53 [125]	0.10945(10)	155.13(7)	0.010(5)	71(36) ($J=100$)
¹² C ³² S ₂ (ν_2)	10.53 [125]	0.1096(1)	155.03(7)	0.010(5)	72(36) ($J=100$)
¹² C ³² S ³⁴ S	10.53 [125]	0.1062(1)	155.08(7)	0.010(5)	74(37) ($J=100$)

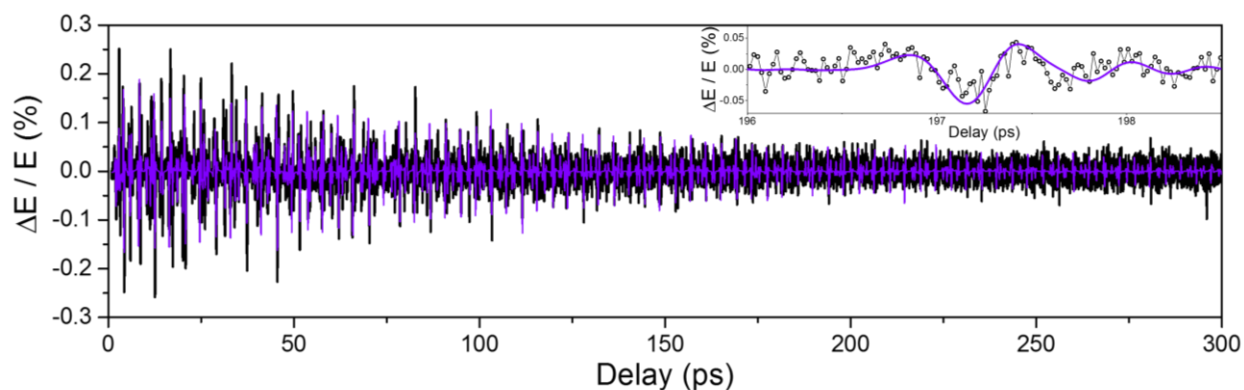


Figure 4.17 Measured (black) and fit (violet) BD signal of air out to 300 ps of delay. Inset shows revival signal and fit about 197 ps. (Reproduced with permission from Ref. [120]).

To obtain information about the dephasing rate Γ in air, a BD measurement was performed out to 300 ps of delay. Figure 4.17 shows the measured revival signal from 1 to 300 ps in black, and the fit in violet. Additionally, the Fourier transform of such a long scan provides the rotational Raman spectrum (see Equation (4.37)), which is shown in black Figure 4.18 (calculated after zero-padding to a delay of 1.5 ns) along with fits for O₂ (blue) and N₂ (red). In addition to the thermal distribution, the consequence of nuclear spin statistical effects can be seen in the amplitude of the

rotational Raman peaks (see Table 4.4). The nuclear statistics of O₂ dictate that the rotational levels have only odd J values. For a molecule with both odd and even rotational levels populated, the amplitudes of adjacent peaks will alternate at a ratio determined by the nuclear statistics of the molecule. As seen in the N₂ spectrum fitting where the intensity of adjacent peaks follows the ratio of symmetric to antisymmetric states, $6_{\text{even}}:3_{\text{odd}}$.

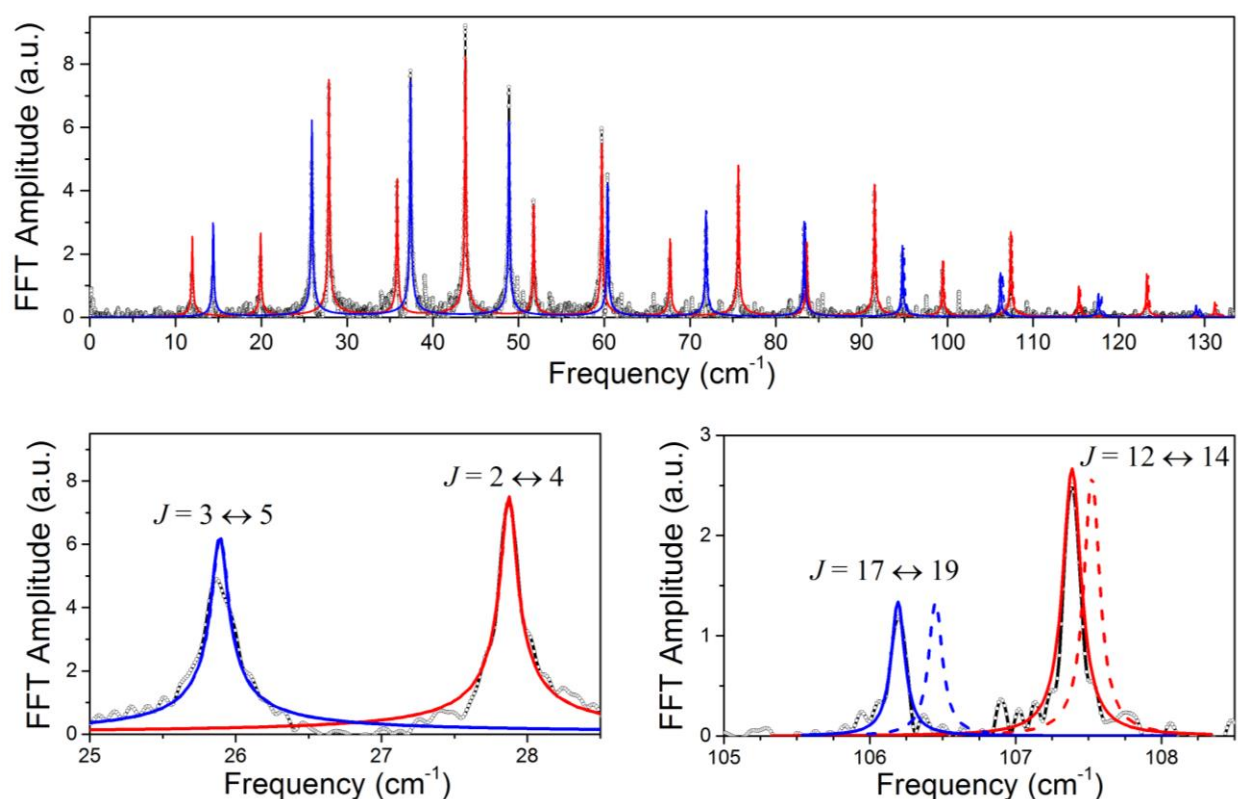


Figure 4.18 (top) Fourier transform of the BD signal for air (black) with the fitting for N₂ (red) and O₂ (blue). Zoomed in plots for (lower left) low and (lower right) high rotational states along with fits both neglecting (dashed) and including (solid) centrifugal distortion. (Reproduced with permission from Ref. [120].)

The spectral lines for rotational transitions are evenly spaced until the higher rotational levels where a centrifugal distortion lengthens the bond and decreases the rotational frequency. This causes the lines to not all be evenly spaced, making the system not a true frequency comb. In Equation (4.45) the centrifugal distortion constant D characterizes the reduction in energy of large

J (rapidly rotating) rotational states as centrifugal forces cause the atomic separation to increase [114]. Because of the large bond strength, D is typically several orders of magnitude smaller than B , and thus centrifugal distortion only impacts high rotational states. The results can be seen in the lower plots of Figure 4.18, where fits for low rotational states with (solid lines) and without (dashed lines) D lie on top of each other. However, for higher rotational states there is a significant discrepancy from the measurement when neglecting centrifugal distortion. From the fitting we find $D(\text{O}_2) = 5.6(6) \times 10^{-4} \text{ cm}^{-1}$ and $D(\text{N}_2) = 5.1(4) \times 10^{-4} \text{ cm}^{-1}$, which agree well with [121] (see Table 4.5). In $^{16}\text{O}_2$, at $J = 19$, this gives a bond length increase of 90(10) fm, and for $^{14}\text{N}_2$ at $J = 14$, it gives a bond length increase of 29(6) fm.⁷

A J dependence of the linewidths, and thus dephasing rates $\Gamma_{J,J-2}$, can be seen by comparing the widths of the peaks at low and high frequency in the lower left and lower right plots in Figure 4.18, respectively. Fitting each peak in the rotational Raman spectrum with a Lorentzian function yields $\Gamma_{J,J-2}$, which is plotted versus J in Figure 4.19. State-changing collisions, of energy change $\Delta E_{J,J'} = |E_J - E_{J'}|$ (where $J \neq J'$) that increases with J [16, 40, 41], cause decay of the rotational ensemble's coherence. Higher J rotational states require a high energy collision to change states, which are less common than lower energy collisions. Thus higher rotational states are more resilient to collisions and have a narrower linewidth. We fit the linewidths following [115] including only the minimum ΔJ transitions (one for N_2 , two for O_2) in the exponential gap law, where the probability of collision transition is $P_{J,J'} = ae^{-cBJ}$, where a and c are fitting parameters.

⁷ The errors quoted here are relative to the value of B , that is they do not include the uncertainty in the total bond length, as quoted after the measurement of B and in Table 4.5.

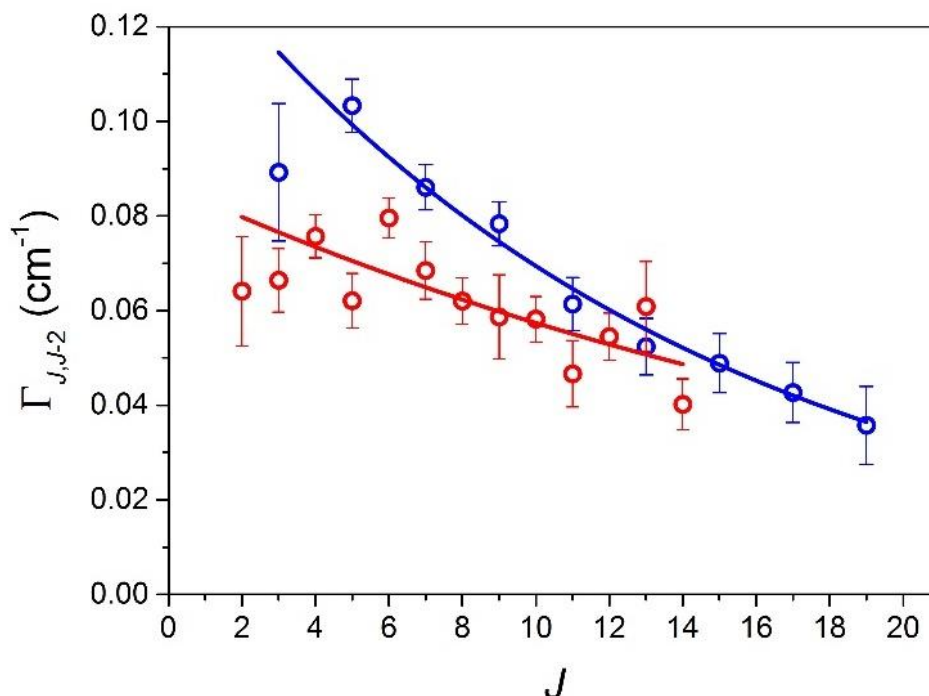


Figure 4.19 (circles) Measurements of linewidth $\Gamma_{J,J-2}$ versus J for (red) N_2 and (blue) O_2 , with (curves) exponential fits. (Reproduced with permission from [120].)

Coherent rotational revivals have the same polarization dependence as the libration and diffusive reorientation mechanisms in liquid CS_2 . In the same manner in that case, the application of the magic angle in BD measurements allows for an unambiguous determination of the bound-electronic nonlinearity of gases. Using a half-wave plate, the angle of the polarization of the probe with respect to the pump beam was varied for angles, $\varphi = 0^\circ$ (parallel, black), 90° (perpendicular, red), and 54.7° (magic angle, blue) with the data (circles) and fit (solid lines) shown in Figure 4.20 for air. For perpendicular polarizations the BD signal from the coherent rotational revivals changes sign and reduces to half the amplitude of the signal with parallel polarizations. At the magic angle, the revival signal is suppressed below the noise floor and only the bound-electronic signal remains about zero delay. This provides measurement of $n_{2,el}$ of air. Although we have a relative measurement, as discussed above, the use of known $\Delta\alpha$'s allows the signal from the coherent rotational

revivals to be used as a reference. We therefore obtain $n_{2,el}$ of air relative to the $\Delta\alpha$'s of N₂ and O₂, as shown in Table 4.5. The fit at the magic angle in Figure 4.20 corresponds to $n_{2,el}(\text{air}) = (1.0 \pm 0.1) \times 10^{-23} \text{ m}^2/\text{W}$ which agrees well with literature values [126, 127]. Because of the gaseous mixture, we are unable to extract separate values of γ of the two individual molecules.

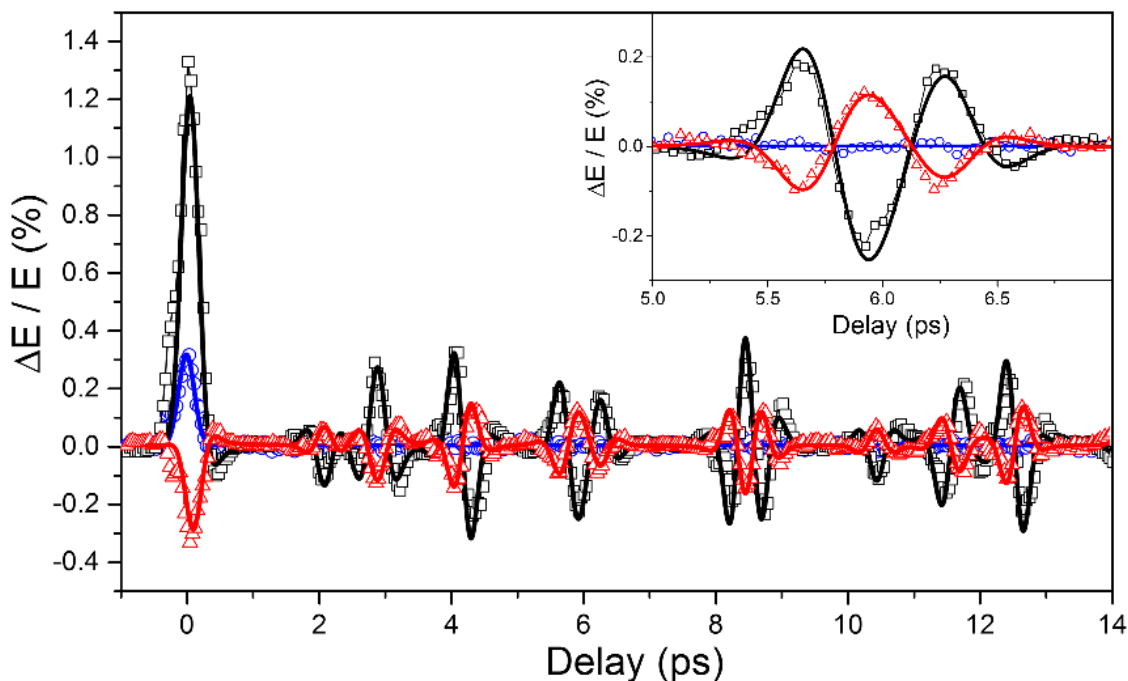


Figure 4.20 Polarization dependence of BD signal from air for (black) parallel, (red) perpendicular, and (blue) magic angle polarizations. Inset shows signal about a delay of 6 ps. (Reproduced with permission from [120].)

Gaseous CS₂ was also measured by filling a 10 cm fused silica cell ~1/3 full with the liquid CS₂ (Sigma-Aldrich, 270660, $\geq 99.9\%$) and heating the cell windows to approximately 50 °C to help evaporate the liquid and to prevent condensation on the cell windows. The sample cell was positioned such that the beams crossed just above the liquid CS₂ surface. The pump, generated from the TOPAS-HE, at 1250 nm had an irradiance $I_{0,b} = 140 \text{ GW}/\text{cm}^2$ ($E_b = 62 \text{ }\mu\text{J}$), and the

probe was generated from WLC and filtered to 950 nm, with spot sizes of 468 μm and 90 μm , respectively.

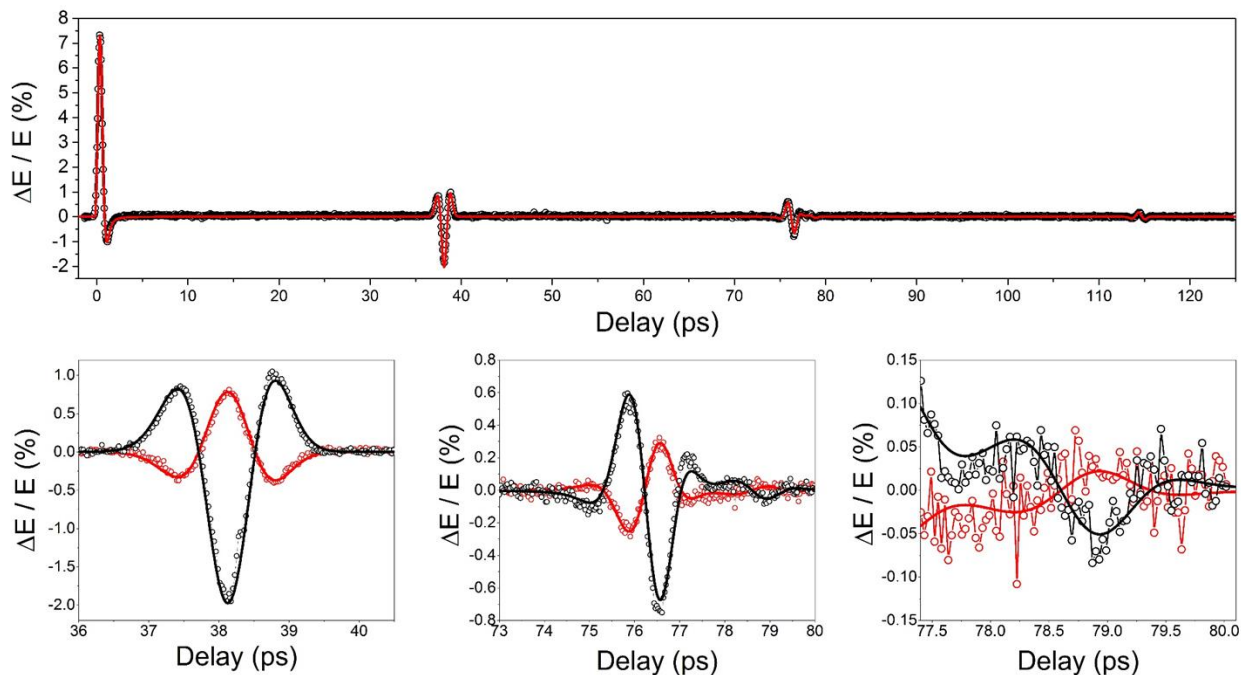


Figure 4.21 Measured (black) BD signal from gaseous CS_2 and fit (red), including (top) full delay range, as well as zoom ins at the (bottom left) $1/4$, (bottom center) $1/2$, and (bottom right) $1/2$ revival of $^{12}\text{C}^{32}\text{S}^{34}\text{S}$. (Modified with permission from [120].)

Figure 4.21 shows the measured BD signal for the coherent rotational revivals in gaseous CS_2 with co-polarized pump and probe beams. The finer structure of the signal can be seen in the lower plots, with the fractional revivals occurring at $1/4T$, $1/2T$, and $3/4T$. The fit corresponds to $B(^{12}\text{C}^{32}\text{S}_2) = 0.10945 \pm 0.0001 \text{ cm}^{-1}$ and $T(^{12}\text{C}^{32}\text{S}_2) = 152.4 \pm 0.1 \text{ ps}$ which agrees well with [115, 128, 129]. Based on this, the bond length, via Equation (4.46), is $155.2 \pm 0.4 \text{ pm}$ (see Table 4.5), which agrees well with [115]. Additionally, the $1/2T$ revival of the isotopologue $^{12}\text{C}^{32}\text{S}^{34}\text{S}$ can be seen in the bottom right plot in Figure 4.21, which was fit assuming 8% concentration (determine from natural abundance of S isotopes, see APPENDIX C: [115]) with $B(^{12}\text{C}^{32}\text{S}^{34}\text{S}) = 0.1062$

$\pm 0.0001 \text{ cm}^{-1}$. We are therefore able to use BD to identify different isotopologues within a gas. Additionally, 15 % of the molecules are in the first excited vibrational state, the doubly-degenerate bending mode at $\nu_2 = 397 \text{ cm}^{-1}$ [115]. These two modes oscillate in the plane either perpendicular or parallel to the axis of rotation, and are symmetric and antisymmetric upon nuclear interchange, respectively, and therefore have opposite spin statistics [130]. We treat the modes with a single rotational constant and equal weighting of even and odd J states. The rotational and centrifugal distortion constants found from the fit, which agree with [115, 128, 129], are given in Table 4.5.

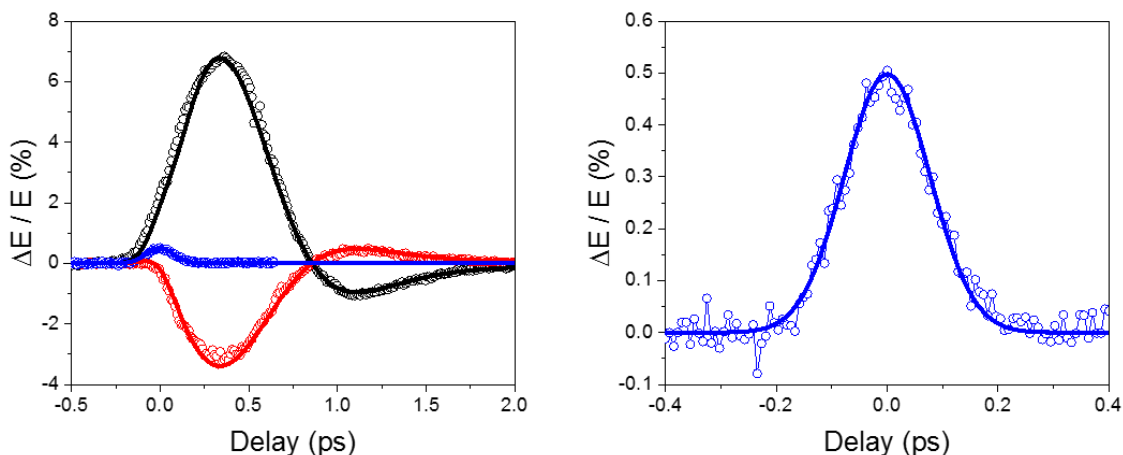


Figure 4.22 (circles) Measured and (curves) fit BD measurements of CS₂ gas. (left) Polarization dependence for (black) parallel, (red) perpendicular, and (blue) magic angle with (right) zoomed in plot at the magic angle [120].

Because Δn depends on $(\Delta\alpha)^2$, which for N₂ and O₂ is approximately two orders of magnitude less than CS₂ (see Table 4.5), we do not observe any contribution from air in the measurements of gaseous CS₂, since a much lower irradiance was used. In the CS₂ measurements, therefore, only the single species contributes to the BD signal. Thus we may extract the orientationally averaged second hyperpolarizability from the measurements at the magic angle, yielding $\gamma(\text{CS}_2 \text{ gas}) = (1.9 \pm 0.4) \times 10^{-61} \text{ C}^4\text{m}^4/\text{J}^3 [(1.5 \pm 0.3) \times 10^{-36} \text{ esu}]$. This is close to the value obtained from BD measurements on liquid CS₂ (from Figure 4.12) at the same average photon energy (1.15 eV,

1080 nm), where $\gamma(\text{CS}_2 \text{ liquid}) = (2.3 \pm 0.5) \times 10^{-61} \text{ C}^4\text{m}^4/\text{J}^3 [(1.8 \pm 0.4) \times 10^{-36} \text{ esu}]$. It is important to note that in liquid phase the local field correction factor $f^{(3)} = 5.35$ [27, 28]. Thus local field effects have a significant impact on $n_{2,el}$ in liquid phase, (see Equations (2.16) and (4.4)). This is of interest for theoretical purposes to compare calculated values of γ , which are typically performed for isolated molecules [131], as well as testing local field correction factors [16, 17]. Given the agreement between the liquid and gas phase measurements, the Lorentz local field corrections appear to work well.

CHAPTER 5: TWO-PHOTON GAIN IN SEMICONDUCTORS

As discussed in § 1.2. , 2PE comes in three varieties; spontaneous, singly-stimulated and doubly-stimulated. Here we give a brief overview and historical perspective of each, as well as a discussion of the potential of two-photon lasers.

5.1. Two-Photon Emission

Spontaneous 2PE, also called two-photon decay, is the process by which an electron in an excited state spontaneously transitions to a lower level by simultaneous emission of two photons. The sum of the photon energies is given by the energy difference between the two levels. Maria Göppert-Mayer was the first to recognize that spontaneous 2PE was possible, and that the individual photon energies are not determined and may take on any value less than the transition energy [2]. Initial interest in spontaneous 2PE came from a problem in astronomy. Planetary nebulae are primarily composed of atomic hydrogen, and one would expect their emission spectrum to consist of these spectral lines which are very discrete. However, as early as the 1930's it was observed that they exhibited a continuous emission spectrum over the range of 390-480 nm [132]. Attempts to explain this feature by several methods, including ion formation, free-electron captures, and scattering, were all unsuccessful [133]. Breit and Teller [3] found that spontaneous 2PE was the dominant decay mechanism of the metastable $2s$ level of hydrogen, and that an emission spectrum was very broad, covering wavelengths greater than 122 nm including the observed spectrum from planetary nebulae. Since then, spontaneous 2PE has been shown to produce polarization [10] and energy [134] entangled photon pairs, and has been measured in a variety of ions, including helium [135], neon [136], argon [137, 138], krypton [138], and sulfur [139], K-shell vacancies in molybdenum [140], and InAs quantum dots [141], and bulk GaAs [13].

Göppert-Mayer also demonstrated that, in addition to spontaneous 2PE, both singly- and doubly-stimulated 2PE were also possible [2]. A photon of energy less than the transition's $\hbar\omega < E_{fi}$ may singly-stimulated the emission of a duplicate photon plus a second photon of complementary energy. Göppert-Mayer stated that this complementary photon behaves as if it was produced by a “virtual oscillator”, i.e., spontaneously, with amplitude that is dependent on the incident irradiance. Lambropoulos described singly-stimulated 2PE as “a process in which the emission of one of the photons is induced and the other spontaneous... this process is half noise and half signal.” [8]. This process, of course, is observable even without population inversion, simply due to the fact that there is no competing absorption process. The first direct observation of singly-stimulated 2PE was conducted by Yatsiv et al. [142] who spectrally resolved the $6s \rightarrow 4s$ two-photon transition of potassium. With an excited $6s$ state, and “priming” (singly-stimulating) with a $3.68 \mu\text{m}$ beam, the authors spectrally distinguished the complementary 2PE from the cascaded one-photon emission involving the $5p$ state at 404 nm . Because of the close tuning of the $3.68 \mu\text{m}$ priming beam to the $6s \rightarrow 5p_{3/2}$ transition ($\Delta E < 2 \text{ meV}$, $\Delta E/\hbar\omega_b < 0.5 \%$), the 2PE was resonantly enhanced to a great extent. Singly-stimulated 2PE has also been observed in deuterium [143], helium [144], sodium [145], and bulk GaAs [13].

Just as one-photon stimulated emission is the reverse process of one-photon absorption, doubly-stimulated 2PE is the reverse of 2PA. An electron in the excited state, when perturbed simultaneously by two photons whose energy sum matches the transition energy, has a certain probability of transitioning to the ground state. This produces two additional photons that are replicas of the incident two, having equal energy, phase, direction, etc. Doubly-stimulated 2PE was first demonstrated by Loy in ammonia vapor [146], and later by others in lithium [147], Rydberg states of rubidium [148], and a bulk AlGaAs waveguide [74]. Utilizing this process, Sorokin and

Braslau [5] suggested the development of a degenerate 2PL (D-2PL). Almost simultaneously, Prokhorov [4], in his Nobel lecture, noted that the frequencies of the two incident photons could be different and indicated that a 2PL could potentially be tunable to any frequency less than that of the transition used, i.e., they could be made nondegenerate. He also pointed out that, while they would require an external trigger to initialize, D-2PL's had a much more rapid increase in photon density than traditional one-photon lasers due to the inherent nonlinearity of the gain processes. In addition to the suggestion to use doubly-stimulated 2PE as a light source itself, it was also proposed that it may be useful for amplification. Letokhov [6] showed that a material exhibiting 2PG will compress an incident pulse. The peak of the pulse, where the photon concentration is highest, experiences large 2PG while the wings on the pulse experience less. Pulse compression will occur regardless of whether or not there is net amplification of the pulse energy. This was recently demonstrated in a bulk AlGaAs waveguide [149]. These initial phenomenological investigations of stimulated 2PE lead to a wealth of theoretical studies and eventually physical realization of two-photon amplifiers and lasers. Thus far, only one group has demonstrated a two-photon laser using dressed states of barium [11] and potassium [150], but involved transitions from dressed states of the atom plus laser field system rather than eigenstates of the unperturbed atoms. This is due to the fact that most other materials suffer from various competing processes, e.g. excited state absorption, one-photon lasing, stimulated anti-Stokes Raman scattering, and parametric wave mixing [151].

Ironsides [152] was the first to suggest the use to bulk semiconductors for doubly-stimulated D-2PE. He argued that for a particular carrier concentration, doubly-stimulated 2PE would become more probable than 2PA for an energy region above the band gap. The 2PG coefficient can be expressed as a modification of α_2 by the distribution of carrier populations

$$\gamma_2(\omega_a; \omega_b) = \alpha_2(\omega_a; \omega_b) \cdot (f_c(\hbar\omega_a, \hbar\omega_b) - f_v(\hbar\omega_a, \hbar\omega_b)) \quad (5.1)$$

where

$$f_{c,v}(\hbar\omega_a, \hbar\omega_b) = \frac{1}{1 + e^{\frac{E_{c,v} \pm \frac{m_r}{m_{c,v}}(\hbar\omega_a + \hbar\omega_b - E_g) - E_{F_{c,v}}}{k_B T}}} \quad (5.2)$$

are the non-equilibrium Fermi functions for electrons in the conduction band (subscript c) and valence band (subscript v), where $E_c = E_g$ is minimum energy of the conduction band, $E_v = 0$ is the maximum energy of the valence band, $m_{c,v}$ are the effective masses of electrons and holes, $m_r = (1/m_c + 1/m_v)^{-1}$ is the reduced mass, $E_{F_{c,v}}$ are the quasi-Fermi energies, k_B is the Boltzmann constant, and T is the temperature. Equations (5.1) and (5.2) have been generalized from Ironside [152] to allow the two photons to be of unequal energy [153]. In the low temperature limit all of the energy levels in the conduction and valence bands are full to E_{F_c} and E_{F_v} , respectively. This gives complete population inversion for the energy range

$$E_g < \hbar\omega_a + \hbar\omega_b < E_{F_c} - E_{F_v} \quad (5.3)$$

where doubly-stimulated 2PE will occur with maximum 2PG coefficient $\gamma_2 = \alpha_2$.

Ironside went on to suggest a two-photon amplifier device based on a double heterostructure similar to that of traditional one-photon semiconductor lasers. He proposed using an injection current to obtain population inversion which would allow and an incident beam to experience D-2PG as it propagated through the active waveguiding region. However, one-photon emission would need to be suppressed, which could be achieved with the addition of anti-reflection or absorption coatings to the end facets of the structure designed for photon energies at and above the band gap energy. The structure has all the benefits of traditional one-photon semiconductor lasers where the active layer acts simultaneously as a gain medium as well as a waveguide.

Optical pumping was also considered by Marti et al. [154] in semiconductor quantum wells (QWs) confined in a microcavity. A pump pulse of with photon energy greater than the band gap energy would excite carriers high up into the conduction band, which would then non-radiatively decay through intraband scattering to the band-edge. A second pulse with photon energy slightly greater than $E_g/2$ which is resonant in the cavity would then be injected before significant inter-band relaxation could occur. Relaxation times of different regions of the bands were considered, and the resulting 2PL behavior was similar to previous findings discrete leveled systems in terms of gain increasing with photon density until saturation [5, 155].

There have been several of publications dealing with 2PE from semiconductors from Orenstein and collaborators who were the first to report observations of spontaneous, singly-stimulated [13], and doubly-stimulated [74] 2PE in semiconductors. The first of these experiments used a 200 μm thick sample of GaAs, in which carriers were generated by optically exciting with a 100 mW 514 nm CW argon laser. Spontaneous 2PE was spectrally resolved via a monochromator and detected with lock-in amplification. To ensure that the detected light originated from 2PE, singly-stimulated 2PE was observed by launching a stimulating beam into the pumped medium and measuring the emission at the complementary photon energy. The authors spectrally resolved spontaneous 2PE, and singly-stimulated 2PE from stimulating beams of photon energies 0.761 eV and 0.775 eV with complementary peaks at 0.854 eV and 0.840 eV; in both cases the photon energy sum was approximately 1.62 eV. In addition, when the stimulating beam was present, emission at other photon energies, which the authors attributed to spontaneous 2PE, was suppressed. After increasing the power of the excitation laser to 180 mW, the authors observed the dependence of singly-stimulated 2PE on the power of a stimulating beam with photon energy of 0.946 eV. The spectral width of the complementary emission was determined by the distribution of carriers in the

bands due to the fact that for a given the photon energy $\hbar\omega_a$ of the stimulating beam, the complementary photon energy $\hbar\omega_b$ need only satisfy Equation (5.3). The authors also measured spontaneous and singly-stimulated 2PE in an electrically pumped GaInP/AlGaInP QW waveguide via coincidence counting techniques, and obtained similar spectrally resolved results.

The group then observed D-2PG in an electrically pumped AlGaAs *p-i-n* heterostructure [74]. A stimulating pulse at 1560 nm, corresponding to photon energy slightly larger than $E_g/2$, was coupled into the guiding layer, and 2PG (doubly-stimulated 2PE) was observed in two manners. The first was by measuring spontaneous one-photon emission as both the input irradiance of the stimulating pulse and the injection current were varied. For zero injection current, the stimulating pulse underwent 2PA which generated carriers. These carriers then decayed via spontaneous one-photon emission at wavelength around 800 nm. This technique is equivalent to two-photon absorption induced fluorescence spectroscopy [156]. With no injection current, one-photon emission increased quadratically with input irradiance, indicating that carriers were generated by 2PA. For increasing injection current, the one-photon emission (fluorescence) induced by 2PA was reduced, with two-photon transparency, i.e. $\Delta N = 0$, at an injection current near $1300 \text{ A/cm}^2 \mu\text{m}$. Injection currents above this level produced a reduction in one-photon emission, which the authors attributed to a reduction in the carrier concentration due to recombination by doubly-stimulated 2PE. To verify that this was indeed due to 2PG, they measured the output irradiance of the stimulating beam as a function of input irradiance. To correct for linear losses that depended on the injection current such as free-carrier absorption (FCA), the output irradiance was normalized to a linear slope of one at low input irradiances. For injection currents above the two-photon transparency threshold, the output increased quadratically with input. For high injection currents, the effect of 2PG on the output irradiance exceeded that of 2PA for zero injection current, indicating $\gamma_2 >$

α_2 . The authors attributed this to band gap renormalization, which caused a decrease in band gap energy with carrier concentration, and in turn caused a drastic increase in γ_2 due to the E_g^{-3} dependence (see Equation (5.4)). The group was also the first to demonstrate compression of ultrafast pulses [149] as predicted by Letokhov [6] using the same system. It should be noted that Orenstein and coworkers did not report net 2PG that exceeded the losses.

Several other aspects of 2PE in semiconductors have also been considered. In particular, Orenstein and collaborators were initially interested in semiconductor QWs as an efficient source of entangled photon pairs. They showed theoretically that, with the aid of a microcavity to suppress one-photon emission, spontaneous 2PE from semiconductor QWs could produce polarization entangled photon pairs at a rate orders of magnitude higher than standard SPDC sources [157]. Additionally, they theoretically examined spontaneous 2PE from intersubband transitions in semiconductor QWs, and found that the photon pairs were hyperentangled, i.e., entangled in both polarization and energy [134]. 2PE in semiconductor QDs has undergone numerous theoretical studies, including enhancement within photonic crystal nanocavities [158, 159], and suggestion of 2PLs [160].

Despite this host of work on the subject, a 2PL involving doubly-stimulated 2PE from one unperturbed eigenstate to another (in contrast to that of Gauthier and coworkers [11, 12, 150, 151, 155, 161]) has yet to be reported. This is primarily due to the fact that the 2PG processes is weak (in comparison to 1PG), and requires high irradiances, which gives rise to a host of competing processes. There are, however, means to enhance the 2PG coefficients of materials, for example, via intermediate state resonance enhancement (see § 2.2.1.). In semiconductors this enhancement

is greatest for extremely nondegenerate photon pairs. The second-order perturbation theory approach has been applied to calculate the 2PA spectrum of direct-gap semiconductors. For a two-parabolic band model, this gives a 2PA coefficient [14]

$$\alpha_2(\omega_a; \omega_b) = K \frac{\sqrt{E_p}}{n_a n_b E_g^3} F_2 \left(\frac{\hbar\omega_a}{E_g}; \frac{\hbar\omega_b}{E_g} \right), \quad (5.4)$$

where $K = 3100 \text{ cm GW}^{-1} \text{ eV}^{5/2}$ [162] is a material independent constant in units such that E_p , the Kane energy parameter, and E_g , the band gap, are have units of eV and α_2 has units of cm/GW, and the spectral function F_2 is given by

$$F_2(x_1; x_2) = \frac{(x_1 + x_2 - 1)^{3/2}}{2^7 x_1 x_2^2} \left(\frac{1}{x_1} + \frac{1}{x_2} \right)^2. \quad (5.5)$$

Equation (5.5) reduces to that for D-2PA as $\omega_b \rightarrow \omega_a$, which was calculated by Wherrett [163]

$$F_2(x) = \frac{(2x - 1)^{3/2}}{(2x)^5} \quad (5.6)$$

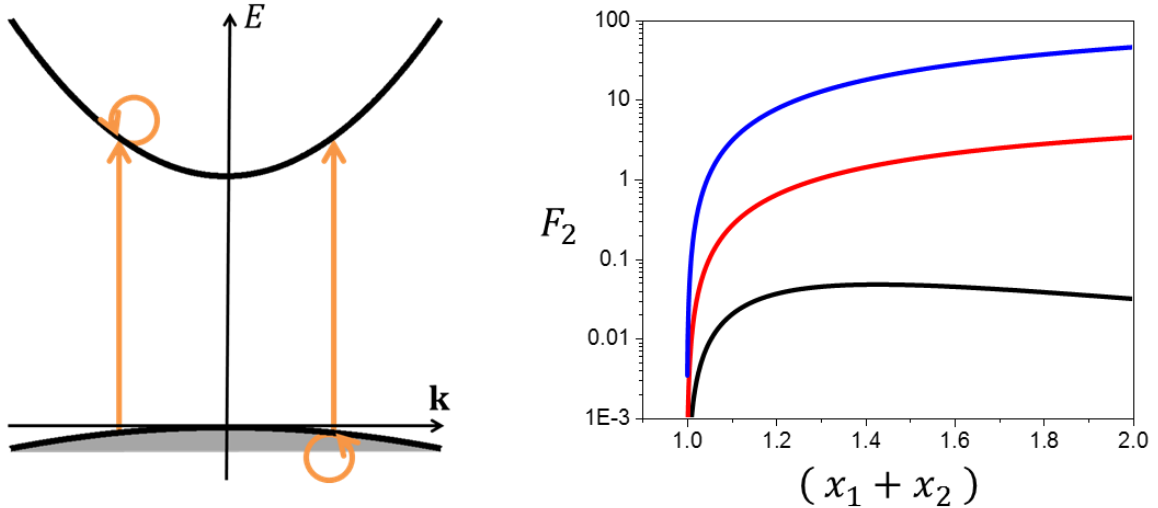


Figure 5.1 (left) Possible paths for 2PA in semiconductors interband (line) followed by intraband (circle), or *vice versa*. (right) Spectral dependence of 2PA in direct gap semiconductors for (black) degenerate, Equation (5.6), and nondegenerate, Equation (5.5), for (red) $\hbar\omega_b = 0.2E_g$, and (blue) $\hbar\omega_b = 0.1E_g$.

Figure 5.1 shows an enhancement of several orders of magnitude for decreasing values of x_2 in Equation (5.5), i.e., greater nondegeneracy, over the degenerate case. This has been examined experimentally for several direct-gap semiconductors by Cirloganu *et al.* [15], who found an enhancement of α_2 of 270 times in ZnO for $\hbar\omega_b = 0.08E_g$ compared to the degenerate value at equal photon energy sum. In addition, this enhancement has been utilized in photodiodes for detection sub-band gap light including infrared pulses of photon energy much less than the band gap [164].

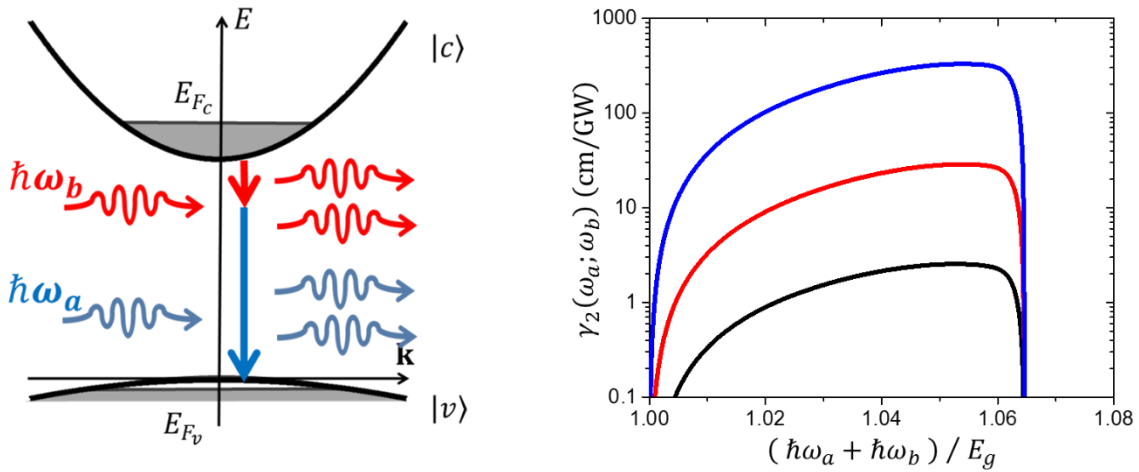


Figure 5.2 (left) Energy-momentum diagram illustrating doubly-stimulated ND-2PE (ND-2PG) in semiconductors [152]. (right) 2PG spectrum for GaAs at $T = 20$ K, $N = 2 \times 10^{18} \text{ cm}^{-3}$ for (black) degenerate, for (red) $\hbar\omega_b = 0.2E_g$, and (blue) $\hbar\omega_b = 0.1E_g$.

The observed enhancement in the 2PA coefficient of semiconductors when using extremely nondegenerate photon pairs should also translate to 2PG, since they are simply inverse processes. Shown in Figure 5.2 is a calculation of the 2PG coefficient γ_2 in GaAs based on Equations (5.1) and (5.2), at temperature $T = 20$ K and carrier concentration $N = 2 \times 10^{18} \text{ cm}^{-3}$. This large enhancement of over two orders of magnitude from the degenerate case, gives reason to believe that a semiconductor based 2PL could operate in the extremely nondegenerate regime. This may allow

for a broad tunability range, from just below the band gap energy to the mid-infrared; in GaAs for example from 900 nm to 11 μm .

5.2. Experimental Observation of Two-Photon Gain

This section provides an overview of the work done towards the goal of observing and measuring the 2PG in bulk semiconductors. Experiments were conducted on GaAs samples provided by Gregory Salamo at the University of Arkansas, which were grown by molecular beam epitaxy. As shown in Figure 5.3 (a), the received sample consisted of the GaAs layer of interest (either 1 μm or 4 μm thick) sandwiched between buffer layers of AlGaAs intended to protect the GaAs surfaces to prevent surface recombination of the excited carriers. AlGaAs has a larger band gap energy than GaAs and therefore appears transparent to all of the wavelengths used in this work. A 2.5 nm GaAs cap layer was applied to prevent oxidation of the topmost AlGaAs layer. The entire structure was grown on a GaAs wafer which was etched off using a solution of H_2O_2 , ammonia, and water which selectively etches GaAs over AlGaAs [165]. The structures were mounted either free standing by adhering to a metal ring, or glued to a sapphire plate using optically transparent adhesive (NOA 81, Norland Products). Figure 5.3 (b) shows the linear transmission spectrum of the 1 μm sample after processing. The reduced transmission for photon energies greater than the band gap energy of GaAs, $E > 1.42 \text{ eV}$ ($\lambda < 875 \text{ nm}$), is due to linear absorption in the 1 μm GaAs layer. At smaller photon energies (longer wavelengths), oscillatory behavior is observed, indicative of Fabry-Perot (thin film) interference. The AlGaAs band-edge can also be seen, which for $x = 0.47$ $E_g(\text{AlGaAs}) = 2 \text{ eV}$ ($\lambda_g(\text{AlGaAs}) = 620 \text{ nm}$), which gives the sharp cut off in transmission for higher photon energies (short wavelengths).

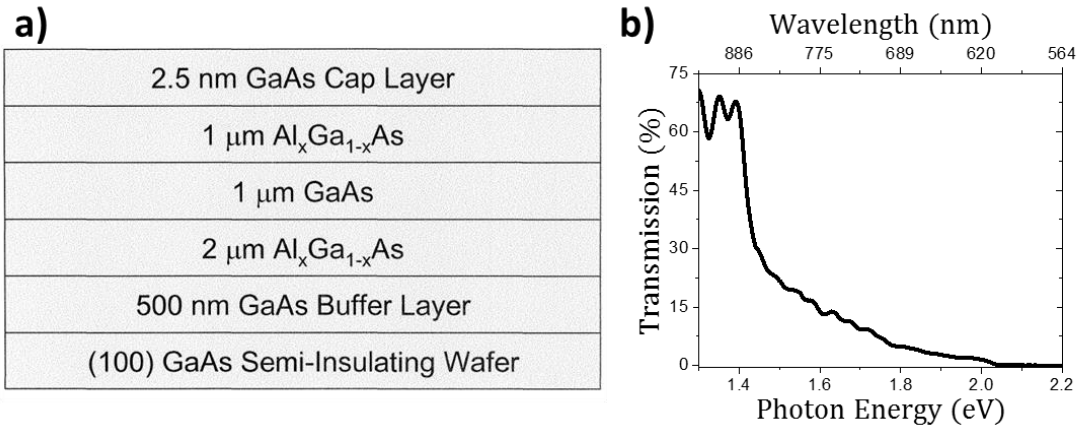


Figure 5.3 (a) Example structure of unprocessed GaAs samples. Here, $x = 0.47$ for the Al concentration of the Al-GaAs buffer layers. The 4 μm thick GaAs was very similar. (b) Transmission spectrum of 1 μm thick GaAs sample glued to sapphire after processing

5.2.1. Degenerate Two-Photon Gain

The first task was to generate population inversion, which was required to observe 2PG. The 1.59 eV (780 nm) fundamental from the Clark-MXR Ti:sapphire laser itself was used as an optical excitation to generate carriers and achieve population inversion near the band-edge. The reason for this sort of excitation method was to allow for rapid generation of the gain, and to allow a study of the temporal dynamics, which would not be possible with CW excitation. After the pulse arrived, the carriers very rapidly relaxed to the band-edge, and remained there for the duration of their lifetime. This allowed us to take advantage of the generated gain before recombination began to deplete the population inversion.

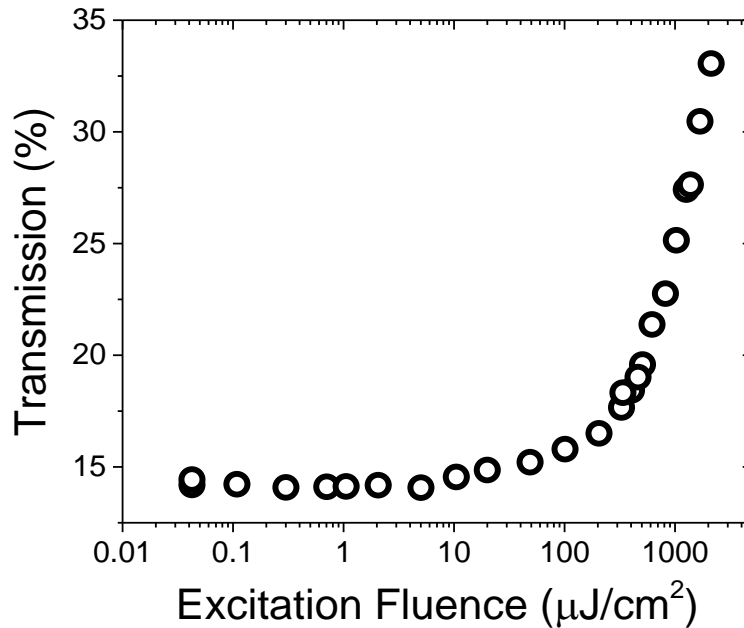


Figure 5.4 Plot of the transmission of the 1.59 eV (780 nm) excitation pulse versus input fluence.

To determine the required fluence necessary to generate population inversion, the transmission of the 1.59 eV (780 nm) excitation pulse as a function of fluence was measured (see Figure 5.4). At low fluence, the transmission was 14 %, which agrees with the measured transmission spectrum in Figure 5.3 (b). This value was due to a combination of both Fresnel reflections from the sample surfaces and one-photon absorption in the GaAs layer. As the fluence was increased, the leading edge of the pulse began to generate a sufficient carrier concentration to start saturating the absorption, thereby reducing the absorption that the remainder of the pulse experienced. Clearly, we started to see a drastic increase in the transmission for excitation fluences above several hundred $\mu\text{J}/\text{cm}^2$, and by the time we reached the maximum fluence used, 2100 $\mu\text{J}/\text{cm}^2$, the transmission more than doubled, indicating that a rather large carrier concentration was generated.

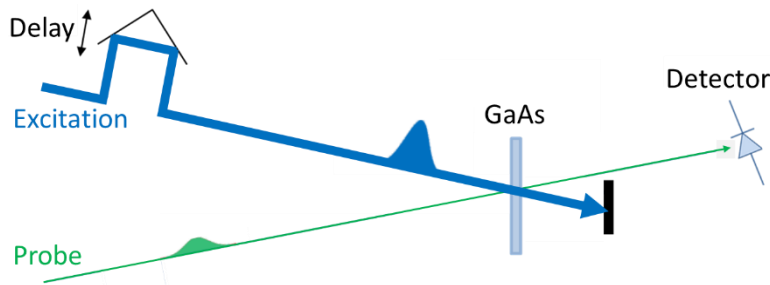


Figure 5.5 Illustration of setup for one-photon gain excite-probe experiments

The next step in the process was to determine the spectral region that experienced the greatest carrier concentration, which determined the photon energy that experienced the greatest gain. To do this, an excite-probe experiment was conducted, where the 1.59 eV (780 nm) excitation pulse was used to generate a carrier population in the 4 μm thick GaAs sample, and the change in transmission of a weak probe pulse, with photon energy close to the band gap energy, from 1.55 eV to 1.39 eV (800 nm to 890 nm), was observed. Here, the probe was focused to a smaller spot size than that of the excitation such that the probe experienced an approximately uniform carrier distribution. The probe pulse was delayed with respect to the excitation pulse, and the change in transmission was measured for several probe photon energies (wavelengths), as shown in Figure 5.6. The differential transmission was proportional to the change in the absorption coefficient, and thus to the carrier concentration within the regions of the band that were coupled by the probe. Figure 5.6 therefore shows a measure of the energy distribution of carriers as a function of time delay after the excitation. Shortly after zero delay there was an increase in the transmission (decrease in absorption) due to carriers filling the bands. Over the entire delay range, there was a noticeable reduction in the energy of maximum transmission change, indicated in Figure 5.6 by the black curve. This is most likely attributable to the diffusion of carriers throughout the thickness of the sample [166]. Since the absorption coefficient of the 1.59 eV (780 nm) excitation pulse is

so large ($>10^4 \text{ cm}^{-1}$), the skin depth $1/\alpha_1$ is less and $1 \text{ }\mu\text{m}$. Thus carriers were only generated within the first $1 \text{ }\mu\text{m}$ or so and then diffused throughout the remainder of the $4 \text{ }\mu\text{m}$ thick GaAs layer. As electrons higher up in the band diffused they were able to relax down closer to the band-edge since these states were not occupied deeper within the sample. This resulted in an overall shift in the photon energy of maximum transmission change over time. Clearly, the photon energy that experienced the greatest increase in transmission was at 1.45 eV (855 nm), which reached a maximum at a delay of about 300 ps . We thus selected this energy to use for future experiments, since here we will have the greatest carrier concentration and therefore potentially the largest gain. After 500 ps , the transmission change dropped off back towards zero as the carriers recombined.

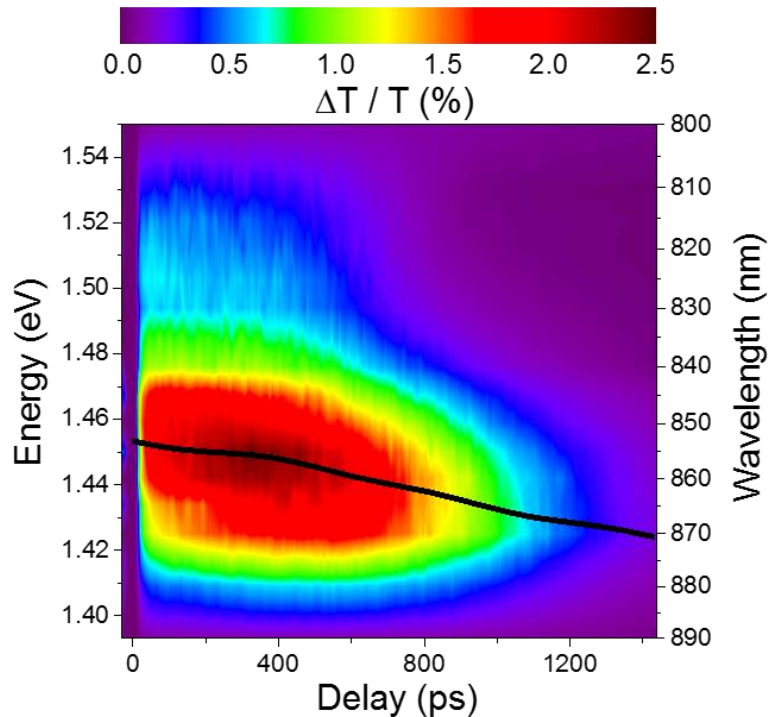


Figure 5.6 Results of excite-probe experiment showing change in transmission (color axis) of probe versus delay (horizontal axis) for several photon energies (vertical axis). The black line indicates the photon energy (wavelength) of maximum transmission change versus delay.

While this experiment showed an increase in transmission, it did not generate a sufficient carrier concentration to yield net gain, which is necessary to guarantee that stimulated emission occurs. The excitation fluence was increased well above the levels used in the previous experiment to attempt to observe net gain, meaning a transmission greater than 100 %. Figure 5.7 (a) shows the total transmission of the 1.46 eV (850 nm) probe (measured as the ratio of the detector signal with the sample to without it) as a function of time delay after the excitation pulse. The corresponding absorption coefficient α_1 , calculated by

$$\alpha_1 = -\frac{1}{L} \ln \left(\frac{T}{(1-R)^2} \right), \quad (5.7)$$

where R is the reflectivity which was estimated by the transmission of photon energies below the band gap, and L is the sample thickness, is shown in Figure 5.7 (b). The solid line with the error bar indicates the gain threshold, i.e., transmission above which stimulated emission dominates absorption. For low excitation fluences (black curve) there was a monotonic increase in transmission with delay, though not sufficient to demonstrate gain. Once the excitation fluence exceeded 0.8 mJ/cm^2 (orange curve) the probe transmission exceeded gain threshold, but only for a short duration within the first picosecond, after which the transmission reduced to near the threshold. Yet higher fluences increased the transmission further, eventually showing net gain (transmission $> 100 \%$) at 3.2 mJ/cm^2 where the gain was able to overcome the other losses in the sample, including reflections and scattering. However the gain still only remained for about one picosecond.

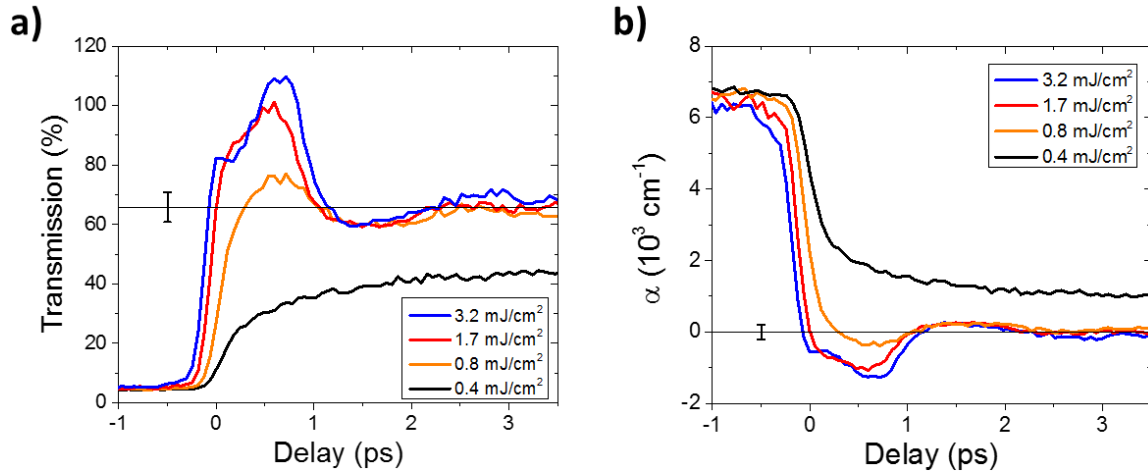


Figure 5.7 Results of excite-probe experiment to observe net one-photon gain, where (a) is the directly measured total transmission, and (b) is the absorption coefficient calculated from (a) using Equation (5.7). The straight line with error indicates gain threshold where stimulated emission dominates absorption.

One possible explanation for the short-lived gain is that it was rapidly depleted by ASE. Once excited carriers relax the band-edge they may radiatively recombine. Since the gain is so large ($\gamma_1 \sim 10^3 \text{ cm}^{-1}$), each spontaneously emitted photon stimulates the emission of many more, each time removing an electron-hole pair that would have interacted with the probe pulse. This effect occurs until stimulated emission is no longer favored over absorption, which is exactly what was observed as the transmission settled to the gain threshold after 2 ps. This behavior was not observed at low excitation fluence, where population inversion was not achieved, which further supports the possibility that ASE depleted the gain.

Since we have observed one-photon gain at a probe energy of 1.46 eV (850 nm), at least over a short delay range after the excitation pulse, we moved to two-photon experiments with the same energy sum. In addition, the delay at which the maximum one-photon gain was observed was used for two-photon experiments as well.

The next objective was to measure two-photon gain in the sample. Initially, degenerate experiments were chosen since the pump photon energy would be the greatest (shortest wavelength), where free-carrier absorption (FCA) losses were expected to be the smallest [167, 168]. For these degenerate two-photon experiments, half the photon energy of that used for one-photon gain, 0.73 eV (1700 nm), was used.

Observing the fluorescence from a material can provide information on the way the electrons were excited. Specifically, by measuring the dependence of the fluorescence on the irradiance of the excitation can distinguish 2PA, which will present a quadratic dependence, from one-photon, which has a linear dependence. Here, a pump beam at half the photon energy of that used for one-photon experiments, 0.73 eV (1700 nm), was used to generate a carrier population, and the fluorescence was observed as a function of the pump irradiance. The addition of the 1.59 eV (780 nm) excitation pulse produced a population inversion via one-photon absorption. The temporal delay between the excitation and pump pulses was set to where the peak in the one-photon gain was observed (see Figure 5.7). The fluorescence was measured at a 90° angle with respect to the incident beams to help minimize scattering from the excitation and pump pulses and also to ensure that the measured signal was indeed fluorescence and not SHG. In addition, spectral filters were used to isolate only photon energies in the region of the fluorescence spectrum of GaAs. A typical spectrum, taken with only the 0.73 eV (1700 nm) pump beam (excitation beam blocked) is shown in Figure 5.8 (b). Lock-in amplification was used to isolate the change in the fluorescence signal due only to the pump pulse by modulating the beam with a mechanical chopper (see Figure 5.8 (a)).

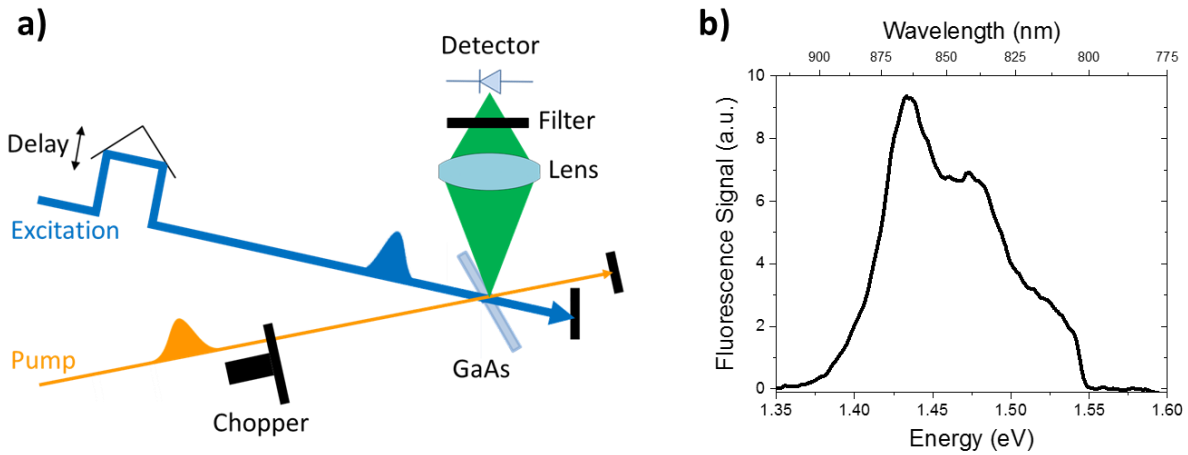


Figure 5.8 (a) Illustration of experimental setup for fluorescence experiments, and (b) measured fluorescence spectrum of 4 μm thick GaAs sample with only 0.73 eV (1700 nm) pump beam.

The measured change in the fluorescence signal versus input pump irradiance is plotted in Figure 5.9 for several excitation fluences. Without any excitation pulse (black), there was an increase in fluorescence since the pump pulse was generating carriers through multiphoton absorption. For an excitation fluence of 0.5 mJ/cm^2 (red), the fluorescence was actually reduced for low pump irradiances. This was due to the excitation pulse generating a population inversion, which caused 2PG. Thus the pump pulse depleted the population by stimulating carriers to recombine through doubly-stimulated 2PE, which left fewer electrons fluoresce. However, for pump irradiances greater than 8 GW/cm^2 , the fluorescence actually increased. For higher excitation fluence (blue), the same trend was observed, but the irradiance where the signal changed sign from negative to positive increased. This increase in fluorescence must have been due to a higher order non-linear absorption mechanism, i.e., three-photon absorption, since it only becomes dominant for sufficiently high irradiances. We thus have a combination of 2PG, which goes as I^2 , and 3PA, which goes as I^3 . The solid curves are fits to third-order polynomials. There is a window of irradiances where 2PG results in a net reduction in fluorescence, but 3PA wins out at large irradiances given the higher order dependence.

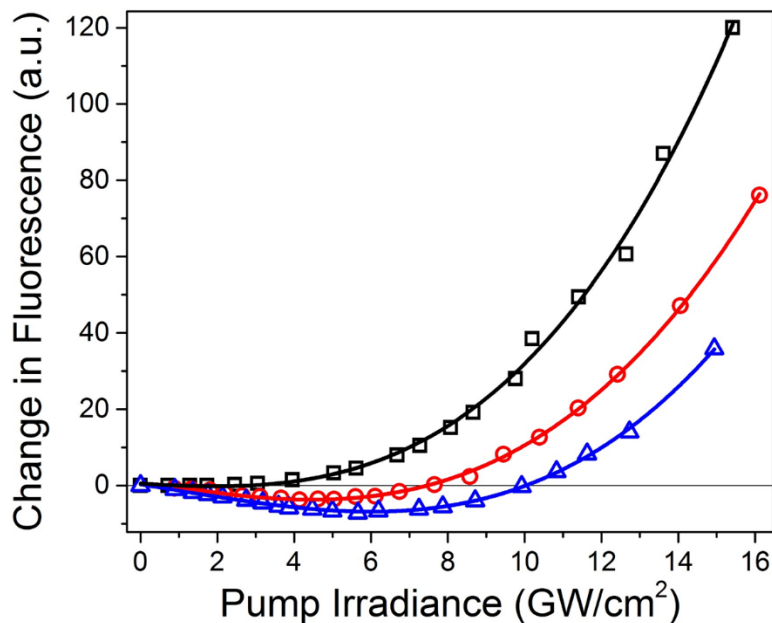


Figure 5.9 Measured (symbols) change in fluorescence due to the 0.73 eV ($\lambda = 1700$ nm) pump beam versus irradiance for several 1.59 eV (780 nm) excitation fluences. Curves are third order polynomial fits.

In addition to measuring the change in fluorescence, direct transient transmission measurements were also conducted. To do this, the change in transmission of a weak probe beam due to a strong pump beam, each at 0.73 eV (1700 nm), was monitored as illustrated in Figure 5.10. Initially the experiment was performed without the 1.59 eV (780 nm) excitation pulse to observe only the nonlinear effects due to the 0.73 eV (1700 nm) pump pulse. To mitigate the effects of scattering of the pump pulse to the detector, the probe was polarized orthogonally to the pump, and a polarizer was placed in front of the detector to block out the pump pulse (not shown).

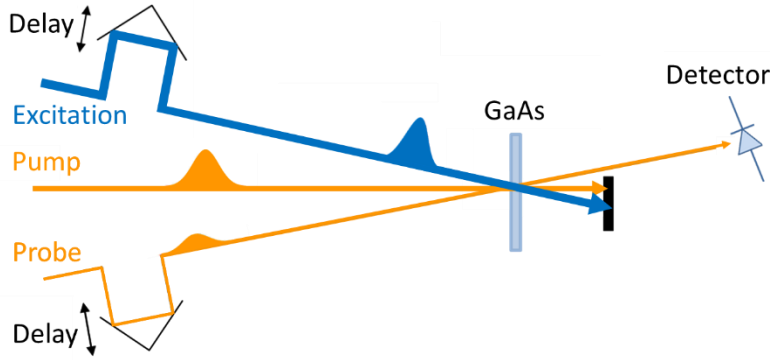


Figure 5.10 Illustration of setup for degenerate excite-pump-probe experiments.

The measurement results are shown in Figure 5.11, where the normalized transmission of the probe was measured for several values of the pump irradiance I_b . As can be seen at low pump irradiance, see Figure 5.11 (b), there was a reduction in transmission at zero delay when the pump and probe pulses were temporally overlapped within the sample due to 2PA. At positive delays, the transmission was also reduced, though to a lesser extent, due to the fact that the pump itself generated free carriers via 2PA that then absorb probe photons via FCA. Since 2PA of the pump itself has a quadratic irradiance dependence, while 2PA of the probe due to the pump has a linear dependence on I_b , the 2PA induced FCA dominates the 2PA of the probe for high pump irradiances. The fluctuations/oscillations on the signal (see Figure 5.11 (b)) are believed to be due to aliased interference between a small leakage of the pump to the detector and the probe. The solid curves represent theoretical fits to the data using

$$\frac{\partial I_a}{\partial z} = -2\alpha_{2,\perp} I_b I_a - \sigma_{FCA} N I_a, \quad (5.8)$$

$$\frac{\partial I_b}{\partial z} = -2\alpha_{2,\perp} I_a I_b - \alpha_{2,\parallel} I_b^2 - \alpha_3 I_b^3 - \sigma_{FCA} N I_b, \quad (5.9)$$

$$\frac{\partial I_b}{\partial z} = -2\alpha_{2,\perp} I_a I_b - \alpha_{2,\parallel} I_b^2 - \alpha_3 I_b^3 - \sigma_{FCA} N I_b, \quad (5.10)$$

where I_a (I_b) is the probe (pump) irradiance, $\alpha_{2,\perp}$ ($\alpha_{2,\parallel}$) is the 2PA coefficient for the perpendicular (parallel) polarizations, α_3 is the (degenerate) 3PA coefficient, N is the carrier concentration, and σ_{FCA} is the free-carrier absorption cross section. Also included was the saturation effects of the 2PA coefficients since the region of the band was close to the band gap. The values for the 2PA coefficients used in the fit were $\alpha_{2,\parallel} = 3$ cm/GW, $\alpha_{2,\perp} = 1.2$ cm/GW, $\alpha_3 = 0.1$ cm³/GW², and $\sigma_{FCA} = 1.4 \times 10^{-16}$ cm², each of which agree well with theory [14, 167, 169, 170] and previous measurements [15, 171, 172]. This simplistic model, which does not include the distribution of the carriers within the bands, is meant to show a consistency of the mechanisms, rather than an accurate measurement of material properties. It does show that there are many competing processes that dominate the 2PA of the probe and limit the pump irradiance that can be used.

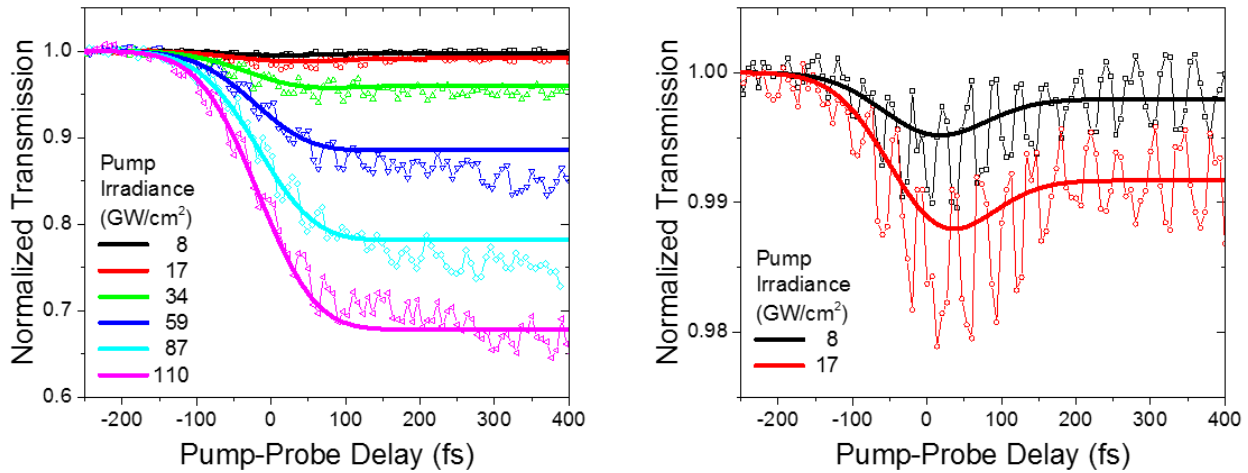


Figure 5.11 Measured transient normalized transmission from a degenerate pump-probe. Curves represent fits from Equations (5.8) - (5.10).

Next, the excitation beam was added back to the experiment, and was set to arrive ~ 1.2 ps before the pump and probe pulses. Using lock-in detection and modulating the pump beam isolated the effect of the pump on the probe transmission, and eliminated the FCA induced by the excitation

pulse from the measured signal. Given the large FCA observed in the pump-probe measurements, the irradiance of the pump was kept low to ensure FCA did not contaminate the 2PG signal. Figure 5.12 shows the measured change in normalized transmission ΔT (in %) of the probe for a pump irradiance of 12 GW/cm^2 . The data taken with the excitation blocked (black), shows a reduction in transmission only at zero delay due to 2PA. The addition of the excitation, at a fluence of 0.4 mJ/cm^2 , results in an observed increase in normalized transmission at only at zero delay, indicative of 2PG.

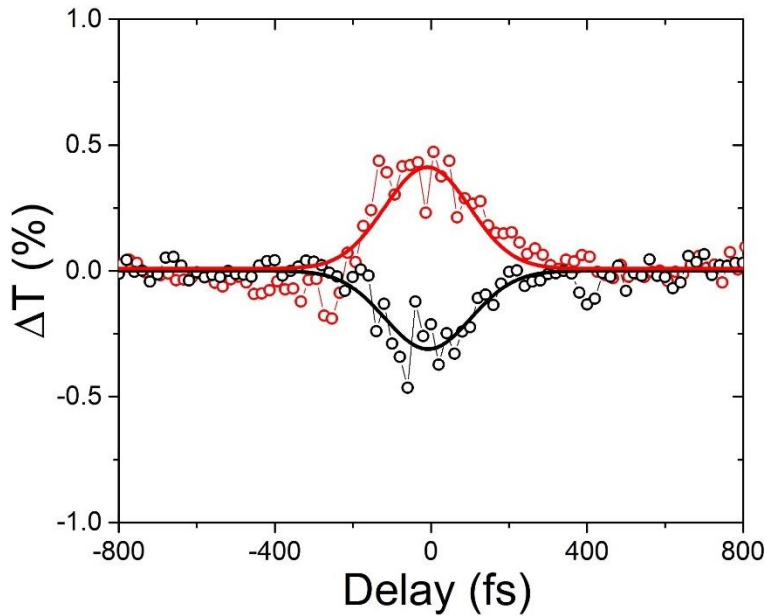


Figure 5.12 Results of excite-pump-probe experiment showing change in normalized transmission ΔT demonstrating (black) 2PA and (blue) 2PG.

The excitation fluence was increased to 1.3 mJ/cm^2 , and the pump-probe measurement was repeated for various pump irradiances, the results of which are shown in Figure 5.13. At zero delay there was an increase in transmission that scaled linearly with the pump irradiance (see Figure 5.13 (b)) which was consistent with 2PG. However, the increased transmission remained for longer than

the pulse duration, extending as long as 0.5 ps, after which a net reduction in normalized transmission was observed. These non-instantaneous effects may perhaps be due to changes in the observed total linear absorption coefficient by the probe. For example, the pump itself may undergo 2PG, which will deplete the total carrier concentration, and therefore reduce intervalence band and free-carrier absorption. However, more complicated dynamics, involving the various valence and conduction bands, have a larger impact (see § 5.3.3.). The pump may also be absorbed via direct heavy-hole to split-off band transitions, which take some time to relax ($\tau_{SH} \sim 0.4$ ps [173, 174]) back to the heavy-hole band. During this time period, the FCA observed by the probe is saturated, yielding an increased transmission. The conduction band may also contribute to these dynamics when electrons in the Γ -valley are excited to the X-valley by the pump via phonon-assisted FCA. Direct absorption from the X-valley to the next higher conduction band greatly increases the absorption of the probe. Clearly these dynamical loss mechanisms represent a complicated many-body problem. Additionally, thermal cooling of the excited carrier may play an important role, especially during the first ~ 1.5 ps after zero delay.

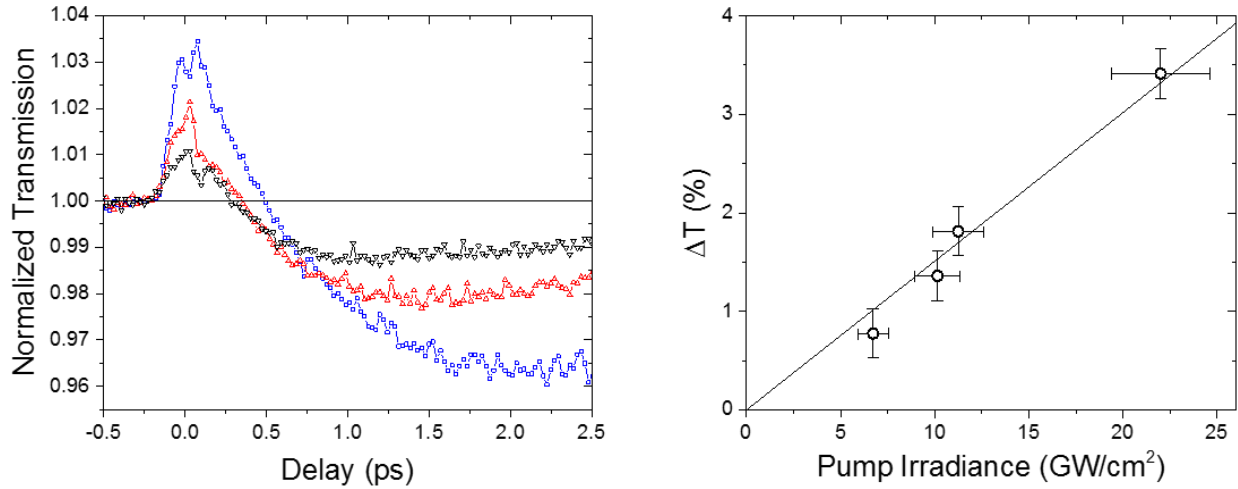


Figure 5.13 (left) Normalized probe transmission with an excitation fluence of 1.3 mJ/cm^2 for pump irradiances (black) 7 GW/cm^2 , (red) 10 GW/cm^2 , (red) 22 GW/cm^2 , and (blue) change in normalized transmission at zero delay versus pump irradiance where circles are data, and solid line is a linear fit.

These observations provided evidence of degenerate 2PG in bulk GaAs. However, there were evidently very strong competing processes in the form of FCA and 3PA that not only complicated the measurements, but also made the possibility of obtaining *net* 2PG (gain > losses) highly unlikely. For this purpose, the enhancement of 2PG when using nondegenerate photons seemed necessary to overcome the significant losses.

5.2.2. Extremely Nondegenerate Two-Photon Gain

To see if the predicted and observed enhancement in 2PA for END photon pairs carries over to enhancement of 2PG, a second experimental setup was constructed using the Coherent laser system. Here the DFG attachment to the TOPAS-800 was used to generate a pump beam in the mid-IR. However, the spectrum of the emission from the DFG was found to be incredibly broad. Measurements of the spectrum were performed using an Oriel monochromator (Cornerstone 130 1/8m), which had a grating with 150 lines/mm. Figure 5.14 shows measurements at a centered wavelength of $3.75 \text{ } \mu\text{m}$ (333 meV), the FWHM is $0.6 \text{ } \mu\text{m}$ (55 meV), while at $7.86 \text{ } \mu\text{m}$

(163 meV), the FWHM is 2.9 μm (55 meV). This large bandwidth would make measurements difficult, since the photon energy sum with a probe pulse in the near-IR would be very broad, and straddle the band gap of GaAs. For this purpose, a narrow bandpass filter from Iridian Spectral Technologies Ltd., centered at 7.75 μm (160 meV), with FWHM 195 nm (4 meV), were used to reduce the bandwidth and increase the spectral resolution.

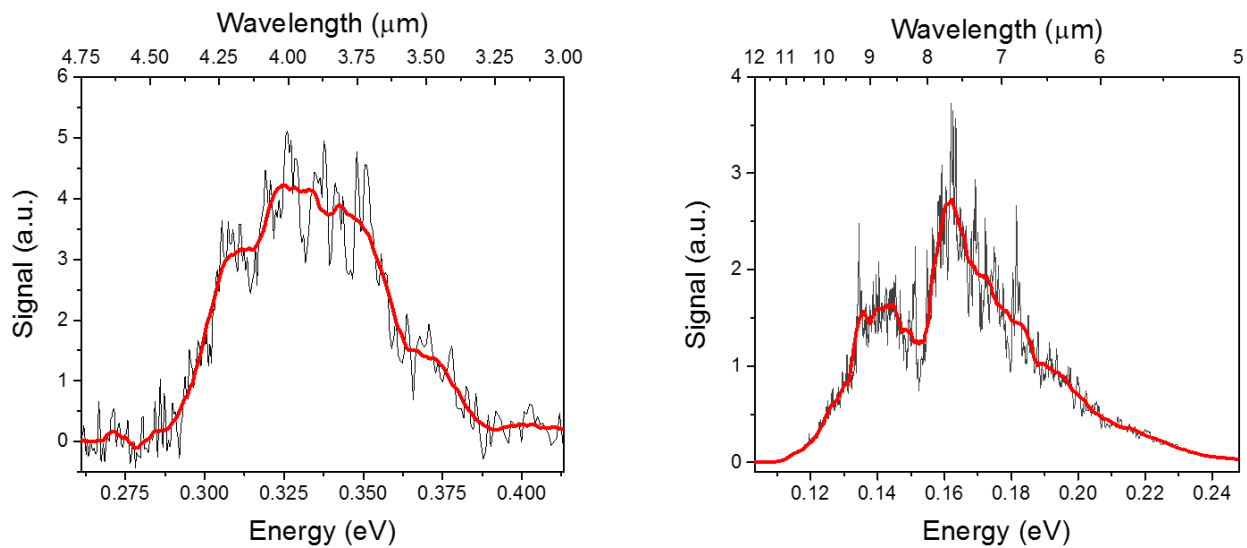


Figure 5.14 Measured spectrum of DFG output using Orielt Monochromator (Cornerstone 130 1/8m) and HgCdTe detector for a nominal wavelength of (left) 3.7 μm and (right) 8 μm . Black curves are measured data, and red curves are smoothed.

A WLC is generated by focusing a small portion of the 800 nm fundamental ($\sim 4.4 \mu\text{J}$) into a 5 mm thick sapphire plate. 977 nm (1.27 eV) was selected using a narrow (FWHM 10 nm, 13 meV) bandpass filter to be used as the probe. A half-wave plate and polarizer was used to ensure linear polarization of the probe, and a second half-wave plate was used to rotate the polarization to be either parallel or perpendicular to the pump. The pump and probe were focused to 30 μm and 20 μm (both $\text{HW}1/e^2\text{M}$), respectively, and overlapped on the 4 μm thick GaAs sample. The sum of the pump and probe photon energies is 1.43 eV (14 meV FWHM), which is slightly greater than

the band gap energy of GaAs, where population inversion is expected. The change in transmission of the probe is monitored via a lock-in amplifier, set to the frequency of an optical chopper that modulates the pump, as the temporal delay between the pulses is varied.

Initially, the excitation is blocked, and the measurements yield a signal that is proportional to the cross-correlation of the pump and probe pulses due to ND-2PA. Figure 5.15 shows the normalized probe transmission for parallel pump and probe polarizations in the solid black curve, from which $\alpha_{2,\parallel}$ is determined. A half-wave plate is then used to rotate the probe's polarization to be perpendicular to the pump's (dashed black curve) to give $\alpha_{2,\perp}$. The ratio $\alpha_{2,\parallel}/\alpha_{2,\perp} \approx 2.4$, which is consistent with the theory of Ref. [170]. A peak excitation fluence of 2.8 mJ/cm^2 is then added approximately 1.2 ps before the pump to generate a population inversion near the band edge, and the pump-probe measurement is repeated for both polarizations of the probe. At zero pump-probe delay we now observe an increase in transmission for both parallel (solid red curve) and perpendicular (dashed red curve) polarizations, however the ratio of the increases is less than 2.4. Additionally there is a reduction in transmission at positive delay that is consistent with the measurements in the degenerate case. However, here the photon energy of the pump is only 163 meV, which is less than both the split-off energy, $\Delta = 341 \text{ meV}$, and the energy difference between the bottom of the Γ and X valleys, 480 meV, and Γ and L valleys, 280 meV [175]. Therefore, the pump does not have sufficient energy to transfer carriers either from the heavy-hole band to the split-off band, or from the Γ -valley to the X-valley. The cause of these dynamics may be due to carrier heating (see § 5.3.3. and Figure 5.28). Notice that this signal at positive delays is identical for both parallel and perpendicular polarizations. This indicates that the mechanism that causes the transmission change is independent of polarization, which is consistent with intervalence band and free-carrier absorption induced carrier heating.

We can eliminate this effect from the measurement by defining $\Delta T = T_{\parallel} - T_{\perp}$, i.e., the difference between transmission for parallel and perpendicular polarizations, and isolate the effect of 2PG. Figure 5.15 shows ΔT both without (black) and with (red) the excitation, where the change in transmission is only present near zero delay and follows the same cross-correlation shape in both cases. These measurements may then be fit for the 2PA/G coefficient, which will be related to the parallel case by $\alpha_{2,\parallel}/2.4$. Without the excitation the measurement yields $\alpha_{2,\parallel} = 38 \pm 8$ cm/GW, which is in agreement with both theoretical [14] and measured [15] values and is significantly enhanced over the degenerate case of the same photon energy sum. With the excitation providing population inversion, we fit the data with $\gamma_{2,\parallel} = 12 \pm 5$ cm/GW.

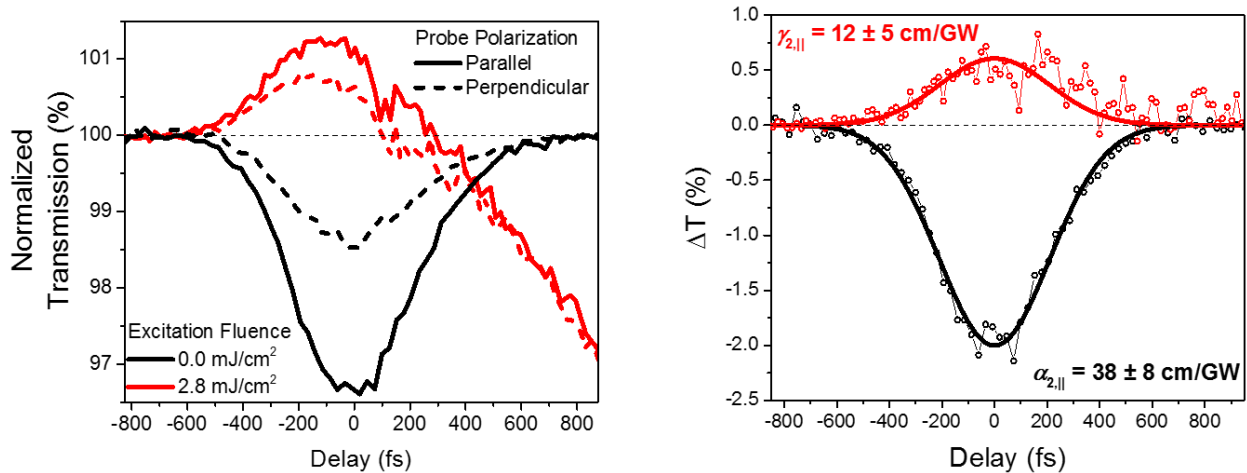


Figure 5.15 (left) Normalized probe transmission versus pump-probe delay for parallel (solid) and perpendicular (dashed) polarizations both with excitation fluence F_0 of zero (black) and 2.8 mJ/cm² (red). (right) Difference in normalized probe transmission ΔT for parallel and perpendicular polarizations versus pump-probe delay with (red) and without (black) excitation.

The conversion of absorption to gain depends on the population inversion. To demonstrate this, we repeat the experiment for several lower excitation fluences and plot ΔT at zero delay in Figure 5.16. Without the excitation, i.e., zero fluence, $\Delta T = -2$ %, corresponding to 2PA. As the

excitation fluence is increased, the carrier population near the band edge grows, causing a reduction in the 2PA, which eventually changes into 2PG above $\sim 1 \text{ mJ/cm}^2$. At higher fluences the 2PG saturates due to the saturation of absorption of the excitation. We only expect gain where population inversion is present near the band edge. To further verify the presence of 2PG, we increase the photon energy sum by changing the probe wavelength. At higher energy sums, ΔT with and without the excitation is the same, indicating the carrier density at these energies is insufficient to produce inversion. These observations provided evidence of 2PG in bulk GaAs, and constitutes the first report, to my knowledge, of nondegenerate two-photon gain in any medium.

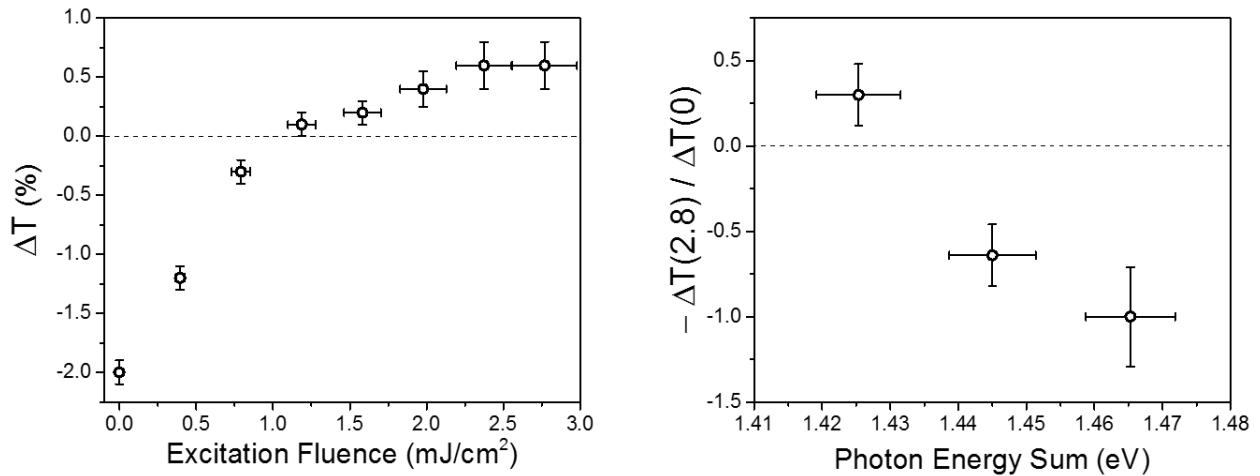


Figure 5.16 (left) Difference in normalized probe transmission ΔT for parallel and perpendicular polarizations versus excitation fluence at zero pump-probe delay. (right) Ratio of ΔT at $F_0 = 2.8 \text{ mJ/cm}^2$ to $F_0 = 0$ versus photon energy sum.

5.3. Competing Processes

Like many other proposed 2PG media, semiconductors suffer from a variety of effects that may limit their applicability for a 2PL. Here we discuss both those effects that directly impact the optical losses of the material, the dominant ones being linear absorption in the form on free-carrier

(phonon-assisted) and intervalence band (direct) absorption, as well as the next higher order absorption process, three-photon absorption (3PA) (see Figure 5.17). Free-carrier absorption occurs when an excited electron or hole absorbs a photon, but requires the simultaneous absorption or emission of a phonon to conserve momentum, and is therefore referred to as an indirect process. The direct band-to-band absorption processes, including both intervalence band and three-photon absorption, depend only on the band structure of the material, and the coupling of these states via the electric field. A detailed description of each of these mechanisms is provided in this section.

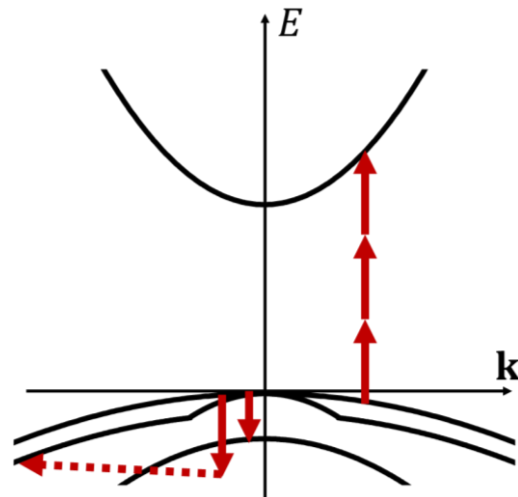


Figure 5.17 Energy band diagram including heavy-hole, light-hole, and split-off valence bands showing phonon assisted FCA, intervalence band absorption, and 3PA.

5.3.1. Kane's Band Structure

The absorption coefficient of a material may be derived from the electronic structure of the material via Fermi's Golden rule, which may be applied to one-, two-, and three-photon absorption as well [116, 169, 170, 176]. Evaluation of the coefficients requires knowledge of the electronic structure, as well as the coupling between states, meaning we need to know the energies and wave functions of the electronic states of the material. For direct-gap semiconductors we use Kane's

band structure [177, 178], which models the electronic states of the direct gap materials with four (each doubly spin degenerate) bands: a single conduction band, and three valence bands, heavy-hole, light-hole, and split-off bands.

Calculation of Kane's band structure begins with the Hamiltonian

$$\hat{H} = \frac{p^2}{2m_0} + V - \boldsymbol{\mu}_m \cdot \mathbf{B}, \quad (5.11)$$

where $p = -i\hbar\nabla$ is the momentum operator, V is the potential energy, $-e$ is the electron charge, $\boldsymbol{\mu}_m$ is the magnetic dipole moment of the electron (not to be confused with the electric dipole moment), and \mathbf{B} is the magnetic field. In addition to the standard kinetic and potential energy terms, the energy associated with the interaction of the magnetic dipole moment of the electron with the magnetic field is also included. In the laboratory (or lattice) frame, there is no magnetic field, however in the electron frame, which is in orbit about the nuclei, there is a magnetic field of the form [179]

$$\mathbf{B} = -\frac{\mathbf{v} \times \mathbf{E}}{c^2}, \quad (5.12)$$

where $\mathbf{v} = \mathbf{p}/m_0$ is the velocity of the electron, and $\mathbf{E} = \nabla V/e$ is the electric field produced by the nuclei. Additionally, the magnetic dipole moment of an electron is

$$\boldsymbol{\mu}_m = -\frac{e\hbar}{2m_0}\boldsymbol{\sigma}. \quad (5.13)$$

where $\boldsymbol{\sigma}$ the Pauli spin matrix. The electron wave functions in a periodic potential, such as a crystalline lattice may be expressed using the Bloch theorem

$$\psi_{n,\mathbf{k}} = \frac{1}{L^{3/2}} u_{n,\mathbf{k}}(\mathbf{r}) e^{i\mathbf{k}\cdot\mathbf{r}}, \quad (5.14)$$

where L^3 is the volume. Substituting Equations (5.11) - (5.14) into the time-independent Schrödinger equation (TISE) gives [177, 178]

$$\left(\frac{p^2}{2m_0} + \frac{\hbar}{m_0} \mathbf{k} \cdot \mathbf{p} + V + \frac{\hbar}{4m_0^2 c^2} [\nabla V \times (\mathbf{p} + \hbar \mathbf{k})] \cdot \boldsymbol{\sigma} \right) u_{n,\mathbf{k}}(\mathbf{r}) = E'_{n,\mathbf{k}} u_{n,\mathbf{k}}(\mathbf{r}) \quad (5.15)$$

where $E'_{n,\mathbf{k}} = E_{n,\mathbf{k}} - \hbar^2 k^2 / 2m_0$. The second term on the LHS is the $\mathbf{k} \cdot \mathbf{p}$ interaction, and the fourth (proportional to \mathbf{p}) is the k-independent (atomic like) spin-orbit interaction. The fifth term (proportional to $\hbar \mathbf{k}$) is a k-dependent spin-orbit interaction, which we may neglect because it is small compared to the fourth term, since $\hbar |\mathbf{k}| \ll |\mathbf{p}|$.

We now wish to find solutions to Equation (5.15) for both the energies $E'_{n,\mathbf{k}}$ and the associated Bloch wave functions $u_{n,\mathbf{k}}(\mathbf{r})$. Do to so, we assume a known solution to the TISE in the absence of the magnetic dipole interaction, of which the wave functions are

$$\begin{aligned} |iS \downarrow\rangle, & \quad \frac{1}{\sqrt{2}} |(X - iY) \uparrow\rangle, & |Z \downarrow\rangle, & \quad \frac{1}{\sqrt{2}} |(X + iY) \uparrow\rangle, \\ |iS \uparrow\rangle, & \quad \frac{-1}{\sqrt{2}} |(X + iY) \downarrow\rangle, & |Z \uparrow\rangle, & \quad \frac{1}{\sqrt{2}} |(X - iY) \downarrow\rangle, \end{aligned} \quad (5.16)$$

S denotes a wave function of spherical symmetry, much like the s orbital of hydrogen (spherical harmonic Y_0^0), corresponds to the conduction band with energy E_c , and X , Y , and Z denotes wave function which have symmetry of the p orbitals of hydrogen oriented in the x , y , and z directions (spherical harmonics Y_1^{-1} , Y_1^0 , and Y_1^1), respectively and correspond to the valence band with energy E_v . The up and down arrows indicate the electron spin, and the top four wave functions are degenerate with the bottom four, respectively. We can therefore write the Hamiltonian as a matrix with elements

$$\hat{H}_{mn} = \langle \psi_n | \hat{H} | \psi_m \rangle, \quad (5.17)$$

where the $|\psi_m\rangle$ are those of (5.16), and \hat{H} is the factor in parenthesis on the LHS of Equation (5.15). The Hamiltonian, choosing \mathbf{k} along the z-axis, is then

$$\begin{pmatrix} \hat{H} & 0 \\ 0 & \hat{H} \end{pmatrix}, \quad \text{where } \hat{H} = \begin{pmatrix} E_g & 0 & kP & 0 \\ 0 & -2\Delta/3 & \sqrt{2}\Delta/3 & 0 \\ kP & \sqrt{2}\Delta/3 & -\Delta/3 & 0 \\ 0 & 0 & 0 & 0 \end{pmatrix}, \quad (5.18)$$

where

$$P \equiv -i \frac{\hbar}{m_0} \langle S | p_z | Z \rangle, \quad (5.19)$$

is the Kane momentum parameter, and

$$\Delta \equiv i \frac{3\hbar}{4m_0^2 c^2} \left\langle X \left| \frac{\partial V}{\partial x} p_y - \frac{\partial V}{\partial y} p_x \right| Y \right\rangle, \quad (5.20)$$

is the split-off energy, and we have let $E_c = E_g$, and $E_v = -\Delta/3$. We may generalize to arbitrary

\mathbf{k} by the rotation transformations

$$\begin{pmatrix} X' \\ Y' \\ Z' \end{pmatrix} = \begin{pmatrix} \cos \theta \cos \phi & \cos \theta \sin \phi & -\sin \theta \\ -\sin \phi & \cos \phi & 0 \\ \sin \theta \cos \phi & \sin \theta \sin \phi & \cos \theta \end{pmatrix} \begin{pmatrix} X \\ Y \\ Z \end{pmatrix}, \quad (5.21)$$

and

$$\begin{pmatrix} \uparrow' \\ \downarrow' \end{pmatrix} = \begin{pmatrix} e^{-i\phi/2} \cos \theta/2 & e^{i\phi/2} \sin \theta/2 \\ -e^{-i\phi/2} \sin \theta/2 & e^{i\phi/2} \cos \theta/2 \end{pmatrix} \begin{pmatrix} \uparrow \\ \downarrow \end{pmatrix}, \quad (5.22)$$

and $S' = S$, since it is spherically symmetric, where θ and ϕ are the polar and azimuthal angles of spherical coordinates, respectively.

The energies of the bands may be found by solving the eigenvalue problem, which is equivalent to solving

$$|\hat{H} - E' \hat{I}| = 0, \quad (5.23)$$

where \hat{I} is the identity matrix. This gives

$$E' = 0, \quad (5.24)$$

$$E'^3 + a_2 E'^2 + a_1 E' + a_0 = 0, \quad (5.25)$$

where

$$a_0 = -k^2 P^2 \frac{2\Delta}{3}, \quad (5.26)$$

$$a_1 = -(E_g \Delta + k^2 P^2), \quad (5.27)$$

$$a_2 = \Delta - E_g, \quad (5.28)$$

Equation (5.24) gives the energy of the heavy-hole band, and the three solutions to Equation (5.25) correspond to the conduction, light-hole, and split-off bands. This may be solved using the trigonometric method by [180]

$$E' = 2\sqrt{Q} \cos\left(\frac{1}{3} \arccos\left(\frac{R}{\sqrt{Q^3}}\right) - m \frac{2\pi}{3}\right) - \frac{a_2}{3}, \quad (5.29)$$

where

$$R = \frac{1}{2} \frac{9a_1 a_2 - 27a_0 - 2a_2^3}{27}, \quad (5.30)$$

$$Q = \frac{a_2^2 - 3a_1}{9}. \quad (5.31)$$

The corresponding eigenstates are

$$\phi_{i\alpha} = a_i |iS \downarrow\rangle' + \frac{b_i}{\sqrt{2}} |(X - iY) \uparrow\rangle' + c_i |Z \downarrow\rangle', \quad (5.32)$$

$$\phi_{i\beta} = a_i |iS \uparrow\rangle' - \frac{b_i}{\sqrt{2}} |(X + iY) \downarrow\rangle' + c_i |Z \uparrow\rangle', \quad (5.33)$$

$$\phi_{hh\alpha} = \frac{1}{\sqrt{2}} |(X + iY) \uparrow\rangle', \quad (5.34)$$

$$\phi_{hh\alpha} = \frac{1}{\sqrt{2}} |(X - iY) \downarrow\rangle', \quad (5.35)$$

where the subscript i refers to the conduction (c), light-hole (lh), and split-off (so) bands, and α and β refer to the two spins. The a_i , b_i , and c_i are k -dependent coefficients, related to the energies by

$$a_i = \frac{kP \left(E_i' + \frac{2\Delta}{3} \right)}{N_i}, \quad (5.36)$$

$$b_i = \frac{\left(\frac{2\Delta}{3} \right) (E_i' - E_g)}{N_i}, \quad (5.37)$$

$$c_i = \frac{(E_i' - E_g) \left(E_i' + \frac{2\Delta}{3} \right)}{N_i}, \quad (5.38)$$

where $N_i = \sqrt{a_i^2 + b_i^2 + c_i^2}$ provides normalization.

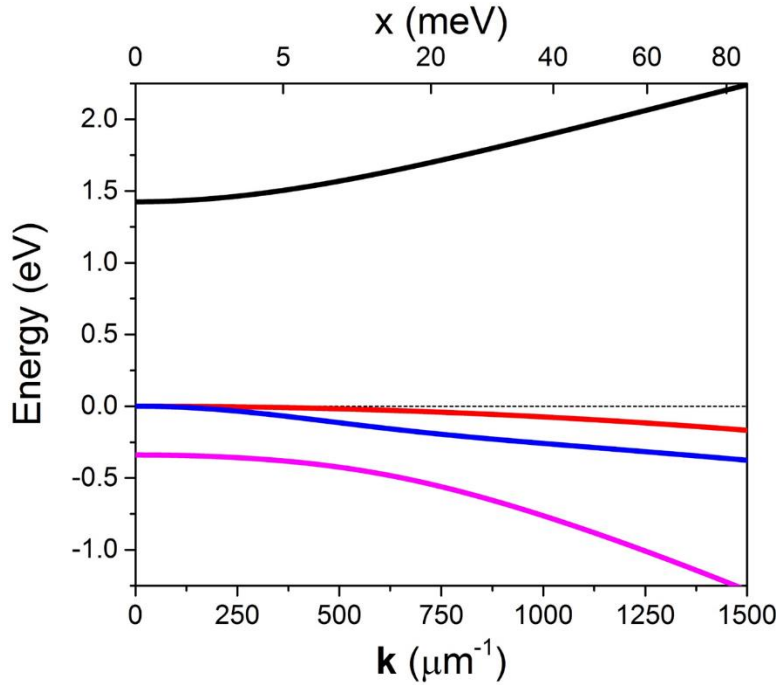


Figure 5.18 Kane's band structure of GaAs including (black) conduction, (red) heavy-hole, (blue) light-hole, and (magenta) split-off bands.

The band structure and wave functions depend only on three parameters, the band gap energy E_g , split-off energy Δ , and Kane energy parameter

$$E_p = \frac{2m_0P^2}{\hbar^2}. \quad (5.39)$$

The calculated band structure of GaAs, with $E_g = 1.424$ eV, $\Delta = 0.34$ eV, and $E_p = 28.9$ eV [181, 182], is shown in Figure 5.18. Since we now know both the energies and wave functions of the electronic eigenstates of any zinc blende direct gap semiconductor, we can calculate various band-to-band absorption coefficients.

5.3.2. Three-Photon Absorption

The 3PA coefficient of a material may be derived from the electronic structure of the material via Fermi's Golden rule, which for the nondegenerate 3PA where one photon at ω_a and two at ω_b are absorbed is

$$\begin{aligned} R_3 = \frac{2\pi}{V\hbar} \sum_{i,f} & \left| \sum_{j,l} \left[\frac{\langle \psi_f | \hat{H}_a | \psi_l \rangle \langle \psi_l | \hat{H}_b | \psi_j \rangle \langle \psi_j | \hat{H}_b | \psi_i \rangle}{(E_{li} - \hbar\omega_b - \hbar\omega_b)(E_{ji} - \hbar\omega_b)} \right. \right. \\ & + \frac{\langle \psi_f | \hat{H}_b | \psi_l \rangle \langle \psi_l | \hat{H}_a | \psi_j \rangle \langle \psi_j | \hat{H}_b | \psi_i \rangle}{(E_{li} - \hbar\omega_a - \hbar\omega_b)(E_{ji} - \hbar\omega_b)} \\ & \left. \left. + \frac{\langle \psi_f | \hat{H}_b | \psi_l \rangle \langle \psi_l | \hat{H}_b | \psi_j \rangle \langle \psi_j | \hat{H}_a | \psi_i \rangle}{(E_{li} - \hbar\omega_b - \hbar\omega_a)(E_{ji} - \hbar\omega_a)} \right] \right|^2 \delta(E_{fi} - \hbar\omega_a - 2\hbar\omega_b). \end{aligned} \quad (5.40)$$

where $|\psi_j\rangle$ are the electronic eigenstates of the material, R_3 is the three-photon transition rate per unit volume, which is expressed in terms of a summation over all possible initial and final states i and f that are separated in energy by $E_{fi} = \hbar\omega_a + 2\hbar\omega_b$, via all possible permutations of two

intermediate states j and l . For the absorption process, the final state is within the conduction band, the initial state is within one of the valence bands, either heavy-hole, light-hole, or split-off band, and the intermediate states may be any of these. There are many possible pathways included in Equation (5.40), some of which are illustrated in Figure 5.19 Some possible pathways for 3PA. Evaluation of Equation (5.40) requires knowledge of the electronic structure, that is the E_j , as well as the coupling between states, $\langle \psi_l | \hat{H}_a | \psi_j \rangle$.

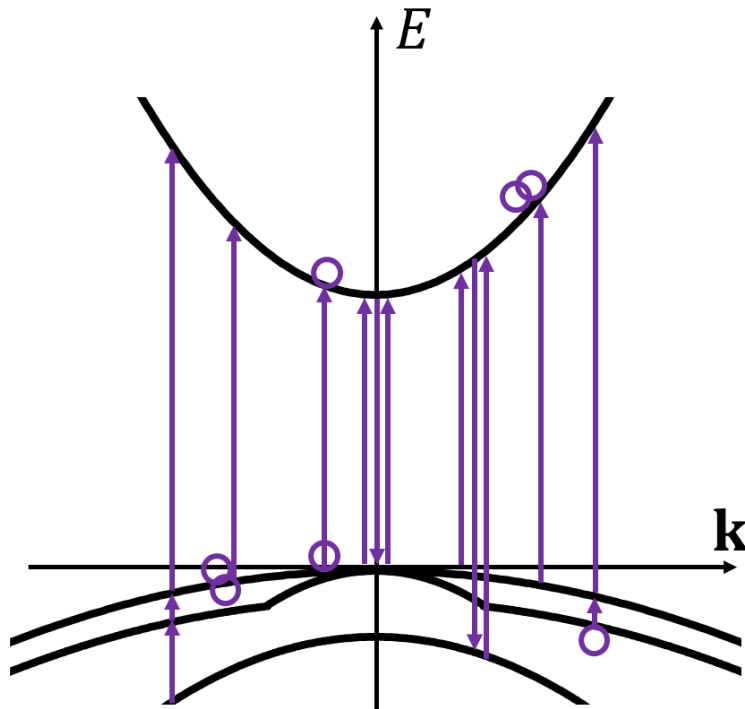


Figure 5.19 Some possible pathways for 3PA.

The interaction Hamiltonian is given by (neglecting the A^2 term) [116]

$$\hat{H}_a = -\frac{e}{m_0} \mathbf{A}_a \cdot \hat{\mathbf{p}}, \quad (5.41)$$

and likewise for \hat{H}_b . Since the vector potential is related to the irradiance by $\mathbf{A} = \frac{1}{2\omega} \sqrt{\frac{2I}{\epsilon_0 n_a c}}$, the matrix elements become

$$\langle \psi_l | \hat{H}_a | \psi_j \rangle = -\frac{e}{i2m_0\omega_a} \sqrt{\frac{2I_a}{\epsilon_0 n_a c}} \langle \psi_l | \hat{\mathbf{a}}_a \cdot \hat{\mathbf{p}} | \psi_j \rangle. \quad (5.42)$$

We now want to write the matrix element in terms of scaled momentum matrix elements

$$M_{lj}^{(a)} = \frac{\hbar}{m_0 P} \hat{\mathbf{a}}_a \cdot \langle \psi_l | \hat{\mathbf{p}} | \psi_j \rangle, \quad (5.43)$$

which may be evaluated using Kane's model (see § 5.3.1.). With these substitutions, Equation (5.42) becomes

$$\langle \psi_l | \hat{H}_a | \psi_j \rangle = -\frac{eP}{i2\hbar\omega_a} \sqrt{\frac{2I_a}{\epsilon_0 n_a c}} M_{fi}^{(a)}. \quad (5.44)$$

The ND-3PA coefficient α_3 is related to the three-photon transition rate by

$$\frac{\partial I_a}{\partial z} = -3\alpha_3(\omega_a; \omega_b, \omega_b) I_a I_b^2 = -\hbar\omega_a R_3, \quad (5.45)$$

where the factor of 3 serves the same purpose as the factor of 2 in Equation (2.15), and ensures the results of two-beam and single-beam experiments yield the same results (see APPENDIX D:).

Equations (5.40) - (5.45) may be combined to express the ND-3PA coefficient

$$\pi e^6 E_p^3 \quad (5.46)$$

$$\sum_{i,f} \left| \sum_{j,l} \left[\frac{M_{fl}^{(a)} M_{lj}^{(b)} M_{ji}^{(b)}}{(E_{li} - \hbar\omega_b - \hbar\omega_b)(E_{ji} - \hbar\omega_b)} \right. \right. \\ \left. \left. + \frac{M_{fl}^{(b)} M_{lj}^{(a)} M_{ji}^{(b)}}{(E_{li} - \hbar\omega_a - \hbar\omega_b)(E_{ji} - \hbar\omega_b)} \right. \right. \\ \left. \left. + \frac{M_{fl}^{(b)} M_{lj}^{(b)} M_{ji}^{(a)}}{(E_{li} - \hbar\omega_b - \hbar\omega_a)(E_{ji} - \hbar\omega_a)} \right] \right|^2 \delta(E_{fi} - \hbar\omega_a - 2\hbar\omega_b),$$

where we have substituted $P^2 = \hbar^2 E_p / 2m_0$ [170, 182].

Currently, the summations are over all possible states. In bulk semiconductors, these states are very closely spaced in energy (closer than their own linewidths) [116]. We may simplify the summation to be only over the relevant bands if we assume the bands to be continuous. This allows the summation over a given band to become an integral over the continuous distribution of states within that band. Taking the limit of the summation over states (in one dimension), as the length goes to infinity allows the summation over states to become an integral over states

$$\sum_{m_x=-\infty}^{\infty} f_{m_x} \Big|_{L_x \rightarrow \infty} = \int_{-\infty}^{\infty} f(m_x) dm_x. \quad (5.47)$$

Choosing to integrate in k-space, we have $k_x = 2\pi m_x / L_x$, or $m_x = k_x L_x / 2\pi$

$$\int_{-\infty}^{\infty} f(m_x) dm_x = \frac{L_x}{2\pi} \int_{-\infty}^{\infty} f(k_x) dk_x. \quad (5.48)$$

In three dimensions

$$\int_{-\infty}^{\infty} f(m_x, m_y, m_z) d^3 m = \frac{V}{(2\pi)^3} \int_{-\infty}^{\infty} f(\mathbf{k}) d^3 \mathbf{k}, \quad (5.49)$$

where we have used $L_x L_y L_z = V$. Thus, the absorption coefficient becomes an integral over the states within each band, and a summation over the bands, assuming the initial state is within one of the (spin-degenerate) valence bands (heavy-hole, light-hole, and split-off), and the final state is within the (spin-degenerate) conduction band. Since Kane's band structure assumes spherical symmetry (in k -space), meaning that the energy of each band to only depends on $|\mathbf{k}| = k$, it is convenient to integrate in spherical coordinates, where $d^3\mathbf{k} = k^2 \sin(\theta) dk d\theta d\phi$. With these substitutions into Equation (5.46) becomes

$$\alpha_3(\omega_a; \omega_b, \omega_b) = \frac{\pi e^6 E_p^3}{V 2^5 3 \epsilon_0^3 n_a n_b^2 c^3 \omega_a \omega_b^4 m_0^3} \cdot$$

$$\frac{V}{(2\pi)^3} \int \sum_{v,c} \left| \sum_{j,l=v,c} \left[\frac{M_{cl}^{(a)} M_{lj}^{(b)} M_{jv}^{(b)}}{(E_{lv}(k) - \hbar\omega_b - \hbar\omega_b)(E_{jv}(k) - \hbar\omega_b)} \right. \right.$$

$$+ \frac{M_{cl}^{(b)} M_{lj}^{(a)} M_{jv}^{(b)}}{(E_{lv}(k) - \hbar\omega_a - \hbar\omega_b)(E_{jv}(k) - \hbar\omega_b)}$$

$$\left. \left. + \frac{M_{cl}^{(b)} M_{lj}^{(b)} M_{jv}^{(a)}}{(E_{lv}(k) - \hbar\omega_b - \hbar\omega_a)(E_{jv}(k) - \hbar\omega_a)} \right] \right|^2$$

$$\cdot \delta(E_{cv}(k) - \hbar\omega_a - 2\hbar\omega_b) k^2 \sin(\theta) dk d\theta d\phi,$$
(5.50)

where the scaled momentum matrix elements, e.g., $M_{lj}^{(a)}$, depend on k , θ , and ϕ .

The delta function within the integral in Equation (5.50) can be simplified using the relation

$$\delta(f(x)) = \sum_i \frac{\delta(x - x_i)}{\left| \frac{\partial f(x)}{\partial x} \right|_{x=x_i}} \quad (5.51)$$

where x_i are the roots of $f(x)$. This allows us to rewrite

$$\delta(E_{cv}(k) - \hbar\omega_a - 2\hbar\omega_b) = \frac{\delta(k - k_r)}{\left| \frac{\partial E_{cv}(k)}{\partial k} \right|_{k=k_r}} \quad (5.52)$$

where k_r is the electron wavenumber of resonance that satisfies $E_{cv}(k_r) = \hbar\omega_a + 2\hbar\omega_b$. For calculation purposes it is convenient to make the substitution $x = \hbar^2 k^2 / 2m_0$, meaning $k^2 = 2m_0 x / \hbar^2$. Then

$$\frac{\partial}{\partial k} = \frac{\partial}{\partial x} \frac{\partial x}{\partial k} = \frac{\sqrt{2}\hbar\sqrt{x}}{\sqrt{m_0}} \frac{\partial}{\partial x}. \quad (5.53)$$

With this, Equation (5.50) becomes

$$\begin{aligned} \alpha_3(\omega_a; \omega_b, \omega_b) &= \frac{1}{3} \frac{e^6 E_p^3 \hbar^2}{2^7 \sqrt{2} \pi^2 \varepsilon_0^3 n_a n_b^2 c^3 m_0^{\frac{3}{2}}} \cdot \frac{1}{\hbar\omega_a} \frac{1}{(\hbar\omega_b)^4} \\ &\cdot \int \sum_{v,c} \left| \sum_{j,l=v,c} \left[\frac{M_{cl}^{(a)} M_{lj}^{(b)} M_{jv}^{(b)}}{(E_{lv}(x_r) - \hbar\omega_b - \hbar\omega_b)(E_{jv}(x_r) - \hbar\omega_b)} \right. \right. \\ &\quad + \frac{M_{cl}^{(b)} M_{lj}^{(a)} M_{jv}^{(b)}}{(E_{lv}(x_r) - \hbar\omega_a - \hbar\omega_b)(E_{jv}(x_r) - \hbar\omega_b)} \\ &\quad \left. \left. + \frac{M_{cl}^{(b)} M_{lj}^{(b)} M_{jv}^{(a)}}{(E_{lv}(x_r) - \hbar\omega_b - \hbar\omega_a)(E_{jv}(x_r) - \hbar\omega_a)} \right] \right|^2 \\ &\cdot \frac{\sqrt{x_r}}{\left| \frac{\partial E_{cv}(x)}{\partial x} \right|_{x=x_r}} \sin(\theta) d\theta d\phi. \end{aligned} \quad (5.54)$$

where the scaled momentum matrix elements, e.g., $M_{lj}^{(a)}$, depend on x_r , θ , and ϕ . Equation (5.54) may be evaluated for specific polarizations of the two input beams. For the case of parallel polarizations, we may take both to be in the z-direction [170], in which case the M 's are independent

of ϕ , and integration over ϕ simply gives a factor of 2π . In the case of arbitrary linear polarizations, we can choose the pump (at ω_b) to be polarized in the z-direction, and then find the matrix elements that corresponding probe polarization.

Table 5.1 Parameters for zinc blende semiconductors

Semiconductor	E_g (eV)	Δ (eV)	E_p (eV)	Reference
GaAs	1.424	0.34	28.9	[175, 182]
ZnSe	2.7	0.37	24.2	[170]
GaN	3.2	0.017	25.0	[175]
ZnS	3.7	0.07	20.4	[170]

A MATLAB script was written to evaluate the ND-3PA coefficient using Equation (5.54) in terms of only four input parameters, E_g , Δ , E_p , and the refractive indices, which allows for rapid calculation for several semiconductors. Table 5.1 shows these parameters for a few zinc blende semiconductors. Figure 5.20 shows the calculated D-3PA spectrum of GaAs, including the contributions from when each of the three valence bands as the initial state. The oscillatory behavior, observed particularly when the initial band is the light-hole band, is due to quantum interference between the many pathways (see Figure 5.19).

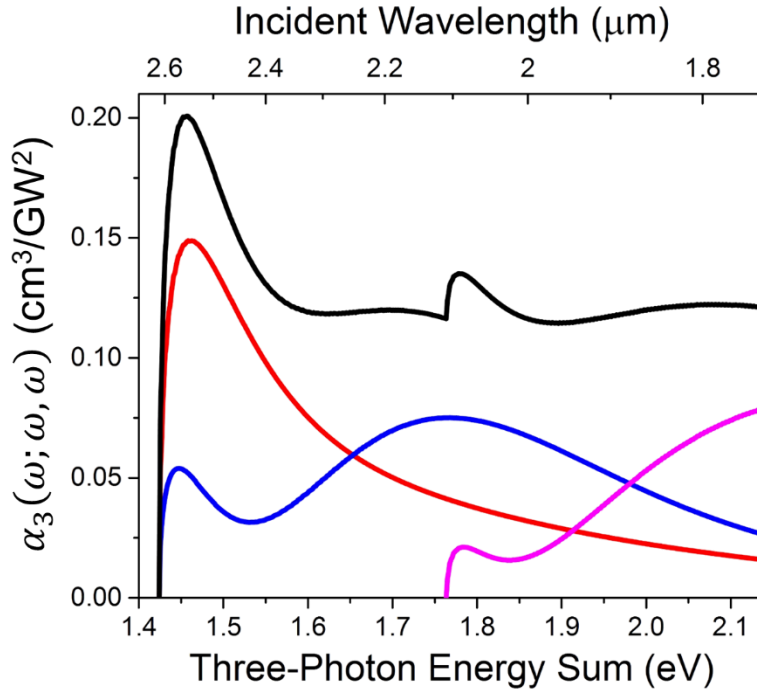


Figure 5.20 Calculated D-3PA spectrum of GaAs including individual contributions from each initial band (red) heavy-hole, (blue) light-hole, (magenta) split-off, and (black) total.

Previously, Claudiu Cirloganu [169, 171], Peter Olszak [183], and Davorin Peceli [172] performed Z-scan measurements on GaAs, ZnSe and ZnS samples to determine the D-3PA coefficients to compare them to the theoretical model employed here. The analysis was similar to that of the standard OA Z-scan for 2PA [47], but the equation governing the evolution of the irradiance was

$$\frac{\partial I}{\partial z} = -\alpha_3(\omega; \omega, \omega)I^3. \quad (5.55)$$

Figure 5.21 shows a comparison of the results of these Z-scan measurements performed using both the femtosecond Clark-MXR system, in closed circles, as well as the picosecond EKSPLA system, in open circles. The picosecond system was used for GaAs measurements since the large bandwidth of the femtosecond system prevented high spectral resolution measurements, making the measurements near the band edge unreliable. In each plot, the solid curve shows the theory as

calculated via Equation (5.54) in the case when $\omega_b = \omega_a$ using the parameters in Table 5.1. The dashed curves are a scaling of the calculating by a factor of 4.5 for GaAs, 2 for ZnSe, and 2.5 for ZnS.

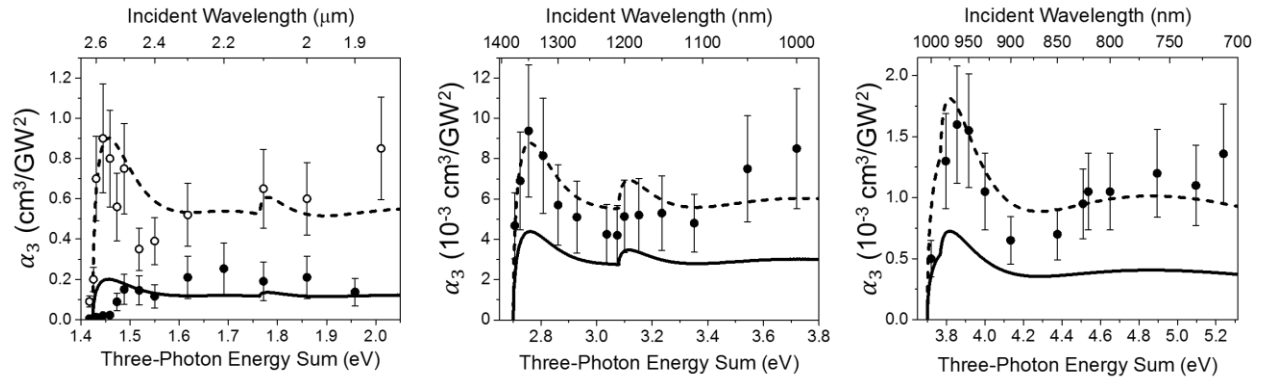


Figure 5.21 (circles) Z-scan measurements, (black curves) theory, as well as (red curve) scaled theory of D-3PA spectrum of (left) GaAs, (middle) ZnSe, and (right) ZnS, with scaling factors 4.5, 2, and 2.5, respectively.

The ND-3PA spectrum was also calculated for GaAs, as shown in Figure 5.22, plotted on a logarithmic scale versus three-photon energy sum and the nondegeneracy, which is the ratio of the photon energies $\hbar\omega_a/\hbar\omega_b$. Plotting in this way readily allows observation of the effects of nondegeneracy at the same photon energy sum. The peaks in the spectrum are due to resonance between valence bands. For example, the peak at a nondegeneracy of about 3 for three-photon energy sums greater than 1.8 correspond to intermediate state resonance between the split-off and heavy-hole bands. This region of the spectrum, however, is where 2PA occurs, since here $\hbar\omega_a + \hbar\omega_b > E_g$, as indicated by the shaded white region in the right plot of Figure 5.22

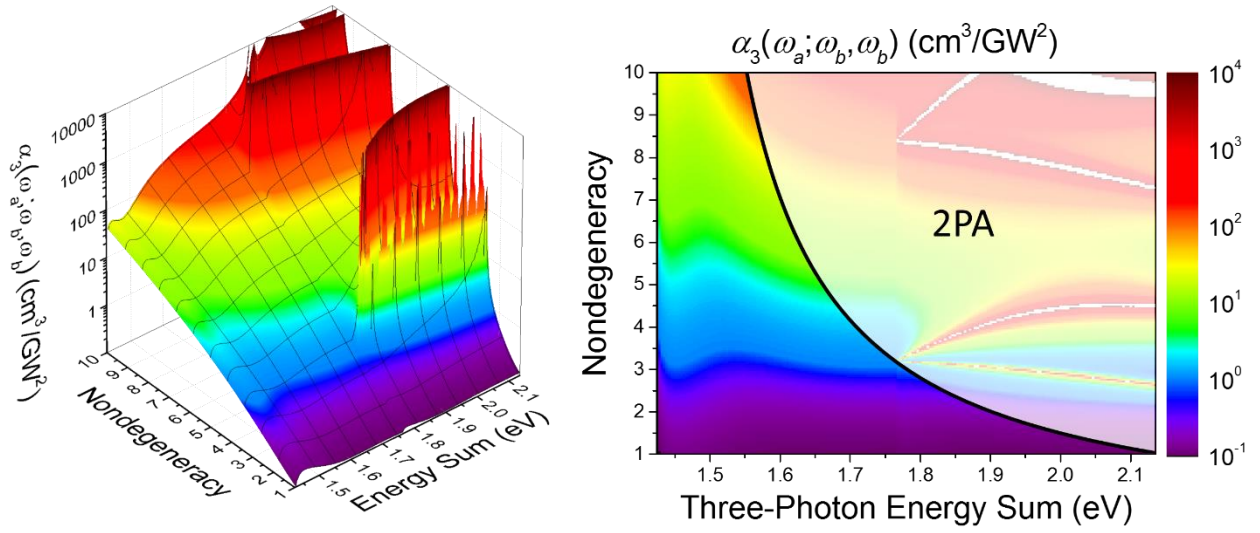


Figure 5.22 (left) 3D plot and (right) 2D projection of the ND-3PA spectrum of GaAs plotted versus three-photon energy sum and nondegeneracy factor. The white-shaded region in the left plot is where 2PA is possible.

We can clearly see that the lowest value of α_3 is at the degenerate case, when $\hbar\omega_a/\hbar\omega_b = 1$. As the nondegeneracy is increased, i.e., as $\hbar\omega_b$ decreases while $\hbar\omega_a$ increases such that the sum $\hbar\omega_a + 2\hbar\omega_b$ remains constant, $\alpha_3(\omega_a; \omega_b, \omega_b)$ increases drastically. Pathways involving two intraband (self) transitions, which have a zero frequency resonance, are greatly enhanced. In fact, this enhancement is even greater than that observed in 2PA. For example, the term in Equation (5.54) containing a denominator $(E_{lv} - \hbar\omega_b - \hbar\omega_b)(E_{jv} - \hbar\omega_b)$ is most greatly enhanced for nondegenerate photon pairs. When $l = j = v = lh\alpha$, for example, $E_{lv} = E_{jv} = 0$, and the denominator simplifies to $-2(\hbar\omega_b)^2$. This term therefore grows much faster than the equivalent term in the 2PA case, which goes as $-\hbar\omega_b$. The addition of a third-photon yields another intermediate state that may be near resonance and give additional enhancement. A direct comparison of this enhancement between the two- and three-photon absorption cases is shown in Figure 5.23. The equivalent ND-2PA calculation based on Kane's band structure was used [170]. Nondegenerate

α_2 and α_3 were calculated for GaAs, for fixed photon energy sums of 1.44 eV and 1.6 eV, respectively. The coefficients were then normalized to their values in the degenerate case. For a nondegeneracy of 10, α_2 is enhanced by a factor of 134, while α_3 is enhanced by a factor of 2410.

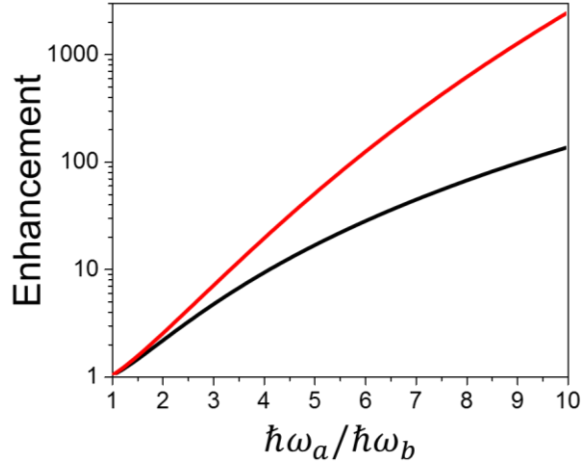


Figure 5.23 Enhancement of (black) 2PA (at $\hbar\omega_a + \hbar\omega_b = 1.44$ eV) and (red) 3PA (at $\hbar\omega_a + 2\hbar\omega_b = 1.6$ eV) versus photon energy ratio.

The same pump-probe experiment (without the excitation) used to measure END-2PG (see § 5.2.2.) was used to measure the END-2PA coefficient of GaAs, in the same 4 μm thick sample. The probe wavelength was increased slightly such that $\hbar\omega_a + \hbar\omega_b < E_g$ to prevent ND-2PA. Figure 5.24 shows the normalized transmission change as a function of delay with respect to the 7.75 μm pump for both probe wavelengths of 1020 nm and 1040 nm. Fits were done using

$$\frac{\partial I_a}{\partial z} = -3\alpha_3(\omega_a; \omega_b, \omega_b)I_a I_b^2, \quad (5.56)$$

and assumed that the pump was undepleted. Also shown is the 3PA spectrum for GaAs for two cases. In black is the D-3PA coefficient together with Z-scan measurements (see Figure 5.21), and in red is the ND-3PA coefficient for a fixed pump frequency, corresponding 7.75 μm . The solid curves are calculated from theory, and the dotted lines are the theory scaled by a factor of 2.5. This

experimentally shows that the Kane's band structure calculations correctly predict enhancement of the ND-3PA coefficient over the degenerate case. This constitutes, to my knowledge, both the first theoretical investigation and the first experimental measurement of nondegenerate three-photon absorption in solid state media. The observed increase in α_3 with nondegeneracy implies 3PA will be a major competing process for a 2PSL, and will limit the maximum irradiance possible.

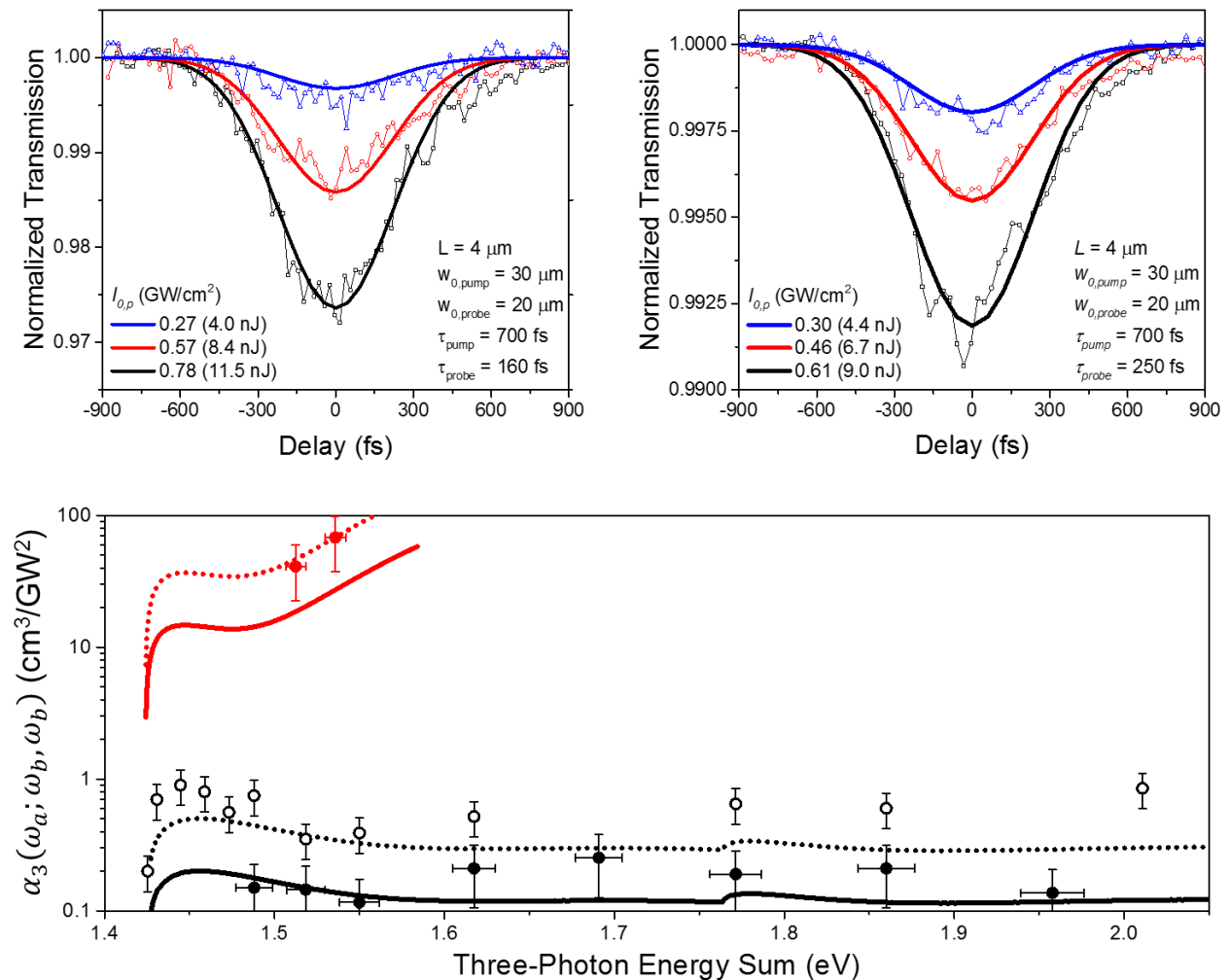


Figure 5.24 (top) Pump-probe measurements of $\alpha_3(\omega_a; \omega_b, \omega_b)$ in GaAs. (black) D- and (red) END-3PA coefficient where $\lambda_b = 7.75 \mu\text{m}$. (bottom) Comparison of (circles) measurement results to both (solid curves) theory and (dashed curves) theory $\times 2.5$.

5.3.3. Intervalence Band Absorption

While 3PA will dominate 2PG in the high irradiance limit, on the low irradiance limit, linear losses dominate. The primary linear loss is due to intervalence band absorption, which becomes especially large for longer wavelengths, when the photon energy becomes resonant with the energy difference between the bands where the greatest carrier concentration is located. Unlike in the case of 3PA, intervalence band absorption will not be present at thermal equilibrium, where there is not a significant population of holes in the valence bands. Upon excitation, however, the holes will predominantly occupy the top of the heavy-hole band, from which they may absorb a photon and be promoted to the light-hole or split-off bands. The intervalence band absorption coefficient depends on the occupation probabilities of the two bands involved. For example, the absorption coefficient for the absorption between the split-off and heavy-hole bands is given by

$$\alpha_{sohh}(\omega) = \alpha_{sohh,0}(\omega) \left(f_{hh}(E_{hh}(k_r)) - f_{so}(E_{so}(k_r)) \right), \quad (5.57)$$

where $\alpha_{sohh,0}(\omega)$ is the absorption coefficient assuming the initial state is occupied and the final state is empty, f_{hh} and f_{so} are the Fermi-Dirac distribution of carriers in the heavy-hole and split-off bands, respectively, and k_r is the electron wavenumber at resonance when $E_{hh}(k_r) - E_{so}(k_r) = \hbar\omega$. The same holds true for the other absorption processes, i.e., heavy-hole to light-hole and light-hole to split off. Figure 5.25 shows the calculated energy difference between valence bands versus both electron wavenumber (see Figure 5.18). The heavy-hole to light-hole has a small energy difference close to $k = 0$, and increases and becomes constant at large k , which gives rise to a large density of states at about 0.2 eV. Transitions from the light-hole to split-off band begins at $\Delta = 0.34$ eV, and decreases to 0.31 eV at $k = 500 \mu\text{m}^{-1}$ due to the smaller effective mass of the light-hole band near $k = 0$.

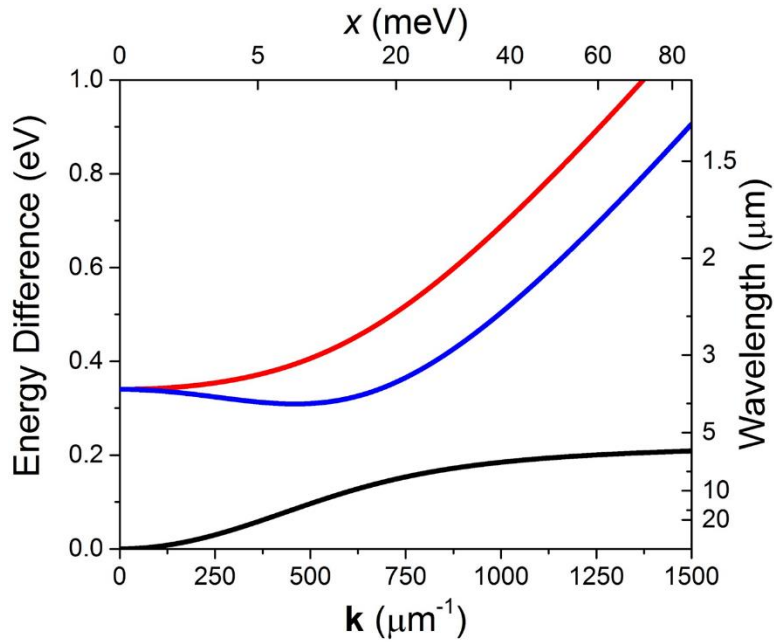


Figure 5.25 Energy difference for (black) heavy-hole to light-hole, (red) heavy-hole to split-off, and (blue) light-hole to split-off intervalence band absorption.

These coefficients may be calculated using the same approach we used for calculating α_3 , only must simpler. Since it is only a one-photon absorption process, we can start with the familiar Fermi's Golden Rule for one-photon absorption

$$R_1 = \frac{1}{V} \frac{2\pi}{\hbar} \sum_{i,f} |\langle \psi_f | \hat{H} | \psi_i \rangle|^2 \delta(E_{fi} - \hbar\omega), \quad (5.58)$$

where we are interested in the initial states of the holes being either within the heavy-hole or light-hole band, and the final states being either in the light-hole or split-off band. We then follow the same analysis presented in § 5.3.2. , using

$$\frac{\partial I}{\partial z} = -\alpha_{sohh,0}(\omega)I = -\hbar\omega R_{1,sohh}, \quad (5.59)$$

and arrive with an expression for the intervalence absorption coefficient

$$\alpha_{sohh,0}(\omega) = \frac{e^2 E_p \sqrt{m_0}}{4\sqrt{2}\pi\epsilon_0 n_0 c \hbar^2} \left(\frac{1}{\hbar\omega} \right) \cdot \int \sum_{\alpha,\beta} |M_{sohh}(x_r, \theta)|^2 \frac{\sqrt{x_r}}{\left| \frac{\partial}{\partial x} E_{sohh}(x) \right|_{x=x_r}} \sin(\theta) d\theta, \quad (5.60)$$

and likewise for the other terms, where we have chosen the polarization to be along the z-axis of the crystal. We can now apply Kane's band structure and calculate the various intervalence band absorption processes via Equation (5.60). Figure 5.26 shows the calculations of $\alpha_0(\omega)$ for each intervalence absorption.

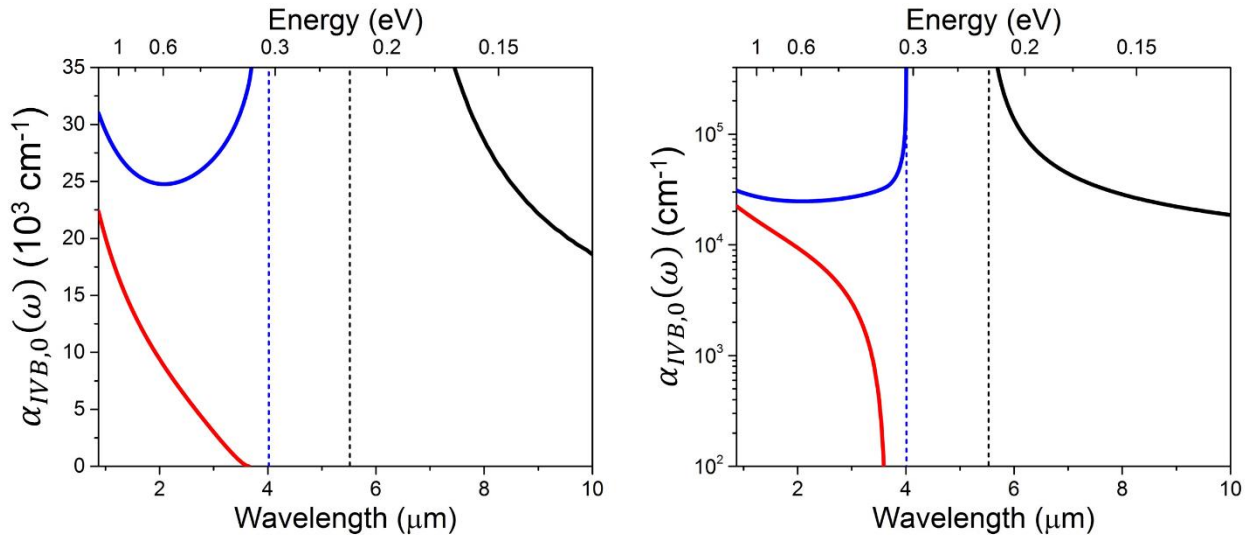


Figure 5.26 Intervalence band absorption coefficients (neglecting carrier distributions) on (left) linear and (right) logarithmic scales, for (red) heavy-hole to split-off, (blue) light-hole to split-off, and (black) heavy-hole to light-hole transitions. Vertical dashed lines indicate cut off wavelengths.

We can take into account carrier distributions with Equation (5.57), and assume the three bands are described by a single Fermi distribution. The quasi-Fermi level for the valence bands were calculated using the Unger approximation relating the hole number density N_h to the quasi-

Fermi energy E_{Fv} [184, 185]. Figure 5.27 shows the calculated intervalence band absorption coefficient in GaAs with a carrier concentration of $2 \times 10^{18} \text{ cm}^{-3}$, at a temperature of 300 K, include the heavy-hole to split-off band in red, light-hole to split-off band in blue, and heavy-hole to light-hole band in black. Since the excited holes are located near the band edge about $k = 0$, only photons of energies that interact with these regions of the bands experience significant absorption. For this reason, even though the joint density of states for heavy-hole to light-hole transitions is very large at 0.21 eV (5.9 μm), the absorption coefficient is quite small since these regions of the bands are far from $k = 0$ where no holes present.

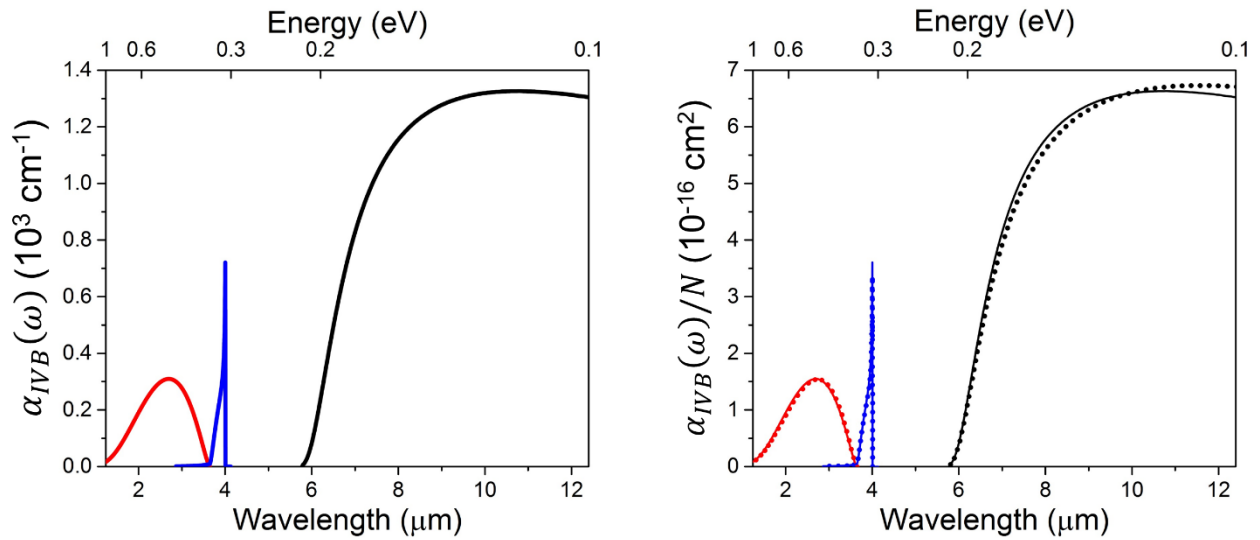


Figure 5.27 Calculated intervalence band (left) absorption coefficient and (right) coefficient divided by hole number density for (solid) $2 \times 10^{18} \text{ cm}^{-3}$ and (dotted) 10^{15} cm^{-3} at 300 K for (red) heavy-hole to split-off, (blue) light-hole to split-off, and (black) heavy-hole to light-hole transitions.

For energies several $k_B T$ less than Fermi energy, the Fermi distributions may be approximated by

$$f(E) = \frac{1}{1 + \exp\left(\frac{E - E_F}{k_B T}\right)} \approx 1 - \exp\left(\frac{E - E_F}{k_B T}\right). \quad (5.61)$$

In this case Equation (5.57) may be simplified, since the split-off band is not occupied by holes,

$$\alpha_{sohh}(\omega) = \alpha_{sohh,0}(\omega) \exp\left(\frac{E - E_{F_v}}{k_B T}\right). \quad (5.62)$$

For small carrier densities, the hole concentration may be approximated by a Boltzmann distribution [186] which allows the quasi-Fermi level to be expressed as

$$E_{F_v} = -k_B T \ln\left(\sqrt{2} \left(\frac{\pi \hbar^2}{m_v^* k_B T}\right)^{3/2} N_h\right), \quad (5.63)$$

where m_v^* is the effective mass of the density of states for the valence bands. In this case, the absorption coefficient is proportional to the number density and may be expressed in terms a cross section $\alpha_{IVB} = \sigma_{IVB} N_h$, where

$$\sigma_{sohh}(\omega) = \alpha_{sohh,0}(\omega) \left[\sqrt{2} \left(\frac{\pi \hbar^2}{m_v^* k_B T}\right)^{\frac{3}{2}} e^{\frac{E}{k_B T}} \right]. \quad (5.64)$$

The right plot in Figure 5.27 shows the calculated intervalence band absorption coefficient divided by the hole number density (i.e., the absorption cross section) for both (solid) $2 \times 10^{18} \text{ cm}^{-3}$ and (dashed) 10^{15} cm^{-3} . The cross sections in Figure 5.27 agree fairly well with calculations of Krishnamurthy et al. [167], but neglect line broadening. We can see that even for large carrier densities, the variation in α_{IVB}/N_h between low and high carrier concentration is relatively small. Because m_v^* is large ($0.53m_0$ in GaAs) [175], the quasi-Fermi energy $E_{F_v} \approx 39 \text{ meV}$, which is still greater than the top of the valence band edge. This means approximating of the Fermi distribution as a Boltzmann function is still fairly valid.

This cross section is of course temperature dependent, since the distribution of the carriers in the bands depend on their temperature. Carrier heating therefore affects the losses in the system, and impacts the performance of a potential 2PL. To demonstrate the temperature dependence of

this loss mechanism, we calculate the absorption coefficients for various carrier temperatures (assuming constant lattice temperature of 300 K). Increasing the carrier temperature reduces the loss at long wavelengths, while increasing it at short wavelengths. This is consistent with the observations in Figure 5.15, where the 7.75 μm pump was absorbed both via intervalence band and free-carrier absorption, resulting in an increase in the carrier temperature. This in turn raised the heavy-hole to split-off band absorption coefficient, yielding the reduced transmission at 977 nm observed at positive delays in Figure 5.15.

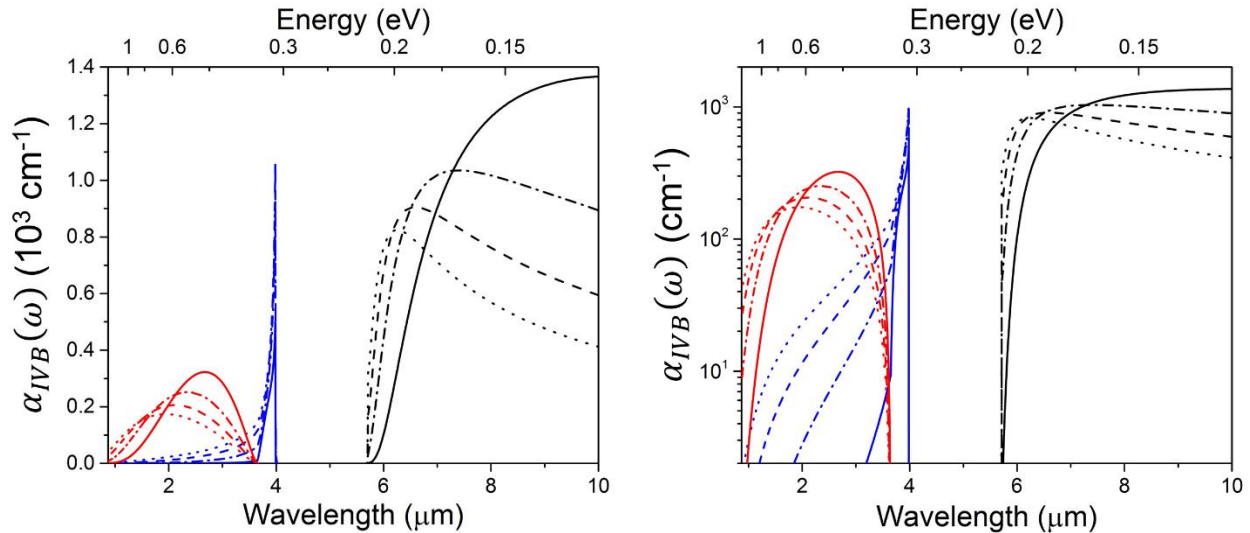


Figure 5.28 Temperature dependence of intervalence band absorption on (left) linear and (right) logarithmic scales. Carrier temperatures of (solid) 300 K, (dash-dot) 500 K, (dash) 700 K, and (dot) 900 K are shown for (red) heavy-hole to split-off, (blue) light-hole to split-off, and (black) heavy-hole to light-hole transitions.

5.3.4. Free-carrier Absorption

In addition to direct band-to-band absorption, indirect absorption is also possible. Excited carriers act as though they were free (albeit with reduced masses based on the band structure), and form a sort of electron (or hole) plasma. The classical Drude model can be used to calculate the

susceptibility of such a system, which is treated as a classical oscillator with a zero frequency resonance. The equation of motion in the frequency domain may be written as

$$(m^*\omega^2 + i\Gamma m^*\omega) \cdot \mathbf{r}(\omega) = e\mathbf{E}(\omega), \quad (5.65)$$

where m^* is the effective carrier mass, Γ is the damping rate, $\mathbf{r}(\omega)$ is the displacement vector, and e is the elementary charge. The linear susceptibility $\chi^{(1)}(\omega)$ of is related to the displacement by $-e\mathbf{r}(\omega) = \varepsilon_0\chi^{(1)}(\omega) \cdot \mathbf{E}(\omega)$, which becomes

$$\chi^{(1)}(\omega) = -\frac{Ne^2}{\varepsilon_0 m} \frac{1}{\omega^2 + i\Gamma\omega} = -\frac{\omega_p^2}{\omega^2 + \Gamma^2} + i\frac{\Gamma}{\omega} \frac{\omega_p^2}{\omega^2 + \Gamma^2} \quad (5.66)$$

where $\omega_p^2 = Ne^2/\varepsilon_0 m$ is the plasma frequency, N is the carrier concentration. The absorption coefficient is related to the imaginary part of the susceptibility by $\alpha(\omega) = \text{Im}\{\chi^{(1)}\}\omega/nc$, which becomes

$$\alpha_{FCA}(\omega) = \frac{\Gamma}{n(\omega)c} \frac{\omega_p^2}{\omega^2 + \Gamma^2} \quad (5.67)$$

Thus, for high frequencies, i.e., $\omega \gg \Gamma$, we thus get $\alpha_{FCA}(\omega) \propto 1/\omega^2 \propto \lambda^2$, yielding a simple relation for the spectral behavior of FCA.

Unfortunately, excited carriers in semiconductors do not behave precisely as the Drude model would predict. There is indeed a trend of increasing FCA with wavelength, but the details differ significantly. If a photon is not resonant with the energy difference between bands, it may be assisted by a phonon, a quasiparticle of vibrational energy of the crystal lattice. Phonons possess much more momentum than photons, but much less energy, and can aid in the absorption process by providing extra momentum to an electron (or hole) to excite it to a higher energy within the same band with a larger momentum (see Figure 5.17). The same process can also happen to holes in the valence band. Fan et al. [187], using second-order perturbation theory (as with 2PA above),

calculated $\alpha_{FCA}(\omega) \propto \lambda^{1.5}$. This process of FCA is still found to be proportional to the carrier concentration, and thus a cross section description is valid, where $\alpha_{FCA} = \sigma_{FCA}N$. In GaAs, phonon assisted FCA of electrons in the Γ -valley have values of σ_{FCA} at $\lambda = 2 \mu\text{m}$ of $\sim 4 \times 10^{-18} \text{ cm}^2$ [188]. These cross sections are typically smaller than the effects of direct intervalence band absorption, but can become problematic for a ND-2PSL as the cross section grows for longer wavelengths.

5.4. Prospect of a Semiconductor Two-Photon Laser

As we have found, there are many competing processes that greatly complicate the investigation of two-photon gain in bulk GaAs. The long-term goal and original motivation for this work was to demonstrate a two-photon semiconductor laser. In light of these complications, however, this may be more difficult than originally presumed. Indeed, in none of the above experiments was net 2PG (gain > losses) observed. In this chapter, we step back and look at the prospect of using bulk GaAs for a 2PL in various regimes.

5.4.1. Degenerate Two-Photon Laser

We start in the degenerate case, with two photons of equal energy, and include the dominant loss terms of linear (both intervalence band and free-carrier) absorption and 3PA, in the SVEA equation for the evolution of the irradiance

$$\frac{\partial I}{\partial z} = (-\alpha_1 + \gamma_2 I - \alpha_3 I^2)I. \quad (5.68)$$

The operating principle of any laser action is that the gain must exceed the losses. In this case that means, that the D-2PG term, $\gamma_2 I^2$, must be greater than the sum of the linear and 3PA losses (assuming other losses are negligible).

In the low irradiance limit, such that 3PA may be neglected (i.e., $\gamma_2 I \gg \alpha_3 I^2$), the dominant loss mechanism is linear absorption. Given the linear nature, and the nonlinear nature of 2PG, we may overcome this loss mechanism with sufficiently high irradiance. The condition for the minimum irradiance for laser action is

$$I > \frac{\alpha_1}{\gamma_2}. \quad (5.69)$$

Likewise, in the high irradiance limit, such that linear losses may be neglected (i.e., $\gamma_2 I^2 \gg \alpha_1 I$), the dominant loss mechanism is 3PA. Since this loss mechanism has a higher order irradiance dependence than the gain, for sufficiently high irradiances, 3PA will always win out over 2PG. Thus, 3PA sets a condition for the maximum irradiance limit for laser action, namely

$$I < \frac{\gamma_2}{\alpha_3}. \quad (5.70)$$

In the case where neither limit is applicable, the conditions are

$$\frac{\gamma_2 - \sqrt{\gamma_2^2 - 4\alpha_{FCA}\alpha_3}}{2\alpha_3} < I < \frac{\gamma_2 + \sqrt{\gamma_2^2 - 4\alpha_{FCA}\alpha_3}}{2\alpha_3}, \quad (5.71)$$

which are more restrictive than Equations (5.69) and (5.70).

The two different loss mechanisms give an operation range for the irradiance which may be calculate based on the relevant values of α_1 , γ_2 , and α_3 . We can estimate these numbers from calculations and previous measurements either presented here or available in the literature. In the following we intentionally choose conservative estimates of the uncertainty in these values. In GaAs, at 0.73 eV (1700 nm), based on previous 2PA measurements, $\alpha_2 = 3 \pm 1$ cm/GW [15],

which we will assume to be the maximum value that γ_2 may take for the degenerate case. This is an idealization, since there won't be perfect population inversion at finite temperature. In reality, γ_2 should be calculated at a specific carrier density and temperature to include the proper Fermi-Dirac distributions of carriers. Here, however, we choose a best case scenario to determine if under ideal conditions a 2PSL is possible.

The linear absorption depends on the carrier concentration and, for high carrier concentrations N , α_{FCA} also becomes nonlinear in the N [188], particularly with regard to the direct transitions, e.g. heavy-hole to split-off band, which depend on the occupation of the initial and final states. However, given the complexity of these relationships, we approximate α_{FCA} to be linear in N such that we may use cross sections. This approximation has been validated by the calculations in § 5.3.3. where we showed that, for the carrier concentrations used, the α_{IVB}/N depends little on N (see Figure 5.27). Based on the above calculations as well as measurements by Peceli [172, 189] and theory by Krishnamurthy et al. [167], $\sigma_1 = (1.0 \pm 0.5) \times 10^{-16} \text{ cm}^2$. For a carrier concentration of $N = 2 \times 10^{18} \text{ cm}^{-3}$, $\alpha_1 = (200 \pm 100) \text{ cm}^{-1}$. Equation (5.69) give a minimum necessary irradiance for 2PG to overcome the linear losses of $I > 70 \pm 40 \text{ GW/cm}^2$.

The 3PA coefficient α_3 has been measured via Z-scan by both Cirloganu [171] and Peceli [172, 189]. Extrapolating from their plots (Figure 6.8 (c) from Cirloganu [171], and Figure 1 (a) from Peceli et al. [189]), α_3 is between 0.1 and 1.0 cm^3/GW^2 , which is comparable with the calculation presented in § 5.3.2. (see Figure 5.21). Thus, by Equation (5.70), the maximum value of I is between 1.0 and 30 GW/cm^2 . However, this entire range is less than the minimum threshold determined from the linear losses, even given the large uncertainty, which means that there is no irradiance where the gain exceeds the losses, and thus two-photon laser action will not occur in the degenerate case. Another way to see this is by inspecting the term within the square root of

Equation (5.71), $\gamma_2^2 - 4\alpha_{FCA}\alpha_3$. This term must be positive to yield an irradiance window where lasing may occur; thus, we require $\gamma_2 > \sqrt{4\alpha_{FCA}\alpha_3}$. However, given the above values, $\sqrt{4\alpha_{FCA}\alpha_3}$ lies between 6.7 and 35 cm/GW, which exceeds the actual value (assuming complete population inversion, i.e., $f_c - f_v = 1$) of $\gamma_2 = 3 \pm 1$ cm/GW. Thus, the losses are always larger than the gain. Figure 4.1 shows term in parenthesis in the right-hand-side of Equation (5.68), that is, the net gain, as a function of irradiance. The black curve shows the average value, and the grey shaded regions represented the errors in the material parameters. For no value of the irradiance is the two-photon gain ever able to yield net gain.

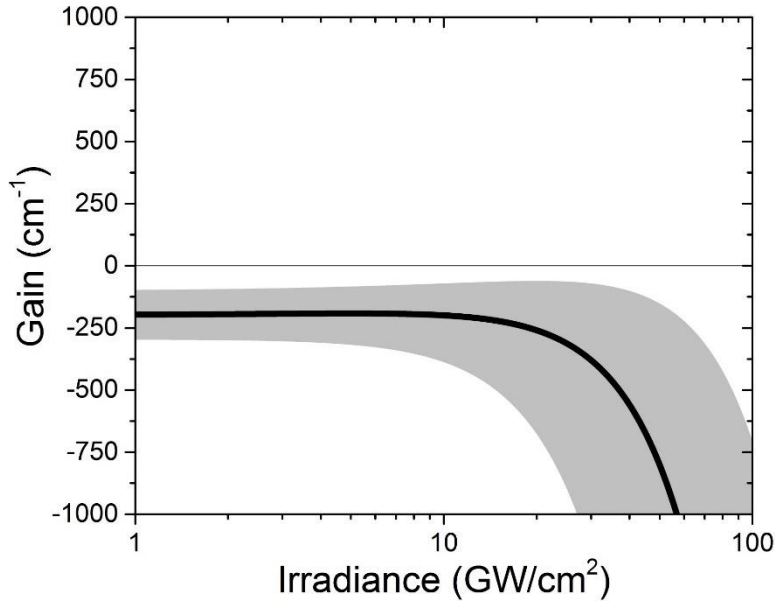


Figure 5.29 Plot of the RHS of Equation (5.68) divided by I (i.e., the net gain) versus irradiance. The shaded region represents the error based on literature values quoted in the text.

We may ask if we can decrease the wavelength (increase the photon energy) to interact with regions of the bands with higher densities of states such that γ_2 increases enough to overcome this problem. In practice we are limited to the region near the band-edge in which we can generate

population inversion. Hence, to increase the wavelength, and thus γ_2 , we must also increase the carrier concentration in order to maintain population inversion. Doing so increases the FCA coefficient α_{FCA} . For example, say we wanted to double the excess photon energy above the band-edge $\Delta E = \hbar\omega - E_g$ from 39 meV (1700 nm) to 78 meV (1656 nm). The 2PG coefficient could then be increased from 3 ± 1 cm/GW to 6 ± 1 cm/GW, a factor for 2. But the number of carriers required to maintain population inversion increases drastically. To achieve the same population inversion, the carrier density has to be increased by a factor of $(\Delta E)^{3/2}$ [190]. In this case, to double the excess energy requires $2\sqrt{2} \approx 2.83$ times the carrier concentration. This means that there will also be about 2.83 times the amount of FCA as well, from $\alpha_{FCA} = 200 \pm 100$ cm⁻¹ to $\alpha_{FCA} = 566 \pm 282$ cm⁻¹. Using these new numbers, the value of $\sqrt{4\alpha_{FCA}\alpha_3}$ is now between 11 and 59 cm/GW, which is still larger than γ_2 . Therefore, changing the photon energy does not allow the gain to overcome the losses.

5.4.2. Nondegenerate Two-Photon Laser

If a degenerate 2PL in bulk GaAs is not possible, then how about a nondegenerate one. The coupled SVEA propagation equations for the irradiances of the two beams at frequencies ω_a and ω_b (where $\omega_a > \omega_b$) are

$$\begin{aligned} \frac{\partial I_a}{\partial Z} = & -\alpha_1(\omega_a)I_a + 2\gamma_2(\omega_a; \omega_b)I_bI_a - \alpha_2(\omega_a; \omega_a)I_a^2 - 3\alpha_3(\omega_a; \omega_b, \omega_b)I_aI_b^2 \\ & - 6\alpha_3(\omega_a; \omega_a, \omega_b)I_a^2I_b, \end{aligned} \quad (5.72)$$

$$\begin{aligned} \frac{\partial I_b}{\partial z} = & -\alpha_1(\omega_b)I_b + 2\gamma_2(\omega_b; \omega_a)I_a I_b - 3\alpha_3(\omega_b; \omega_a, \omega_a)I_a^2 I_b \\ & - 6\alpha_3(\omega_b; \omega_b, \omega_a)I_b^2 I_a. \end{aligned} \quad (5.73)$$

APPENDIX D: contains a derivation of the factors of 2, 3 and 6 for the two-beam interaction terms. Competing with the 2PG, we have included linear, degenerate two-photon, and two different three-photon absorption terms. For the high photon energy, $\hbar\omega_a$, the included losses are FCA and degenerate 2PA, which, since $2\hbar\omega_a > E_g$, is expected to be the limiting loss for high irradiances well before 3PA. For the low energy photon, $\hbar\omega_b$, the losses include only FCA. In principle the lowest order N-photon absorption that is allowed, i.e., $N\hbar\omega_b > E_g$, where N is the number of photons, will also contribute to the losses. However, this is expected to be small compared to the other losses, and will not dominate until much higher irradiances, where 3PA dominates the 2PG anyway, and is therefore neglected for simplicity.

In a sustained 2PL, the number of photons in each beam should be the same, since the gain mechanism creates one at each frequency simultaneously. Thus we have the good ND-2PL condition

$$\frac{I_a}{\hbar\omega_a} = \frac{I_b}{\hbar\omega_b}. \quad (5.74)$$

Solving Equation (5.74) for I_b and substituting it into Equation (5.72) allows us to rewrite our propagation equation for the beam at ω_a

$$\begin{aligned} \frac{\partial I_a}{\partial z} = & \left(-\alpha_1(\omega_a) + \left\{ 2\gamma_2(\omega_a; \omega_b) \left(\frac{\omega_b}{\omega_a} \right) - \alpha_2(\omega_a; \omega_a) \right\} I_a \right. \\ & \left. - \left\{ 3\alpha_3(\omega_a; \omega_b, \omega_b) \left(\frac{\omega_b}{\omega_a} \right)^2 + 6\alpha_3(\omega_a; \omega_a, \omega_b) \left(\frac{\omega_b}{\omega_a} \right) \right\} I_a^2 \right) I_a, \end{aligned} \quad (5.75)$$

or alternatively for the beam at ω_b , via Equation (5.73),

$$\begin{aligned} \frac{\partial I_b}{\partial z} = & \left(-\alpha_1(\omega_b) + 2\gamma_2(\omega_a; \omega_b)I_b \right. \\ & \left. - \left\{ 6\alpha_3(\omega_a; \omega_b, \omega_b) + 3\alpha_3(\omega_b; \omega_a, \omega_a) \left(\frac{\omega_a}{\omega_b} \right)^2 \right\} I_b^2 \right) I_b. \end{aligned} \quad (5.76)$$

where we have used the relations $\gamma_2(\omega_b; \omega_a) = \gamma_2(\omega_a; \omega_b)\omega_b/\omega_a$ and $\alpha_3(\omega_b; \omega_b, \omega_a) = \alpha_3(\omega_a; \omega_b, \omega_b)\omega_b/\omega_a$ (see APPENDIX D:).

The first requirement is that the 2PG term, i.e., the coefficient in the second term (multiplying I_a) in Equation (5.75), be positive in order to have the ND-2PG beat out the D-2PA. The photon energy sum is fixed to the region of population inversion, in this case $\hbar\omega_a + \hbar\omega_b = 1.03 \times E_g$, where the density of states is relatively low. These two terms, plotted as a function of the nondegeneracy factor $\hbar\omega_a/\hbar\omega_b$, is shown in Figure 5.30. Close to degeneracy, the degenerate 2PA of the large photon energy beam (blue) increases drastically as $\hbar\omega_a$ increases since these photons interact with regions of the bands of increasing density of states. The ND-2PG term (red) remains less than the D-2PA term for relatively small nondegeneracies ($\hbar\omega_a/\hbar\omega_b < 6$) since the resonance effects of the intermediate states do not become significant until extreme nondegeneracy. ND-2PG only wins out over D-2PA for extremely nondegenerate photon pairs, i.e., $\hbar\omega_a/\hbar\omega_b > 6$, which requires $\hbar\omega_b < 0.21$ eV ($\lambda_b > 6$ μm).

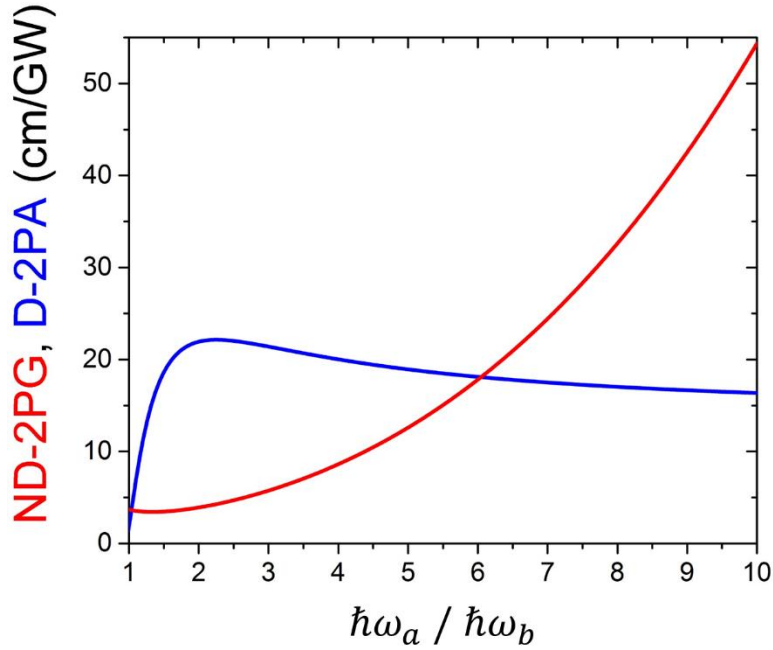


Figure 5.30 Plot of the (red) ND-2PG and (blue) D-2PA terms in Equation (5.75) versus nondegeneracy.

We can now perform the same analysis as we did above for the degenerate case, and plot the net gain (including both linear and 3PA losses) versus the irradiance to see if there is a window where ND-2PG exceeds the losses. For lasing to occur, the gain must exceed the losses for both beams simultaneously. For a nondegeneracy factor $\hbar\omega_a/\hbar\omega_b = 10$, and a photon energy sum of 1.45 eV the two photon energies are then $\hbar\omega_a = 1.32$ eV ($\lambda_a = 941$ nm) and $\hbar\omega_b = 0.132$ eV ($\lambda_b = 9.41$ μm). At 9.41 μm , Mayer et al. [168] measured photoexcited linear absorption corresponding to a cross section of $\sigma_1(\omega_b) = 2.9 \times 10^{-16}$ cm^2 , while Krishnamurthy et al. [167] calculate $\sigma_{IVB}(\omega_b) = 6 \times 10^{-16}$ cm^2 , which is consistent with the calculations presented in § 5.3.3. (see Figure 5.27). We therefore let $\sigma_1(\omega_b) = (5 \pm 2) \times 10^{-16}$ cm^2 . From the standard two-parabolic band model, we can calculate (naïvely assuming complete population inversion) $\gamma_2(\omega_a; \omega_b) = 200$ cm/GW in this case, and allow an uncertainty of 100 cm/GW . The ND-3PA losses are calculated (see § 5.3.2.) $\alpha_3(\omega_a; \omega_b, \omega_b) = 200$ cm^3/GW^2 and $\alpha_3(\omega_b; \omega_a, \omega_a) =$

$0.4 \text{ cm}^3/\text{GW}^2$. The uncertainty in these numbers can be estimated by comparing the calculations to measurements, as shown in Figure 5.21 and Figure 5.24. Nearly all of these measurements have been greater than the calculated, typically by a factor of 2-3. We therefore allow a factor of 4 (to be conservative) uncertainty in the 3PA coefficients, and let $\alpha_3(\omega_a; \omega_b, \omega_b) = 50 - 800 \text{ cm}^3/\text{GW}^2$, and $\alpha_3(\omega_b; \omega_a, \omega_a) = 0.1 - 1.6 \text{ cm}^3/\text{GW}^2$. Using these parameters, the resulting net gain is plotted in Figure 5.31, which can be seen to be negative across the entire irradiance range. Even though the 2PG coefficient is greater enhanced when using extremely nondegenerate photon pairs, both linear and nonlinear losses are increased as well. Just like the degenerate case, the END-2PG is unable to overcome both the linear absorption and 3PA. Therefore, within the rate-equation model we have presented (neglecting temperature, many body, coherent effects, etc.), we have found that an END-2PSL of bulk GaAs is not possible.

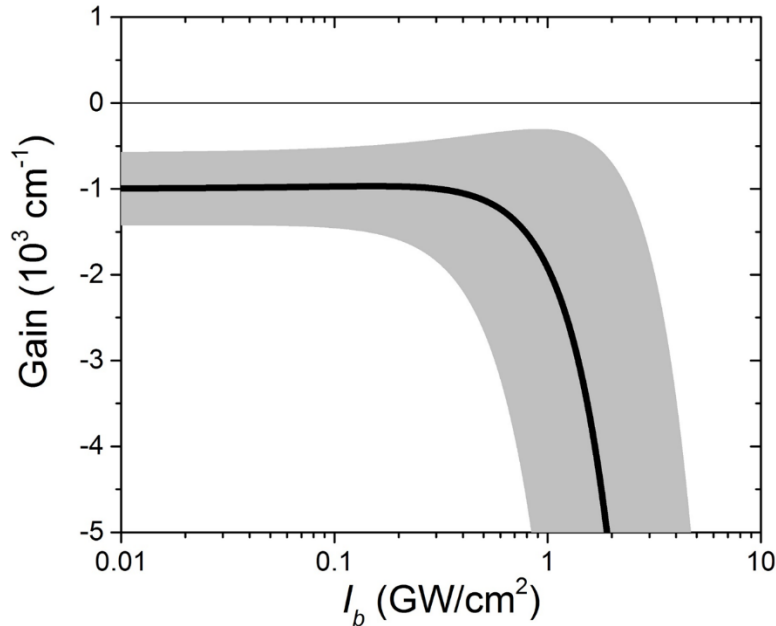


Figure 5.31 Net gain for an END-2PSL ($\hbar\omega_a/\hbar\omega_b = 10$) in GaAs, via Equation (5.76), versus irradiance. The shaded region represents the error based on values quoted in the text.

5.4.3. Other Semiconductors

The main competing processes of linear absorption (both intervalence band and phonon assisted) and 3PA depend on the semiconductor material itself. It has been shown that the 3PA coefficient depends on the band gap energy as $\alpha_3 \propto E_g^{-7}$ [163, 191]. The 2PG coefficient also depends on the band gap, but only as $\gamma_2 \propto E_g^{-3}$, so increasing the band gap will reduce the 3PA more so than the 2PG. Therefore investigating semiconductors of larger band gaps may be beneficial. Zinc blende GaN is a prime candidate: it has a large band gap, $E_g = 3.2$ eV, and a common semiconductor laser medium [175, 192]. We stick with zinc blende GaN, since Kane's band structure does not apply wurtzite structure, the other common crystalline structure of GaN. We can perform the same analysis as we have in this chapter on GaAs, including calculating the ND-3PA and intervalence band absorption coefficients, to determine if net 2PG is possible in GaN.

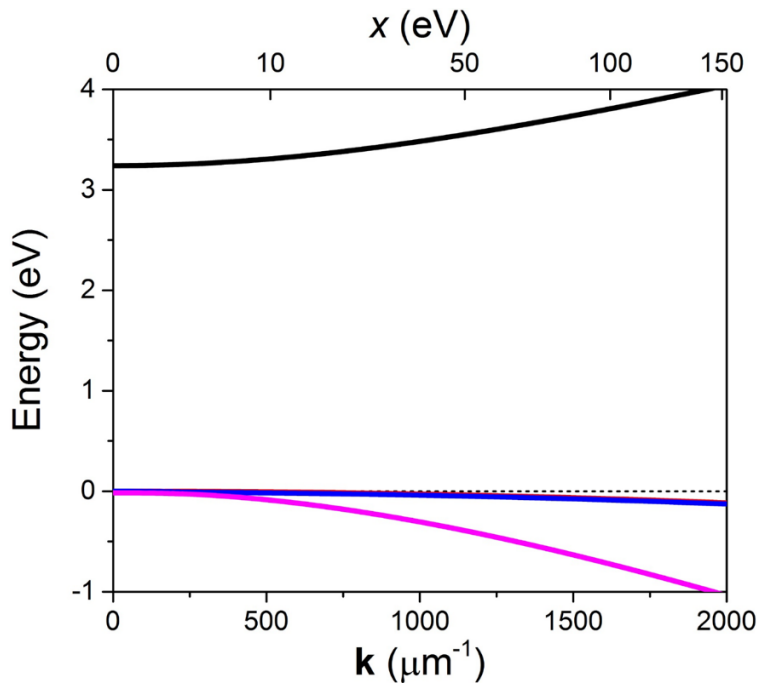


Figure 5.32 Kane's band structure of zinc blende GaN, including (black) conduction (red) heavy-hole, (blue) light-hole, and (magenta) split-off bands.

Figure 5.32 shows Kane's band structure of zinc blende GaN, using the parameters listed in Table 5.1, which has a much large band gap than GaAs, and a very small split-off energy. Additionally, the light-hole band is very close to the heavy-hole band, which actually overlay one another in this plot. We apply this band structure to calculate the D-2PA and D-3PA spectra, which are shown in the left and right plots of Figure 5.33, respectively. The 2PA coefficient in GaN $\sim 6\times$ smaller than GaAs, and the calculated 3PA coefficient is $\sim 75\times$ smaller, which is promising for mitigating the effects of 3PA dominating 2PG.

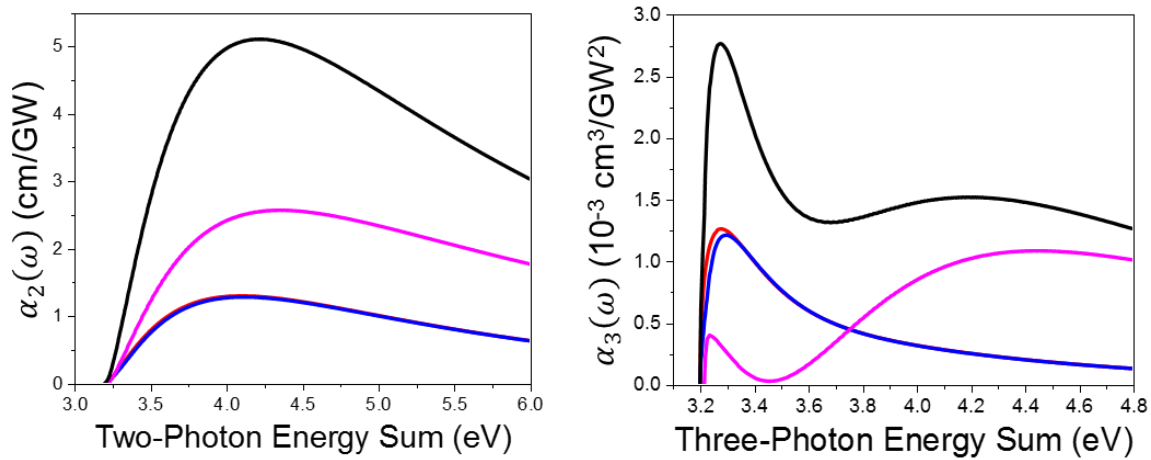


Figure 5.33 Calculated (left) D-2PA and (right) D-3PA coefficients in GaN including contributions from the (red) heavy-hole, (blue) light-hole, and (magenta) split-off bands, as well as (black) total.

The linearly losses must also be considered. The calculated intervalence band absorption coefficient is shown in Figure 5.34. Because the heavy-hole and light-hole bands are so close to one another, the intervalence band absorption between the two only occurs at very long wavelengths, where phonon absorption dominates anyway [193], and does not contribute to the spectral range shown. The similarity of the heavy- and light-hole band also means that the heavy-hole to split-off and light-hole to split-off transitions will have similar coefficients, as seen in the plot. The right plot of Figure 5.34 shows the absorption coefficient divided by the hole number density for

both low and high carrier concentrations of 10^{15} cm^{-3} and $8 \times 10^{18} \text{ cm}^{-3}$, respectively. This number density was chosen because it gives population inversion at the same excess energy, i.e., $(E_{F_c} - E_{F_v}) - E_g$, in GaN as we had in GaAs above. A larger density is required since the effective masses of both valence and conduction bands are greater than in GaAs [175]. Just as in GaAs, the two cases have very similar values of α_{IVB}/N since even for a high number density, the quasi-Fermi level E_{F_v} is still above the valence band edge, due to large effective density of states.

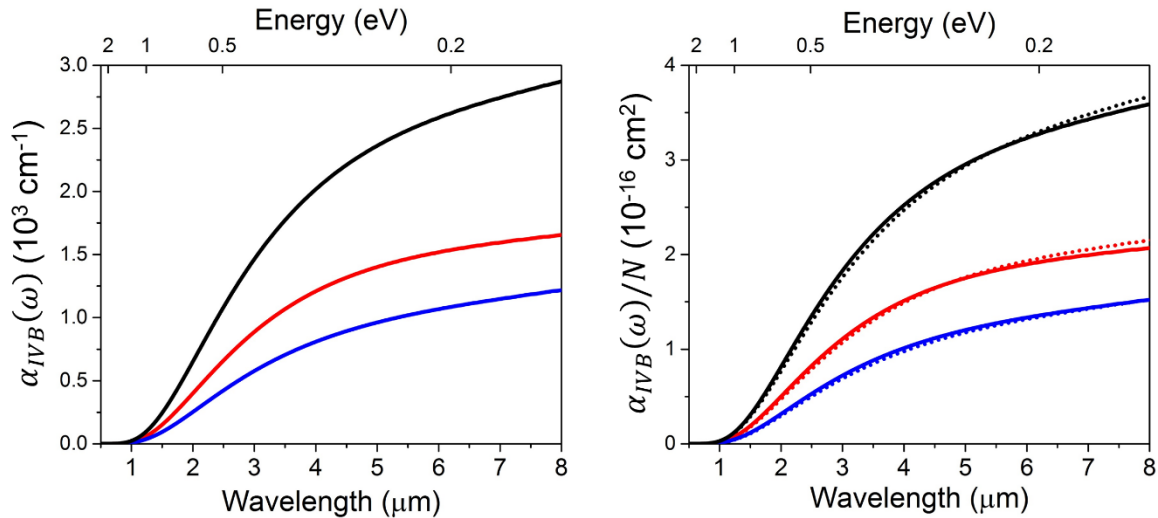


Figure 5.34 (left) Intervalence band absorption coefficient and (right) its division by the number density for (solid) $N_h = 8 \times 10^{18} \text{ cm}^{-3}$ and (dotted) 10^{15} cm^{-3} , showing both (red) heavy-hole to split-off and (blue) light-hole to split-off transitions, as well as (black) their total.

Using these calculations, we perform the same analysis of a degenerate 2PSL made of GaN, which will operate at a wavelength of 760 nm, as well as the nondegenerate case with a nondegeneracy of 10, in which case $\lambda_a = 418 \text{ nm}$ and $\lambda_b = 4.18 \text{ }\mu\text{m}$. The parameters used in the calculation are shown in Table 5.2, most of which were taken from the above calculations that were generalized to the ND case. A value σ_1 for the degenerate case was extrapolated from [194]. The same approximations made above in the treatment of GaAs, such as complete population inversion and

the good 2PL approximation, are also used here. Figure 5.35 shows the results for both (left) degenerate and (right) nondegenerate cases, for both of which the net gain is always negative, meaning 2PG never dominates the linear and three-photon absorption losses. The initially predicted reduction in α_3 due to the larger band gap energy was insufficient to allow high enough irradiance for the 2PG to overcome linear losses. These linear losses were not significantly reduced compared to GaAs, which was particularly detrimental, since γ_2 was reduced as well. Based on these results, it is not possible to construct a 2PSL out of bulk GaN.

Table 5.2 Parameters for GaN 2PSL analysis

Parameter	Degenerate	Nondegenerate
γ_2 (cm/GW)	0.16 ± 0.08	24 ± 10
α_3 (cm ³ /GW ²) ⁸	$(0.36 - 5.8) \times 10^{-3}$	$0.86 - 13.7$ $(0.01 - 2.0) \times 10^{-3}$
σ_1 (cm ⁻¹)	$(6 \pm 3) \times 10^{-18}$ [194]	$(2.6 \pm 1.3) \times 10^{-16}$
N (cm ⁻³)	8×10^{18}	8×10^{18}

⁸ For the nondegenerate case, the top range is for $\alpha_3(\omega_a; \omega_b, \omega_b)$ and the lower is for $\alpha_3(\omega_b; \omega_a, \omega_a)$.

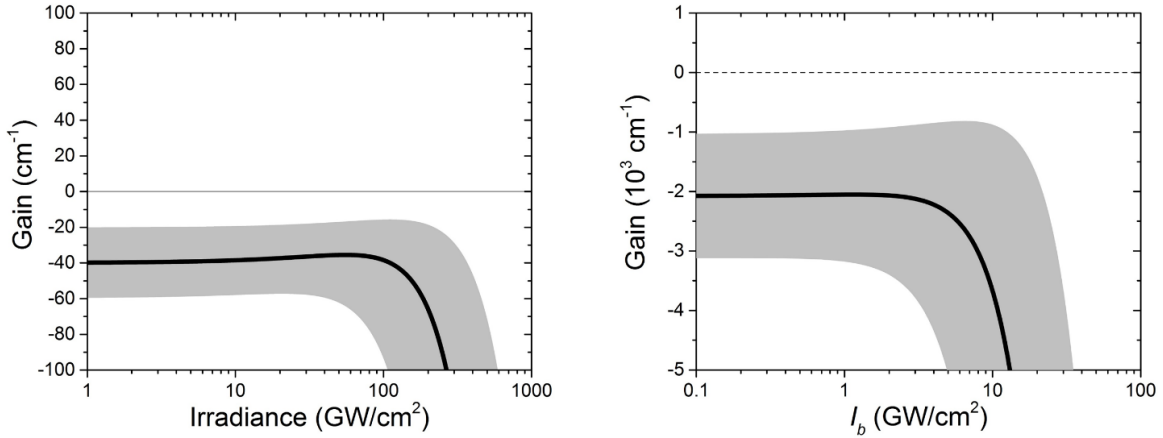


Figure 5.35 Net gain in GaN for both (left) degenerate and (nondegenerate) cases.

Semiconductor quantum wells (QW's) have the advantage of a large density of states near the band edge, which has been utilized extensively for one-photon semiconductor lasers [182]. This enhancement of the density of states may also improve 2PG, making quantum wells a potential alternative to bulk semiconductors for a 2PSL. However, 2PA in semiconductor quantum wells have been studied relatively little in comparison to bulk semiconductors [195-199], and no theoretical or experimental work on ND- 2PA has thus far been reported. Theoretical and experimental work is currently underway to determine the ND-2PA spectrum of QW's including their polarization dependence, since the anisotropy of the structure impacts the 2PA coefficient for fields polarized parallel or perpendicular (or one of each) to the confinement direction [200, 201]. Much work remains to analyze their potential use for 2PSL's, including experimental verification of the theoretical cautions of 2PA, as well as comparison to their linear and 3PA losses.

In this analysis presented here, we have not taken into account higher order losses or saturation effects which would of course limit the final irradiance levels. In addition, we have not looked at the nonlinear refractive effects that cause changes in the beams upon propagation, such as self- or cross-focusing and phase modulation. We have also neglected linear effects such as

GVM and group velocity dispersion (GVD), which will significantly affect the dynamics for media thicker than the pulse length. Should QW's or another material system yield net gain (as analyzed above), these effects would need to be considered in the design and fabrication of a 2PSL.

CHAPTER 6: CONCLUSIONS AND FUTURE WORK

The purpose of this work was twofold: 1) to investigate the temporal and polarization dependence of the third-order nonlinear optical response of simple molecules, 2) to study nondegenerate two-photon gain and competing losses in GaAs to determine if it could be used for a two-photon laser media.

6.1. Ultrafast Nonlinear Response of Simply Molecules

In the nonresonant regime, the third-order nonlinear optical response of simple molecules may be described within the Born-Oppenheimer approximation, which allows the separation of the bound-electronic response from the motion of the nuclei. The response of liquid CS₂ comes from four different mechanisms, bound-electronic plus three nuclear: collision, libration, and diffusive reorientation, which we have treated as linearly independent. We applied the beam deflection technique to fully characterize the magnitudes, temporal dynamics, and polarization dependence of each mechanism, providing the full third-order response function. To do so entailed expanding upon the beam deflection analysis to account for a noninstantaneous Raman response as well as group velocity mismatch. The outcome of both Z-scan measurements and degenerate four-wave mixing experiments were accurately predicted using this response function, which verified both the validity of the characterization as well as the experimental methodology.

This measurement procedure can be applied to a wide variety of common molecular liquids that have noninstantaneous responses. Detailed knowledge of the nonlinear response function of these solvents can greatly aid a number of nonlinear optical applications, from filamentation and supercontinuum generation to ultrafast time-resolved imaging. Additionally, the NLO properties

of organic dyes developed for all-optical switching applications are typically characterized in solution, where the nonlinearity of the solvent must be accounted for in the measurement. A comprehensive study to accurately determine of the NLO response common solvents can greatly benefit the nonlinear spectroscopy community. The beam deflection technique itself can also be expanded upon to measure a host of other nonlinear effects including excited-state/free-carrier refraction and higher order nonlinearities, including three-photon absorption.

Molecular gases were also measured with the beam deflection technique, providing detailed information about the degree of alignment of the molecular ensemble. The rotational and centrifugal distortion constants, and therefore the moment of inertia and bond length can be determined from these measurements. Measurements of gaseous CS₂ revealed our capability to identify different isotopologues. In addition, application of the magic angle which completely eliminates the rotational contribution from the measurements, allows for accurate determination of the bound-electronic nonlinear refractive index, and the orientationally averaged second hyperpolarizability of isolated molecules. This may be especially useful for comparison to theoretically calculated values of the second hyperpolarizability, which typically compare to measurements performed in solution and/or other frequency arguments, e.g., THG or electric-field induced SHG [83, 90]. Our results may also be compared to measurements in liquid phase, to test the validity of local field correction factors. The fact that our measurements of liquid and gas phase CS₂ yield very similar values of γ (within measurement error) suggest that the Lorentz-Lorenz local field provides an accurate description [16, 17].

The measurements presented here have all been relative in amplitude, with the magnitude of γ (and/or $n_{2,el}$) relative to the anisotropy of the (linear) polarizability $\Delta\alpha$. This is essentially due to the violation of the thin-sample approximation, and uncertainty in the effective beam overlap.

Thus gas phase measurements can benefit greatly by the introduction of a thin sample, such as a gas jet within a vacuum (or at least low pressure) environment. Such a sample would allow for absolute measurements of the induced refractive index change, and therefore of the material properties themselves. This would be particularly beneficial for molecules that did not display coherent rotational revivals upon which relative measurements have been based.

6.2. Two-Photon Gain in Semiconductors

Semiconductors, specifically GaAs, were investigated for two-photon gain because they have large two-photon absorption coefficients, which can be greatly enhanced using extremely nondegenerate photon pairs. It was hypothesized that, perhaps, this enhancement would be sufficient to generate large enough two-photon gain to overcome the competing loss mechanisms, which is a necessary condition for building a two-photon laser. Experimental observations of both degenerate and nondegenerate two-photon gain in GaAs were presented. This constitutes, to our knowledge, the first reported experimental demonstration of nondegenerate two-photon gain (a.k.a. doubly-stimulated two-photon emission). This was done via pump-probe experiment using extremely nondegenerate photon pairs and a third excitation beam to generate a population inversion.

To determine if the observed 2PG would be sufficient to operate a 2PSL, the competing processes were analyzed theoretically. The competing processes of three-photon and intervalence band absorption were theoretically analyzed based on Kane's band structure. It was found that the same mechanism that enhanced the 2PG, namely intermediate state resonance, also enhanced 3PA,

but by an even greater amount due to the additional resonance from the additional photon. Intervalence band absorption was found to be quite large for the carrier concentrations and wavelengths necessary to achieve nondegenerately enhanced 2PG.

With these analyses, the possibility of achieving net two-photon gain (gain > losses) was examined in both the degenerate and nondegenerate cases. This analysis was conducted in a “best case scenario” framework, where complete population inversion was assumed, meaning $\gamma_2 = \alpha_2$. In the degenerate case, it was found that the combination of free-carrier, intervalence band, and three-photon absorption overwhelms 2PG, even in this idealized case. For nondegenerate photon pairs, more competing processes enter into play, including degenerate 2PA of the larger photon energy beam. ND-2PG only beats out D-2PA for extremely nondegenerate photon pairs, where it was found that a ratio $\omega_a/\omega_b > 6$ was necessary. This of course required that one of the photons be very small in energy (long in wavelength), which in turn enhanced the ND-3PA and increased the intervalence band absorption as well. With the combination of these factors, the enhancement in ND-2PG was found to be insufficient to overcome these loss mechanisms and allow for a two-photon semiconductor laser in GaAs. The larger band gap semiconductor GaN was also analyzed in the same manner, but the same conclusion was obtained. Thus, within this rate-equation model, a 2PSL of bulk semiconductors does not seem possible.

Other material systems may be of future interest. Semiconductor quantum wells have enhanced density of states near the band edge, and may show greater enhancement for nondegenerate photon pairs. Much further work must be done, however, to analyze the free-carrier, intervalence band, and three-photon absorption spectra to determine if they may be viable candidate for 2PSLs. Semiconductor quantum dots may have the benefit of structuring the density of states to disallow

specific competing processes by, for example, not having a state with energy $\hbar\omega_a + 2\hbar\omega_b$ above the ground state.

Other potential applications that may be worthwhile to pursue include using 2PG as an amplifier rather than a laser. It should be possible to achieve net gain in one beam at a time, most likely for the larger photon energy beam which has smaller free-carrier and intervalence band absorption. In this case the strong “pump” beam would be in the mid-IR would not achieve net gain, but may allow for a broadly tunable amplifier.

The spectrum of nondegenerate three-photon absorption should also be thoroughly experimentally examined. The procedure outlined in § 5.3.2. can be applied to any direct gap zinc blende semiconductor, and is therefore a powerful tool to predict the 3PA coefficient. Further experimental validation of the approach is necessary.

APPENDIX A: NOTATION AND SYMBOLS

A	Magnetic vector potential (V·s/m)
<i>a, b</i> (sub/superscript)	Wave, photon, or state identifier
<i>a_i, b_i, c_i</i>	Kane's model k-dependent eigenstate coefficients
B	Rotational constant (m ⁻¹)
B	Magnetic field density (T)
C	Normalization constant
<i>c</i>	Speed of light in vacuum (299792458 m/s)
<i>c</i> (subscript)	Collisional mechanism
<i>c, v</i> (subscript)	Conduction and valence bands
<i>c. c.</i>	Complex conjugate
<i>circ</i> (sub/superscript)	Circular polarization
<i>c_n</i>	Complex probability amplitude
D	Centrifugal distortion constant (m ⁻¹)
\tilde{D}	Real time domain electric displacement field (C/m ²)
<i>d</i>	Distance form sample to detector (in Beam Deflection) (m)
<i>d</i> (subscript)	Diffusive reorientation mechanism
E	Energy (J, eV)
\tilde{E}	Real time domain electric field (V/m)
E	Frequency domain electric field (V/m)
<i>E_g</i>	Band gap Energy (J, eV)
<i>E_{F_{c,v}}</i>	Quasi-Fermi energy of conduction and valence bands (J, eV)
<i>E_p</i>	Kane energy parameter (28.9 eV for GaAs [202][202][202])

ε	Complex electric field amplitude (V/m)
e	Elementary electric charge ($\approx 1.602 \times 10^{-19}$ C)
el (subscript)	Bound-electronic
F	Fluence (J/m^2)
\mathcal{F}	Fourier transform
f	Fermi-Dirac distribution, Fermi function
f (subscript)	Final state in optical transition
F_2	Spectral function for α_2 in direct gap semiconductors
FCA (subscript)	Free-carrier absorption
$f^{(n)}$	n^{th} order local field correction factor
$g(\omega)$	Distribution function
g_J	Nuclear spin weighting factor
\hat{H}	Hamiltonian operator
\hat{H}_0	Time-independent Hamiltonian operator
\hat{H}_{int}	Interaction Hamiltonian operator
h	Plank's constant ($\approx 6.626 \times 10^{-34}$ J·s)
\hbar	Reduced Plank's constant ($h/2\pi \approx 1.055 \times 10^{-34}$ J·s)
hh (subscript)	Heavy-hole band
I	Irradiance (W/m^2)
\mathcal{J}	Moment of inertia ($\text{kg}\cdot\text{m}^2$)
i	Imaginary unit ($\sqrt{-1}$)
i (subscript)	Initial state in optical transition

<i>iso</i> (superscript)	Isotropic symmetry component
<i>IVB</i> (subscript)	Intervalence band absorption
<i>J</i>	Total angular momentum quantum number
<i>j</i> (subscript)	Intermediate state
<i>K</i>	Material independent constant ($3100 \text{ GW}\cdot\text{cm}^{-1}\cdot\text{eV}^{-5/2}$)
<i>k</i>	Wavevector (m^{-1})
<i>k</i>	Wavenumber ($ \mathbf{k} , \text{m}^{-1}$)
<i>k_B</i>	Boltzmann constant ($\approx 1.38 \times 10^{-23} \text{ J/K}$)
<i>k_r</i>	Electron wavenumber at resonance (m^{-1})
<i>L</i>	Sample thickness (m)
<i>l</i>	length (m)
<i>l</i> (subscript)	Intermediate state, Librational mechanism
<i>lh</i> (subscript)	Light-hole band
<i>lin</i> (sub/superscript)	Linear polarization
<i>loc</i> (subscript)	Local field
<i>M</i>	Secondary total angular momentum quantum number
<i>m</i>	Mass (kg)
<i>m₀</i>	Electron mass ($\approx 9.11 \times 10^{-31} \text{ kg}$)
<i>m_r</i>	Reduced mass (kg)
<i>M_{mn}</i>	Matrix element
<i>N</i>	Number density (m^{-3})
<i>n</i>	Linear refractive index

n_2	Nonlinear refractive index (m^2/W)
$n_{2,\text{eff}}$	Effective (time dependent) nonlinear refractive index (m^2/W)
n_g	Group index
NL (super/subscript)	Nonlinear
ns (subscript)	Nuclear spin (wave function)
nu (subscript)	Nuclear
P	Power (W), Kane momentum parameter
$\tilde{\mathbf{P}}$	Real time domain polarization density vector (C/m^2)
\mathbf{P}	Frequency domain polarization density vector (C/m^2)
\mathcal{P}	Complex polarization density amplitude (C/m^2)
\mathbf{p}	Momentum ($\text{kg}\cdot\text{m}/\text{s}$)
R	Reflectivity, Transition rate per unit volume ($\text{s}^{-1}\cdot\text{m}^{-3}$)
$R(t)$	Noninstantaneous nonlinear refractive response function
\mathbf{r}	Position vector (m)
$r(t)$	Normalized temporal response function
r (subscript)	Resonant
re (superscript)	Reorientational symmetry component
rot (subscript)	Rotational (wave function)
S	Wave function with symmetry of s orbital (spherically symmetric)
S_n	Nuclear spin quantum number
so (subscript)	Split-off band
T	Temperature (K), Dimensionless time, Revival period (s), Transmission

\mathcal{T}	Dimensionless probe pulse width (HW1/eM of I)
t	Time (s)
T_d	Dimensionless delay
T_J	Rotational revival weighting factor
$u_{n,\mathbf{k}}(\mathbf{r})$	Bloch function
V	Potential (J, eV), Volume (m ³)
v	Velocity (m/s)
v (subscript)	Vibrational mechanism
v_g	Group velocity (m/s)
vib (subscript)	Vibrational (wave function)
W	Transition rate (s ⁻¹)
w	Beam spot size (HW1/e ² M of I) (m)
X, Y, Z	Wave functions with symmetry of p orbitals
Y_l^m	Spherical harmonic
x, y, z (subscript)	Cartesian coordinates
Z	Dimensionless propagation distance
z	Distance (in propagation direction) (m)
z_0	Rayleigh range (m)
α	Polarizability (C·m ² /V = F·m ² = C ² m ² /J)
α, β (subscripts)	Spin indices
α_1	One-photon absorption coefficient (m ⁻¹)

α_2	Two-photon absorption coefficient (m/W)
α_3	Three-photon absorption coefficient (m ³ /W ²)
β	First hyperpolarizability (C ³ m ³ /J ²)
Γ	Dephasing (damping) rate (rad/s)
γ	Second hyperpolarizability (C ⁴ m ⁴ /J ³)
γ_1	One-photon gain coefficient (m ⁻¹)
γ_2	Two-photon gain coefficient (m/W)
Δ	Split-off energy (J, eV)
δ_{2PA}	Two-photon absorption cross section (s·m ⁴ , GM)
δ_{3PA}	Three-photon absorption cross section (s ² ·m ⁶)
$\Delta\alpha$	Change in absorption coefficient (m ⁻¹), Polarizability anisotropy (F·m ²)
ΔE	Energy difference or uncertainty (J)
ΔJ	Change in total angular momentum quantum number upon transition
Δl	Increase in bond length due to centrifugal distortion (m)
ΔN	Population inversion density (m ⁻³)
Δn	Refractive index change
ΔP	Change in power (W)
ΔT	Change or difference in transmission
Δt	Time interval (s)
ΔT_{p-v}	Difference in transmission from peak to valley in CA Z-scan
Δt	Time interval (s)
$\Delta\phi$	Slowly varying phase (rad)

$\Delta\omega$	Frequency difference (rad/s)
ϵ_0	Permittivity of free space ($\approx 8.85 \times 10^{-12}$ F/m)
$\Theta(t)$	Heaviside (unit step) function
θ	Angle of electric field with respect to molecular axis (rad)
κ	Imaginary component of complex refractive index
λ_0	Free space wavelength (m)
μ	Electric dipole moment (C·m)
μ_{fi}	Transition dipole moment (C·m, D)
μ_m	Magnetic dipole moment (N·m/T = J/T = A·m ²)
ρ	Group velocity mismatch parameter, Density matrix
ρ_f	Free charge density (C/m ³)
σ	Cross section (m ²), Standard deviation
σ	Pauli spin matrix
τ	Lifetime (s), Pulse width (s)
τ_d	Temporal delay (s)
τ_f	Fall time (s)
τ_r	Rise time (s)
ϕ_i	Eigenstates of Kane's model
φ	Angle between pump and probe electric fields (rad)
$\chi^{(n)}$	n th order susceptibility ((m/V) ⁿ⁻¹)
$ \Psi\rangle$	Quantum state (wave function)
$ \psi\rangle$	Stationary quantum state (wave function), eigenstate of \hat{H}_0

ω	Angular frequency of radiation (rad/s)
0	Central, Peak
*	Complex conjugate
(subscript)	Parallel
\perp (subscript)	Perpendicular
\uparrow, \downarrow	Spin directions
\wedge	Operator, Unit vector

APPENDIX B: PAULI EXCLUSION PRINCIPLE IN 2PA

One way to describe the two-photon absorption is via second-order perturbation theory. Take, for example, the three level system in Figure B.1, which has one electron initially in the ground state $|1\rangle$. We may think of the two-photon process as happening in two “steps”, one for each photon, the first being a “virtual” transition from $|1\rangle$ to $|2\rangle$. We call this a “virtual” transition since it does not conserve energy ($E_{12} \neq \hbar\omega$), and thus only has a lifetime that is limited by the uncertainty relation $\Delta t = \hbar/\Delta E$. If, within this time Δt a second photon interacts with the electron, it may complete the transition from $|2\rangle$ to $|3\rangle$, so long as $E_{13} = 2\hbar\omega$ (for simplicity, we treat the degenerate case here, but the results can easily be generalized to the nondegenerate case). This process contributes to the two-photon transition rate by

$$W_2 \propto \left| \frac{\langle 3 | \hat{H}_{int} | 2 \rangle \langle 2 | \hat{H}_{int} | 1 \rangle}{E_{12} - \hbar\omega} \right|^2, \quad (\text{B.1})$$

where \hat{H}_{int} is the interaction Hamiltonian.

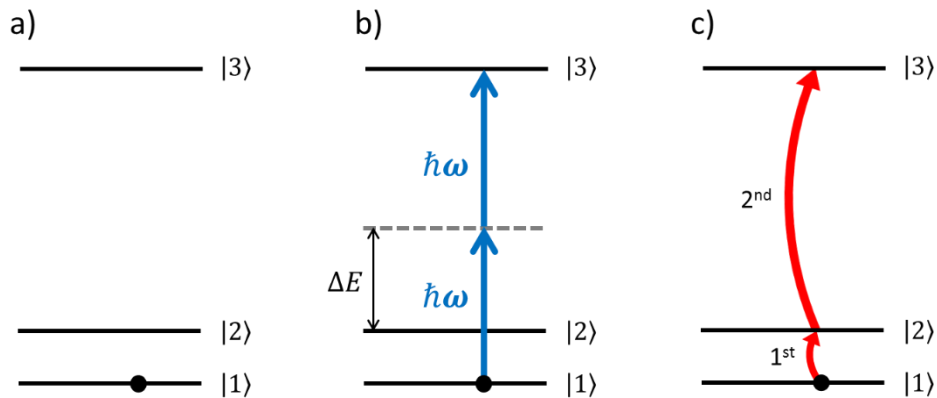


Figure B.1 Energy level diagrams of two-photon absorption for a three-level system a) initial configuration, b) showing photon energies (blue arrows) and energy detuning $\Delta E = |E_{12} - \hbar\omega|$, and c) quantum pathway (red arrows) where $|1\rangle \rightarrow |2\rangle$ occurs first, followed by $|2\rangle \rightarrow |3\rangle$.

Now, what happens if, instead, we have two electrons in our system, initially with one in $|1\rangle$ and one in $|2\rangle$ (see Figure B.2)? We may write this as a two-particle state $|1, 2\rangle$ (or alternatively

$|2, 1\rangle$, but we choose the former without losing generality). If we now impose the Pauli Exclusion Principle, the virtual transition of the electron initially in $|1\rangle$ to $|2\rangle$ is now no longer possible, since $|2\rangle$ is already occupied by another electron. At first glance, it appears that two-photon absorption is now no longer possible, since the intermediate state used in the one-electron case is no longer available. However, there is an alternative. We may instead consider the electron in $|2\rangle$ undergoing a virtual transition to $|3\rangle$, which in the two-particle system we write as $|1, 2\rangle \rightarrow |1, 3\rangle$. Now to complete the transition, the other electron in $|1\rangle$ goes to $|2\rangle$, or $|1, 3\rangle \rightarrow |2, 3\rangle$ (see Figure B.2). This process leads to a two-photon transition rate

$$W_2 \propto \left| \frac{\langle 2, 3 | \hat{H}_{int} | 1, 3 \rangle \langle 1, 3 | \hat{H}_{int} | 1, 2 \rangle}{E_{23} - \hbar\omega} \right|^2. \quad (\text{B.2})$$

If we compare this result to that which we obtained with a single electron, Equation (B.1), we find it is identical, since $\langle 2, 3 | \hat{H}_{int} | 1, 3 \rangle = \langle 2 | \hat{H}_{int} | 1 \rangle$, $\langle 1, 3 | \hat{H}_{int} | 1, 2 \rangle = \langle 3 | \hat{H}_{int} | 2 \rangle$, and $E_{23} - \hbar\omega = -(E_{12} - \hbar\omega)$. Therefore, the contribution to the two-photon transition rate in the two-electron case is the same as it was in the one-electron case. This means that the application of the Pauli Exclusion Principle had no impact on our calculation of two-photon absorption. We are essentially, then, free to ignore it.

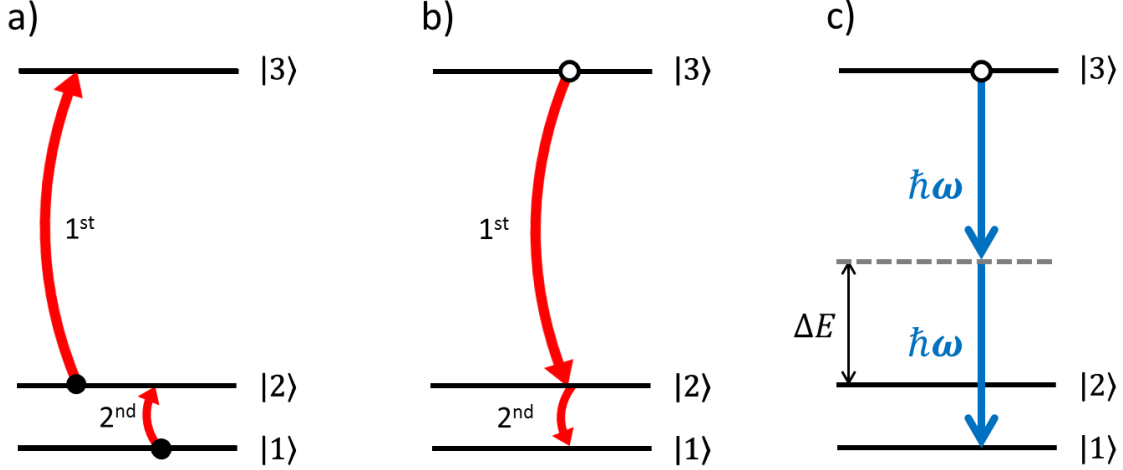


Figure B.2 The three-level system with two electrons: a) quantum pathways (red arrows) of the two-photon and two-electron transition, b) equivalent description in terms of the single “hole,” and c) photon energies (blue arrows) and energy detuning $\Delta E = E_{23} - \hbar\omega$.

Another way to see this equivalence in the two electron case, is to follow the holes. Since we have three states, and two electrons, we can think of |3> as initially being occupied by a hole. The first photon then causes a virtual transition of the hole from |3> to |2>, and the second completes the transition from |2> to |1>. This is illustrated in Figure B.2 b and c. The transition rate is then

$$W_2 \propto \left| \frac{\langle 1 | \hat{H}_{int} | 2 \rangle \langle 2 | \hat{H}_{int} | 3 \rangle}{E_{23} - \hbar\omega} \right|^2. \quad (\text{B.3})$$

Since $\langle 1 | \hat{H}_{int} | 2 \rangle = \langle 2 | \hat{H}_{int} | 1 \rangle^*$, $\langle 2 | \hat{H}_{int} | 3 \rangle = \langle 3 | \hat{H}_{int} | 2 \rangle^*$, $E_{23} - \hbar\omega = -(E_{12} - \hbar\omega)$, and we take the square modulus, this is the same as Equations (B.1) and (B.2).

This can be generalized to a more complex N-level system, where there are multiple quantum pathways for the two-photon absorption process. In this case, those terms involving two-electrons need to be multiplied by an additional negative sign to account for the exchange of electrons in the final state (e.g. |2, 4> versus |4, 2>).

APPENDIX C: NUCLEAR SPIN STATISTICS

In this appendix we analyze the spin statistics of the molecules studied in § 4.4. Recall the total wave function of the molecule may be written

$$\psi_{total} = \psi_{el}\psi_{vib}\psi_{rot}\psi_{ns}, \quad (\text{C.1})$$

where the subscript *el* stands for electronic, *vib* for vibrational, *rot* for rotational, and *ns* for nuclear spin. For molecules with identical nuclei, ψ_{total} must be even or odd upon interchange, depending on whether they, the nuclei, are bosons (integer spin) or fermions (half integer spin), respectively. That is to say, for boson

$$\hat{i}\psi_{total} = \psi_{total}, \quad (\text{C.2})$$

and for fermions

$$\hat{i}\psi_{total} = -\psi_{total}. \quad (\text{C.3})$$

where \hat{i} is the interchange operator [114]. The task of evaluating g_j is then a matter of determining the spin of the nuclei, and the symmetry of the constituent wave functions such that the appropriate symmetry is maintained upon nuclear interchange.

In homonuclear diatomic molecules, the number of possible spin states is given by

$$(2S_n + 1), \quad (\text{C.4})$$

where S_n is the spin quantum number of the nuclei. These states are either symmetric (i.e., $\hat{i}\psi_{ns} = \psi_{ns}$) or antisymmetric (i.e., $\hat{i}\psi_{ns} = -\psi_{ns}$) upon nuclear interchange. The number of symmetric states is

$$(2S_n + 1)(S_n + 1), \quad (\text{C.5})$$

and the number of antisymmetric is

$$(2S_n + 1)S_n. \quad (\text{C.6})$$

^{14}N nuclei are bosons with $S_n = 1$, and therefore ψ_{total} of $^{14}\text{N}_2$ molecules must be symmetric to nuclear interchange [203]. At room temperature, $^{14}\text{N}_2$ has only the electronic ground state occupied, which is symmetric [204]. For homonuclear diatomic molecules the only vibrational mode is a symmetric stretch mode, meaning ψ_{vib} is necessarily symmetric. Therefore, since ψ_{total} must be symmetric, ψ_{rot} and ψ_{ns} must possess the same symmetry. From Equations (C.5) and (C.6) there are 6 symmetric spin states and 3 antisymmetric spin states [114]. Because there are twice as many symmetric nuclear spin states as antisymmetric, even (symmetric) rotational states are twice as populated as odd (antisymmetric). Thus, for $^{14}\text{N}_2$, $g_J = 2/3$ for even rotational quantum numbers J , and $g_J = 1/3$ for odd J , resulting in the 2:1 ratio of even to odd weighting of rotational states.

^{16}O nuclei are also bosons, but with $S_n = 0$ [203]. Again, only the electronic ground state is occupied at room temperature, but it is antisymmetric. As with $^{14}\text{N}_2$, ψ_{vib} is necessarily symmetric. There is only one spin state, which is symmetric [114]. Since ψ_{total} must be symmetric, there are no combinations of constituent wave functions that allow for a symmetric ψ_{rot} . Therefore, $^{16}\text{O}_2$ molecules in the ground electronic state cannot exist in even rotational states, meaning $g_J = 1$ for even J , and $g_J = 0$ for odd J .

CS_2 is a bit more complicated, being a linear triatomic molecule. Unlike N and O nuclei, S have many isotopes of relatively high abundance, of which the four ones are ^{32}S , ^{33}S , ^{34}S , and ^{36}S , the natural abundance and nuclear spin of each is shown in Table C.1. CS_2 molecules can form with any combination of sulfur isotopes, making different isotopologues. Their relative abundances are based on the natural abundance of each isotope, the most common of which is $^{12}\text{C}^{32}\text{S}_2$ (90.07%), followed by $^{32}\text{S}^{12}\text{C}^{34}\text{S}$ (8.06%), and $^{32}\text{S}^{12}\text{C}^{33}\text{S}$ (1.42%), with all other isotopologues

together making up less than 0.5%. The latter two, with two different S isotopes, are not required to be (anti)symmetric upon nuclear interchange, which only applies for indistinguishable particles.

Therefore $g_J = 1$ for all J .

Table C.1 Natural abundance and spin of isotopes of S [205]

Isotope	Natural Abundance (%)	S_n
^{32}S	94.99 ± 0.26	0
^{33}S	0.75 ± 0.02	3/2
^{34}S	4.25 ± 0.24	0
^{36}S	0.01 ± 0.01	0

The symmetric isotopologues $^{12}\text{C}^{32}\text{S}_2$, however, must have a symmetric ψ_{total} since both sulfur nuclei are identical bosons with $S_n = 0$, yielding only one symmetric nuclear spin state. The electronic ground state of $^{12}\text{C}^{32}\text{S}_2$ is symmetric [115]. The symmetry of ψ_{vib} can be assigned by evaluating the distribution of vibrational states at room temperature. The frequencies and occupation probability of the lowest vibrational modes are shown in Table C.2. The ν_1 mode is symmetric stretch mode, and so does not change the weighting from the ground vibrational state. The ν_2 mode is a bending mode, which we treat as having equal weighting between even and odd rotational

states (see § 4.4.2.). $^{12}\text{C}^{32}\text{S}_2$ molecules in the ground electronic and vibrational states cannot exist in odd rotational states, meaning $g_J = 1$ for even J , and 0 for odd J ⁹ [115].

Table C.2 Vibrational modes of $^{12}\text{C}^{32}\text{S}_2$ [206]

Vibrational Mode	Frequency (cm^{-1})	Energy (meV)	Probability at 300 K (%)
ν_2	397 ± 3	49.2 ± 0.4	14.2
ν_1	658 ± 1	81.6 ± 0.1	3.1
$2\nu_2$	793 ± 3	190.3 ± 0.3	1.7

⁹ Strictly speaking, the ν_2 vibrational mode is more complicated, and the degeneracy between the modes can be split, and the rotational Raman transitions have selection rules $\Delta J = 0, \pm 1, \pm 2$. This has been neglected in this analysis.

**APPENDIX D: CONSISTENCY BETWEEN ONE AND TWO BEAM
EXPERIMENTS**

D.1. One Versus Two Beam Experiments

Here we seek to derive the coefficients on the nonlinear interactions (e.g. NLR) for experiments with different number of beams. The guiding principle is that whether a single beam experiment, such as Z-scan, or a two-beam experiment, such as pump-probe or beam deflection, should yield the exact same measurement of the material properties. For third-order (nearly instantaneous bound-electronic) NLR and 2PA, there is a factor of two difference between one and two beam cases, as seen in Equations (2.14) and (2.15). We can see this by starting with the third-order polarization, given by

$$\tilde{\mathbf{P}}^{(3)} = \varepsilon_0 \chi^{(3)} (\tilde{\mathbf{E}} \cdot \tilde{\mathbf{E}} \cdot \tilde{\mathbf{E}}), \quad (\text{D.1})$$

where we treat the material response as instantaneous (and therefore dispersionless). The field of a single beam is given by

$$\tilde{\mathbf{E}} = \frac{1}{2} \mathcal{E} e^{i(\mathbf{k} \cdot \mathbf{r} - \omega t)} + \frac{1}{2} \mathcal{E}^* e^{-i(\mathbf{k} \cdot \mathbf{r} - \omega t)}, \quad (\text{D.2})$$

which we can think of as the sum of two counter rotating waves in the complex plane, such that their sum is real, and simply $\mathcal{E} \cos(\mathbf{k} \cdot \mathbf{r} - \omega t)$. Looking at the product of the field, and first expanding only the first product we get

$$\tilde{\mathbf{E}} \cdot \tilde{\mathbf{E}} \cdot \tilde{\mathbf{E}} = \left(\frac{1}{4} \mathcal{E}^2 e^{i(2\mathbf{k} \cdot \mathbf{r} - 2\omega t)} + \frac{2}{4} |\mathcal{E}|^2 + \frac{1}{4} \mathcal{E}^{*2} e^{-i(2\mathbf{k} \cdot \mathbf{r} - 2\omega t)} \right) \cdot \tilde{\mathbf{E}}. \quad (\text{D.3})$$

The square of the field generates a term at the second harmonic, 2ω (plus complex conjugate) and twice the cross term at zero frequency. The 2ω term combines with the third field in the product to give a term that oscillates at 3ω and another at ω ,

$$\begin{aligned}
& \frac{1}{4} \mathcal{E}^2 e^{i(2\mathbf{k}\cdot\mathbf{r}-2\omega t)} \left(\frac{1}{2} \mathcal{E} e^{i(\mathbf{k}\cdot\mathbf{r}-\omega t)} + \frac{1}{2} \mathcal{E}^* e^{-i(\mathbf{k}\cdot\mathbf{r}-\omega t)} \right) \\
& = \frac{1}{8} \mathcal{E}^3 e^{i(3\mathbf{k}\cdot\mathbf{r}-3\omega t)} + \frac{1}{8} |\mathcal{E}|^2 \mathcal{E} e^{i(\mathbf{k}\cdot\mathbf{r}-\omega t)}.
\end{aligned} \tag{D.4}$$

and likewise for its complex conjugate, but at -3ω and $-\omega$

$$\begin{aligned}
& \frac{1}{4} \mathcal{E}^{*2} e^{-i(2\mathbf{k}\cdot\mathbf{r}-2\omega t)} \left(\frac{1}{2} \mathcal{E} e^{i(\mathbf{k}\cdot\mathbf{r}-\omega t)} + \frac{1}{2} \mathcal{E}^* e^{-i(\mathbf{k}\cdot\mathbf{r}-\omega t)} \right) \\
& = \frac{1}{8} |\mathcal{E}|^2 \mathcal{E}^* e^{-i(\mathbf{k}\cdot\mathbf{r}-\omega t)} + \frac{1}{8} \mathcal{E}^{*3} e^{-i(3\mathbf{k}\cdot\mathbf{r}-3\omega t)}.
\end{aligned} \tag{D.5}$$

The product of the zero frequency term with the field gives both a term at ω as well as $-\omega$

$$\begin{aligned}
& \frac{2}{4} \mathcal{E} \mathcal{E}^* \left(\frac{1}{2} \mathcal{E} e^{i(\mathbf{k}\cdot\mathbf{r}-\omega t)} + \frac{1}{2} \mathcal{E}^* e^{-i(\mathbf{k}\cdot\mathbf{r}-\omega t)} \right) \\
& = \frac{2}{8} |\mathcal{E}|^2 \mathcal{E} e^{i(\mathbf{k}\cdot\mathbf{r}-\omega t)} + \frac{2}{8} |\mathcal{E}|^2 \mathcal{E}^* e^{-i(\mathbf{k}\cdot\mathbf{r}-\omega t)}.
\end{aligned} \tag{D.6}$$

The third-order polarization then

$$\tilde{\mathbf{P}}^{(3)} = \varepsilon_0 \chi^{(3)} \left(\frac{1}{8} \mathcal{E}^3 e^{i(3\mathbf{k}\cdot\mathbf{r}-3\omega t)} + \frac{3}{8} |\mathcal{E}|^2 \mathcal{E} e^{i(\mathbf{k}\cdot\mathbf{r}-\omega t)} + c. c. \right), \tag{D.7}$$

where the first term is THG, and the second term yields self-nonlinearties, including NLR and 2PA. As in § 2.1. and § 2.2. , from the second term we can derive n_2 and α_2 in terms of the real and imaginary parts of $\chi^{(3)}$, respectively (see Equations (2.16) and (2.17)).

The total field of a two beam experiment is given by

$$\tilde{\mathbf{E}} = \frac{1}{2} \mathcal{E}_a e^{i(\mathbf{k}_a \cdot \mathbf{r} - \omega_a t)} + \frac{1}{2} \mathcal{E}_b e^{i(\mathbf{k}_b \cdot \mathbf{r} - \omega_b t)} + c. c.. \tag{D.8}$$

Looking at the product of the field, and first expanding only the first product we get

$$\begin{aligned}
\tilde{\mathbf{E}} \cdot \tilde{\mathbf{E}} \cdot \tilde{\mathbf{E}} = & \left(\frac{1}{4} \mathcal{E}_a^2 e^{i(2\mathbf{k}_a \cdot \mathbf{r} - 2\omega_a t)} + \frac{1}{4} \mathcal{E}_b^2 e^{i(2\mathbf{k}_b \cdot \mathbf{r} - 2\omega_b t)} \right. \\
& + \frac{2}{4} \mathcal{E}_a \mathcal{E}_b e^{i((\mathbf{k}_a + \mathbf{k}_b) \cdot \mathbf{r} - (\omega_a + \omega_b)t)} + \frac{2}{4} \mathcal{E}_a \mathcal{E}_b^* e^{i((\mathbf{k}_a + \mathbf{k}_b) \cdot \mathbf{r} - (\omega_a - \omega_b)t)} \\
& \left. + c. c. + \frac{2}{4} |\mathcal{E}_a|^2 + \frac{2}{4} |\mathcal{E}_b|^2 \right) \cdot \tilde{\mathbf{E}}.
\end{aligned} \tag{D.9}$$

The first two terms are simply the second harmonics at $2\omega_a$ and $2\omega_b$, and the last two are the zero frequency terms. These are simply products of the individual fields, and are the same as those appearing in the single beam case, Equation (D.3). Now, however, we have additional terms due to the interference of the two beams, which multiply with the third field in the product to give

$$\begin{aligned}
& \frac{2}{4} \mathcal{E}_a \mathcal{E}_b e^{i((\mathbf{k}_a + \mathbf{k}_b) \cdot \mathbf{r} - (\omega_a + \omega_b)t)} \left(\frac{1}{2} \mathcal{E}_a e^{i(\mathbf{k}_a \cdot \mathbf{r} - \omega_a t)} + \frac{1}{2} \mathcal{E}_b e^{i(\mathbf{k}_b \cdot \mathbf{r} - \omega_b t)} + c. c. \right) \\
& = \frac{2}{8} \mathcal{E}_a^2 \mathcal{E}_b e^{i((2\mathbf{k}_a + \mathbf{k}_b) \cdot \mathbf{r} - (2\omega_a + \omega_b)t)} + \frac{2}{8} \mathcal{E}_a \mathcal{E}_b^2 e^{i((2\mathbf{k}_a + \mathbf{k}_b) \cdot \mathbf{r} - (2\omega_a + \omega_b)t)} \\
& + \frac{2}{8} |\mathcal{E}_a|^2 \mathcal{E}_b e^{i(\mathbf{k}_b \cdot \mathbf{r} - \omega_b t)} + \frac{2}{8} \mathcal{E}_a |\mathcal{E}_b|^2 e^{i(\mathbf{k}_a \cdot \mathbf{r} - \omega_a t)}.
\end{aligned} \tag{D.10}$$

and likewise for the complex conjugate. The last term in Equation (D.10) can be thought of a grating term which simply increases the nonlinear interaction in the two beams case (assuming an instantaneous material response). The interference of the two beams generates a refractive index grating (or transmission grating, in the case of 2PA), off of which the pump is diffracted in the direction of the probe (and *vice versa*) with the correct phase an amplitude to effectively double the interaction. This gives a total third-order polarization oscillating at ω_a in the \mathbf{k}_a direction of

$$\varepsilon_0 \chi^{(3)} \left(\frac{3}{8} |\mathcal{E}_a|^2 \mathcal{E}_a + \frac{6}{8} |\mathcal{E}_b|^2 \mathcal{E}_a \right) e^{i(\mathbf{k}_a \cdot \mathbf{r} - \omega_a t)} + c. c. \tag{D.11}$$

Thus we can see that the two beam case (second term) is twice the amplitude of the single beam case (first term). However, the material property itself, be it $\chi^{(3)}$, n_2 , or a_2 , is independent of the

type of experiment used to measure it. Therefore, there must be a factor of two difference between the single-beam and double-beam terms in the equations governing irradiance and phase, as in Equations (2.14) and (2.15).

In the case of 3PA, which is a $\chi^{(5)}$ process, these coefficients become more complicated due to the various different interference terms between the beams. In this case, the fifth-order polarization is (assuming instantaneous and dispersionless as above)

$$\tilde{\mathbf{P}}^{(5)} = \varepsilon_0 \chi^{(5)} (\tilde{\mathbf{E}} \cdot \tilde{\mathbf{E}} \cdot \tilde{\mathbf{E}} \cdot \tilde{\mathbf{E}} \cdot \tilde{\mathbf{E}}). \quad (\text{D.12})$$

To simplify our argument, we apply the multinomial theorem [207], which is the generalization of the binomial theorem to an arbitrary number of elements. It states that a sum of m elements to the n th power may be expanded as a sum of the products of the elements, each with corresponding coefficients. That is

$$(x_1 + x_2 + \dots + x_m)^n = \sum_{k_1+k_2+\dots+k_m=n} \binom{n}{k_1, k_2, \dots, k_m} \prod_{1 \leq t \leq m} x_t^{k_t}. \quad (\text{D.13})$$

where the coefficients

$$\binom{n}{k_1, k_2, \dots, k_m} = \frac{n!}{k_1! k_2! \dots k_m!}. \quad (\text{D.14})$$

These are simply the number of equivalent terms in the expansion. For example, for third-order nonlinearities in the single beam case $m = 2$ (one for each term in Equation (D.2)) and $n = 3$. The coefficient on the x_1^3 term is $3!/(3! 0!) = 1$, and on the $x_1^2 x_2$ term is $3!/(2! 1!) = 3$, just as we have in Equation (D.7).

For 3PA, the single beam case has terms that goes as $\mathcal{E}^3 \mathcal{E}^{*2} = |\mathcal{E}|^4 \mathcal{E}$, since these are the only terms that oscillate at ω and propagate in the \mathbf{k} direction. We can find the coefficients using Equation (D.13) with $m = 2$ and $n = 5$: $5!/(3! 2!) = 10$. Thus there are 10 equivalent terms in

the expansion of Equation (D.12) in the case of a single beam. This corresponds to the process of absorption three-photons out of a single beam.

We can also find the number in the case of two beams. However, there may be either one photons at ω_a and two at ω_b absorbed, or two at ω_a and one at ω_b . These two cases occur as terms in the expansion of Equation (D.12) as $\mathcal{E}_a \mathcal{E}_b^2 \mathcal{E}_b^{*2} = |\mathcal{E}_b|^4 \mathcal{E}_a$ where we get we get a coefficient $5!/(1! 2! 2!) = 30$, and $\mathcal{E}_a^2 \mathcal{E}_a^* \mathcal{E}_b \mathcal{E}_b^* = |\mathcal{E}_a|^2 |\mathcal{E}_b|^2 \mathcal{E}_a$ with $5!/(2! 1! 1! 1!) = 60$. Thus, compared to the single beam case, two-beam 3PA has two terms with coefficients that are 3 and 6 times greater, respectively. Therefore these coefficients on the multi-beam interactions in Equations (5.45), (5.72), and (5.73) are necessary.

D.2 Relation between $\alpha_2(\omega_a; \omega_b)$ and $\alpha_2(\omega_b; \omega_a)$

There is a difference in the ND-2PA coefficients depending on which of the two frequency inputs is being described. This is a consequence of the fact that α_2 is defined in terms of the SVEA equation governing the irradiance, rather than the photon flux, in which case

$$\frac{\partial I_a}{\partial z} = -2\alpha_2(\omega_a; \omega_b)I_a I_b, \quad (\text{D.15})$$

$$\frac{\partial I_b}{\partial z} = -2\alpha_2(\omega_b; \omega_a)I_b I_a. \quad (\text{D.16})$$

where $\alpha_2(\omega_a; \omega_b) \neq \alpha_2(\omega_b; \omega_a)$. These equations describe the simultaneous absorption of one photon at ω_a and one at ω_b , and therefore have the same 2PA rate. This can be seen by converting the irradiances into photon fluxes using $\Phi_i = I_i/\hbar\omega_i$, in which case Equations (D.15) and (D.16) become

$$\frac{\partial \Phi_a}{\partial z} = -2\hbar\omega_b\alpha_2(\omega_a; \omega_b)\Phi_a \Phi_b, \quad (\text{D.17})$$

$$\frac{\partial \Phi_b}{\partial z} = -2\hbar\omega_a\alpha_2(\omega_b; \omega_a)\Phi_b\Phi_a. \quad (\text{D.18})$$

However, because the absorption rates of the two beams are the same, $\partial\Phi_a/\partial z = \partial\Phi_b/\partial z$, therefore

$$\omega_b\alpha_2(\omega_a; \omega_b) = \omega_a\alpha_2(\omega_b; \omega_a). \quad (\text{D.19})$$

Additionally, the two-photon absorption cross section is often used to describe the amount of two-photon absorption per molecule [20], where, for the two beam case, is

$$\frac{\partial \Phi_a}{\partial z} = \frac{\partial \Phi_b}{\partial z} = -2\delta_{2PA}N\Phi_a\Phi_b. \quad (\text{D.20})$$

Comparing this to Equations (D.17) and (D.18) we find

$$\delta_{2PA} = \frac{\hbar\omega_b}{N}\alpha_2(\omega_a; \omega_b) = \frac{\hbar\omega_a}{N}\alpha_2(\omega_b; \omega_a). \quad (\text{D.21})$$

A similar analysis can be made in the three-photon case. The ND-3PA process of one photon at ω_a being absorbed, and two photons at ω_b is governed by

$$\frac{\partial I_a}{\partial z} = -3\alpha_3(\omega_a; \omega_b, \omega_b)I_aI_b^2, \quad (\text{D.22})$$

$$\frac{\partial I_b}{\partial z} = -6\alpha_3(\omega_b; \omega_b, \omega_a)I_b^2I_a. \quad (\text{D.23})$$

Converting to photon flux gives

$$\frac{\partial \Phi_a}{\partial z} = -3(\hbar\omega_b)^2\alpha_3(\omega_a; \omega_b, \omega_b)\Phi_a\Phi_b^2, \quad (\text{D.24})$$

$$\frac{\partial \Phi_b}{\partial z} = -6\hbar\omega_a\hbar\omega_b\alpha_3(\omega_b; \omega_b, \omega_a)\Phi_b^2\Phi_a. \quad (\text{D.25})$$

In this case, $2\partial\Phi_a/\partial z = \partial\Phi_b/\partial z$, therefore

$$\omega_b\alpha_3(\omega_a; \omega_b, \omega_b) = \omega_a\alpha_3(\omega_b; \omega_b, \omega_a). \quad (\text{D.26})$$

A 3PA coefficient may also be defined

$$2 \frac{\partial \Phi_a}{\partial z} = \frac{\partial \Phi_b}{\partial z} = -6\delta_{3PA} N \Phi_a \Phi_b^2. \quad (\text{D.27})$$

Comparing this to Equations (D.24) and (D.25), we find the

$$\delta_{3PA} = \frac{(\hbar\omega_b)^2}{N} \alpha_3(\omega_a; \omega_b, \omega_b) = \frac{\hbar\omega_a \hbar\omega_b}{N} \alpha_3(\omega_b; \omega_b, \omega_a). \quad (\text{D.28})$$

APPENDIX E: SCALED MOMENTUM MATRIX ELEMENTS

Table E.1. Z-components of momentum matrix elements $M_{ij}^Z = \frac{\hbar}{m_0 P} \langle i | p_z | j \rangle$

	$c \alpha$	$c \beta$	$hh \alpha$	$hh \beta$
$c \alpha$	$2a_c c_c \cos \theta$	0	0	$-\frac{a_c}{\sqrt{2}} \sin \theta$
$c \beta$	0	$2a_c c_c \cos \theta$	$-\frac{a_c}{\sqrt{2}} \sin \theta$	0
$hh \alpha$	0	$-\frac{a_c}{\sqrt{2}} \sin \theta$	0	0
$hh \beta$	$-\frac{a_c}{\sqrt{2}} \sin \theta$	0	0	0
$lh \alpha$	$(a_c c_l + c_c a_l) \cos \theta$	$-\frac{(a_c b_l - b_c a_l)}{\sqrt{2}} \sin \theta$	0	$-\frac{a_l}{\sqrt{2}} \sin \theta$
$lh \beta$	$\frac{(a_c b_l - b_c a_l)}{\sqrt{2}} \sin \theta$	$(a_c c_l + c_c a_l) \cos \theta$	$-\frac{a_l}{\sqrt{2}} \sin \theta$	0
$so \alpha$	$(a_c c_s + c_c a_s) \cos \theta$	$-\frac{(a_c b_s - b_c a_s)}{\sqrt{2}} \sin \theta$	0	$-\frac{a_s}{\sqrt{2}} \sin \theta$
$so \beta$	$\frac{(a_c b_s - b_c a_s)}{\sqrt{2}} \sin \theta$	$(a_c c_s + c_c a_s) \cos \theta$	$-\frac{a_s}{\sqrt{2}} \sin \theta$	0

	$lh \alpha$	$lh \beta$	$so \alpha$	$so \beta$
$c \alpha$	$(a_c c_l + c_c a_l) \cos \theta$	$\frac{(a_c b_l - b_c a_l)}{\sqrt{2}} \sin \theta$	$(a_c c_s + c_c a_s) \cos \theta$	$\frac{(a_c b_s - b_c a_s)}{\sqrt{2}} \sin \theta$
$c \beta$	$-\frac{(a_c b_l - b_c a_l)}{\sqrt{2}} \sin \theta$	$(a_c c_l + c_c a_l) \cos \theta$	$-\frac{(a_c b_s - b_c a_s)}{\sqrt{2}} \sin \theta$	$(a_c c_s + c_c a_s) \cos \theta$
$hh \alpha$	0	$-\frac{a_l}{\sqrt{2}} \sin \theta$	0	$-\frac{a_s}{\sqrt{2}} \sin \theta$
$hh \beta$	$-\frac{a_l}{\sqrt{2}} \sin \theta$	0	$-\frac{a_s}{\sqrt{2}} \sin \theta$	0
$lh \alpha$	$2a_l c_l \cos \theta$	0	$(a_l c_s + c_l a_s) \cos \theta$	$\frac{(a_l b_s - b_l a_s)}{\sqrt{2}} \sin \theta$
$lh \beta$	0	$2a_l c_l \cos \theta$	$-\frac{(a_l b_s - b_l a_s)}{\sqrt{2}} \sin \theta$	$(a_l c_s + c_l a_s) \cos \theta$
$so \alpha$	$(a_l c_s + c_l a_s) \cos \theta$	$-\frac{(a_l b_s - b_l a_s)}{\sqrt{2}} \sin \theta$	$2a_s c_s \cos \theta$	0
$so \beta$	$\frac{(a_l b_s - b_l a_s)}{\sqrt{2}} \sin \theta$	$(a_l c_s + c_l a_s) \cos \theta$	0	$2a_s c_s \cos \theta$

Table E.2. X-components of momentum matrix elements $M_{ij}^x = \frac{\hbar}{m_0 P} \langle i | p_x | j \rangle$

	$c \alpha$	$c \beta$	$hh \alpha$	$hh \beta$
$c \alpha$	$2a_c c_c \sin \theta \cos \phi$	0	0	$\frac{a_c}{\sqrt{2}} (\cos \theta \cos \phi + i \sin \phi)$
$c \beta$	0	$2a_c c_c \sin \theta \cos \phi$	$\frac{a_c}{\sqrt{2}} (\cos \theta \cos \phi - i \sin \phi)$	0
$hh \alpha$	0	$\frac{a_c}{\sqrt{2}} (\cos \theta \cos \phi + i \sin \phi)$	0	0
$hh \beta$	$\frac{a_c}{\sqrt{2}} (\cos \theta \cos \phi - i \sin \phi)$	0	0	0
$lh \alpha$	$(a_c c_l + c_c a_l) \sin \theta \cos \phi$	$\frac{(a_c b_l - b_c a_l)}{\sqrt{2}} (\cos \theta \cos \phi - i \sin \phi)$	0	$\frac{a_l}{\sqrt{2}} (\cos \theta \cos \phi + i \sin \phi)$
$lh \beta$	$-\frac{(a_c b_l - b_c a_l)}{\sqrt{2}} (\cos \theta \cos \phi + i \sin \phi)$	$(a_c c_l + c_c a_l) \sin \theta \cos \phi$	$\frac{a_l}{\sqrt{2}} (\cos \theta \cos \phi - i \sin \phi)$	0
$so \alpha$	$(a_c c_s + c_c a_s) \sin \theta \cos \phi$	$\frac{(a_c b_s - b_c a_s)}{\sqrt{2}} (\cos \theta \cos \phi - i \sin \phi)$	0	$\frac{a_s}{\sqrt{2}} (\cos \theta \cos \phi + i \sin \phi)$
$so \beta$	$-\frac{(a_c b_s - b_c a_s)}{\sqrt{2}} (\cos \theta \cos \phi + i \sin \phi)$	$(a_c c_s + c_c a_s) \sin \theta \cos \phi$	$\frac{a_s}{\sqrt{2}} (\cos \theta \cos \phi - i \sin \phi)$	0

	$lh \alpha$	$lh \beta$	$so \alpha$	$so \beta$
$c \alpha$	$(a_c c_l + c_c a_l) \sin \theta \cos \phi$	$-\frac{(a_c b_l - b_c a_l)}{\sqrt{2}} (\cos \theta \cos \phi - i \sin \phi)$	$(a_c c_s + c_c a_s) \sin \theta \cos \phi$	$-\frac{(a_c b_s - b_c a_s)}{\sqrt{2}} (\cos \theta \cos \phi - i \sin \phi)$
$c \beta$	$\frac{(a_c b_l - b_c a_l)}{\sqrt{2}} (\cos \theta \cos \phi + i \sin \phi)$	$(a_c c_l + c_c a_l) \sin \theta \cos \phi$	$\frac{(a_c b_s - b_c a_s)}{\sqrt{2}} (\cos \theta \cos \phi + i \sin \phi)$	$(a_c c_s + c_c a_s) \sin \theta \cos \phi$
$hh \alpha$	0	$\frac{a_l}{\sqrt{2}} (\cos \theta \cos \phi + i \sin \phi)$	0	$\frac{a_s}{\sqrt{2}} (\cos \theta \cos \phi + i \sin \phi)$
$hh \beta$	$\frac{a_l}{\sqrt{2}} (\cos \theta \cos \phi - i \sin \phi)$	0	$\frac{a_s}{\sqrt{2}} (\cos \theta \cos \phi - i \sin \phi)$	0
$lh \alpha$	$2a_l c_l \sin \theta \cos \phi$	0	$(a_l c_s + c_l a_s) \sin \theta \cos \phi$	$-\frac{(a_l b_s - b_l a_s)}{\sqrt{2}} (\cos \theta \cos \phi - i \sin \phi)$
$lh \beta$	0	$2a_l c_l \sin \theta \cos \phi$	$\frac{(a_l b_s - b_l a_s)}{\sqrt{2}} (\cos \theta \cos \phi + i \sin \phi)$	$(a_l c_s + c_l a_s) \sin \theta \cos \phi$
$so \alpha$	$(a_l c_s + c_l a_s) \sin \theta \cos \phi$	$\frac{(a_l b_s - b_l a_s)}{\sqrt{2}} (\cos \theta \cos \phi - i \sin \phi)$	$2a_s c_s \sin \theta \cos \phi$	0
$so \beta$	$-\frac{(a_l b_s - b_l a_s)}{\sqrt{2}} (\cos \theta \cos \phi + i \sin \phi)$	$(a_l c_s + c_l a_s) \sin \theta \cos \phi$	0	$2a_s c_s \sin \theta \cos \phi$

APPENDIX F: COPYWRITE PERMISSION

Matthew Reichert

From: pubscopyright <copyright@osa.org>
Sent: Monday, June 29, 2015 10:30 AM
To: Matthew Reichert
Subject: RE: Figures for dissertation

Dear Mr. Reichert,

Thank you for contacting The Optical Society.

Because you are the author of the source paper from which you wish to reproduce material, OSA considers your requested use of its copyrighted materials to be permissible within the author rights granted in the Copyright Transfer Agreement submitted by the requester on acceptance for publication of his/her manuscript. It is requested that a complete citation of the original material be included in any publication. This permission assumes that the material was not reproduced from another source when published in the original publication.

Please let me know if you have any questions.

Kind Regards,

Susannah Lehman

Susannah Lehman
June 29, 2015
Authorized Agent, The Optical Society

From: Matthew Reichert [mailto:mr22@princeton.edu]
Sent: Friday, June 26, 2015 1:42 PM
To: pubscopyright
Subject: Figures for dissertation

To whom it may concern,

I am currently in the process of completing my dissertation for my Ph.D. in Optics at the University of Central Florida. I'm writing to request permission to use figures published in OSA journal articles that I have co-authored in my dissertation. The specific figures may be found in the following journal articles

Ferdinandus, Manuel R., et al. "Beam deflection measurement of time and polarization resolved ultrafast nonlinear refraction." *Optics letters* 38.18 (2013): 3518-3521.
Figure 2

Ferdinandus, Manuel R., et al. "Dual-arm Z-scan technique to extract dilute solute nonlinearities from solution measurements." *Optical Materials Express* 2.12 (2012): 1776-1790.
Figures 2 and 3

Reichert, Matthew, et al. "Temporal, spectral, and polarization dependence of the nonlinear optical response of carbon disulfide." *Optica* 1.6 (2014): 436-445.
Figures 1 - 6 and S1

Please feel free to contact me at mr22@princeton.edu if you need any further information.

Thank you,

Matthew Reichert
Postdoctoral Research Associate
Department of Electrical Engineering
Princeton University
mr22@princeton.edu

LIST OF REFERENCES

1. Dirac, P.A.M., *The Quantum Theory of Dispersion*. Proceedings of the Royal Society of London. Series A, 1927. **114**(769): p. 710-728.
2. Göppert-Mayer, M., *Über Elementarakte mit zwei Quantensprüngen*. Annalen der Physik, 1931. **401**(3): p. 273-294.
3. Breit, G. and H. Teller, *Metastability of Hydrogen and Helium Levels*. Astrophysical Journal, 1940. **91**: p. 215.
4. Prokhorov, A.M., *Quantum Electronics*. Science, 1965. **149**: p. 828.
5. Sorokin, P.P. and N. Braslau, *Some theoretical aspects of a proposed double quantum stimulated emission device*. IBM J. Res. Dev., 1964. **8**(2): p. 177-181.
6. Letokhov, V.S., *Two-Quantum Amplification of a Short Light Pulse*. JETP Lett, 1967. **7**(8): p. 284.
7. Heatley, D.R., W.J. Firth, and C.N. Ironside, *Ultrashort-pulse generation using two-photon gain*. Opt. Lett., 1993. **18**(8): p. 628-630.
8. Lambropoulos, P., *Quantum Statistics of a Two-Photon Quantum Amplifier*. Physical Review, 1967. **156**(2): p. 286-297.
9. Yuen, H.P., *Two-photon coherent states of the radiation field*. Physical Review A, 1976. **13**(6): p. 2226-2243.
10. Perrie, W., et al., *Polarization Correlation of the Two Photons Emitted by Metastable Atomic Deuterium: A Test of Bell's Inequality*. Physical Review Letters, 1985. **54**(16): p. 1790-1793.
11. Gauthier, D.J., et al., *Realization of a continuous-wave, two-photon optical laser*. Physical Review Letters, 1992. **68**(4): p. 464-467.
12. Pfister, O., et al., *Two-photon stimulated emission in laser-driven alkali-metal atoms using an orthogonal pump-probe geometry*. Physical Review A, 1999. **60**(6): p. R4249-R4252.
13. Hayat, A., P. Ginzburg, and M. Orenstein, *Observation of two-photon emission from semiconductors*. Nat Photon, 2008. **2**(4): p. 238-241.
14. Sheik-Bahae, M., et al., *Dispersion of bound electron nonlinear refraction in solids*. Quantum Electronics, IEEE Journal of, 1991. **27**(6): p. 1296-1309.
15. Cirloganu, C.M., et al., *Extremely nondegenerate two-photon absorption in direct-gap semiconductors [Invited]*. Opt. Express, 2011. **19**(23): p. 22951-22960.

16. Boyd, R.W., *Nonlinear Optics*. 3 ed. 2008: Academic Press. 611.
17. Stegeman, G.I. and R.A. Stegeman, *Nonlinear Optics: Phenomena, Materials and Devices*. Wiley Series in Pure and Applied Optics, ed. G. Boreman. 2012, Hoboken, NJ: John Wiley & Sons, Inc. 488.
18. Agrawal, G.P., *Nonlinear Fiber Optics*. 3 ed. Optics and Photonics, ed. P.L. Kelly, I.P. Kaminow, and G.P. Agrawal. 2001, San Diego, GA: Academic Press.
19. Smith, D.D., et al., *z-scan measurement of the nonlinear absorption of a thin gold film*. Journal of Applied Physics, 1999. **86**(11): p. 6200-6205.
20. Ensley, T.R., et al., *Quasi 3-level Model Applied to Measured Spectra of Nonlinear Absorption and Refraction in Organic Molecules*, To Be Published.
21. Mandelstam, L. and I. Tamm, *The Uncertainty Relation Between Energy and Time in Non-Relativistic Quantum Mechanics*. Journal of Physics, 1945. **IX**(4): p. 249.
22. Hales, J.M., et al., *Resonant enhancement of two-photon absorption in substituted fluorene molecules*. The Journal of Chemical Physics, 2004. **121**(7): p. 3152-3160.
23. Hellwarth, R., *Third-order optical susceptibilities of liquids and solids*. Progress in Quantum Electronics, 1977. **5**: p. 1-68.
24. McMorro, D., et al., *Analysis of Intermolecular Coordinate Contributions to Third-Order Ultrafast Spectroscopy of Liquids in the Harmonic Oscillator Limit*. The Journal of Physical Chemistry A, 2001. **105**(34): p. 7960-7972.
25. Wahlstrand, J.K., et al., *Effect of two-beam coupling in strong-field optical pump-probe experiments*. Physical Review A, 2013. **87**(5): p. 053801.
26. Dogariu, A., et al., *Purely refractive transient energy transfer by stimulated Rayleigh-wing scattering*. J. Opt. Soc. Am. B, 1997. **14**(4): p. 796-803.
27. Samoc, A., *Dispersion of refractive properties of solvents: Chloroform, toluene, benzene, and carbon disulfide in ultraviolet, visible, and near-infrared*. Journal of Applied Physics, 2003. **94**(9): p. 6167-6174.
28. Kedenburg, S., et al., *Linear refractive index and absorption measurements of nonlinear optical liquids in the visible and near-infrared spectral region*. Optical Materials Express, 2012. **2**(11): p. 1588-1611.
29. Ciddor, P.E., *Refractive index of air: new equations for the visible and near infrared*. Applied Optics, 1996. **35**(9): p. 1566-1573.
30. Skauli, T., et al., *Improved dispersion relations for GaAs and applications to nonlinear optics*. Journal of Applied Physics, 2003. **94**(10): p. 6447-6455.

31. Aspnes, D.E., et al., *Optical properties of $Al_xGa_{1-x}As$* . Journal of Applied Physics, 1986. **60**(2): p. 754-767.
32. Kachare, A.H., W.G. Spitzer, and J.E. Fredrickson, *Refractive index of ion-implanted GaAs*. Journal of Applied Physics, 1976. **47**(9): p. 4209-4212.
33. Blakemore, J.S., *Semiconducting and other major properties of gallium arsenide*. Journal of Applied Physics, 1982. **53**(10): p. R123-R181.
34. Sturge, M.D., *Optical Absorption of Gallium Arsenide between 0.6 and 2.75 eV*. Physical Review, 1962. **127**(3): p. 768-773.
35. Casey, H.C., D.D. Sell, and K.W. Wecht, *Concentration dependence of the absorption coefficient for n- and p-type GaAs between 1.3 and 1.6 eV*. Journal of Applied Physics, 1975. **46**(1): p. 250-257.
36. Adachi, S., *The Handbook on Optical Constants of Semiconductors: In Tables and Figures*. 2012: World Scientific.
37. Wall, K.F. and A. Sanchez, *Titanium sapphire lasers*. The Lincoln Laboratory Journal, 1990. **3**(3): p. 447-462.
38. Tavella, F., A. Marcinkevičius, and F. Krausz, *Investigation of the superfluorescence and signal amplification in an ultrabroadband multiterawatt optical parametric chirped pulse amplifier system*. New Journal of Physics, 2006. **8**(10): p. 219.
39. Bonifacio, R. and L.A. Lugiato, *Cooperative radiation processes in two-level systems: Superfluorescence*. Physical Review A, 1975. **11**(5): p. 1507-1521.
40. Chen, Y.H., et al., *Direct Measurement of the Electron Density of Extended Femtosecond Laser Pulse-Induced Filaments*. Physical Review Letters, 2010. **105**(21): p. 215005.
41. Nibbering, E.T.J., et al., *Conical emission from self-guided femtosecond pulses in air*. Optics Letters, 1996. **21**(1): p. 62-64.
42. Braun, A., et al., *Self-channeling of high-peak-power femtosecond laser pulses in air*. Optics Letters, 1995. **20**(1): p. 73-75.
43. Mlejnek, M., E.M. Wright, and J.V. Moloney, *Dynamic spatial replenishment of femtosecond pulses propagating in air*. Optics Letters, 1998. **23**(5): p. 382-384.
44. Brodeur, A., et al., *Moving focus in the propagation of ultrashort laser pulses in air*. Optics Letters, 1997. **22**(5): p. 304-306.
45. Ensley, T.R., et al., *Energy and spectral enhancement of femtosecond supercontinuum in a noble gas using a weak seed*. Optics Express, 2011. **19**(2): p. 757-763.

46. Sheik-Bahae, M., A.A. Said, and E.W. Van Stryland, *High-sensitivity, single-beam n_2 measurements*. Optics Letters, 1989. **14**(17): p. 955-957.
47. Sheik-Bahae, M., et al., *Sensitive measurement of optical nonlinearities using a single beam*. Quantum Electronics, IEEE Journal of, 1990. **26**(4): p. 760-769.
48. Sheik-Bahae, M., et al., *Nonlinear refraction and optical limiting in "thick" media*. Optical Engineering, 1991. **30**(8): p. 1228-1235.
49. Ferdinandus, M.R., et al., *Dual-arm Z-scan technique to extract dilute solute nonlinearities from solution measurements*. Opt. Mater. Express, 2012. **2**(12): p. 1776-1790.
50. Ferdinandus, M., *Techniques for Characterization of Third Order Optical Nonlinearities*, in *CREOL, The College of Optics and Photonics*. 2013, University of Central Florida. p. 207.
51. Ensley, T.R., *White-Light Continuum for Broadband Nonlinear Spectroscopy*, in *CREOL, The College of Optics and Photonics*. 2015, University of Central Florida.
52. Ensley, T.R., et al. *Nonlinear Characterization of Thin Films by the Dual-Arm Z-scan Method*. in *Frontiers in Optics 2013*. 2013. Orlando, Florida: Optical Society of America.
53. Negres, R.A., et al., *Experiment and analysis of two-photon absorption spectroscopy using a white-light continuum probe*. Quantum Electronics, IEEE Journal of, 2002. **38**(9): p. 1205-1216.
54. Temple, P.A., *An introduction to phase-sensitive amplifiers: An inexpensive student instrument*. American Journal of Physics, 1975. **43**(9): p. 801-807.
55. Probst, P.A. and B. Collet, *Low-frequency digital lock-in amplifier*. Review of Scientific Instruments, 1985. **56**(3): p. 466-470.
56. *About Lock-In Amplifiers*. Stanford Research Systems. p. 9.
57. Peceli, D., et al., *Optimization of the Double Pump-Probe Technique: Decoupling the Triplet Yield and Cross Section*. The Journal of Physical Chemistry A, 2012. **116**(20): p. 4833-4841.
58. Reichardt, T.A., et al., *Theoretical investigation of the forward phase-matched geometry for degenerate four-wave mixing spectroscopy*. Journal of the Optical Society of America B, 1998. **15**(10): p. 2566-2572.
59. Eichler, H.J., P. Günter, and D.W. Pohl, *Laser-induced dynamic gratings*. Vol. 50. 1986: Springer-Verlag Berlin.

60. Levenson, M.D. and G.L. Eesley, *Polarization selective optical heterodyne detection for dramatically improved sensitivity in laser spectroscopy*. Applied physics, 1979. **19**(1): p. 1-17.
61. Ferdinandus, M.R., et al., *Beam deflection measurement of time and polarization resolved ultrafast nonlinear refraction*. Optics Letters, 2013. **38**(18): p. 3518-3521.
62. Reichert, M., et al., *Temporal, spectral, and polarization dependence of the nonlinear optical response of carbon disulfide*. Optica, 2014. **1**(6): p. 436-445.
63. Jackson, W.B., et al., *Photothermal deflection spectroscopy and detection*. Applied Optics, 1981. **20**(8): p. 1333-1344.
64. Spear, J.D. and R.E. Russo, *Transverse photothermal beam deflection within a solid*. Journal of Applied Physics, 1991. **70**(2): p. 580-586.
65. Meyer, E., *Atomic force microscopy*. Progress in Surface Science, 1992. **41**(1): p. 3-49.
66. Goodman, J.W., *Introduction to Fourier Optics, 3rd Edition*. 2005: Roberts & Company Publishers.
67. McMorrow, D., W.T. Lotshaw, and G.A. Kenney-Wallace, *Femtosecond optical Kerr studies on the origin of the nonlinear responses in simple liquids*. IEEE Journal of Quantum Electronics, 1988. **24**(2): p. 443-454.
68. Raj, R.K., et al., *High-Frequency Optically Heterodyned Saturation Spectroscopy Via Resonant Degenerate Four-Wave Mixing*. Physical Review Letters, 1980. **44**(19): p. 1251-1254.
69. Milam, D., *Review and Assessment of Measured Values of the Nonlinear Refractive-Index Coefficient of Fused Silica*. Applied Optics, 1998. **37**(3): p. 546-550.
70. Zhao, P., et al. *Beam Deflection Measurements of Nondegenerate Nonlinear Refractive Indices in Direct-gap Semiconductors*. in *CLEO*. 2015. San Jose, CA: Optical Society of America.
71. Kaiser, W. and C.G.B. Garrett, *Two-Photon Excitation in CaF₂: Eu²⁺*. Physical Review Letters, 1961. **7**(6): p. 229-231.
72. Xu, C. and W.W. Webb, *Measurement of two-photon excitation cross sections of molecular fluorophores with data from 690 to 1050 nm*. Journal of the Optical Society of America B, 1996. **13**(3): p. 481-491.
73. Belfield, K.D., et al., *One- and Two-Photon Stimulated Emission Depletion of a Sulfonyl-Containing Fluorene Derivative*. The Journal of Physical Chemistry B, 2009. **113**(20): p. 7101-7106.

74. Nevet, A., A. Hayat, and M. Orenstein, *Measurement of Optical Two-Photon Gain in Electrically Pumped AlGaAs at Room Temperature*. Physical Review Letters, 2010. **104**(20): p. 207404.
75. Hell, S.W. and J. Wichmann, *Breaking the diffraction resolution limit by stimulated emission: stimulated-emission-depletion fluorescence microscopy*. Optics Letters, 1994. **19**(11): p. 780-782.
76. Purwar, H., et al., *Collinear, two-color optical Kerr effect shutter for ultrafast time-resolved imaging*. Optics Express, 2014. **22**(13): p. 15778-15790.
77. Falcão-Filho, E.L., et al., *Robust Two-Dimensional Spatial Solitons in Liquid Carbon Disulfide*. Physical Review Letters, 2013. **110**(1): p. 013901.
78. Pricking, S. and H. Giessen, *Generalized retarded response of nonlinear media and its influence on soliton dynamics*. Optics Express, 2011. **19**(4): p. 2895-2903.
79. Churin, D., et al., *Mid-IR supercontinuum generation in an integrated liquid-core optical fiber filled with CS₂*. Optical Materials Express, 2013. **3**(9): p. 1358-1364.
80. Herrera, O.D., et al., *Slow light based on stimulated Raman scattering in an integrated liquid-core optical fiber filled with CS₂*. Optics Express, 2013. **21**(7): p. 8821-8830.
81. Sahu, S., R.R. Pal, and S. Dhar, *Nonlinear Material Based All-Optical Parallel Subtraction Scheme: an Implementation*. International Journal of Optoelectronic Engineering, 2011. **1**(1): p. 7-11.
82. Ganeev, R.A., et al., *Nonlinear refraction in CS₂*. Applied Physics B, 2004. **78**(3-4): p. 433-438.
83. Willetts, A., et al., *Problems in the comparison of theoretical and experimental hyperpolarizabilities*. The Journal of Chemical Physics, 1992. **97**(10): p. 7590-7599.
84. Kiyohara, K., K. Kamada, and K. Ohta, *Orientational and collision-induced contribution to third-order nonlinear optical response of liquid CS₂*. The Journal of Chemical Physics, 2000. **112**(14): p. 6338-6348.
85. Kivelson, D. and P. Madden, *Light scattering studies of molecular liquids*. Annual Review of Physical Chemistry, 1980. **31**(1): p. 523-558.
86. Tzer-Hsiang, H., et al., *The transient optical Kerr effect of simple liquids studied with an ultrashort laser with variable pulsewidth*. Selected Topics in Quantum Electronics, IEEE Journal of, 1996. **2**(3): p. 756-768.
87. Sato, Y., R. Morita, and M. Yamashita, *Study on Ultrafast Dynamic Behaviors of Different Nonlinear Refractive Index Components in CS₂ Using a Femtosecond Interferometer*. Jpn. J. Appl. Phys., 1997. **36**(Part 1, No. 4A): p. 2109-2115.

88. Debye, P., *Polar molecules*. 1929, Dover.
89. Cubeddu, R., et al., *Self-Phase Modulation and "Rocking" of Molecules in Trapped Filaments of Light with Picosecond Pulses*. *Physical Review A*, 1970. **2**(5): p. 1955-1963.
90. Shelton, D.P. and J.E. Rice, *Measurements and calculations of the hyperpolarizabilities of atoms and small molecules in the gas phase*. *Chemical Reviews*, 1994. **94**(1): p. 3-29.
91. Greene, B.I., et al., *Microscopic dynamics in simple liquids by subpicosecond birefringences*. *Physical Review A*, 1984. **29**(1): p. 271-274.
92. Bucaro, J.A. and T.A. Litovitz, *Rayleigh Scattering: Collisional Motions in Liquids*. *The Journal of Chemical Physics*, 1971. **54**(9): p. 3846-3853.
93. Ziólek, M., M. Lorenc, and R. Naskrecki, *Determination of the temporal response function in femtosecond pump-probe systems*. *Applied Physics B*, 2001. **72**(7): p. 843-847.
94. Diels, J.-C. and W. Rudolph, *Ultrashort laser pulse phenomena*. 2006: Academic press.
95. Firester, A.H., M.E. Heller, and P. Sheng, *Knife-edge scanning measurements of subwavelength focused light beams*. *Applied Optics*, 1977. **16**(7): p. 1971-1974.
96. Malitson, I.H., *Interspecimen Comparison of the Refractive Index of Fused Silica*. *Journal of the Optical Society of America*, 1965. **55**(10): p. 1205-1208.
97. Yariv, A. and P. Yeh, *Optical waves in crystals*. Vol. 10. 1984: Wiley, New York.
98. Constantine, S., et al., *A Novel Technique for the Measurement of Polarization-Specific Ultrafast Raman Responses*. *The Journal of Physical Chemistry A*, 2001. **105**(43): p. 9851-9858.
99. Fecko, C.J., J.D. Eaves, and A. Tokmakoff, *Isotropic and anisotropic Raman scattering from molecular liquids measured by spatially masked optical Kerr effect spectroscopy*. *The Journal of Chemical Physics*, 2002. **117**(3): p. 1139-1154.
100. Xu, Q.-H., Y.-Z. Ma, and G.R. Fleming, *Heterodyne detected transient grating spectroscopy in resonant and non-resonant systems using a simplified diffractive optics method*. *Chemical Physics Letters*, 2001. **338**(4-6): p. 254-262.
101. Wang, D., K. Mittauer, and N. Reynolds, *Raman scattering of carbon disulfide: The temperature effect*. *American Journal of Physics*, 2009. **77**(12): p. 1130-1134.
102. Steffen, T. and K. Duppen, *Time resolved four- and six-wave mixing in liquids. II. Experiments*. *The Journal of Chemical Physics*, 1997. **106**(10): p. 3854-3864.

103. Steffen, T., N.A.C.M. Meinders, and K. Duppen, *Microscopic Origin of the Optical Kerr Effect Response of CS₂–Pentane Binary Mixtures*. The Journal of Physical Chemistry A, 1998. **102**(23): p. 4213-4221.
104. Tokmakoff, A. and G.R. Fleming, *Two-dimensional Raman spectroscopy of the intermolecular modes of liquid CS₂*. The Journal of Chemical Physics, 1997. **106**(7): p. 2569-2582.
105. Scarparo, M.A.F., J.H. Lee, and J.J. Song, *Near-zero-frequency stimulated Raman gain spectroscopy in CS₂*. Optics Letters, 1981. **6**(4): p. 193-195.
106. Corporation, N. *APPLICATION NOTE 29: Prism Compressor for Ultrashort Laser Pulses*. 2006.
107. Sweetser, J.N., D.N. Fittinghoff, and R. Trebino, *Transient-grating frequency-resolved optical gating*. Optics Letters, 1997. **22**(8): p. 519-521.
108. Hecht, E., *Optics, 4th*. International edition, Addison-Wesley, San Francisco, 2002.
109. Kovsh, D.I., et al., *Nonlinear Optical Beam Propagation for Optical Limiting*. Applied Optics, 1999. **38**(24): p. 5168-5180.
110. Hu, H., *Third Order Nonlinearity of Organic Molecules*, in *CREOL, The College of Optics and Photonics*. 2012, University of Central Florida. p. 250.
111. Orr, B.J. and J.F. Ward, *Perturbation theory of the non-linear optical polarization of an isolated system*. Molecular Physics, 1971. **20**(3): p. 513-526.
112. Kuzyk, M.G. and C.W. Dirk, *Effects of centrosymmetry on the nonresonant electronic third-order nonlinear optical susceptibility*. Physical Review A, 1990. **41**(9): p. 5098-5109.
113. Rau, I., et al., *Comparison of Z-scan and THG derived nonlinear index of refraction in selected organic solvents*. Journal of the Optical Society of America B, 2008. **25**(10): p. 1738-1747.
114. Hoskins, L.C., *Pure rotational Raman spectroscopy of diatomic molecules*. Journal of Chemical Education, 1975. **52**(9): p. 568.
115. Kumpli, D.S., H.M. Frey, and S. Leutwyler, *Femtosecond degenerate four-wave mixing of carbon disulfide: High-accuracy rotational constants*. The Journal of Chemical Physics, 2006. **124**(14): p. 144307.
116. Meystre, P. and M. Sargent, *Elements of quantum optics*. 2007: Springer Science & Business Media.

117. Lin, C.H., et al., *Birefringence arising from the reorientation of the polarizability anisotropy of molecules in collisionless gases*. Physical Review A, 1976. **13**(2): p. 813-829.
118. Chen, Y.H., et al., *Single-shot, space- and time-resolved measurement of rotational wavepacket revivals in H₂, D₂, N₂, O₂, and N₂O*. Optics Express, 2007. **15**(18): p. 11341-11357.
119. Siegman, A.E., *Lasers*. 1986, University Science Books: Mill Valley, CA. p. 1283.
120. Reichert, M., et al., *Beam Deflection Measurement of Bound-Electronic and Rotational Nonlinear Refraction in Molecular Gases*. Submitted to Optics Express, 2015.
121. Irikura, K.K., *Experimental Vibrational Zero-Point Energies: Diatomic Molecules*. Journal of Physical and Chemical Reference Data, 2007. **36**(2): p. 389-397.
122. Sutton, L.E., *Tables of Interatomic Distances and Configuration in Molecules and Ions: Supplement 1956-59*. 1965: Chemical Society.
123. McClure, M.R. *Oxygen*. Interactive Periodic Table 2009 [cited 2015 March, 13]; Available from: <http://www2.uncp.edu/home/mcclurem/ptable/o.htm>.
124. Bridge, N.J. and A.D. Buckingham, *The Polarization of Laser Light Scattered by Gases*. Vol. 295. 1966. 334-349.
125. Bogaard, M.P., et al., *Rayleigh scattering depolarization ratio and molecular polarizability anisotropy for gases*. Journal of the Chemical Society, Faraday Transactions 1: Physical Chemistry in Condensed Phases, 1978. **74**(0): p. 3008-3015.
126. Wahlstrand, J.K., Y.H. Cheng, and H.M. Milchberg, *Absolute measurement of the transient optical nonlinearity in N₂, O₂, N₂O, and Ar*. Physical Review A, 2012. **85**(4): p. 043820.
127. Liu, W. and S. Chin, *Direct measurement of the critical power of femtosecond Ti:sapphire laser pulse in air*. Optics Express, 2005. **13**(15): p. 5750-5755.
128. Heritage, J.P., T.K. Gustafson, and C.H. Lin, *Observation of Coherent Transient Birefringence in C₂S Vapor*. Physical Review Letters, 1975. **34**(21): p. 1299-1302.
129. Agar, D., E.K. Plyler, and E.D. Tidwell, *High resolution investigation of some infrared bands of carbon disulfide*. Journal of Research of National Bureau of Standards, 1962. **66A**(3).
130. Herzberg, G., *l-Type Doubling in Linear Polyatomic Molecules*. Reviews of Modern Physics, 1942. **14**(2-3): p. 219-223.

131. Ohta, K., et al., *Ab initio molecular orbital calculation of the second hyperpolarizability of the carbon disulfide molecule: electron correlation and frequency dispersion*. Chemical Physics Letters, 1997. **274**(1–3): p. 306-314.
132. Page, T.L., *The continuous spectra of certain planetary nebulae : a photometric study*. Monthly Notices of the Royal Astronomical Society, 1936. **96**: p. 604.
133. Spitzer, J., L. and J.L. Greenstein, *Continuous Emission from Planetary Nebulae*. Astrophysical Journal, 1951. **114**: p. 407.
134. Hayat, A., et al., *Hyperentanglement source by intersubband two-photon emission from semiconductor quantum wells*. Opt. Lett., 2008. **33**(11): p. 1168-1170.
135. Lipeles, M., R. Novick, and N. Tolk, *Direct Detection of Two-Photon Emission from the Metastable State of Singly Ionized Helium*. Physical Review Letters, 1965. **15**(17): p. 690-693.
136. Elton, R.C., L.J. Palumbo, and H.R. Griem, *Observation of Two-Photon Continuum Emission from Neon IX*. Physical Review Letters, 1968. **20**(15): p. 783-786.
137. Schmieder, R.W. and R. Marrus, *Two-Phonon Decay and Lifetime of the $2^2S_{1/2}$ State of Hydrogenlike Argon*. Physical Review Letters, 1970. **25**(25): p. 1692-1695.
138. Marrus, R. and R.W. Schmieder, *Forbidden Decays of Hydrogenlike and Heliumlike Argon*. Physical Review A, 1972. **5**(3): p. 1160-1173.
139. Ali, R., et al., *Shape of the two-photon-continuum emission from the $1s2s^1S_0$ state in He-like krypton*. Physical Review A, 1997. **55**(2): p. 994-1006.
140. Bannett, Y. and I. Freund, *Two-Photon X-Ray Emission from Inner-Shell Transitions*. Physical Review Letters, 1982. **49**(8): p. 539-542.
141. Ota, Y., et al., *Spontaneous Two-Photon Emission from a Single Quantum Dot*. Physical Review Letters, 2011. **107**(23): p. 233602.
142. Yatsiv, S., M. Rokni, and S. Barak, *Enhanced Two-Photon Emission*. Physical Review Letters, 1968. **20**(23): p. 1282-1284.
143. Bräunlich, P., R. Hall, and P. Lambropoulos, *Laser-Induced Quenching of Metastable Deuterium Atoms. Singly Stimulated Two-Photon Emission and Anti-Stokes Raman Scattering*. Physical Review A, 1972. **5**(3): p. 1013-1025.
144. Zych, L.J., et al., *Laser-Induced Two-Photon Blackbody Radiation in the Vacuum Ultraviolet*. Physical Review Letters, 1978. **40**(23): p. 1493-1496.
145. Gao, J.Y., et al., *Scheme for investigation of two-photon emission in sodium*. J. Opt. Soc. Am. B, 1984. **1**(4): p. 606-608.

146. Loy, M.M.T., *Two-Photon Adiabatic Inversion*. Physical Review Letters, 1978. **41**(7): p. 473-476.
147. Nikolaus, B., D.Z. Zhang, and P.E. Toschek, *Two-Photon Laser*. Physical Review Letters, 1981. **47**(3): p. 171-173.
148. Brune, M., et al., *Realization of a two-photon maser oscillator*. Physical Review Letters, 1987. **59**(17): p. 1899-1902.
149. Nevet, A., A. Hayat, and M. Orenstein, *Ultrafast pulse compression by semiconductor two-photon gain*. Opt. Lett., 2010. **35**(23): p. 3877-3879.
150. Pfister, O., et al., *Polarization Instabilities in a Two-Photon Laser*. Physical Review Letters, 2001. **86**(20): p. 4512-4515.
151. Gauthier, D., J., *Two-photon lasers*, in *Progress in Optics*, E. Wolf, Editor. 2003, Elsevier Science & Technology. p. 205-272.
152. Ironside, C.N., *Two-photon gain semiconductor amplifier*. Quantum Electronics, IEEE Journal of, 1992. **28**(4): p. 842-847.
153. Pattanaik, H., et al. *Two-photon emission in direct-gap semiconductors*. 2011. Optical Society of America.
154. Marti, D.H., M.A. Dupertuis, and B. Deveaud, *Feasibility study for degenerate two-photon gain in a semiconductor microcavity*. Quantum Electronics, IEEE Journal of, 2003. **39**(9): p. 1066-1073.
155. Concannon, H.M. and D.J. Gauthier, *Simple rate-equation model for two-photon lasers*. Opt. Lett., 1994. **19**(7): p. 472-474.
156. Xu, C. and W.W. Webb, *Measurement of two-photon excitation cross sections of molecular fluorophores with data from 690 to 1050 nm*. J. Opt. Soc. Am. B, 1996. **13**(3): p. 481-491.
157. Hayat, A., P. Ginzburg, and M. Orenstein, *High-rate entanglement source via two-photon emission from semiconductor quantum wells*. Physical Review B, 2007. **76**(3): p. 035339.
158. Lin, Z. and J. Vučković, *Enhanced two-photon processes in single quantum dots inside photonic crystal nanocavities*. Physical Review B, 2010. **81**(3): p. 035301.
159. Valle, E.d., et al., *Generation of a two-photon state from a quantum dot in a microcavity*. New Journal of Physics, 2011. **13**(11): p. 113014.
160. del Valle, E., et al., *Two-photon lasing by a single quantum dot in a high-Q microcavity*. Physical Review B, 2010. **81**(3): p. 035302.

161. Concannon, H.M., et al., *Observation of large continuous-wave two-photon optical amplification*. Physical Review A, 1997. **56**(2): p. 1519-1523.
162. Van Stryland, E.W., et al., *Energy band gap dependence of two-photon absorption*. Opt. Lett., 1985. **10**(10): p. 490-492.
163. Wherrett, B.S., *Scaling rules for multiphoton interband absorption in semiconductors*. J. Opt. Soc. Am. B, 1984. **1**(1): p. 67-72.
164. Fishman, D.A., et al., *Sensitive mid-infrared detection in wide-band gap semiconductors using extreme non-degenerate two-photon absorption*. Nat Photon, 2011. **5**(9): p. 561-565.
165. Uenishi, Y., H. Tanaka, and H. Ukita, *Characterization of AlGaAs microstructure fabricated by AlGaAs/GaAs micromachining*. Electron Devices, IEEE Transactions on, 1994. **41**(10): p. 1778-1783.
166. Beard, M.C., G.M. Turner, and C.A. Schmuttenmaer, *Transient photoconductivity in GaAs as measured by time-resolved terahertz spectroscopy*. Physical Review B, 2000. **62**(23): p. 15764-15777.
167. Krishnamurthy, S., et al., *Temperature- and wavelength-dependent two-photon and free-carrier absorption in GaAs, InP, GaInAs, and InAsP*. Journal of Applied Physics, 2011. **109**(3): p. 033102-9.
168. Mayer, E.J., et al., *Infrared absorption spectra of photoexcited holes in undoped GaAs*. Physical Review B, 1992. **46**(3): p. 1878-1881.
169. Cirloganu, C.M., et al., *Three-photon absorption spectra of zinc blende semiconductors: theory and experiment*. Optics Letters, 2008. **33**(22): p. 2626-2628.
170. Hutchings, D.C. and E.W.V. Stryland, *Nondegenerate two-photon absorption in zinc blende semiconductors*. J. Opt. Soc. Am. B, 1992. **9**(11): p. 2065-2074.
171. Cirloganu, C.M., *Experimental and Theoretical Approaches to Characterization of Electronic Nonlinearities in Direct-Gap Semiconductors*, in *CREOL, The College of Optics and Photonics*. 2010, University of Central Florida. p. 160.
172. Peceli, D., *Absorptive and Refractive Optical Nonlinearities in Organic Molecules and Semiconductors*, in *CREOL, The College of Optics and Photonics*. 2013, University of Central Florida. p. 210.
173. Burr, K.C. and C.L. Tang, *Femtosecond midinfrared-induced luminescence study of the ultrafast dynamics of split-off holes in GaAs*. Applied Physics Letters, 1999. **74**(12): p. 1734-1736.
174. Woerner, M., *Ultrafast Hole Relaxation in Semiconductors*. Laser Physics, 1995. **5**(3): p. 611-615.

175. Vurgaftman, I., J.R. Meyer, and L.R. Ram-Mohan, *Band parameters for III–V compound semiconductors and their alloys*. Journal of Applied Physics, 2001. **89**(11): p. 5815-5875.
176. Born, M., *Atomic physics*. 1989: Courier Corporation.
177. Kane, E.O., *Band structure of indium antimonide*. Journal of Physics and Chemistry of Solids, 1957. **1**(4): p. 249-261.
178. Chuang, S.L., *Physics of Optoelectronic Devices*. Wiley Series in Pure and Applied Optics, ed. J.W. Goodman. 1995, New York: Wiley-Interscience.
179. Schwartz, M., *Principles of electrodynamics*. 2012: Courier Corporation.
180. Beyer, W.H., et al., *CRC standard mathematical tables*. 1975, Cleveland, Ohio: CRC Press.
181. Hermann, C. and C. Weisbuch, *k-dot-p perturbation theory in III-V compounds and alloys: a reexamination*. Physical Review B, 1977. **15**(2): p. 823-833.
182. Zory, P.S., *Quantum well lasers*. 1993: Academic Press.
183. Olszak, P.D., *NONLINEAR ABSORPTION AND FREE CARRIER RECOMBINATION IN DIRECT GAP SEMICONDUCTORS*, in *CREOL, the College of Optics and Photonics*. 2010, University of Central Florida: Orlando, FL. p. 148.
184. Unger, K., *Reversible Formulae to Approximate Fermi Integrals*. physica status solidi (b), 1988. **149**(2): p. K141-K144.
185. Coldren, L.A., S.W. Corzine, and M.L. Mashanovitch, *Diode lasers and photonic integrated circuits*. Vol. 218. 2012: John Wiley & Sons.
186. Streetman, B.G. and S. Banerjee, *Solid state electronic devices*. Vol. 4. 2000: Prentice Hall Upper Saddle River, NJ.
187. Fan, H.Y., W. Spitzer, and R.J. Collins, *Infrared Absorption in n-Type Germanium*. Physical Review, 1956. **101**(2): p. 566-572.
188. Spitzer, W.G. and J.M. Whelan, *Infrared Absorption and Electron Effective Mass in n -Type Gallium Arsenide*. Physical Review, 1959. **114**(1): p. 59-63.
189. Peceli, D., et al. *Three-Photon Absorption of GaAs and other Semiconductors*. in *Nonlinear Optics*. 2013. Kohala Coast, Hawaii, United States: Optical Society of America.
190. Saleh, B.E. and M.C. Teich, *Fundamentals of Photonics*. 2nd ed. 2007: Wiley Series in Pure and Applied Optics. ISBN.

191. Brandi, H.S. and C.B.d. Araujos, *Multiphonon absorption coefficients in solids: a universal curve*. Journal of Physics C: Solid State Physics, 1983. **16**(30): p. 5929.
192. Bougrov, V., et al., *Gallium Nitride (GaN)*. Properties of Advanced Semiconductor Materials: GaN, AlN, InN, BN, SiC, SiGe, 2001.
193. Welna, M., et al., *Transparency of GaN substrates in the mid-infrared spectral range*. Crystal Research and Technology, 2012. **47**(3): p. 347-350.
194. Kioupakis, E., et al., *Free-carrier absorption in nitrides from first principles*. Physical Review B, 2010. **81**(24): p. 241201.
195. Spector, H.N., *Two-photon absorption in semiconducting quantum-well structures*. Physical Review B, 1987. **35**(11): p. 5876-5879.
196. Pasquarello, A. and A. Quattropani, *Gauge-invariant two-photon transitions in quantum wells*. Physical Review B, 1988. **38**(9): p. 6206-6210.
197. Tai, K., et al., *Two-photon absorption spectroscopy in GaAs quantum wells*. Physical Review Letters, 1989. **62**(15): p. 1784-1787.
198. Pasquarello, A. and A. Quattropani, *Effect of continuum states on two-photon absorption in quantum wells*. Physical Review B, 1990. **41**(18): p. 12728-12734.
199. Khurgin, J.B., *Nonlinear response of the semiconductor quantum-confined structures near and below the middle of the band gap*. Journal of the Optical Society of America B, 1994. **11**(4): p. 624-631.
200. Pattanaik, H.S., Reichert, Matthew, Khurgin, Jacob B., Hagan, David J., and Van Stryland, Eric W., *Large Enhancement of Two-photon Absorption in Quantum Well Structures for Extremely Nondegenerate Photon Pairs*. to be submitted.
201. Pattanaik, H.S., *TWO-PHOTON ABSORPTION IN BULK SEMICONDUCTORS AND QUANTUM WELL STRUCTURES AND ITS APPLICATIONS*, in *CREOL, The College of Optics and Photonics*. 2015, University of Central Florida: Orlando, FL. p. 136.
202. Ostromek, T.E., *Evaluation of matrix elements of the 8×8 $k \cdot p$ Hamiltonian with k -dependent spin-orbit contributions for the zinc blende structure of GaAs*. Physical Review B, 1996. **54**(20): p. 14467-14479.
203. Fuller, G.H., *Nuclear Spins and Moments*. Journal of Physical and Chemical Reference Data, 1976. **5**(4): p. 835-1092.
204. Atkins, P. and J. De Paula, *Elements of physical chemistry*. 2012: Oxford University Press.
205. de Laeter John, R., et al., *Atomic weights of the elements. Review 2000 (IUPAC Technical Report)*, in *Pure and Applied Chemistry*. 2003. p. 683.

206. Shimanouchi, T., *Tables of Molecular Vibrational Frequencies Consolidated. Volume I.* 1972, DTIC Document.
207. Abramowitz, M. and I.A. Stegun, *Handbook of mathematical functions.* Vol. 1. 1972: Dover New York.